Plasma Physics Reports, Vol. 30, No. 6, 2004, pp. 443–472. Translated from Fizika Plazmy, Vol. 30, No. 6, 2004, pp. 483–513.

TOKAMAKS

Kinetics of Impurity Charge-State Distributions in Tokamak Plasmas

V. A. Shurygin

Nuclear Fusion Institute, Russian Research Centre Kurchatov Institute, pl. Kurchatova 1, Moscow, 123182 Russia

Received May 21, 2003

Abstract—An analysis of impurity behavior in tokamak plasmas with the use of the observation results on impurity emission shows that it is necessary to distinguish between the ion dynamics (for example, ion transport) and ion kinetics, i.e., the processes related to the motion of ions on the charge states and/or excited states due to atomic processes in plasma. This paper presents a systematic analysis of the kinetics of impurity charge-state distributions and the related effects, as well as their typical scales and conditions for their observation. The quantitative analysis is performed in terms of the lowest moments of charge-state distributions such as the average charge m and dispersion D. Analytic approaches to solving charge-state kinetic equations are considered. An approach based on the symmetry properties of the kinetic matrix is proposed for the first time. The simplest types of impurity charge-state kinetics and the most important limiting cases are considered. A detailed analysis of the nonstationary behavior of the function of the moments $D(m)$ of the charge-state distribution is presented. A quantitative analysis of the available experimental and model charge-state distributions of C, O, Ne, and Ar impurities in the JET, DIII-D, TORE SUPRA, ALCATOR-C, TEXTOR, PLT, TFR, and DAMAVAND tokamaks is performed in terms of the moments $D(m)$. It is shown that the moments $D(m)$ of the model charge-state distributions of the above impurities in the plasma core are essentially insensitive to the empirical diffusion coefficient. The equivalent curves $D(m)$ obtained for the plasma periphery can be attributed to the convective fluxes of ionizing and/or recombining impurity ions. © *2004 MAIK "Nauka/Interperiodica".*

1. INTRODUCTION

An important characteristic of the behavior of a plasma impurity in a tokamak is its ionization state, usually represented by the distribution of ions on their charge states [1, 2]. Systematic observations and an analysis of the impurity emission that are performed, e.g., in investigating the impurity transport and radiative losses, as well as in solving the various problems of plasma diagnostics, lead to the necessity of a detailed study of the impurity charge-state distribution.

A complete description of a set of discrete impurity charge states is usually considered to be a key problem of such research. A comprehensive analysis of the behavior of impurity charge-state distributions is fairly sophisticated. Indeed, it is necessary to take into account both the dynamics of ions, i.e., their motion in the plasma (in particular, ion transport), and their kinetics, i.e., the change of the ion distributions on charge states and/or excited states due to atomic processes in plasma. As a rule, the behavior of impurities is described by a standard set of coupled transport equations with the use of empirical coefficients of diffusion D_A and convection V_A (which are usually anomalous with respect to the their neoclassical values) and the database on atomic processes. Impurity transport codes such as MIST [3], STRAHL [4], RITM [5], and SANCO [6] are widely used.

However, both in experimental practice and within the framework of computer simulations, a more correct formulation of the problem appears that is related to the need for distinguishing (both qualitatively and quantitatively) between the dynamics (transport) and kinetics (atomic processes) of impurity ions. It is the solution of this problem at which impurity transport investigations are aimed.

At first glance, the use of transport equations allows one to solve this problem automatically. However, in practice, the analysis of the difference between the dynamics and kinetics of impurity ions is largely ignored. In fact, it is substituted and restricted by the procedure of the determination of D_A and V_A.

The problem is that, to calculate D_A and V_A, it is necessary to assume that the simulations of charge-state kinetics are perfectly accurate [7]. Only in this case do D_A and V_A provide the actual impurity transport. In fact, the fitting coefficients D_A and V_A comprise all errors of kinetic simulations (both theoretical and experimental). The kinetic processes, which are difficult to take into account in analysis but are often observed in experiments, lead to anomalous values of D_A and V_A. Let us consider the possible consequences of this practice.

First, there is a lower limit of the sensitivity of these calculations to D_A and V_A. It depends strongly on the uncertainties of the analysis. However, in spite of the above limitations, the coefficient D_A varies within a

1063-780X/04/3006-0443$26.00 © 2004 MAIK "Nauka/Interperiodica"

very wide range (see, e.g., [8]): from 0.02 m^2/s (which corresponds to neoclassical values) to 3×10^2 m^2/s (a typical value used to describe disruptions in tokamaks). The lower limit assumes an almost perfect accuracy of the description of all the atomic processes, while the upper limit is directly related to uncertainties in the kinetics under the disruption conditions and represents the scales of these uncertainties. The lack of the analysis of these uncertainties results in that the feasibility of the modeling is arbitrarily extended to the four (!) orders of magnitude of D_A, beginning with the neoclassical scales. After several decades of research efforts, the question as to whether the neoclassical values of these coefficients can be determined by modeling against the background of actual uncertainties still remains open.

Second, even a small underestimation of impurity kinetics caused by inaccuracies in atomic data and plasma parameters results in a significant overestimation of impurity transport [9–11]. The uncertainties in kinetics (the reaction cross sections, the rates of ionization and recombination, and the related effects that sometimes remain beyond the scope of calculations) are capable of completely changing the meaning of the quantities D_A and V_A as fitting coefficients representing impurity transport. In other words, if these uncertainties are significant, the obtained values of D_A and V_A generally become unrelated to the investigation of impurity transport.

It should be noted that the main parametric dependences of the anomalous impurity transport coefficients (D_A and V_A) have not yet been found (see, e.g., [12]). The results of attempts to solve this problem [13] completely contradict the neoclassical scalings of impurity transport and are in striking contrast to the nonstationary accumulation phases observed under the conditions of improved plasma confinement.

Third, another significant shortcoming of long-term simulations of impurity transport is not only the lack of quantitative evaluations of the relationship between the effects of impurity dynamics and kinetics but also the lack of a systematic concept of the typical scales of the kinetic effects.

However, in spite of the above shortcomings of impurity simulations, the experimental data used in these simulations seem to be very valuable for the study of impurity charge-state distributions. In fact, besides the determination of D_A and V_A, the simulations are also aimed at finding the impurity charge-state distributions corresponding to the observed profiles of impurity emission. The simulation method can be related not only to the use of D_A and V_A but also to the modification of ionization and recombination rates [7, 11]. Charge-state distributions obtained with different models can be considered equivalent if they correspond to the experimental emission profiles. The importance of the equivalent distributions lies in the fact that they are almost independent of the assumed relation between the impurity dynamics and kinetics. These model distributions, rather than the values of D_A and V_A, present the empirical result of the analysis of impurity emission observations. Thereby, the studies of impurity charge-state distributions provide an empirical basis for the quantitative distinguishing between the dynamics and kinetics of impurity ions.

A basis for the approach proposed and the main goal of this paper are a systematic analysis of the kinetics of impurity charge-state distributions and the related effects, as well as their typical scales and conditions for their observations. The other goal is to show that the required quantitative analysis of impurity charge-state distributions can be performed using the lowest moments of the distributions, such as the average charge and dispersion. Let us first consider the available data.

An extreme simplification of the simulations of impurity charge-state distributions, namely, the assumption about a steady-state balance between the processes of ionization and recombination in the absence of thermodynamic equilibrium in a plasma, which is well known as a stationary model of coronal equilibrium (see, e.g., [2]), have been widely used in practice. A further simplification is provided by the assumption that the charge-state distribution can only be described by the plasma electron temperature T_e. This assumption was often used in the earlier stage of impurity studies in tokamak plasmas [14, 15] and is still sometimes used to calculate the radiative losses [16].

Among various uncertainties in the numerical solution of a set of coupled continuity equations more comprehensively describing the behavior of impurity charge-state distributions, we can note an uncertainty in the contribution of the excitation–autoionization states to the cross sections for ionization and dielectronic recombination [1].

Some important atomic processes can occur beyond the scope of impurity transport calculations. Thus, some of the impurity transport codes applied to tokamaks before the middle of the 1980s did not take into account the charge-exchange recombination of impurities against the background neutral atoms (see, e.g., [3, 17]); this process, however, is frequently the most important effect. In fact, impurity charge-exchange recombination leads to a significant shift in the charge-state distribution toward a lower average charge [18–20], so that the charge-exchange recombination term can substantially affect the charge-state distribution, whereas the influence of the radiative and dielectronic processes, as well as radial transport, can be of minor importance [21].

An opposite (with respect to the charge-exchange effect) shift of the center of the charge-state distribution can be caused by the ionization of metastable states of ions [1] and the interaction of impurities with suprathermal plasma electrons [2, 22–24].

We also note the effect of the shift of the ionization equilibrium during oscillations and stochastic fluctuations of T_e [25]; charge-exchange effects in collisions between highly ionized ions of the light impurity species [26]; and the multiple electron-impact ionization of atoms and ions [27], which is related to the detachment of one or more electrons from an ion. It is important to take into account the excitation of impurity ions by fast heavy particles [28], as well as the changes in the effective cross sections due to the charge exchange of impurity ions with excited hydrogen atoms [29].

An alternative to using D_A and V_A is to correctly take into account atomic data. Thus, it was shown that, in the TEXTOR tokamak [30], taking into account charge-exchange processes between neutrals and impurity ions provides a complete interpretation of all the experimental findings dealing with the structure of X-ray spectra without invoking large (anomalous) diffusion coefficients D_A.

However, alternative interpretations of the experimental data are rather rare and, as a rule, are related to the analysis of nonstationary processes. For example, taking into account impurity charge exchange is required in measurements of the time evolution of X-ray spectra in tokamak plasmas in the startup phase of a discharge or during a disruption [31, 32] since the bursts of emission of charge-exchanged neutrals are observed in a rapid phase of disruptions [33]. Here, an alternative way is the use of the highest possible values of the diffusion coefficient: $D_A \sim 10^2$–10^3 m^2/s [8, 34].

Let us consider another example. During the pulsed gas puffing of argon in the T-10 tokamak, the sharp decay (in a time of less than 1 ms after gas puffing) of chromium resonant line emission was observed. To interpret these results, both the dynamic and kinetic approaches were discussed. The interpretation dealing with the impurity dynamics [35] considers the sharp decrease in chromium influx to the plasma core due to the appearance of argon at the periphery. This interpretation indirectly assumes the total anomaly in both the dynamic and kinetic processes. For this reason, an interpretation in terms of an analysis of kinetic processes, namely, the interaction of suprathermal component of the electron energy distribution function with impurity ions, which determines the chromium line emission before and after gas puffing, was proposed in [36].

To describe the time evolution of the radial profiles of the spectral line emission of oxygen and scandium impurities in the startup phase of a discharge in the TFR tokamak, impurity charge exchange with neutrals and the interaction of impurities with suprathermal electrons were taken into account in [11]. An alternative way here is the use of transport coefficients in the range $D_A = 0.2$–0.5 m^2/s [37].

Account of similar kinetic effects is, as a rule, related to additional terms in the expressions for the sums of the ionization and recombination rates and needs preliminary development. In general, available theoretical concepts related to kinetic effects were mainly developed in simplified analytical models, beyond the scope of numerical codes [38–42]. Attempts to overcome the problem of a large number of equations in the set describing the kinetics of the impurity charge-state distribution have been made there.

Using the approximation of a continuous variation of the ionic charge, it was found that the motion of the distribution center in charge-state space can be diffusive in character [38]. It was shown that the Gaussian distribution is well suited to describe the form of the charge-state distribution of medium- and high-Z impurities when the distribution center occurs close to the middle of the L, M, etc., shells. In the same approximation, a kinetic equation of the Fokker–Plank type for the continuous charge-state distribution function [11] was obtained; the solution to this equation allowed one to find the effect of a significant broadening of the distribution during a recombination transition between two stationary states inside a single (L) atomic shell of iron impurity [40]. In this case, the charge-state diffusion coefficient is 5–100 m^2/s [11]. However, only an appreciable disbalance between charge-state diffusion and charge-state convection, which is observed, e.g., during a rapid phase of disruption in a tokamak, may result in noticeable kinetic effects [31]. In particular, the same order of magnitude (~100 m^2/s) that is required for D_A [8] is normally obtained for the coefficient of charge-state diffusion.

The complexity of numerical calculations of the time-dependent effects increases for medium- and high-Z impurities. Besides the number of equations in the set in question, the number of atomic shells to be taken into account also increases and stepwise changes of the ionization potentials and atomic cross sections for transition (between shells) states appear, the description of which presents a serious problem for all the approximate approaches. Therefore, the studies of impurity charge-state kinetics are mainly represented by calculations for carbon impurity [1, 2, 41–43]. In particular, the emergence of "quasi-steady" states was found in [1]. The cause of this effect is the almost independent time evolution of charge states that belong to different atomic shells. For light impurities, a model of two (or three) most abundant ions, which results in a single equation for the average ion charge, was developed in [41, 42].

This paper presents a systematic approach to the study of impurity charge-state kinetics. The approach is based on the solution of a set of coupled equations for the impurity distribution function over discrete charge states and on the analysis of its lowest moments such as the average charge, dispersion, and skewness. Analytical approaches to solving charge-state kinetic equations with the use of the symmetry properties of the kinetic matrix and efficient methods for computing its eigen-

values are first presented here. The most important extreme cases are also considered.

Typical values of the charge-state dispersion, the ranges of its variations for different impurities, its behavior in transition processes, and the sensitivity to the coefficients D_A and V_A were not studied before. We can only mention approximate expressions for the dispersion and the indication to its nonmonotonic behavior [38, 39].

The paper is organized as follows. The set of coupled kinetic equations for the impurity distribution function on discrete charge states is considered in Section 2. The lowest moments and the equations describing the time evolution of different charge-state distributions are considered in Section 3. The corresponding solutions to a set of coupled kinetic equations and their behavior in the limiting cases are also considered here. The results of calculations of stationary and nonstationary effects of charge-state kinetics in the "dispersion–average charge" coordinates are presented for carbon, oxygen, argon, and iron impurities in Sections 4–7. The kinetics of impurity charge-state distributions during sawtooth oscillations of the plasma electron temperature T_e is analyzed in Section 8. The results from simulations of the measured impurity emission profiles for several large- and medium-size tokamaks and the calculated charge-state distributions presented in dispersion–average charge coordinates are reviewed in Section 9. The results obtained are summarized in Section 10.

2. EQUATIONS OF CHARGE-STATE KINETICS

A set of coupled equations of charge-state kinetics is usually written for the local densities of discrete impurity charge-states [1, 38, 44, 45]:

$$\frac{dn_k}{dt} = R_{k+1}n_{k+1} - (R_k + S_k)n_k + S_{k-1}n_{k-1}, \quad (1)$$

where $k = 0, 1, 2, \ldots, Z$ and R_k and S_k are the summarized (over all the processes) rates of recombination and ionization (with $R_0 = S_{-1} = R_{Z+1} = S_Z = 0$), which include as a factor the plasma electron density n_e. To describe the escape of ions from the region in question, the terms of the form $-n_k/\tau$ are sometimes added to the right-hand side of Eqs. (1). The summation of all of Eqs. (1) gives zero on the right-hand side, which results in the condition $n_i(t) = \sum n_k(t) = \text{const}$ for the total impurity density. The escape of ions is described by the condition

$$\dot{n}_i = -n_i/\tau. \quad (2)$$

In any case, Eqs. (1) contain indirect condition for $n_i(t)$, which is sometimes presented as a boundary condition for the influx of neutral impurity into the plasma [44].

We will use a more convenient set of coupled equations [43],

$$\frac{df_k}{dt} = R_{k+1}f_{k+1} - (R_k + S_k)f_k + S_{k-1}f_{k-1}, \quad (3)$$

where

$$f_k(t) = n_k(t)/n_i(t). \quad (4)$$

Set (3), in contrast to set (1), allows one to exclude $n_i(t)$ from consideration. To solve Eqs. (3), one needs some initial conditions, $f_k(0) \geq 0$. Furthermore, we have the condition

$$\sum_{k=0}^{Z} f_k(t) = 1. \quad (5)$$

The physical meaning of a distribution function on discrete charge states $f_k(t)$ is the probability of any impurity particle in plasma occurring in a charge state k (see, e.g., [46]). Hence, the ionization and recombination of impurity can be considered to be the processes of their random walk over discrete charge states. Set (3) presents a typical illustration of the theory of random processes: a Markovian process of the birth (ionization) and death (recombination) with a continuous time for a discrete spectrum of states (see, e.g., [47]). This set is a particular case of the Kolmogorov equations. It can be derived (see, e.g., [48]) from the formula for the total probability for ions to occur in a given charge state; this probability is expressed through the conditional probabilities of ionization and recombination. The assumption about the inconsistency of any pair of atomic reactions on the right-hand side of Eqs. (3) is used as an additional condition. Note that Eqs. (3) is not related to the assumption about the coronal equilibrium.

The set of impurity charge states is a connected or ergodic association since there are no sources or absorbers of these states, but one can transit from any charge state of this association to any other one. The rates of ionization and recombination are the conditional probabilities of a transition to a given state. The probabilities of ionic charge states are also conditional; i.e., they depend of the present state of an ion and independent of when and how it had fallen in this state. Thus, the necessary condition for Markovian processes is realized: a future state depends on the past only through the present one [47].

Up to now, little attention has been paid to these features (meanwhile, see [46]). For example, it was noted in [25, 38, 41] that, after some time, the impurity "forgets" its initial charge-state distribution. However, this is only one side of its kinetics. An essential property of a set of kinetic equations is its ergodic nature or, in other words, the existence of a finite limit toward which the charge-state distribution moves as a whole at each instant of time [47].

Finally, we note that the given formulation of the problem of studying the kinetics of impurity charge-state distributions in the form of Eqs. (3) turns out to be a particular case of the problem of the behavior of atomic systems under the action of stochastic external Markovian-type perturbations [49].

3. KINETICS OF CHARGE-STATE DISTRIBUTIONS

To describe the distribution function on discrete charge states $f_k(t)$, one can use its lowest moments. The first moment is the mathematical expectation $m(t)$, the second one is the dispersion $D(t)$, the third one is the skewness $A(t)$, etc. In the case of impurity distribution on its discrete charge states, $m(t)$ is referred to as the average charge or the distribution center. The most abundant state is referred to as the mode of a distribution. The expressions for the lowest moments have the following form:

$$m = \sum_{k=0}^{Z} k f_k, \tag{6}$$

$$D = \sum_{k=0}^{Z} k^2 f_k - m^2, \tag{7}$$

etc. Differentiating Eqs. (6) and (7) with respect to time and using Eqs. (3), we obtain

$$\begin{aligned} \frac{dm}{dt} &= \sum_{k=0}^{Z} (S_k - R_k) f_k, \\ \frac{dD}{dt} &= \sum_{k=0}^{Z} [S_k + R_k + 2(k-m)(S_k - R_k)] f_k. \end{aligned} \tag{8}$$

Similar expressions can be obtained for the higher moments, e.g., for the skewness $A(t)$.

Its follows from Eqs. (8) that, depending on the relation between S_k and R_k, several basic types of the motion of a charge-state distribution are possible. A plasma in which ionization processes dominate (so that $\dot{m} > 0$) may be called a nonstationary ionized plasma. In the opposite case (at $\dot{m} < 0$), it may be called a nonstationary recombined plasma. Thus, using the sign of $\dot{m}$, one can distinguish the ionization and recombination kinetics of charge-state distributions.

In the case of $\dot{m}(t) \cong 0$, it is convenient to present charge-state kinetics in terms of transport phenomena as diffusion and convection over charge states. For example, if $\dot{D}(t) > 0$, then this type of motion, which is related to the broadening of a distribution with a dominating charge-state diffusion (see [11]), may be called diffusive kinetics. The case of $\dot{D}(t) \le 0$ corresponds to the domination of charge-state convection, and the corresponding type of kinetics may be called convective kinetics.

It follows from Eqs. (8) that the fastest rate $\dot{m}$ of the motion of the distribution center takes place in two extreme cases: at $S_k \gg R_k$ and at $S_k \ll R_k$. These cases may be called dominating (or extreme if all $R_k \longrightarrow 0$) ionization and dominating (or extreme if $S_k \longrightarrow 0$) recombination, respectively.

The coefficients on the right-hand side of Eqs. (3) form the kinetic matrix

$$K = \begin{bmatrix} -S_0 & R_1 & 0 & & & 0 \\ S_0 & -(R_1+S_1) & R_2 & 0 & & \\ 0 & S_1 & -(R_2+S_2) & R_3 & 0 & \\ & 0 & \cdots & \cdots & \cdots & 0 \\ & & 0 & S_{Z-2} & -(R_{Z-1}+S_{Z-1}) & R_Z \\ 0 & & & 0 & S_{Z-1} & -R_Z \end{bmatrix}. \tag{9}$$

Using matrix (9), set (3) can be rewritten in the form

$$\dot{\mathbf{f}}(t) = K(t)\mathbf{f}(t), \tag{10}$$

where $\mathbf{f}(t)$ is the distribution function on discrete states, represented as a vector in the space of its components $f_k(t)$.

The properties of the matrix K and especially the possibility of its transformation to a diagonal form play a decisive role in solving Eq. (10). A proper analysis, ways of transforming the matrix K, and approaches to simulating its eigenvalues and eigenvectors are presented in Appendix 1.

The solution to set (10) at $t > 0$ can be written in the form

$$\mathbf{f}(t) = G(t) \cdot \mathbf{f}(0), \tag{11}$$

where $G(t)$ is an operator (matrix) of the time evolution of an impurity charge-state distribution and $\mathbf{f}(0)$ is an initial distribution. A study of the solutions to Eqs. (3) by approximate approaches (see [38–40, 44]) shows that the time evolution of the initial distribution taken, e.g., in the form of a stationary coronal distribution, has the character of a progressive shift of the distribution center with a change of the total impurity charge. Solution (11) together with the presented kinetic process may be called a translation of an impurity charge-state distribution. Hence, the problem of solving Eq. (10) is to find $G(t)$ for a given charge-state translation.

Let us consider the behavior of a charge-state distribution in the case of a stationary matrix K. For example, let the balance between the ionization and recombination processes in plasma be changed instantaneously and, then, the rates of these atomic reactions remain unchanged. It is well known [50, 51] that, in this case, the solution has the form

$$\mathbf{f}(t) = \exp(Kt) \cdot \mathbf{f}(0). \quad (12)$$

where $\exp(Kt)$ is a matrix function that presents here $G(t)$. According to the Sylvester theorem (see, e.g., [51]), the expansion of this matrix function yields

$$G(t) = \exp(Kt) = \sum_{k=0}^{Z} \exp(\lambda_k t) \prod_{i \neq k} \frac{(K - \lambda_i E)}{(\lambda_k - \lambda_i)}. \quad (13)$$

However, to use solution (13) with a set of known eigenvalues λ_k, one has to multiply and sum the elements of a large number (Z) of matrices. As early as $Z \geq 10$, the counting errors, which are governed by the inaccuracy in calculating λ_k, increase rapidly. Solution (13) can be of practical use only in the cases of light impurities or of a triangle matrix K (when the eigenvalues, i.e., the diagonal elements of K, are known exactly).

From the point of view of the computational expenditure, it is expedient to use the symmetry properties of the kinetic matrix. Indeed, using representations (A1.2) and (A1.6) for K and calculating its eigenvalues (the elements of the matrices Λ, D_K, and T), we obtain

$$G(t) = D_K^{-1} T \exp(\Lambda t) T^t D_K \quad (14)$$

and

$$G(t) = U \exp(\Lambda t) U^{-1}. \quad (15)$$

It follows from expression (14) that the expression for $G(t)$ is a product of five matrices, three of them being diagonal. Note that it is simpler to use expression (14) than (15) since the elements of the transposed matrix T^t (in contrast to the elements of U^{-1}) are calculated together with the elements of the matrix T. We will further use expression (15) as a short form of expression (14), implying that $U^{-1} = T^t D_K$ and $U = D_K^{-1} T$.

Expression (14) determines the time evolution of a charge-state distribution starting from some initial state $\mathbf{f}(0)$ to a final state, which is unambiguously determined by the matrix K. This final state is presented by the eigenvector $\mathbf{u}_0$, which is normalized to unity and corresponds to the zero eigenvalue. In the frame of a stationary model, this state is usually referred to as a stationary coronal distribution.

The translation of a charge-state distribution from some initial state to a final one at a stationary matrix K may be called a stationary or simple translation of the charge-state distribution.

Solutions in the form of a simple translation are related to rapid (as compared to λ_k^{-1}, where $k \cong m$) variations in the ionization and recombination rates (e.g., as a result of a stepwise change in T_e). When $\dot{m} > 0$, these solutions may be called ionization (positive) temperature translations, and when $\dot{m} < 0$, they may be called recombination (negative) temperature translations. The case with $\dot{m} \cong 0$ and $\dot{D}(t) > 0$ corresponds to the distribution broadening, which, as was pointed out above, has a character of charge-state diffusion; therefore, this case may be called a diffusive translation. The case with $\dot{m} \cong 0$ and $\dot{D}(t) < 0$ corresponds to the narrowing of a distribution due to dominating convection; therefore, this case may be called a convective translation.

There are two important extreme cases of a simple translation of charge-state distributions. These cases correspond to a situation in which one can neglect in Eqs. (3) either the terms that describe ionization or the terms that describe recombination. In practice, these approximations can be used to describe the impurity behavior when the equilibrium between ionization and recombination shifts appreciably over a short time period. Similar situations occur in tokamak plasmas, e.g., in the startup phase of a discharge, during pellet injection, in the course of a rapid plasma heating or cooling, and during disruptions.

Solutions corresponding to the case in which the ionization processes predominate will be referred to as dominant (or extreme) ionization translations. In the opposite case, solutions will be referred to as dominant (or extreme) recombination translations. In both cases, the matrix K becomes triangular (or almost triangular for dominant translations). Analytical expressions describing extreme charge-state translations are presented in Appendix 2.

Let us consider charge-state kinetics in terms of the lowest moments in the case of extreme recombination of impurity. We will assume that the dominant atomic process is the charge exchange of impurity with neutrals. In this case, the recombination rate can be represented as $R_k = rk$, where r is a constant that is independent of the impurity species (see [11] and also formulas (47) and (48) below). Excluding time from Eqs. (8) and (9), assuming that $R_k \gg S_k$, and using formulas (6) and (7), we obtain

$$\frac{dD}{dm} = -1 + 2\frac{\sum k^2 f}{\sum kf} - 2m = -1 + 2\frac{D}{m}. \quad (16)$$

We note that the distribution function does not enter into Eq. (16), while this function is usually required when using formulas (6)–(8). The solution to Eq. (16) under the initial conditions $D(t=0) = D_0$ and $m(t=0) = m_0$ has the simple form

$$D(m) = \left(\frac{D_0 - m_0}{m_0^2}\right)m^2 + m. \quad (17)$$

From Eqs. (6)–(8) we find that

$$\begin{aligned} m(t) &= m_0\exp(-rt), \\ D(t) &= D_0\exp(-2rt) + m_0(1 - \exp(-rt))\exp(-rt). \end{aligned} \quad (18)$$

It follows from Eq. (17) that the time evolution of the dispersion $D(m)$ is represented by a convex (since usually $D_0 \ll m_0$) parabola whose maximum lies at the line $D_{\max} = m_{\max}/2$ (see Eq. (16)). The time over which the distribution shifts to the point $(m_{\max}, D_{\max})$ is equal to

$$t_{\max} = \frac{1}{r}\ln\left(\frac{2}{1 - D_0/m_0}\right). \quad (19)$$

It also follows from Eqs. (17) and (18) that a moving distribution forgets the initial value of D_0 faster ($\sim\exp(-2rt)$) than the initial value of m_0($\sim\exp(-rt)$). An expression similar to formula (17) can be obtained for other moments. In particular, for skewness we have

$$A(m) = \left(\frac{A_0 + m_0 - 3D_0}{m_0^3}\right)m^3 + 3\left(\frac{D_0 - m_0}{m_0^2}\right)m^2 + 2m. \quad (20)$$

It can be seen from Eqs. (18) and (20) that the initial value A_0 is forgotten faster than D_0. Since the distribution function with a finite number of discrete states can be expressed exactly in terms of the lowest moments, its behavior in the case of interest eventually depends only on m_0 and r. The trajectories of the distribution motion in the space of moments (e.g., $D(m)$ or $A(m)$) are universal (i.e., have the form of a parabola for the case of $D(m)$) for distributions with the same initial conditions and are independent of the impurity species. The distributions move according to the same scheme: over a time period longer than $(3r)^{-1}$, a distribution is formed that is described more or less exactly by the two moments, m and D; i.e., the distribution is almost Gaussian. Note that steps of the ionization potentials and of the cross sections in transit ranges between atomic shells do not affect this distribution. Further, it follows from Eq. (18) that, over a time period longer than $(2r)^{-1}$, the distribution is rearranged in such a way that $D \cong m$; i.e., it is close to a Poisson distribution. Numerical illustrations of such behavior of impurities in the course of their extreme recombination are presented in Section 7.

Thus, in the case of extreme recombination through charge exchange with neutrals, charge-state kinetics can be described in terms of moments, without invoking a solution to the equation for the distribution function (see also [47]). Moreover, using Eqs. (17) and (20) and condition (5), one can find the behavior of charge-state distribution from Eqs. (6) and (7).

Formulas (17)–(20) can be used to approximately describe recombination kinetics over times $t \ll t_{\max}$ and $rt \ll 1$. In the latter case, from Eq. (11) we have the linear estimate $D(t) \approx D_0 + m_0 rt$, which indicates an initial increase in the dispersion in the case of extreme (and also dominant) recombination. Indeed, from Eqs. (8) we have $\dot{m} = -rm < 0$ and $\dot{D} = r(m - 2D) > 0$ if $m > 2D$, which takes place for hot plasmas.

Let us now consider the solution to Eq. (10) in the case of a nonstationary matrix K. The time interval of interest $(0, t)$ can be divided into n equal parts $\Delta t = t_n - t_{n-1}$. The $S_k(t_n)$ and $R_k(t_n)$ values inside each time interval are assumed to be constant and to vary stepwise on the boundary of each interval. According to Eq. (14), the solution in the first interval can be represented in the form

$$\mathbf{f}_1(t_1) = U_1\exp(\Lambda_1\Delta t)U_1^{-1}\mathbf{f}(0). \quad (21)$$

For the second interval, solution (21) can be regarded as an initial condition. The solution for the second interval can then be represented in a form similar to that for the first interval:

$$\mathbf{f}_2(t_2) = U_2\exp(\Lambda_2\Delta t)U_2^{-1}\mathbf{f}_1(t_1). \quad (22)$$

Applying this procedure up to the end of the time interval of interest, we obtain

$$G(t) = \lim_{n\to\infty}\prod_n [U_n\exp(\Lambda_n\Delta t)U_n^{-1}], \quad (23)$$

where the expression under the sign of limit on the right-hand side is an integral product or, in other words, a multiplicative integral [50]. A specific feature of this is the noninterchangeability of the matrices-factors (expressions in square brackets). The finite limit in Eq. (23) exists at negative eigenvalues of the diagonal matrices Λ_n and can be calculated approximately. It follows from Eq. (23) that, in the case of a nonstationary matrix K, the operator of the charge-state distribution motion is represented as a product of elementary operators that describe simple translations.

Thus, it follows from formulas (14), (15), and (23) that any solution to set (3) can be represented by simple translations. This indicates their great importance for an analysis of impurity charge-state kinetics.

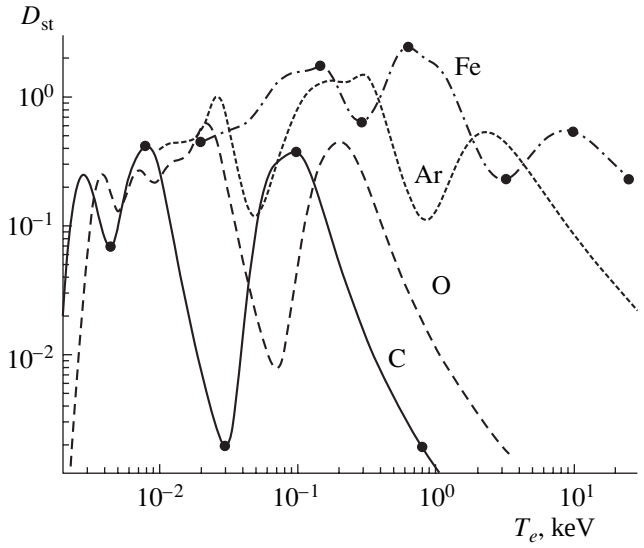

Fig. 1. Dispersion of the stationary charge-state distributions of C, O, Ar, and Fe impurities as a function of T_e, calculated by formulas (6), (7), (45), and (46) at $\xi_n = 0$. Charge-state distributions corresponding to the points on the curves for C and Fe are shown in Figs. 3a and 3b, respectively.

4. DISPERSION OF STATIONARY CHARGE-STATE DISTRIBUTIONS.

Initial moments m and D of charge-state distributions are important numerical characteristics that allow one to compare the impurity behavior in very different plasma processes. However, before this, it is necessary to consider the impurity behavior under conditions of a balance between impurity ionization and recombination. In particular, in the stationary case, set (15), as is well known, can be reduced to the form

$$f_{k+1}R_{k+1} = f_k S_k, \tag{24}$$

and its solution, using condition (5), can be represented (see, e.g., [1, 41]) as follows:

$$f_0 = \left(1 + \sum_{n=1}^{Z}\prod_{i=1}^{n}\frac{S_{i-1}}{R_i}\right)^{-1},$$

$$f_k = \left(1 + \sum_{n=0}^{k-1}\prod_{i=n}^{k-1}\frac{R_{i+1}}{S_i} + \sum_{n=k+1}^{Z}\prod_{i=k+1}^{n}\frac{S_{i-1}}{R_i}\right)^{-1}, \tag{25}$$

where $1 \le k \le Z-1$,

$$f_Z = \left(1 + \sum_{n=0}^{Z-1}\prod_{i=n}^{Z-1}\frac{R_{i+1}}{S_i}\right)^{-1}.$$

In the present work, the rates of atomic processes for carbon, oxygen, argon, and iron impurities were calculated using the data obtained by Post [52]. The ionization rate corresponds to the formula of Lotz [53]. The rates of radiative and dielectronic recombination were also calculated using the data from [1, 52].

The rates of charge-exchange recombination were calculated by the formula

$$R_k = n_e\xi_n\langle\sigma_1^{cx}(k)v_n\rangle(1+\beta). \tag{26}$$

Here, v_n is the velocity of neutral atoms (hydrogen or deuterium); $\xi_n = n_n/n_e$ is the relative density of neutrals; and $\sigma_1^{cx}(k)$ is the cross section for the charge-exchange of a hydrogen atom in the ground state, taken in the form [54]

$$\sigma_1^{cx}(k, E) = \frac{Ak\ln\left(B\dfrac{\sqrt{k}}{E}\right)}{1 + CE^2/k + D(E/\sqrt{k})^{4.5}}, \tag{27}$$

where E is the energy (averaged over the distribution) of neutrals, $A = 5.967 \times 10^{-17}$, $B = 5.87 \times 10^5$, $C = 1.913 \times 10^{-3}$, and $D = 1.383 \times 10^{-7}$; and β is a factor that takes into account the contribution of the excited states of neutral atoms [29, 30], whose cross sections increase sharply with increasing the first quantum number n of the excited levels ($\sigma_n^{cx} \sim n^4$). In our simulations, it was assumed that β increases to 1–10 with increasing temperature T_e and/or as a result of the impurity excitation processes.

The results of calculations of stationary charge-state distributions are usually represented in the form of dependences of the relative densities of ionic charge states versus T_e [1–3, 16, 41]. In some papers, the dependences $m(T_e)$ are presented (see, e.g., [2, 19]); however, there is no data on dispersion.

Figure 1 shows the dispersion of stationary charge-state distributions D_{st} versus the plasma electron temperature T_e for carbon, oxygen, argon, and iron impurities. The dispersion is calculated by formulas (6), (7), (24), and (25) without allowance for impurity charge exchange with neutrals. The nonmonotonic behavior of $D_{st}(T_e)$ is ensured by the set of atomic shells and subshells of impurity in question and by the fact that the ionization rates S_k vary stepwise during the transitions of $m(T_e)$ between neighboring shells. This can be demonstrated more clearly if we represent the dependences $D_{st}(T_e)$ and $m(T_e)$ by one function $D_{st}(m)$. Each point here gives a sufficiently complete representation (which, however, is not unambiguous) of the corresponding charge-state distributions.

Calculations of $D_{st}(m)$ for stationary (coronal) charge-state distributions in the case of iron and argon impurities with the use of different data about electron-impact ionization cross sections [3, 7, 30, 52, 53, 55–57] are compared in Figs. 2a and 2b. Atomic data for iron presented here by the function $D_{st}(m)$ were used in the impurity transport codes developed for the PLT [3] and TFR [7] tokamaks before 1983. The inaccuracies of

these atomic data are characterized by the difference in the curves $D_{st}(m)$. A comparison with the scales of kinetic effects, as well as with the scale of the influence of diffusive–convective impurity transport, shows that there are appreciable restrictions on the accuracy of an analysis of the impurity behavior, especially at the plasma periphery.

The least data scatter in the rates of impurity ionization occurs, as a rule, for highly ionized charge states, starting from the He-like ions usually located in the plasma core. Figure 2b gives an idea of the scatter in the data on the ionization rate for argon, which is commonly used to study impurity transport in tokamaks (see below). It can be concluded from Fig. 2b that the transport and line emission models for argon are related to significant uncertainties in the ionization cross sections for the charge states lower than a He-like state (for $m < 15.5$ and $T_e < 0.5$ keV), which are typical for the peripheral regions of the plasma in large- and medium-size tokamaks.

It can also be seen from Figs. 2a and 2b that the minima of D_{st} are located in the regions where m passes (as T_e increases) from one atomic shell to another, whereas the maxima correspond to m lying inside each shell. From a comparison of $D_{st}(T_e)$ (Fig. 1) with the corresponding temperature dependence of the radiative losses (see, e.g., [1]), it follows that the locations of the maxima (over T_e) of these two curves almost coincide, but the ranges of the so-called radiation barrier fall on the L shells for low-Z impurities and on the M shells for medium-Z impurities.

A comparison of the distributions that correspond to the extreme values of D_{st} is of interest. Figures 3a and 3b show the distributions for carbon and iron impurities, respectively, for the T_e values at which the extremes of $D_{st}(T_e)$ are reached. It can be seen from these figures that the distributions that correspond to the minima of D_{st} for the K–L, L–M, etc., transitions of m have sharp and clearly pronounced maxima (modes) for He-, Ne-, Ar-like, etc., ion states of each impurity. The most abundant transitive distributions (designated in Figs. 3a and 3b as KL, LM and MN, respectively) are represented by a small number of charge states (usually, by three states, as was noted in [25, 41] in analyzing the behavior of He-like carbon ions). The systematic character of transitive distributions is clearly seen in Figs. 3a and 3b. Distributions denoted in Fig. 3 as Z are mainly represented by the nuclei of impurity ions and usually occur at large T_e. These distributions can also be attributed to transitive ones. When the maxima of D_{st} are reached, the centers of the distributions remain within K, L, etc., shells, and these distributions are respectively designated in Figs. 3a and 3b.

As was noted above, charge-exchange recombination of impurities with neutral (hydrogen or deuterium) atoms may have a significant effect on their stationary charge-state distributions. In particular, the calculated

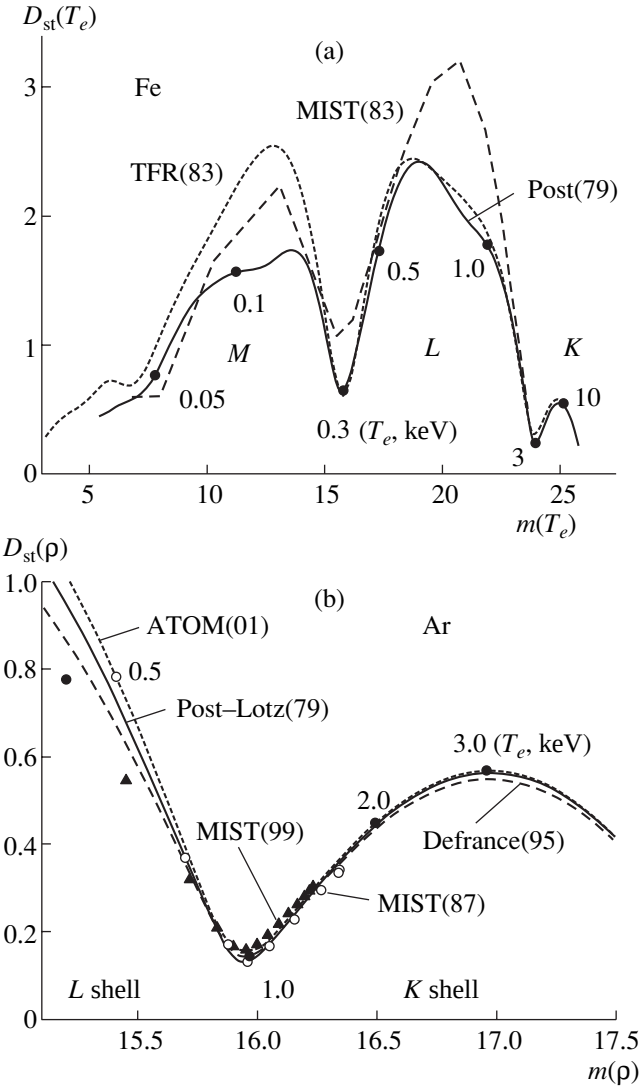

Fig. 2. Dispersion D and average charge m (the lowest moments) of stationary charge-state distributions as parametric functions of T_e (in keV), calculated for the coronal equilibrium and using different ionization and recombination rates at $\xi_n = 0$ for (a) iron and (b) argon impurity. The solid line in plot (a) shows the results of calculations by the data from Post [52] and Lotz [53], closed circles show T_e (in keV), the dashed line shows the data for PLT obtained with the MIST code [3], and the short-dashed line shows the data for TFR [7] after correction for the ionization rates (an approximately twofold decrease in the rates from Lotz) using the results of emission observation. The solid line in plot (b) shows the results of calculations by the data from Post [52] and Lotz [53], open circles correspond to model distributions (MIST) in the ALCATOR-C tokamak [55], triangles correspond to model distributions (MIST) in the TEXTOR tokamak [30], the dashed line shows the moments calculated using the data of [56], and the short-dashed line is obtained using the data of the ATOM code [57].

dependences $m(T_e)$ for different ξ_n are presented in [2, 19]. Similar dependences at $\xi_n = 0$–10^{-3} for iron impurity are shown in Fig. 4. Here, one can note an impor-

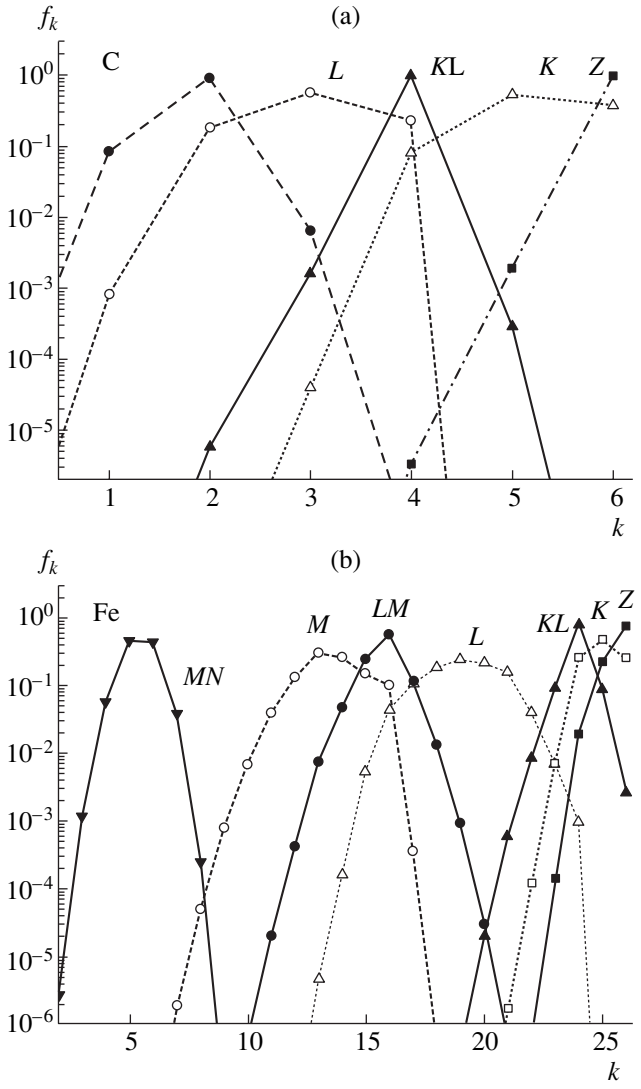

Fig. 3. Extreme (with respect to dispersion) stationary impurity charge-state distributions corresponding to the points in Fig. 1 at $\xi_n = 0$ (a) for carbon at T_e = (*Z*) 800, (*K*) 100, (*KL*) 30, and (*L*) 8 eV (the dashed line corresponds to T_e = 4.5 eV) and (b) for iron at (*Z*) 25, (*K*) 10, (*KL*) 3.3, (*L*) 0.65, (*LM*) 0.3, (*M*) 0.15, and (*MN*) 0.02 keV.

tant effect, namely, a decrease in m with increasing T_e (see also [2, 19]). This can be explained by the fact that, in the range of T_e = 1–10 keV, the ionization rates of most of the atomic shells can decrease with increasing T_e. In particular, for iron ions Fe^{10+}–Fe^{20+} (k = 10–20), the maximum of $S_k(T_e)$ lies within the range T_e = 1–10 keV, while for carbon ions with k = 3–5, it lies within the range T_e = 1–3 keV.

The results of calculations (for the same conditions as in Fig. 4) illustrating the effect of charge exchange on the dispersion D_{st} are shown in Fig. 5. The most appreciable variation in the width of the distribution under the action of charge-exchange recombination is

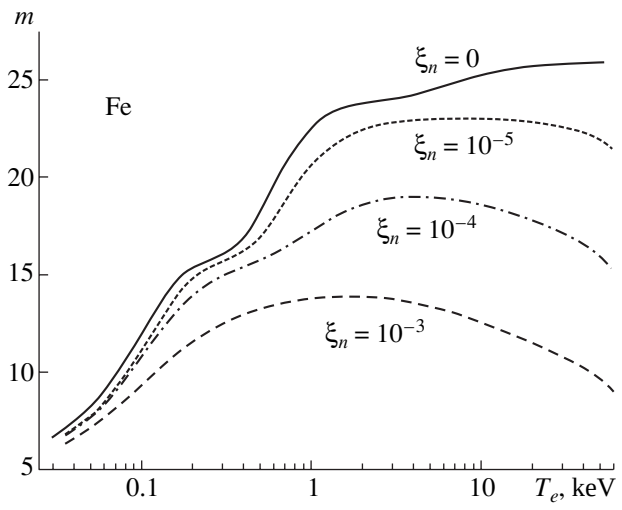

Fig. 4. Effect of the rate of charge-exchange recombination (the relative density of neutral atoms ξ_n) on the temperature dependence of the average charge $m(T_e)$ of stationary charge-state distributions for iron impurity.

observed in the range of T_e > 2–3 keV. It is convenient to represent both dependences $m(T_e)$ and $D_{st}(T_e)$ (see Figs. 4, 5) by one function $D_{st}(m)$, which is shown for iron impurity at different ξ_n in Fig. 6.

It can be seen from Fig. 6 that the dispersion of stationary charge-state distributions calculated with allowance for charge-exchange recombination is a double-valued function. Two branches of this function can be identified as an ionization brunch, along which the distribution center shifts toward higher m as T_e increases, and a recombination one, along which the distribution shifts toward lower m as T_e increases. It can also be seen from Fig. 6 that the recombination branch of $D_{st}(m)$ appreciably shifts toward smaller T_e and m as ξ_n increases. Thus, for sufficiently large ξ_n, due to the charge exchange of impurity, the increase in the steady-state value of T_e by more than 3–5 keV does not result in further impurity ionization, but, in contrast, it is accompanied by impurity recombination and an increase in D_{st}. The range in which D_{st} and m vary can be seen from a comparison of the locations of the points lying on the curves in Fig. 6 and corresponding to the same T_e and the different ξ_n.

5. DISPERSION OF NONSTATIONARY CHARGE-STATE DISTRIBUTIONS

Ergodic properties of charge-state kinetics distinguish stationary charge-state distributions against a lot of the possible initial distributions, since any impurity charge-state distribution in a tokamak plasma relaxes toward a stationary charge-state distribution. In considering simple charge-state translations, we will assume that the initial distributions are represented by station-

ary distributions (25). In Fig. 6, these distributions are shown by points located on the curves $D_{st}(m)$.

The trajectories of simple translations begin with similar curves and end with them. Consequently, using these trajectories (see Fig. 6), simple translations can be classified as follows: First, they can be classified by the type (direction) of kinetics as ionization and recombination translations (or, by the sign of $\dot{m}$, as positive and negative translations, respectively). We note the cases in which ionization or recombination processes are dominant, i.e., extreme (and dominant) ionization or recombination translations (see Sections 6 and 7), and also the particular cases of diffusive and convective translations. Second, simple translations can be classified by the parameter that causes the distribution motion, e.g., temperature (T_e) translations, charge-exchange (ξ_n) translations, etc. Third, they can be classified by the location of $m(t)$: translations within one atomic shell may be called internal translations, whereas translations between neighboring shells may be called external ones. Moreover, one can distinguish translations within the same ionization or recombination branch of $D_{st}(m)$ or between these branches.

It is convenient to represent these simple translations by the trajectories $D(m)$, each point of which corresponds to a fixed instant of time and/or to some calculated distribution. The function $D(m)$ gives an idea of the motion of a charge-state distribution as a whole and also shows the features of the translations of different types. Moreover, the function $D(m)$ provides a virtually correct and complete description of the three most abundant charge states, e.g., in analyzing both charge-state distributions of light impurities and transitional distributions, in particular, when the He-like state or a nucleus appears to be a mode of the distribution.

We note some other advantages of the function $D(m)$. Since n_e enters as a factor in all the expressions for R_k and S_k, then, as follows from Eqs. (6)–(8), it drops out from the expression for dD/dm; consequently, the trajectories of simple translations depend on neither n_e nor n_i. Each trajectory $D(m)$ appears to be a probability characteristic of the charge state of any ion of a given impurity species. In this case, D takes the sense of the dispersion of the charge-state probability. However, the speed $\dot{m}$ of the motion of the charge-state distribution center along the trajectory significantly depends of n_e. In our calculations, we assumed that $n_e = 10^{13}$ cm^{-3}. A variation in n_e results in a proportional change in the value of $\dot{m}$ (see, e.g., Eq. (6)).

Figure 7 shows the results of calculations of simple ionization and recombination temperature translations within the L shell of iron impurity at $\xi_n = 10^{-5}$ and at an instantaneous change of T_e from 0.5 to 1 keV and then back, so that the beginning of one trajectory coincides with the end of another one. Let us introduce the following notation for these translations: T_e: 0.5 ⟶ 1.0 keV and T_e: 1.0 ⟶ 0.5 keV. The arrows by the curves in Fig. 7 show the direction of motion along the trajectories and the points on the curves display some given instants in the course of motion of a charge-state distribution. A systematic difference between ionization and recombination translations is clearly seen here. As a rule, the trajectory of the ionization translation is located as a whole below the stationary curve $D_{st}(m)$,

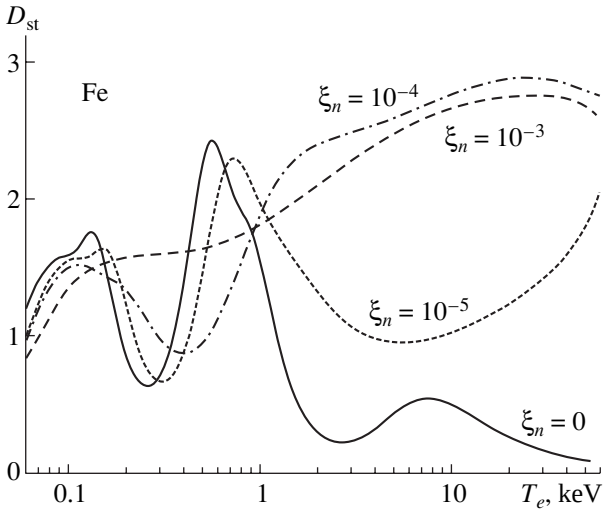

Fig. 5. Effect of the rate of charge-exchange recombination (the relative density of neutral atoms ξ_n) on the temperature dependence of the dispersion $D(T_e)$ of stationary charge-state distributions for iron impurity.

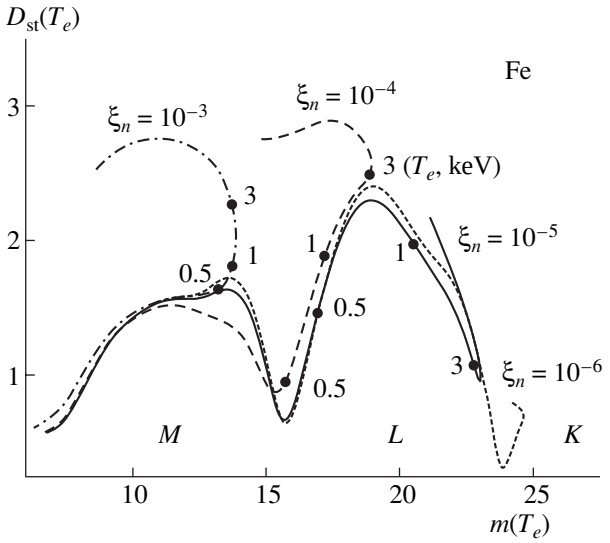

Fig. 6. Dispersion D and average charge m (the lowest moments) of stationary charge-state distributions of iron impurity as parametric functions of T_e for $\xi_n = 10^{-3}$, 10^{-4}, 10^{-5}, and 10^{-6}. The symbols show the moments $D(m)$ for $T_e = 0.5$, 1, and 3 keV.

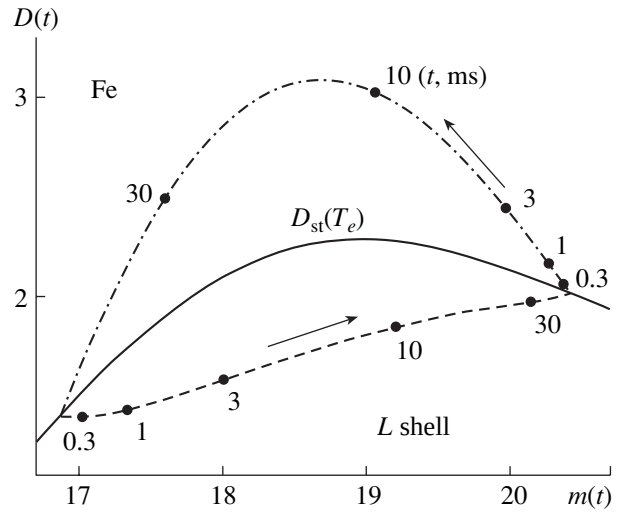

Fig. 7. Trajectories (time evolutions) of charge-state distribution moments of iron impurity at $\xi_n = 10^{-5}$ and at an instantaneous change in T_e. The dashed line corresponds to the change of the temperature from 0.5 to 1 keV (simple ionization translation T_e: 0.5 ⟶ 1.0 keV), and the dashed-and-dotted line, from 1 to 0.5 keV (simple recombination translation T_e: 1.0 ⟶ 0.5 keV). The stationary function $D_{st}(m)$ taken from Fig. 6 is presented for comparison. The symbols show the time evolution of the moments at $n_e = 10^{13}$ cm^{-3}, the arrows show the direction of motion, and the time t (in ms) is measured from the start of motion.

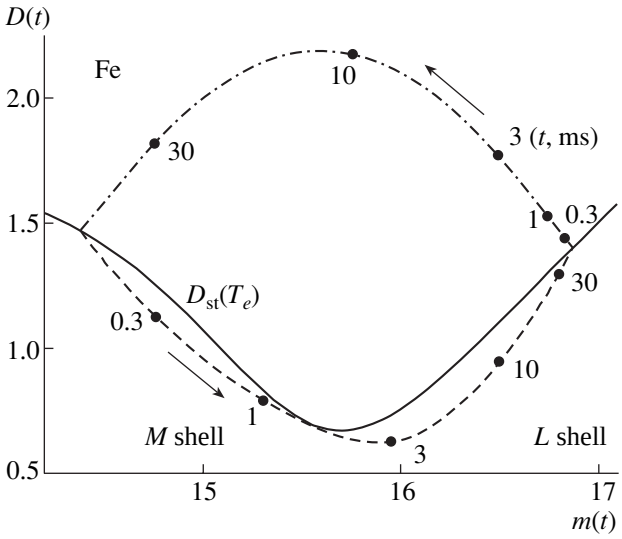

Fig. 8. Trajectories (time evolutions) of charge-state distribution moments of iron impurity between the L and M shells at $\xi_n = 10^{-5}$ and at an instantaneous change in T_e. The dashed line corresponds to the change of the temperature from 0.18 to 0.5 keV (simple ionization translation T_e: 0.18 ⟶ 0.5 keV), and the dashed-and-dotted line, from 0.5 to 0.18 keV (simple recombination translation T_e: 0.5 ⟶ 0.18 keV). The other notation is the same as in Fig. 7.

while the trajectory of the recombination translation is located appreciably higher than the stationary curve. An appreciable broadening of the charge-state distribution was first found in an analysis of a simple recombination translation of iron impurity within the L shell [40].

Figure 8 shows the results of calculations of simple translations between the M and L shells of iron impurity (T_e: 0.18 ⟶ 0.5 and 0.5 ⟶ 0.18 keV). Calculations of translations between neighboring shells (when $m(t)$ falls into the transition region between the shells) presents the most serious problems for any approximate approach to an analysis of charge-state kinetics because the accuracy of such calculations is extremely low due to the large difference in the rates and potentials of ionization of neighboring (but belonging to the different shells) charge-states. In this range of $m(t)$, a Gaussian approximation [38] turns out to be quite inappropriate for calculating a continuous (over k) distribution function (see, e.g., [11, 38, 40]). An attempt (not quite successful) to qualitatively analyze such a situation was made in [41]. The example presented in Fig. 8 is of interest because of the difference between the smallest value of D for the ionization translation and the largest value of D for the recombination translation. For comparison, the charge-state distributions corresponding to these values of D at $m = 15.8$ are shown in Fig. 9.

To calculate translations related to variations in the effective rate of impurity charge exchange with neutral atoms, we will assume that the temperature is fixed (e.g., $T_e = 1$ keV) and that ξ_n changes stepwise. The corresponding trajectories and the curve $D_{st}(m)$ along which ξ_n varies from 10^{-3} to 10^{-6} are shown in Fig. 10. Four pairs of simple charge-exchange translations ξ_n: 10^{-3} ⟷ 10^{-4}, 10^{-4} ⟷ 10^{-5}, 10^{-5} ⟷ 10^{-6}, and 10^{-3} ⟷ 10^{-5} are shown in this figure. For the latter translation, the speed of the motion of the distribution center is shown in Fig. 10 by points. In this figure, the same difference of the ionization and recombination translations with respect to the curve $D_{st}(m)$ can be seen, as was pointed above when discussing the examples presented in Figs. 7 and 8.

Diffusive and convective (temperature and charge-exchange) translations with $m(t) \cong$ const are represented by an almost vertical line in the plot of $D(m)$. Figure 11 presents an example of similar translations for iron impurity. The direct and reverse translations T_e: 0.7 ⟷ 50 keV almost coincide in this figure. Some instants in the course of motion of a charge-state distribution along the trajectories are also indicated here. The physical sense of these translations is the distribution motion caused by the interaction of the flux of hot electrons with impurity ions when the impurity falls into this flux (or escapes from it).

Figure 11 shows translations between the ionization and recombination branches of the curve $D_{st}(m)$ and also the translations within the recombination branch.

We note the inverted relation between variations in T_e and the types of possible translations in the range of $T_e > 3$–5 keV: a stepwise increase in $T_e(t)$ leads to a decrease in $m(t)$, so that, according to the above terminology, we have a recombination translation, whereas a stepwise decrease in $T_e(t)$ results in an ionization translation.

The translations that are shown in Figs. 10 and 11 and have the same final state (T_e = 1 keV, $\xi_n = 10^{-5}$ for Fig. 10 and T_e = 4 keV, $\xi_n = 10^{-4}$ and T_e = 50 keV, $\xi_n = 10^{-4}$ for Fig. 11) are of special interest. It can be seen from the figures that the corresponding trajectories of translations rapidly converge in the final stage and then coincide, independently of the initial state (e.g., T_e = 0.15 and 50 keV in Fig. 11). These examples clearly illustrate the ergodic character of impurity charge-state kinetics.

6. DISPERSION IN THE CASE OF EXTREME IONIZATION

The cases of extreme ionization and recombination translations are of interest because of the large speeds and wide range of changes in D and m and as an approach to the description of charge state kinetics when ionization/recombination processes are dominant.

Let us consider impurity ionization from the neutral state assuming that an instant influx of a neutral carbon (or argon) impurity into the plasma core with T_e = 1 keV, $n_e = 10^{13}$ cm^{-3}, and $\xi_n = 10^{-5}$ takes place. Figure 12 shows the results from calculations of a corresponding simple ionization translation for carbon (using formulas (11) and (14)). The time evolution of the moments of the distribution in the course of its motion along the trajectory $D(m)$ are shown by the points on the curve. For comparison, the curve $D_{st}(m)$ is also shown. Note that T_e = 1 keV is larger than the ionization potentials for H- and He-like carbon ions (490 and 392 eV, respectively). For this reason, the curves of extreme ionization translation calculated by formulas (A2.9) and (A2.10) almost coincide with the simple translation curve calculated by formulas (11) and (14).

The results from calculations of three ionization translations for argon (T_e: 0 ⟶ 1 keV, 0.01 ⟶ 1 keV, and 0.02 ⟶ 1 keV at T_e = 1 keV, $n_e = 10^{13}$ cm^{-3}, and $\xi_n = 10^{-5}$) are shown in Fig. 13. Here, the curve of extreme ionization translation T_e: 0 ⟶ 1 keV and the curve $D_{st}(m)$ are also shown for comparison. It can be seen from the figure that all these translations follow the same trajectory during 0.1–0.3 ms, independently of the initial state. Clearly, this is a consequence of the ergodic character of the kinetics of charge-state distributions. The trajectory of extreme ionization translation coincides with the trajectory of the simple ionization translation of an impurity from the neutral state up

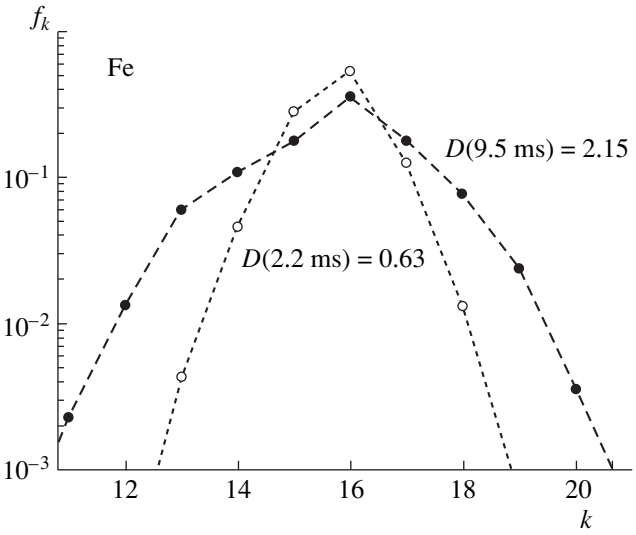

Fig. 9. Charge-state distributions of iron impurity during simple temperature translations shown in Fig. 8 at n_e = 10^{13} cm^{-3}, and $\xi_n = 10^{-5}$. Open circles show the distribution at T_e: 0.18 ⟶ 0.5 keV and t = 2.2 ms (when $D(t) \approx D_{min}$), and closed circles show the distribution at T_e: 0.5 ⟶ 0.18 keV and t = 9.5 ms (when $D(t) \approx D_{max}$). The time elapsed after the start of motion is shown in parentheses.

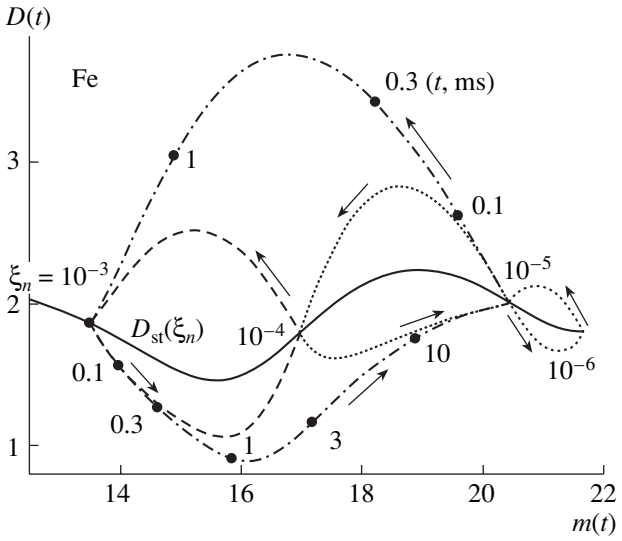

Fig. 10. Trajectories (time evolutions) of charge-state distribution moments of iron impurity at T_e = 1 keV and at an instantaneous change in the relative neutral density ξ_n (simple translations ξ_n: 10^{-3} ⟷ 10^{-4}, 10^{-4} ⟷ 10^{-5}, 10^{-5} ⟷ 10^{-6}, and 10^{-3} ⟷ 10^{-5}). The stationary curve $D_{st}(\xi_n)$ is presented for comparison, and the values of ξ_n are indicated along the curve. The points show time evolution of charge-state distribution at the given instants of time t (in ms), and the arrows show the direction of motion along the trajectories.

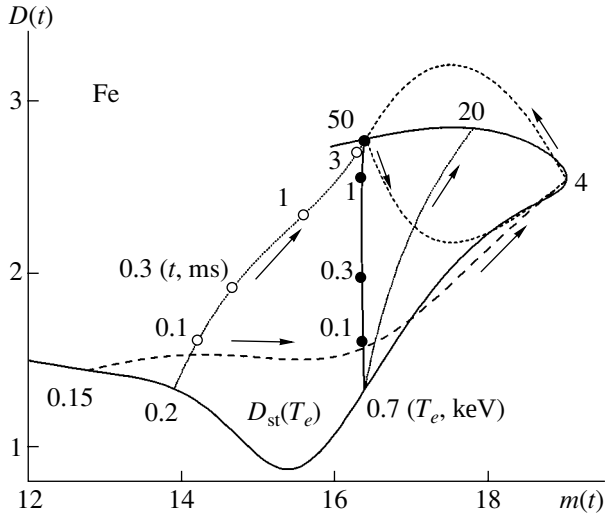

Fig. 11. Simple temperature translations between ionization and recombination branches of the curve $D_{st}(m)$ at n_e = 10^{13} cm^{-3}, and $\xi_n = 10^{-4}$: diffusive and convective translations T_e: 0.7 ⟶ 50 keV; an ionization translations T_e: 0.15 ⟶ 4 keV, 0.2 ⟶ 50 keV, and 0.7 ⟶ 20 keV; and a translation within the recombination branch T_e: 4 ⟶ 50 keV. The points show the time evolution of the distribution moments. The time t is in ms.

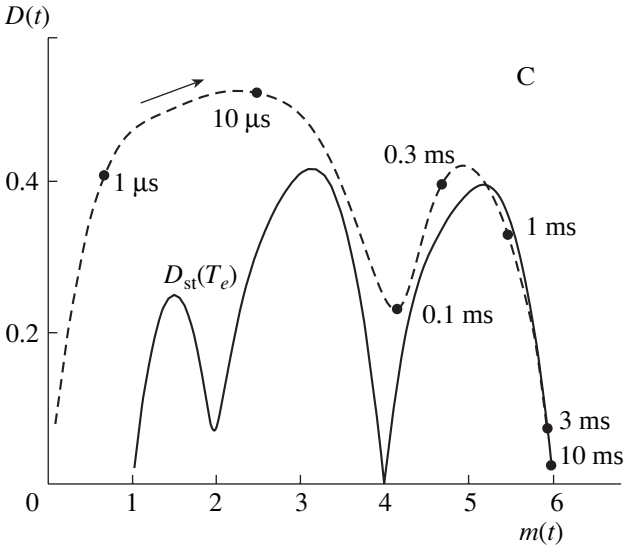

Fig. 12. Trajectories (time evolutions) of charge-state distribution moments during ionization of carbon impurity from the neutral state at $n_e = 10^{13}$ cm^{-3}, $\xi_n = 10^{-5}$, and T_e: 0 ⟶ 1 keV. The dashed line corresponds to a simple ionization translation calculated by formula (14) and almost coincides with that corresponding to an extreme ionization translation calculated by formulas (A2.9) and (A2.10)). The other notation is the same as in Figs. 7 and 8.

to the instant t = 0.3 ms and differs slightly from it after this instant.

It was shown in [38] that, in the course of impurity ionization from the neutral state, the charge-state distribution function becomes close to a Gaussian one and is deflected from it when a final stationary state is approached. The time evolution of the charge-state distribution of an argon impurity during the translation T_e: 0 ⟶ 1 keV is shown in Fig. 14. The corresponding Gaussian curves provide a good fit to these distributions if one use the data on $m(t)$ and $D(t)$ from Fig. 13 and the formula

$$f_G(k, t) = \frac{1}{\sqrt{2\pi D}} \exp\left[-\frac{(k-m)^2}{2D}\right]. \qquad (28)$$

It follows from Fig. 14 that distributions close to a Gaussian distribution (28) emerge at the very beginning of ionization (as early as 10 μs after the start of ionization) and remain up to the time when the distribution center approaches the final state.

In the case of the simple ionization translation of impurity from the neutral state, we may note regular oscillations of $D(m)$ occurring at T_e < 20–30 eV. Figure 15 shows several translations calculated by formulas (11) and (14) for carbon impurity at T_e = 15–100 eV. The trajectory for T_e = 5 eV in the figure is the extreme ionization translation calculated by formulas (A2.9) and (A2.10). The minima of dispersion become more pronounced and fall on integer m as T_e decreases. An appreciable amount of impurity is collected here in a certain period of time.

The initial portions of ionization translations from the neutral state (see Figs. 12, 13, 15) are presented by an almost straight line $dD/dm = 1$ or $D(t) = m(t)$; i.e., the initial portion of $D(m)$ corresponds to a Poisson distribution. For this, it is necessary that all the coefficients of a kinetic set be the same. We note that, here, such a distribution is merely related to the ionization of neutral atoms.

It is clear from the above figures that, in many cases, $D < 1$ and the corresponding charge-state distributions are close in shape to the transitive stationary distributions shown in Figs. 3a and 3b. Indeed, in these cases, most of the distributions are represented, as a rule, by the three most abundant states, while the contribution of the rest states to m and D can be ignored. Inverting formulas (6) and (7) and using Eq. (5), one can find that the probabilities of such states are expressed in terms of m and D:

$$f_{k\pm1}(t) = \frac{1}{2}[D + (m-k)^2 \pm (m-k)],$$
$$f_k(t) = 1 - [D + (m-k)^2], \qquad (29)$$

where m and D also depend on t. In the case $m \approx k$, we find from Eqs. (29) that $f_m \cong 1 - D(m)$ and $f_{m\pm1} \cong D/2$.

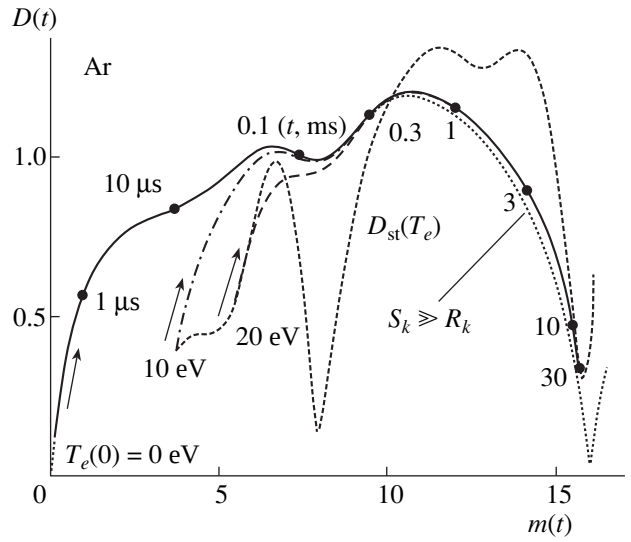

Fig. 13. Trajectories (time evolutions) of charge-state distribution moments during ionization of argon impurity from the neutral state at $n_e = 10^{13}$ cm^{-3} and $\xi_n = 10^{-5}$: simple ionization translations T_e: 0 ⟶ 1 keV, 10 eV ⟶ 1 keV, and 20 eV ⟶ 1 keV, calculated by formula (14), and extreme ionization translation T_e: 0 ⟶ 1 keV. The short-dashed line corresponds to calculations by formulas (A2.9) and (A2.10). The other notation is the same as in Fig. 12.

Since $f_m > f_{m\pm1}$, we have $1 - D > D/2$, so that $D < 2/3$ or, in general case,

$$D < \frac{2}{3} - (m-k)^2, \qquad (30)$$

where also $m \approx k$. Inequality (30) shows the range of $D(m)$ in which the description of charge-state distributions can be reduced to the description of only three charge states located around the center of the distribution and representing its most abundant part. The moments m and $D < 2/3$ allows one to find from Eq. (29) the probabilities of these charge states for transitive charge state distributions. Using the following moments (e.g., skewness), it is possible to extend (to others k) a solution of type (29), which allows one to refine the calculations but, at the same time, makes the solution more complicated.

7. DISPERSION IN THE CASE OF EXTREME RECOMBINATION

When impurity charge exchange with neutrals predominates, the distribution centers of extreme recombination translations move at a rather high speed and the translations exhibit, as was shown above, universal character in the sense that the trajectories $D(m)$ appear to be parabolic for all plasma impurities. Extreme recombination translation means the transition of an impurity into a state that is capable of radiating a large amount of energy, taking it away from the electron plasma component. A similar situation occurs in the rapid phase of disruptions in tokamak plasmas. One of the key questions here is the question of the feasible scales of impurity charge-state distribution kinetics [31]. Hence, the question of the rate of charge-exchange recombination and the factors affecting it deserve detailed consideration.

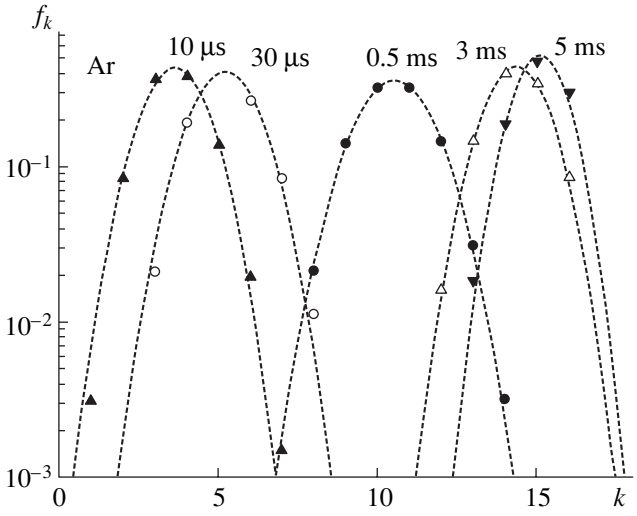

Fig. 14. Time evolution of a charge-state distribution during ionization of argon impurity from the neutral state (the extreme ionization translation T_e: 0 ⟶ 1keV) at $n_e = 10^{13}$ cm^{-3} and $\xi_n = 10^{-5}$. The instants of time are depicted near the distributions.

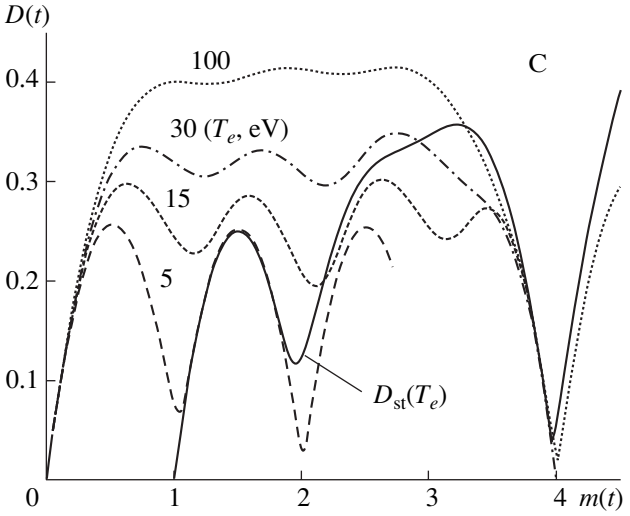

Fig. 15. Time evolution of the moments of charge-state distribution during ionization of carbon impurity from the neutral state (simple ionization translations T_e: 0 ⟶ 15 eV, 0 ⟶ 30 eV, and 0 ⟶ 100 eV, calculated by formula (14)). The dashed line corresponds to the extreme ionization translation T_e: 0 ⟶ 5 eV. The stationary function $D_{st}(m)$ is also shown for comparison.

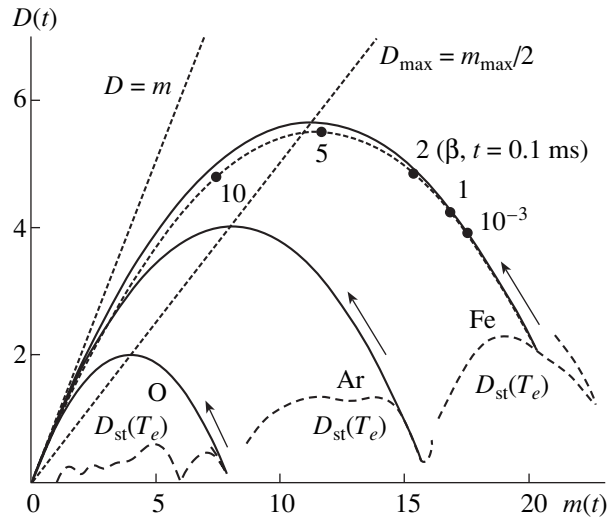

Fig. 16. Time evolution of the distribution moments at instantaneous changes in T_e (1 ⟶ 0 keV), ξ_n (10^{-5} ⟶ 10^{-3}), and β (10^{-5} ⟶ (10^{-3}, …, 10)) for Fe, Ar, and O impurities (solid lines). The stationary functions $D_{st}(m)$ are shown for comparison by the dashed lines. The trajectory of moments with allowance for formula (27) is shown by the short-dashed line. The points show the moments of distributions for several values of β, the time elapsed from the start of motion being t = 0.1 ms in each case. The arrows show the direction of motion along the trajectories.

Indeed, it follows from formulas (26) and (27) that the energy dependence of the charge-exchange rate is very weak (up to an energy of ~25 keV); therefore, the effective rates of charge-exchange impurity recombination are determined by two factors. The first of these is the density of neutral (hydrogen or deuterium) atoms n_n, while the second is the contribution from the excited states of these neutrals. In fact, the states of neutrals excited to the level n = 3–4 have charge-exchange cross sections two orders of magnitude higher than the cross section of charge exchange from the ground state. It can be assumed for estimates that 1% (β ≅ 1) of neutrals excited to the level n = 3–4 doubles the effective charge-exchange rate, 2% (β ≅ 2) of neutrals trebles it, and so on.

The influx of fast neutrals (with an energy of about 1 keV) into the plasma core is observed in the rapid phase of disruption [31–33]. These neutrals are produced at the plasma periphery (in the vicinity of the last closed magnetic surface) as a result of charge exchange of the accelerated ions of the main component with the background neutrals. The population of the excited states of these neutrals in the plasma core, where $\xi_n \cong 10^{-5}$, can increase by several orders of magnitude due to the influx of excited neutrals arriving from the periphery, where $\xi_n \cong 10^{-3}$.

Let us assume that $n_e = 10^{13}$ cm^{-3}, T_e = 1 keV, and β increases during a rapid phase of disruption up to 10. Moreover, we will assume that, during a rapid phase, the effective temperature T_e sharply (over several tens of microseconds) decreases to 100 eV and T_i increases stepwise to several keV due to the observed acceleration [33].

Let us calculate the trajectory $D(m)$ of an extreme recombination translation under this conditions and the speed of the distribution motion as a function of β in the range $10^{-3} < \beta < 10$. Similar values of β were obtained in detailed calculations of the excitation kinetics of atomic hydrogen [30, 58]. The trajectories of extreme recombination translations calculated by formula (A2.14) (where $R_k = rk$) for iron, argon, and oxygen impurities are shown in Fig. 16. The curves $D_{st}(m)$ for these elements are shown here for comparison. The figure also shows the trajectory for iron impurity, calculated with allowance for the dependence of the charge-exchange cross section on k in form (27) [54]. We note that the trajectories of translations calculated by formulas (A2.14), (6), and (7) correspond to a high accuracy to parabolic law (10), which was obtained without calculating a one-dimensional charge-state distribution. In particular, it can be seen that the maxima of the curves are located on the straight line $D_{max} = m_{max}/2$.

The moments of the charge-state distribution for iron impurity at the instant 0.1 ms (just after the start of motion) are shown in Fig. 16 by points that correspond to different values of β. In fact, the location of points is determined by the product $n_e\xi_n(1 + \beta)$. It can be seen from the figure that, already at β = 2, the distribution center shifts over 0.1 ms to the M shell, where the radiative losses sharply increase, which should result in a burst of the line impurity radiation.

Above, we have considered the cases of extreme and dominant recombination translations in which a moving distribution consequently forgets the initial values of the higher moments and a charge-state distribution close to a Gaussian one is produced. Figure 17 shows distributions that occur in the case of iron impurity (see Fig. 16). It can be seen from the figure that, in the initial distribution, only three (or maybe four) charge states are well fitted by a Gaussian curve. The charge-state distribution center then shifts rapidly (since this is an extreme translation) and the distribution approaches a Gaussian one. A similar example for oxygen impurity is presented in Fig. 18.

8. CHARGE-STATE DISPERSION DURING SAWTOOTH OSCILLATIONS OF T_e

Sawtooth oscillations of the plasma electron temperature T_e are of special interest in fusion research in tokamaks. Therefore, charge-state translations that are generated due to sawtooth oscillations of T_e are considered here as examples of solutions to the set of kinetic equations (3) in the case of a nonstationary matrix $K(t)$.

Figure 19 shows several sawtooth temperature translations for carbon impurity. The translations were

calculated for sawtooth variations in $T_e(t)$ from the minimum value of 80 eV up to the maximum value of 120 eV. The translations differ by the starting location of the distribution ($T_e(0)$ = 80 and 120 eV) and by the period of oscillations (τ = 60 and 1 ms). Two simple temperature translations (T_e: 80 $\longrightarrow$ 100 eV and T_e: 120 $\longrightarrow$ 100 eV) displaying certain average locations of the distribution are also shown for comparison by the dashed lines.

It can be seen from Fig. 19 that, in the case of large-period oscillations (60 ms), the translation trajectory takes the final shape of a closed petal already after three to four periods and does not depend of the initial distribution. Note that the location of the petal is shifted with respect to the final (ergodic) point of simple temperature translations (dashed lines) and the shift is the largest for the larger oscillation frequency, i.e., for translations with τ = 1 ms. These charge-state oscillations converge toward a common point that is located near the curve $D_{st}(m)$ (but not on the curve itself). The amplitudes of oscillations in $D(t)$ and $m(t)$ are appreciably smaller in this case.

The final closed trajectory (the petal in Fig. 19) has two branches with opposite signs (directions) of charge-state translations and a point at which the sign of translation changes sharply. The entire trajectory is located to the left of this point. This instant coincides with the instant of a sawtooth crash in $T_e(t)$. Similar behavior of the impurity charge states during a sawtooth crash in $T_e(t)$ was observed in the measurements of the time evolution of the ArXVI/ArXVII signal. A sharp step without any time delay (within the time resolution) was recorded during sawtooth oscillations in the TEXTOR tokamak [59].

The relative dimensions and the location of the ergodic petal depend on many parameters, e.g., on the oscillation period, as is seen in Fig. 19. In a tokamak plasma, one can expect an increase in the oscillation amplitude $D(m)$ due to the oscillations of the parameters n_e, T_e, T_i, ξ_n, and β. The difficulty in distinguishing the impurity dynamics and kinetics is related here to an uncertainty in the relative contribution of the oscillations of these parameters to the oscillations of the observed impurity emission. The time evolution of the impurity emission can be erroneously related to the impurity dynamics (transport) if one consider this evolution to be a consequence of variations in the total impurity density n_i only.

Figure 20 presents the same examples of charge-state translations for carbon impurity as in Fig. 19, but for the case of inverted sawtooth oscillations. By comparing these two figures, one can see that the location of the ergodic petal changes insignificantly. However, in the case of inverted sawtooth oscillations, the portion of the trajectory with a sharp turning is displaced onto the opposite side of the petal, so that the entire trajectory lies to the right (rather than to the left) of this portion. The direction of motion of the charge-state distribution center along the ergodic trajectory (counterclockwise direction for $D(m)$) also does not change. An increase in the oscillation frequency results in the opposite (as compared to Fig. 19) shift of the translation trajectories with respect to simple translations.

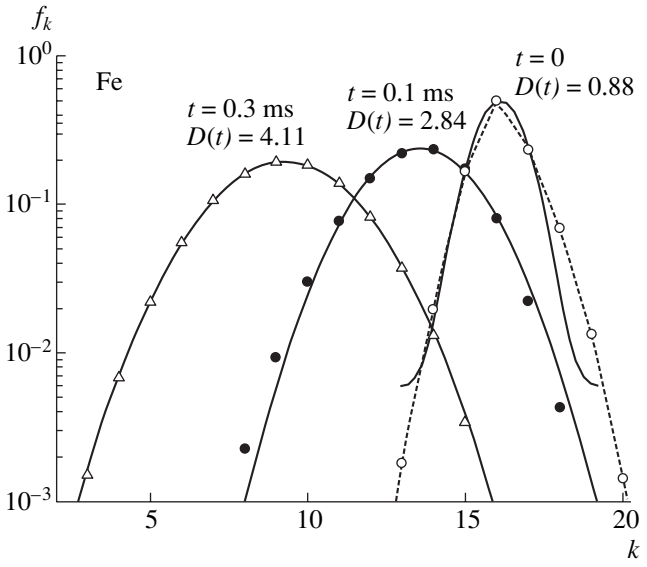

Fig. 17. Charge-state distributions of iron impurity for three instants of time during an extreme recombination translation shown in Fig. 16. Solid lines are Gaussian functions corresponding to discrete distributions.

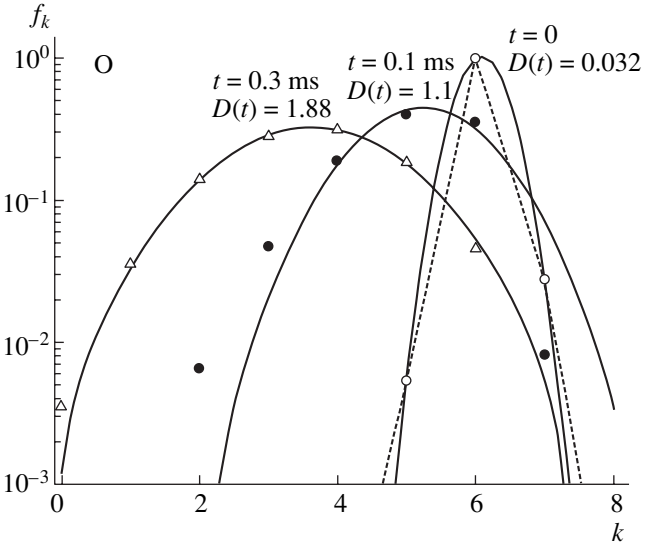

Fig. 18. The same as in Fig. 17, but for an oxygen impurity.

Figure 21 presents examples of ergodic petals in the case of direct sawtooth temperature translations for iron impurity for different effective rates of charge-exchange recombination, which is governed by the rel-

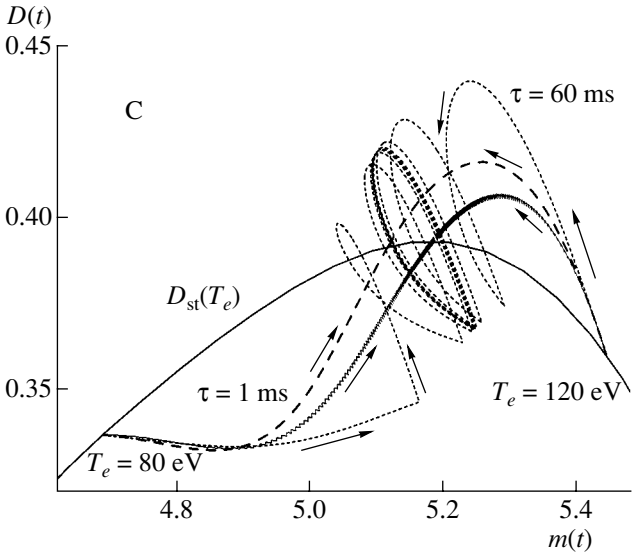

Fig. 19. Time evolution of charge-state distribution moments of carbon impurity during sawtooth oscillations of T_e (80 eV in the minimum, and 120 eV in the maximum): translations with different initial values of T_e ($T_e(0)$ = 80 and 120 eV) and different oscillation periods (τ = 60 and 1 ms). The directions of motion along the translation trajectories are shown by arrows. Simple temperature translations T_e: 80 ⟶ 100 eV and T_e: 120 ⟶ 100 eV (dashed lines) and the stationary curve $D_{st}(T_e)$ are also shown for comparison.

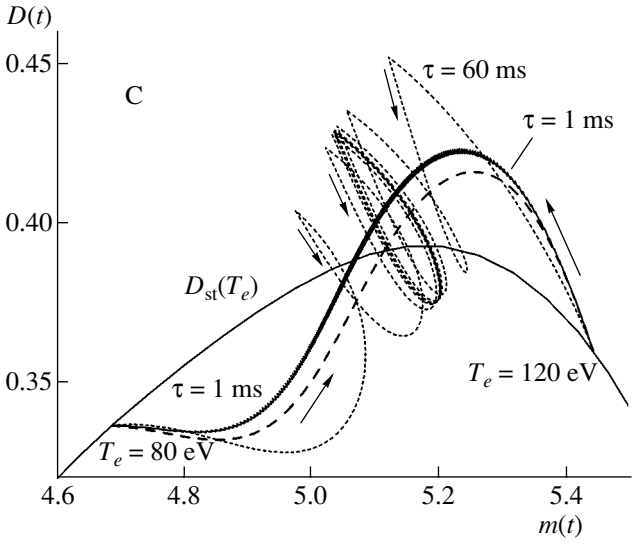

Fig. 20. The same as in Fig. 19, but for the case of inverted sawtooth oscillations of T_e.

ative density of neutrals ξ_n. It can be seen that the increase in the effective rate of charge-exchange recombination appreciably changes both the form and location of the ergodic petal with respect to the curve $D_{st}(m)$, whereas the direction of motion along the ergodic trajectory remains unchanged (counterclockwise).

9. EXPERIMENTS AND SIMULATIONS

As was stated above, the charge-state distributions obtained in simulations (especially their moments m and D) to a large degree do not depend on the adopted concept of the relationship between the effects of impurity dynamics and kinetics. In fact, these m and D represent the main content of the experimental data dealing with real charge-state distributions. However, the data of original papers that will be dealt with later (the so-called model profile distributions) are the result of processing impurity emission observations with the use of the transport codes mentioned above. These model radial distributions are further represented by the equivalent (or dynamic) curves $D(m)$ calculated using definitions (6) and (7).

Among these profile distributions of the moments $D(m)$, one should set aside those calculated with D_A = 0 and V_A = 0, i.e., purely kinetic (or coronal) distributions of the moments $D(m)$, which describe only the impurity charge-state kinetics. The other (i.e., dynamic) distributions of the moments, as compared to the kinetic distributions, give a quantitative estimate of the sensitivity of transport codes to variations in D_A and V_A and, when the experimental data are used, show the radial distributions of the moments $D(m)$ for real charge-state distributions.

When the fitting coefficients D_A and V_A of transport codes (usually MIST [3]) are assumed to be constant throughout the plasma column, model profiles of charge-state distributions do not quite satisfactorily agree with experimental emission profiles used in calculations. As a rule, the distortions of $D(m)$ increase from the plasma core toward the plasma edge, and the use of the profiles of $D_A(\rho)$ and $V_A(\rho)$ only partially solves this problem. In simulations in which the atomic rate coefficients are modified to fit the emission profiles [11], the distortions of model distributions also occur closer to the plasma edge.

A large number of profile density distributions of impurity ions have been obtained in studies of argon impurities in large- and medium-size tokamaks. As a rule, the steady-state phase of discharges is well documented.

Similar radial profiles for the TEXTOR tokamak [60] transformed into $D(m)$ are presented in Fig. 22. The initial profiles were obtained for several values of the anomalous diffusivity D_A using the MIST transport code with allowance for the profiles of the density $n_e(\rho)$ and temperature $T_e(\rho)$, where $\rho = r/a$ is a normalized radius. Here, $T_e(\rho)$ varies along each curve $D(m)$. The plasma center is located at point ρ = 0.

Since sawtooth oscillations are usually observed in tokamak plasmas, we present here two examples of ergodic sawtooth translations (with an oscillation period of 50 ms and typical relative variations in the parameters T_e, T_i, and ξ_n) calculated for argon impurity under the conditions of the TEXTOR tokamak using

data of [55]. It was assumed in these calculations that $\Delta\xi_n/\xi_n = 0.3$ for $\xi_n = 1.6 \times 10^{-6}$ and 6×10^{-6} at temperatures of $T_e(0) = 1.6$ and 1 keV, respectively.

A comparison of the curves corresponding to different values of D_A ($D_A = 0$, 0.1, and 1 m^2/s), which are assumed to be constant throughout the plasma, shows that the central part of plasma column (up to $\rho = 0.32$) is almost insensitive to variations in D_A in the range <0.1 m^2/s. As D_A increases to 1 m^2/s, variations in D for the external part of the column ($\rho > 0.32$) are also small (as can be estimated from the figure, $\Delta D \le 0.1$ at D = 0.2–0.6) and variations in the average charge are $\Delta m \le 0.1$ (at $m \approx 16$). Appreciable variations in D ($\Delta D(m) \approx 0.1$) begin at $D_A \ge 0.1$ m^2/s for $m \le 16$ in the range of the L shell, starting from the He-like Ar^{16+} ion. As can be seen from the dimensions of ergodic petals, the possible uncertainties in kinetics (e.g., an uncertainty in ξ_n) that can be related to sawtooth oscillations appear to be almost the same.

Thus, the low limit of the sensitivity of the MIST transport code to D_A for the central regions of the plasma in TEXTOR is no lower than 0.1 m^2/s. In this case, an anomaly of the value D_A is an necessary attribute of the empirical approach, rather than of impurity transport itself.

The same refers to the results of simulations of argon charge-state distributions (with the same MIST code) in the ALCATOR-C tokamak [61]. These results are shown as $D(m)$ in Fig. 23. Here, the amplitude of oscillations in $D(m)$, which correspond to the same sawtooth oscillations as in Fig. 22, increases appreciably with increasing plasma density. However, from [60, 61], it is not clear whether or not impurity charge exchange with neutrals was taken into account in calculating argon profiles.

It is of interest to analyze the charge-state distributions whose distribution center is shifted to the L shell and for which charge-exchange effects and their dependence on D_A are taken into account. These profile density distributions for argon ions in the plasma of the PLT tokamak [62] (also obtained with the MIST code) are presented in Fig. 24 as functions of D_A. Here, as in Fig. 23, the values of D_A are also considered to be constant throughout the plasma and are specified in this figure together with the relative neutral density $\xi_n(0)$ at the center of the plasma column. The relatively low parameter values of the PLT plasma and taking the diffusion ($D_A = 1$ m^2/s) into account provide an interesting result: a portion of the curve $D(m)$ in the plasma core is almost vertical. A similar effect in Fig. 6 is a consequence of impurity charge exchange; however, in Fig. 23, the occurrence of the almost vertical portion of the curve is due to impurity transport, which shows the possibility of diffusive and convective translations in the plasma core. A relatively small charge-exchange effect with $\xi_n(0) = 2 \times 10^{-6}$ results in the small shift (by $\Delta m = 0.05$) of the entire curve. A comparison of Figs. 24, 22, and 6 shows that there is an equivalence between the charge-exchange effect and the effect of ion diffusion with respect to impurity charge-state distributions. More-

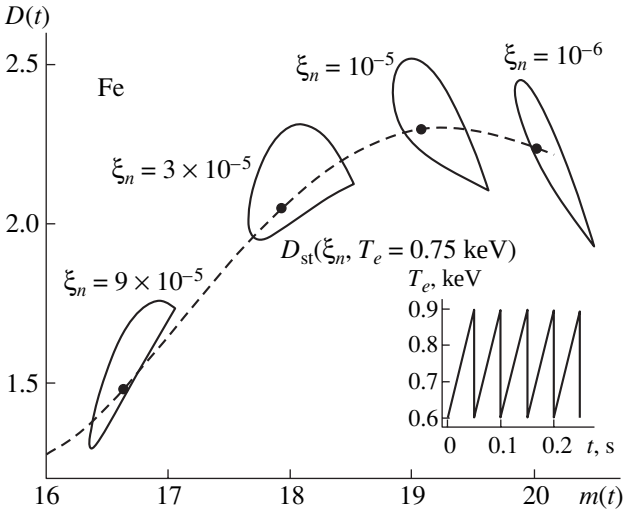

Fig. 21. Ergodic trajectories of charge-state distribution moments of iron impurity during sawtooth oscillations of T_e for different relative neutral densities ξ_n. The stationary function $D_{st}(\xi_n)$ at a constant temperature $T_e = 0.75$ keV is also shown for comparison by the dashed line. The points show the stationary moments for the given values of ξ_n.

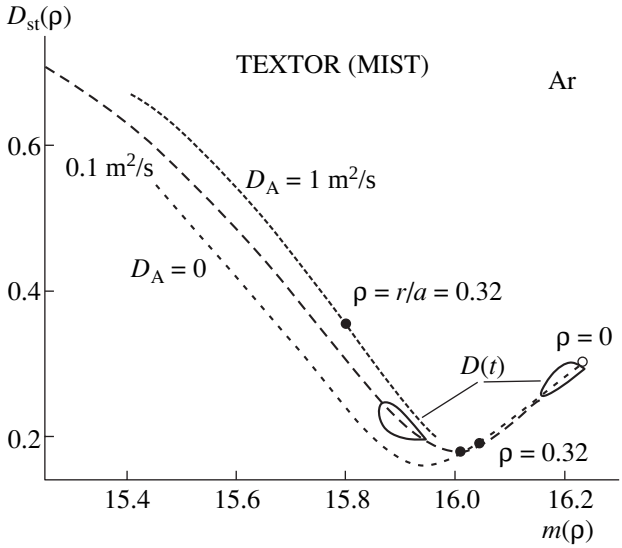

Fig. 22. Stationary parametric radial profiles of charge-state distribution moments of argon impurity plotted for different values of D_A by the data of the MIST code for the TEXTOR tokamak [60] for $T_e = 1.6$ keV and $n_e = 2 \times 10^{13}$ cm^{-3} at the center of the plasma column. The open circle corresponds to the center of the column; the closed circles show the locations of charge-state distribution moments at $\rho = 0.32$ for different D_A; and the closed trajectories $D(t)$ correspond to ergodic sawtooth translations calculated for argon using the data of [55].

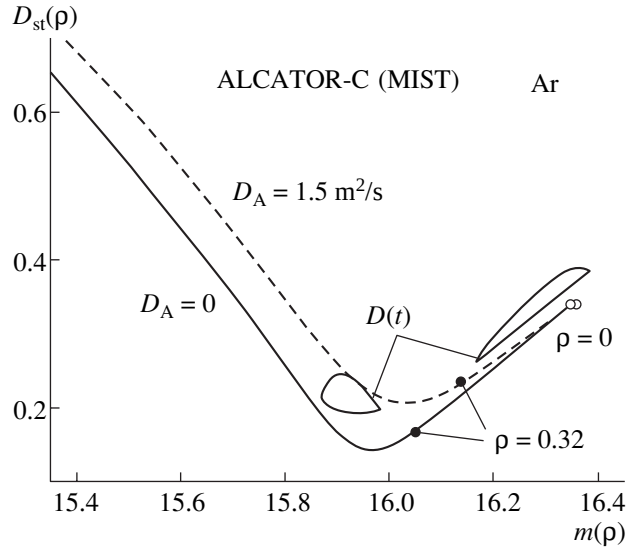

Fig. 23. The same as in Fig. 22, but for the ALCATOR-C tokamak (MIST) [61] at T_e = 1.65 keV and n_e = 3.5 × 10^{14} cm^{-3} at the center of the plasma column.

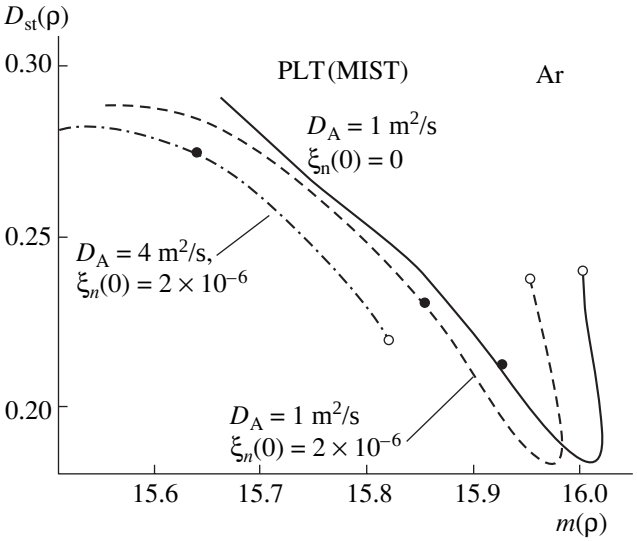

Fig. 24. The same as in Figs. 22 and 23, but for the PLT tokamak (MIST) [62] at T_e = 1.5 keV and n_e = 1.5 × 10^{13} cm^{-3} at the center of the plasma column and with allowance for the charge-exchange effect: $\xi_n(0)$ is the value of the relative neutral density at the center of the column, the open circles correspond to the center of the column (ρ = 0), and the closed circles correspond to ρ = 0.31.

over, the curve also shifts toward the middle of the *L* shell as D_A increases to 4 m^2/s, which is similar to a decrease in the dispersion with increasing ξ_n (see Fig. 6).

For comparison, the curves $D_{st}(m)$ for $D_A > 0.1$ m^2/s presented in Figs. 22–24 are shown together in Fig. 25, which also presents the data from DIII-D [63] and JET [64] (shots nos. 53015 and 53548). It can be seen from Fig. 25 that the data from DIII-D and JET are mainly located within the *K* shell of argon atoms. Only at the periphery of the plasma column do He-like ions become most abundant, thereby representing a mode of charge-state distribution. In simulations, it was assumed that there was a profile distribution of $D_A(\rho)$ that increased from the center toward the periphery. The scales of this increase are specified in the figure. Here, kinetic (coronal) distributions $D_{st}(m)$ (D_A = 0) at ξ_n = 10^{-6} are also shown.

It can be seen that the chosen kinetic distribution $D(m)$ describes quite well the data of both shots from JET and shows that the results of simulations for JET within the *K* shell are almost insensitive to the diffusivity in the range D_A = 0.3–1 m^2/s (except for the region $\rho > 0.8$). However, the distortions and the total uncertainty in the model parameters (e.g., an uncertainty in ξ_n) also increase here. It is interesting to note that, at the plasma periphery, the dispersion curve for DIII-D agrees well with the curve for the central plasma of the PLT tokamak.

A comparison of the curves presented in Fig. 25 allows one to conclude that charge-state distributions close to the He-like state with the distribution center $m \approx 16$ are the most sensitive to diffusivity ($\Delta D \cong 0.1$). Near $m \approx 16$, the sensitivity of the distribution to dynamic effects (and not only to the diffusion of ions) appears to be highest, whereas it is lowest near $m \approx 16.2$. The sensitivity scale $\Delta D(D_A)$, as well as the uncertainty in kinetics (see, e.g., Fig. 2b), is significantly higher for the *L* shell than for the *K* shell. The width and dispersion of the charge-state distribution of argon at the periphery are almost double those of the kinetic (coronal) distribution.

Unfortunately, the above simulations of argon charge-state distributions fail to provide any information about the effect of impurity charge exchange and the related uncertainties on the dispersion of charge-state distributions and on the sensitivity of the model to transport coefficients. However, simple estimates [11] show that this effect can play a decisive role.

In [65], besides the data on charge-state distributions of argon impurity, there are also data for neon impurity. Similar distributions for neon, carbon, and oxygen impurities are presented in [65, 66] for the TORE SUPRA tokamak and the RFX reversed field pinch device. The data for neon impurity in the form of $D(m)$ are shown in Fig. 26. The stationary kinetic (coronal) distribution $D_{st}(m)$ is also shown there. As in the case of argon, a comparison of these data shows the same result: the transport model is insensitive to the coefficient D_A in the central part of the plasma column of DIII-D, TORE SUPRA, and RFX. An appreciable

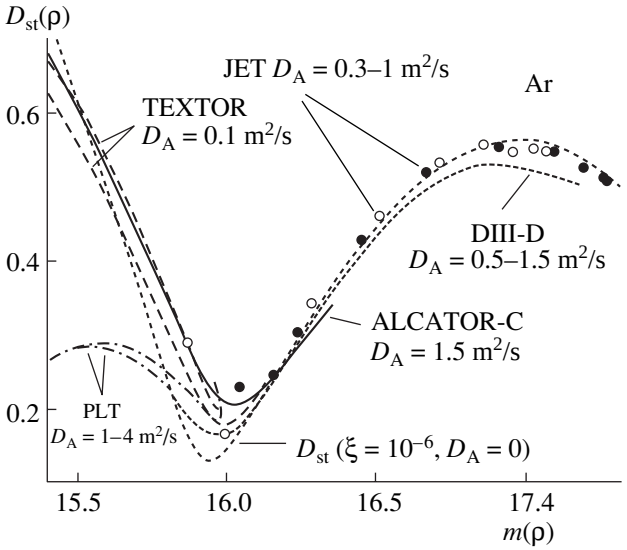

Fig. 25. Comparison of stationary profiles of moments for several tokamaks: the solid line shows the data for ALCATOR-C from Fig. 23, the dashed line shows the data for TEXTOR from Fig. 22, and the dotted line shows the data for DIII-D [63]. The open and closed circles correspond to experimental profiles for two discharges in the JET tokamak (shot nos. 53548 and 53015, respectively) [64], the dashed-and-dotted line shows the data for PLT from Fig. 24, and the short-dashed line corresponds to the calculated kinetic (D_A = 0) distribution of moments as a parametric function of T_e at $\xi_n = 10^{-6}$.

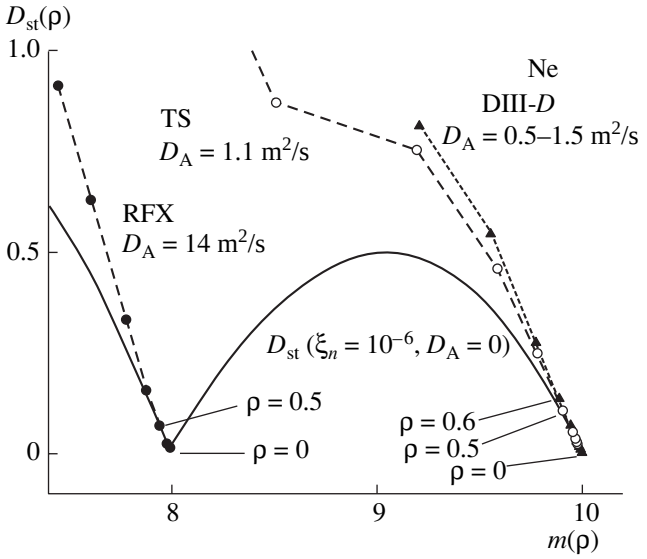

Fig. 26. Stationary parametric radial profiles of charge-state distribution moments of neon impurity: the solid line corresponds to the calculated kinetic (D_A = 0) distribution of moments as a parametric function of T_e at $\xi_n = 10^{-6}$: the open circles show the data for the TORE SUPRA tokamak (TS) [66], the triangles show the results of calculations for DIII-D (MIST) [63], and the closed circles show the results of calculations for RFX [66]. The arrows show the radial positions for some distributions.

increase in the distribution dispersion as compared to the coronal one is observed at the plasma periphery ($\rho > 0.5$).

Similar behavior of $D(m)$ in the case of carbon impurity was observed in the TORE SUPRA and RFX devices [65] (see Fig. 27). The dispersion of the distribution in the central part of the plasma column is also almost the same as in the kinetic (coronal) case and rapidly increases from the center toward the periphery. Since charge-state distributions and, consequently, their characteristics (moments) are independent of the type of the model (dynamic or kinetic), one can attempt (even without knowledge of the relation between dynamics and kinetics) to find some kinetic equivalents for the obtained dependences $D(m)$. In the case of carbon, such equivalent curves are the dominant recombination translations T_e: 0.4 keV–22 eV and T_e: 2.4 keV–14 eV, as is shown in the figure. Similar equivalents can easily be found also for the curves $D(m)$ obtained in the DIII-D, TORE SUPRA, and RFX devices for neon impurity (see Fig. 26).

The dependences $D(m)$ obtained for oxygen impurity in the TFR tokamak (using the simulation data [11]) and in the RFX device [65] are shown in Fig. 28. Three curves for TFR are reproduced by three groups of points and correspond to three different instants of time t = 80, 130, and 230 ms from the start of a discharge in TFR. The difference of $D(m)$ from the coronal curve (taken at $\xi_n = 10^{-6}$) manifests itself here at $\rho > 0.6$. This case differs from others in that a kinetic model (rather than a usual transport model with D_A and V_A) was used in simulations of the emission profiles and radial variations of the fitting parameters were taken into account (see [11]). It is probably for this reason that the peripheral values of $D(m)$ differ only slightly from the stationary kinetic (coronal) curves. In standard simulations, these differences (see Figs. 26, 27) are significant, which could be related to simulation errors at the periphery, rather than to the transport itself.

The data on charge-state dispersion in RFX are of interest since they lie in the region $m \approx 6$, i.e., at significantly higher values of the dispersion than any possible stationary kinetic distributions (one example is presented by the dashed line in Fig. 28). Extremely large values of D_A and V_A (10–20 m^2/s and 40–90 m/s, respectively) were used to model the experimental charge-state profile distributions in [65]. Similar behavior of $D(m)$ with respect to kinetic distribution can be seen in Fig. 12, but only for carbon. Hence, the equivalent distribution $D(m)$ for the RFX data in Fig. 28 appears to be a curve that presents the trajectory of a dominant ionization translation, e.g., T_e: 10 eV–1.5 keV at $\xi_n = 8 \times 10^{-5}$. On the other hand, if one assumes that convective impurity transport is dominating at the periphery, then the equivalent time dependence $D(t)$ can be considered to be a spatial translation

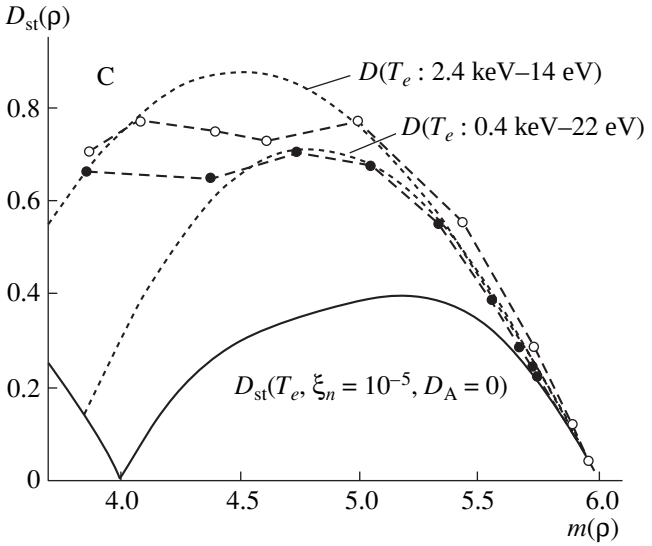

Fig. 27. The same as in Fig. 26, but for carbon impurity: the closed circles show the results of calculations for RFX [66] at D_A = 10–20 m^2/s, V_A = 40–90 m/s, $T_e(0)$ = 0.4 keV, and $n_e = (2–8) \times 10^{13}$ cm^{-3}; the open circles show the results of calculations for TORE SUPRA (TS) [66] at D_A = 1.5 m^2/s, V_A = 3–4.5 m/s, $T_e(0)$ = 2.4 keV, and $n_e = 3.2 \times 10^{13}$ cm^{-3}; the solid line shows the stationary kinetic distribution of moments $D_{st}(m)$ at $\xi_n = 10^{-5}$ and $D_A = 0$; and the dashed lines corresponds to the calculated dominant recombination translations describing experimental distributions for RFX and TS.

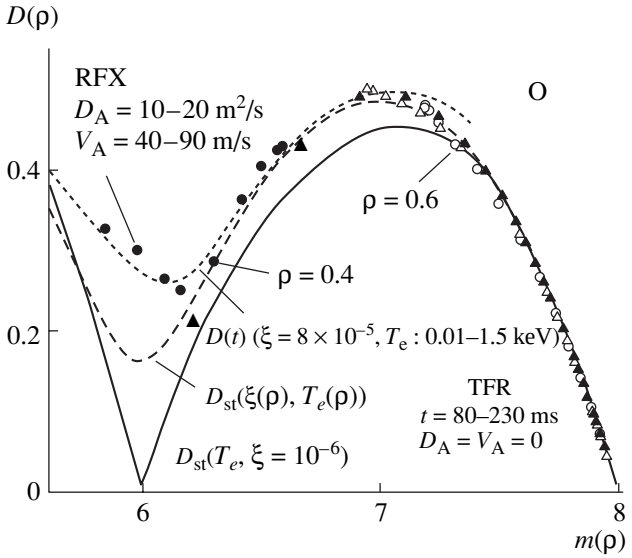

Fig. 28. The same as in Figs. 26 and 27, but for oxygen impurity: the closed circles the results of calculations for RFX [66] at D_A = 10–20 m^2/s, V_A = 40–90 m/s, $T_e(0)$ = 0.3 keV, and $n_e = (2–8) \times 10^{13}$ cm^{-3}; the closed and open triangles and the open circles correspond to calculations by the data from simulations of experimental emission profiles in the TFR tokamak [11] at t = 80, 130, and 230 ms from the start of discharge at $D_A = 0$, $V_A = 0$, $T_e(0)$ = 1 keV, and $n_e = 3.2 \times 10^{13}$ cm^{-3}; the solid line corresponds to the stationary distribution of the moments $D_{st}(m)$ at $\xi_n = 10^{-6}$ and $D_A = 0$; the dashed line shows the results of calculations with allowance for the profiles $\xi_n(\rho)$ and $T_e(\rho)$; and the short-dashed line corresponds to the translation T_e: 0.01 ⟶ 1.5 keV at $\xi_n = 8 \times 10^{-5}$.

that represents the convective flux of ionizing ions directed into the plasma column. Note that, in contrast to the initial model charge-state distributions of [66], an important feature of equivalent dominant ionization translations is that their distributions are almost Gaussian (see Fig. 14).

It is typical for all the data presented in Figs. 22–28 for Ar, Ne, O, and C impurities that the average charge of the distributions varies slightly throughout the entire plasma column (from the center to the very edge of plasma). Figure 29 shows the average charge versus the normalized plasma radius plotted using the above data for argon impurity. These results are considered to be an indication of the anomalous diffusive escape of highly ionized ions from the plasma core to the periphery [9, 11]. However, it can be assumed that there are two dominating convective transport components, which correspond to two oppositely directed fluxes of ionizing and recombining impurity ions.

Indeed, it can be seen from Fig. 29 that, near the plasma edge (starting from $\rho > 0.8$ and up to the chamber wall), there is a region in which the average charge m of argon impurity ions vary very rapidly. Thus, at $\Delta\rho$ = 0.1–0.2, m varies near the edge from 0 (on the chamber wall) up to $m \approx$ 15–16 (at ρ = 0.8–0.9); i.e., $\Delta m/\Delta\rho \approx$ –(80–160). When the convective transport components are dominant, Eq. (8) (for m) under stationary conditions ($\partial m/\partial t = 0$) reduces to the form

$$u_\perp \frac{\partial m}{\partial \rho} = \sum_{k=0}^{Z} (S_k - R_k) f_k, \qquad (31)$$

where $u_\perp$ is the velocity of the transverse motion of impurity ions, which is mainly determined by the drift in crossed fields and is independent of the ion charge [41]. Equation (31) shows that the large gradients of the average charge near the plasma edge can be related to extreme cases of charge-state kinetics, namely, to the domination of either ionization processes with $S_k \gg R_k$ (it follows from Eq. (31) that, in this case, $u_\perp < 0$) or recombination processes with $R_k \gg S_k$ (it follows from Eq. (31) that, in this case, $u_\perp > 0$). In the former case, Eq. (31) describes convective flux of ionizing impurity ions toward the plasma core. In the latter case, it describes the flux of recombining ions escaping from the plasma.

These cases of impurity dynamics are presented by the dominant charge-state translations (by ionization in Fig. 28 and recombination in Fig. 27), i.e., by the equiv-

alent curves of $D(m)$, which describe the charge-state distributions of light impurities at the plasma edge. Being calculated as time dependences, they appear to be equivalent trajectories in space, since $\partial/\partial t = u_\perp \partial/\partial \rho$. The behavior of charge-state distributions varying along these spatial trajectories is qualitatively the same as for dominant ionization and recombination translations. In particular, in the case of a dominant recombination translation, they are located much higher than the corresponding stationary (coronal) curves. Note once again that all of these charge-state distributions determined along trajectories are equivalent with respect to any possible interpretation: diffusive, convective, or kinetic.

Let us consider examples of the recombination translations obtained in analyzing the behavior of impurity charge-state distributions in a rapid phase of a major disruption in the DAMAVAND small tokamak [32]. These data were obtained in simulations of the time evolution of the line emission of He-like CV ions. Two disruptive regimes were studied. In the first regime, a burst and then decay of CV line emission were observed along all the lines of sight both in the center and at the periphery in a rapid phase of disruption at a plasma current of I_p = 32 kA. In the second regime, at I_p = 21 kA, CV line emission turned out to decay in the center, while a burst and then rapid decay of the emission intensity below its initial level were observed at the periphery. These data on the spatial and temporal evolution of CV line emission in both regimes can be explained by the fact that the impurity recombination rate increases approximately by two orders of magnitude in a rapid phase of disruption over a time of 10–20 μs. This is possible because of the charge exchange of carbon ions with excited neutral deuterium atoms, whose generation and escape from the plasma are observed in the vicinity of the last rational magnetic surface (q = 2) in a rapid phase of disruption.

The results of simulations [32] allow one to plot the trajectories of the corresponding recombination translations $D(m)$, which are shown in Fig. 30. The data for two disruptive regimes are shown here by two trajectories for each regime: for the plasma center and for the periphery. The time evolution of the moments $D(m)$ of the charge-state distribution are shown by points along these trajectories within each 50-μs time interval during a rapid phase of disruption. Note that, in both regimes, at the beginning of a rapid phase of disruption, the average charge of peripheral distributions, m_p, is somewhat higher than the average charge of charge-state distributions in the core, m_c, due to the appreciable contribution of the peripheral suprathermal electrons to impurity ionization. By the end of a rapid phase of disruption, the situation becomes the opposite: $m_c > m_p$. The trajectories $D(m)$ of these translations are close to the trajectories of simple recombination translations; therefore, as was pointed above, they are almost independent of both the plasma density and the amount of impurity. Soon after the start of a rapid phase of disruption, the dispersion of charge-state distributions at the periphery begins to exceed the dispersion of charge-state distributions in the core. According to the calculations of similar extreme translations (see Section 7), the shape of a charge-state distribution rapidly approaches a Gaussian one. However, the most important feature of impurity behavior during a disruption is that, 50 μs after the beginning of the fast phase, the most part of the distribution is shifted to the L shell, which corresponds to a substantial increase in the radiative losses.

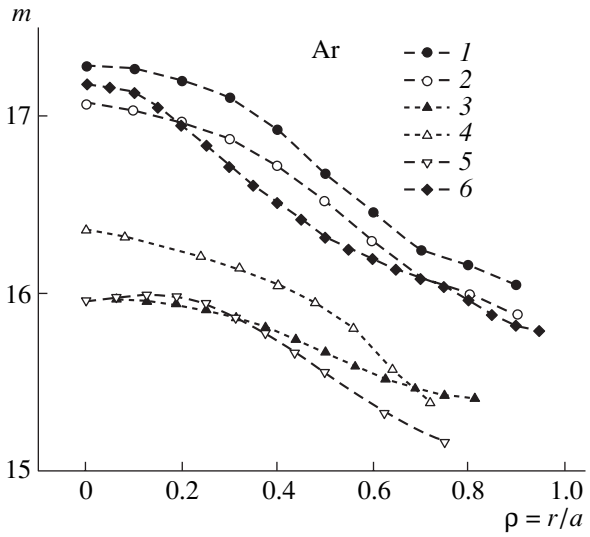

Fig. 29. Average charge of argon impurity as a function of the normalized radius of the plasma column by the data from Figs. 22–25: (*1*) JET (shot no. 53015, (*2*) JET (shot no. 53548), (*3*) TEXTOR, (*4*) ALCATOR-C, (*5*) PLT, and (*6*) DIII-D.

As was shown above, in the course of ionization of impurity from its neutral (or nearly neutral) state in a hot plasma, an impurity charge-state distribution close to a Gaussian one rapidly emerges and retains for a fairly long time period. Thus, one can assume that the emission signals I_k of the most abundant charge states normalized to their maximum values $I_k^{\max}$ can be described by the function

$$I_k/I_k^{\max} = f_k/f_m = \exp\left[-\frac{(k-m)^2}{2D}\right]. \qquad (32)$$

This allows one to determine $m(t)$ and $D(t)$ and the charge-state distribution of a rapidly ionized impurity using the data on the behavior of emission of these charge states, in particular, the data obtained in experiments with the injection of diagnostic pellets and their subsequent evaporation by the laser blow-off technique.

Let us consider similar experiments in the ATC tokamak as an illustration. In these experiments, the time evolution of the intensity I_k of bright emission

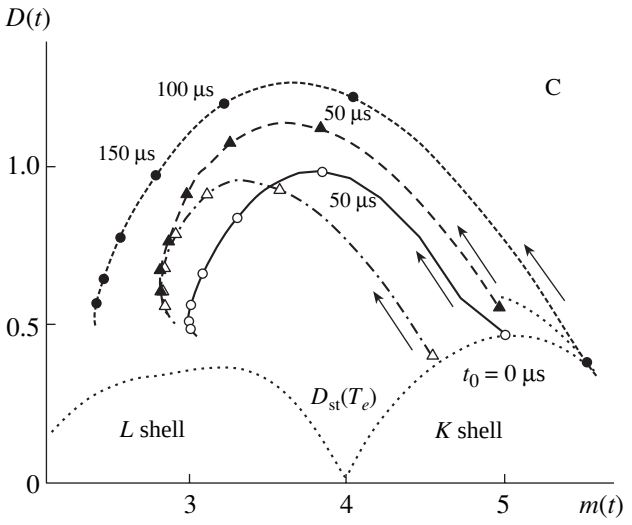

Fig. 30. Recombination translations of carbon impurity plotted using the simulation data on the emission of He-like ions during the rapid phase of a major disruption in the DAMAVAND tokamak [32]. The open circles (solid line) correspond to the center of the plasma column in the first regime, the closed circles (short-dashed line) correspond to the peripheral plasma in the first regime, the closed triangles (dashed-and-dotted line) correspond to the center of the plasma column in the second regime, and the open triangles (dashed line) correspond to the peripheral plasma in the second regime. The symbols along the curves show the time evolution of the moments $D(m)$ at every 50-μs intervals.

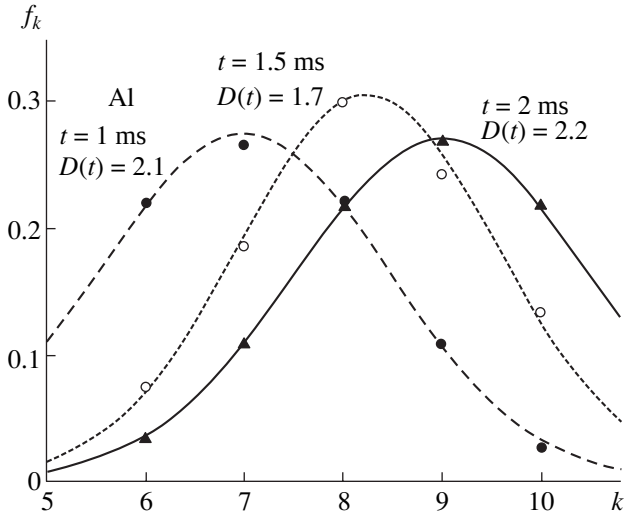

Fig. 31. Charge-state distributions of aluminum impurity plotted for three instants of time: 1, 1.5, and 2 ms after pellet injection into the ATC tokamak [67].

bursts ($\Delta n = 0$ transitions to the ground state) of the neighboring charge states of aluminum, AlV–AlXI, after the injection of a pellet and its subsequent rapid evaporation was investigated [67]. Note that the $I_k/I_k^{\max}$ ratios presented in that paper are integrated along the minor diameter of the column. Figure 31 shows aluminum charge-state distributions plotted using these data for three instants of time: 1, 1.5, and 2 ms after pellet injection. It can be seen from the figure that the time evolution of the aluminum charge-state distribution is quite well described by a Gaussian distribution. Note that the distribution center turns out to lie inside the *L* shell of aluminum atoms at these instants. However, the dispersion of these charge-state distributions is approximately twice as large as the one calculated ($D \approx 1$) for ionization translation from the aluminum neutral state and seems to correspond to a charge-state distribution averaged along the line of sight.

10. CONCLUSIONS

The analysis of impurity behavior in tokamak plasmas using the data from observations of impurity emission is substantially determined by an approach to the solution of the problem of distinguishing between impurity dynamics and kinetics. A necessary condition for the standard empirical approach to the modeling of impurity transport in this case is the assumption of perfect accuracy for the calculations of impurity charge-state kinetics [7]. However, in practice, the empirical transport coefficients D_A and V_A comprise all of the errors of analysis and, therefore, lose to a large extent their relation to the real impurity transport. Thus, for example, in the core of a tokamak plasma, the anomaly of impurity transport is an inherent attribute of the empirical approach, rather than of the real impurity transport. From the other hand, the empirical approach results in an underestimation of the possibility of a detail study of impurity charge-state distributions.

Charge-state distributions obtained in the frames of qualitatively different (dynamic or kinetic) models appear to be equivalent with respect to the initial experimental database. The main characteristics (the lowest moments) of the distributions (such as the average charge *m* and dispersion *D*) are almost independent of the initial assumptions about the relationship between dynamic and kinetic effects. Thereby, the values of *m* and *D* provide a quantitative description of the effects and form a basis for their distinguishing in future.

The paper presents the results of the development of a systematic concept of kinetics of impurity charge-state distributions and the related effects, as well as their typical scales and the conditions for their observation. Analytical approaches to the solution of charge-state kinetic equations with the use the symmetry properties of the kinetic matrix and an efficient technique for calculating its eigenvalues are first considered here. The results of their application to the study of the effects of impurity charge-state kinetics in tokamak plasmas (such as initial impurity ionization, impurity charge exchange with neutral atoms, and the behavior of impurity in disruptive phenomena) have been presented.

It has been shown that the study of elementary forms of impurity charge-state kinetics corresponding to a stationary kinetic matrix and called simple charge-state translations is of great importance for the analysis of impurity charge-state kinetics in nonstationary processes in tokamak plasmas. Any complex types of charge-state kinetics can be represented by these simple translations. A classification of simple translations has been developed.

Simple ionization and recombination translations with their extreme and particular cases (such as diffusive and convective) have been considered. Analytic expressions describing the behavior of the charge-state distribution function in the case of extreme ionization and recombination translations and related to the type of generalized Erlang distributions, well known in the theory of random processes, are obtained. The time evolution of impurity charge-state distributions and their lowest moments has been analyzed for the first time for direct and inverted sawtooth oscillations of the electron temperature T_e.

Here, we have considered only kinetic charge-state translations, namely, possible time evolutions of charge-state distributions related to the variations in the atomic rate coefficients. However, to develop these views, an analysis of dynamic translations, i.e., charge-state translations caused by spatial and temporal variations in the impurity dynamics (transport), is also of interest.

It has been shown that the spatiotemporal behavior of charge-state distributions is conveniently presented in terms of the lowest moments: the average charge m and the dispersion D, i.e., in the form of the function $D(m)$. Note that this approach to the description of kinetics partially reproduces the attempts of [37–41] to reduce the number of kinetic equations to obtain a compact analytical description of kinetics in the frame of approximate models. These approaches result in a loss of the accuracy of description when m falls in the transit regions between neighboring shells. The trajectories $D(m)$ of simple translations not only provide a compact, accurate, and convenient representation of kinetic processes, but are also independent of the densities n_e and n_i.

The charge-state dispersion of stationary distributions for the most typical impurities in tokamak plasmas has been calculated. It has been shown that, when impurity charge-exchange recombination with neutral atoms is of importance, the recombination branch originates on the curve $D_{st}(T_e)$. This leads to an appreciable increase in D and a decrease in the average charge m as T_e increases to higher than 3–5 keV. The recombination branch of $D_{st}(T_e)$ can results in diffusive and convective translations of charge-state distributions. These types of translations originate as a result of impurity interaction with fluxes of suprathermal electrons.

It has been found that, during the initial phase of impurity recombination, the dispersion of a charge-state distribution appreciably increases (proportionally to m in an extreme case) in comparison to its initial (coronal) value, while during impurity ionization, it decreases, as a rule. A systematic difference between simple ionization and recombination translations lies in that the trajectories $D(m)$ of recombination translations are located higher than the curves $D_{st}(m)$, while the trajectories of ionization translations are located below the curves $D_{st}(m)$.

Thus, one can conclude that a systematic broadening of impurity charge-state distributions is typical of nonstationary recombining plasmas. In contrast, nonstationary ionizing plasmas are characterized by a decrease in the dispersion (and width) of charge-state distributions in comparison to the stationary case. Similar behavior is typical of simple ionization translations since they are far from the extreme cases and from the case of dominant ionization.

The results of calculations of charge-state translations illustrate the ergodic character of charge-state kinetics, i.e., the existence of a final (stationary) charge-state distribution toward which a given distribution moves as a whole in any instant of time, forgetting its initial (and transit) states.

In the case of extreme charge-exchange recombination translation, the effect of the consequent forgetting of the initial values of the higher moments of the distribution takes place. Thus, the term related to the initial value of the skewness vanishes faster than that related to the initial value of the dispersion. Their trajectories in the moment space appear to be universal (in particular, parabolic for $D(m)$), and the time evolution of these distributions quite rapidly (over ~100 μs) results in an almost Gaussian distribution.

The appearance of a Gaussian charge-state distribution can also be expected during the ionization of the pellet material vaporized by the laser blow-off technique, which was demonstrated (see Fig. 31) using an analysis of aluminum line emission in experiments in the ATC tokamak as an example.

On the other hand, it has been shown that, independently of Z, many charge-state distributions turn out to be close to the transitive distributions at $D < 2/3$. Such behavior can be represented by a small number of charge states (as a rule, three states are sufficient). Their probabilities are simply expressed in terms of m and D. In particular, a simple relationship ($f_m \cong 1 - D(m)$) relates the dispersion with the behavior of He-like ions of low- and medium-Z impurities if these ions become a mode of distribution.

Using the function of moments $D(m)$, we have performed a quantitative analysis of experimental and model charge-state distributions obtained in the studies of C, O, Ne, and Ar impurities in the JET, DIII-D, TORE SUPRA, ALCATOR-C, TEXTOR, PLT, and TFR tokamaks. It was shown that the dispersion of charge-state distributions obtained with $D_A \le 0.1$ m^2/s

is almost the same as for kinetic distributions with $D_A = 0$ m^2/s. This means that standard impurity transport codes (e.g., MIST) is essentially insensitive to D_A in the center of the plasma column for all the impurity species under study.

An appreciable increase in the charge-state distribution dispersion in comparison to kinetic (coronal) distributions, together with an increase in the errors related to the simulations of kinetics of impurity charge-state distributions (see Figs. 2a, 2b), is observed at the periphery ($\rho > 0.5$). In particular, the scales of errors that can be related to sawtooth oscillations appear to be on the same order of magnitude as variations in $\Delta D(m)$ at $D_A = 1 - 1.5$ m^2/s.

An analysis of the radial distribution of the average charge for Ar, Ne, O, and C impurities shows that there is a region with a large gradient of the average charge, $\Delta m/\Delta\rho \approx -(80–160)$, at the plasma periphery. It was found that the dominant ionization and recombination translations with the corresponding equivalent curves $D(m)$ can provide a description of light impurity charge-state distributions at the plasma periphery. These curves calculated as time dependences provide the convective impurity fluxes at the plasma periphery and can also present the equivalent spatial trajectories. An important feature of these translations is that the corresponding charge-state distributions are close to Gaussian ones. Therefore, one can expect that the impurity charge-state distributions in the peripheral plasma are also close to Gaussian; this points to the possibility of simplifying their calculation and analysis.

The form and characteristic times of the recombination translations obtained in analyzing the carbon charge-state distributions in the rapid phase of a major disruption appear to be the same as in the case of extreme recombination translations calculated for a sharp increase (by two orders of magnitude) in the rate of impurity charge exchange with neutral atoms. A rapid transition of impurity (over a time ~50–100 μs) into the range of the radiation barrier and an appreciable increase in the charge-state distribution dispersion were observed in simulations. Simulations of both the time evolution of carbon emission and the kinetics of the carbon charge-state distribution during a disruption show that, as early as 50 μs after the start of a rapid phase, most of the carbon charge-state distribution is shifted to the L shell, which explains the rapid increase in the radiative losses.

Thus, very different observations of impurity emission in tokamak plasmas point to the necessity of analyzing impurity behavior by distinguishing between dynamics and kinetics of ions. In this connection, under the conditions of restricted accuracy of analysis and in view of the lack of complete atomic data, the standard model analysis of D_A and V_A, in our opinion, has practically no prospects in these studies. As a possible approach to the solution of this problem, we propose a systematic analysis of impurity charge-state kinetics and, first of all, an empirical analysis of the distribution moments, which provide a quantitative description of both the dynamic and kinetic effects.

ACKNOWLEDGMENTS

The author is grateful to V.S. Lisitsa for his criticism, useful discussions, and important insights in performing this work. I also thank V.E. Zhogolev for providing me with subroutines on the rate coefficients of some atomic processes.

APPENDIX 1

KINETIC MATRIX

It follows from Eq. (9) that the kinetic matrix $K = [a_{ij}]$ ($i, j = 1, 2, \ldots, Z + 1$) is singular (since there is a linear dependence of its rows and their sum is zero) and tridiagonal ($a_{ij} = 0$ at $|i - j| > 1$) with positive elements along two subdiagonals; i.e., it belongs to the class of the so-called Jacobian matrices with $a_{i,i+1}a_{i+1,i} > 0$ for all $i = 1, 2, \ldots, Z$. It is well known [68, 69] that Jacobian matrices are similar to symmetric (tridiagonal) matrices. This fact results in the most important feature of the matrix K: all its eigenvalues λ_k are real (and remain real in the case of nonstrict inequalities $a_{i,i+1}a_{i+1,i} \geq 0$). They can be found by solving the characteristic equation $\det(K - \Lambda E) = 0$. Here, Λ is a diagonal matrix composed of eigenvalues and E is a unit matrix, since the determinant of the matrix $B = K - \Lambda E$ is calculated by the recurrent formula [68]

$$\det B(\lambda, i+1) = (S_i + R_i - \lambda)\det B(\lambda, i) - S_{i-1}R_i \det B(\lambda, i-1). \quad \text{(A1.1)}$$

where $i = 2, \ldots, Z$. Moreover, the characteristic equation can be represented in the form of an algebraic equation of power Z, the roots of which provide the spectrum of eigenvalues λ_k and whose coefficients can also be found using expressions (A1.1). The entire spectrum of eigenvalues can be determined using the fact that all the roots of the characteristic equation are real; as a rule, different; negative (with a single exception $\lambda_0 = 0$ due to the singularity of the matrix K); and lie within the range $-S_0 \leq \lambda_k \leq 0$. The Lobachevsky–Dandelin–Graffe method of the squaring (separation) of the roots [70] is well suited to solving this problem. In our calculations, this method appears to be much faster than the interval bisection method [69].

A specific feature of the method of quadratic roots is that, because of the rapid increase in each iteration, the coefficients of the rearranged equations should be expressed in terms of the two quantities: mantissa and power. In this case, they can be calculated separately for the required number of iterations, which depends on the presence of closely located roots. If there are no such roots (which usually takes place for light impurities), five to six iterations are sufficient. In other cases,

closely located roots can appear, e.g., when dielectronic recombination begins to appreciably contribute to R_k. Twelve to fifteen iterations then result in a relative error in determining λ_k less than 10^{-8}–10^{-10} even at a relative difference between roots less than 1%. Note that this difference is much less than the relative error with which S_k and R_k are known.

Using a diagonal matrix D_K with real positive elements, the matrix K can be transformed into a real symmetric matrix W:

$$K = D_K^{-1} W D_K. \tag{A1.2}$$

Then, comparing the elements on the subdiagonals of the right and left matrices, one can obtain a set of coupled uniform equations for the diagonal elements d_k of the matrix D_K:

$$S_k d_{k+1}^2 = R_{k+1} d_k^2. \tag{A1.3}$$

For some $k = m$, we can take $d_m = 1$; then, from Eq. (A1.3) we find

$$d_{m+i} = \sqrt{\prod_{n=1}^{i} \frac{R_{m+n}}{S_{m+n-1}}}, \quad i = 1, \ldots, Z+1-m,$$
$$d_{m-i} = \sqrt{\prod_{n=1}^{i} \frac{S_{m-n}}{R_{m+1-n}}}, \quad i = 1, \ldots, m-1. \tag{A1.4}$$

Further, from Eqs. (A1.2)–(A1.4), we find all the elements of the real symmetric matrix,

$$W = \begin{bmatrix} -S_0 & \sqrt{S_0 R_1} & 0 & & & 0 \\ \sqrt{S_0 R_1} & -(R_1+S_1) & \sqrt{S_1 R_2} & 0 & & \\ 0 & \cdots & \cdots & \cdots & 0 & \\ & 0 & \sqrt{S_{k-1} R_k} & -(S_k+R_k) & \sqrt{S_k R_{k+1}} & 0 \\ & & 0 & \cdots & \cdots & \cdots \\ 0 & & & 0 & \sqrt{S_{Z-1} R_Z} & -R_Z \end{bmatrix}. \tag{A1.5}$$

According to the theorem on the spectral expansion of Hermitian matrices (see, e.g., [68]), the symmetric matrix W can be transformed into the diagonal matrix Λ using a real orthogonal matrix T (here, the transposed matrix is equal to the inverted matrix, $T^t = T^{-1}$):

$$W = T \cdot \Lambda \cdot T^t. \tag{A1.6}$$

In addition, there is a unitary matrix $U = D_K^{-1} T$, the rows of which constitute a set of eigenvectors $\mathbf{u} = (\mathbf{u}_0, \ldots, \mathbf{u}_Z)$ of the matrix K. They can be found by solving the set of $Z + 1$ linear equations [69]:

$$K \cdot \mathbf{u}_i = \lambda_i \cdot \mathbf{u}_i. \tag{A1.7}$$

It follows from Eq. (A1.7) that each eigenvector $\mathbf{u}_i$ allows arbitrary normalization. On the other hand, in solving Eq. (A1.7) sequentially, accuracy can be lost due to the equation in which $(\lambda_i + S_i + R_i) \cong 0$. Due to the arbitrary normalization, this equation can be excluded. Uniform set (A1.7) then splits into two nonuniform systems, which can be solved independently and sequentially using recurrent expressions. The set of eigenvectors of the matrix W, i.e., the columns of the matrix T (and, consequently, the rows of T^{-1}) can be found in the same way.

APPENDIX 2

EXTREME CASES OF IONIZATION/RECOMBINATION

In order to find $f_k(t)$ from Eqs. (3), which represents the extreme cases ($S_k \gg R_k$ and $S_k \ll R_k$) of dominant ionization/recombination, they can be sequentially integrated or expansion (13) can be used. However, these methods are algebraically complicated, especially, at large Z. The use of formulas (14) and (15) in similar cases can be complicated or even impossible due to the accumulation of numerical errors. Hence, we present a derivation of the required analytical expressions. In particular, for a set of coupled equation

$$\frac{df_k}{dt} = -S_k f_k + S_{k-1} f_{k-1}, \tag{A2.1}$$

where the coefficients S_k are independent of time, we use the method of separation of independent variables

$$f_k(t) = X_k Y(t). \tag{A2.2}$$

We then have

$$Y(t) = C\exp(\lambda t), \tag{A2.3}$$

where λ is the separation constant and C is also a constant. For a discrete variable k we have a uniform set of coupled first-order finite-difference equations

$$S_{k-1}X_{k-1} - S_kX_k = \lambda X_k, \tag{A2.4}$$

where $k = 1, \ldots, Z$. Its solution (see, e.g., [71]) takes form (accurate to a constant)

$$X_k = X_Z\prod_{i=k}^{Z-1}\frac{S_{i+1}-S_j}{S_i}. \tag{A2.5}$$

Here, $j = 0, 1, \ldots, Z-1$, $\lambda = -S_j$ are diagonal terms and, at the same time, eigenvalues of the initial lower triangular matrix. A general solution is a sum of all particular solutions corresponding to the eigenvalues of the kinetic matrix,

$$f_k(t) = \sum_{j=0}^{Z-1}C_j\exp(-S_jt)\prod_{i=k}^{Z-1}\frac{(S_{i+1}-S_j)}{S_i}. \tag{A2.6}$$

Constants C_j can be sequentially found from Eqs. (A2.6) (the corresponding matrix is also triangle) using given initial conditions.

Let us start from the simple case of impurity ionization from the neutral state. Using the corresponding initial conditions $f_0(0) = 1$ and $f_{k\neq 0}(0) = 0$, we obtain

$$C_0 = \left(\prod_{i=0}^{Z-1}\frac{S_{i+1}-S_0}{S_i}\right)^{-1}. \tag{A2.7}$$

The general formula for C_j ($j \geq 1$) then takes the form

$$\begin{aligned} C_j &= \prod_{i=0}^{j-1}\frac{S_i}{S_i-S_j}\left(\prod_{i=j}^{Z-1}\frac{S_{i+1}-S_j}{S_i}\right)^{-1} \\ &= \prod_{i=0}^{Z-1}S_i\frac{1}{\prod\limits_{i=0,\,i\neq j}^{Z-1}S_i-S_j}. \end{aligned} \tag{A2.8}$$

Substituting expressions (A2.7) and (A2.8) into Eqs. (A2.6), we obtain

$$\begin{aligned} f_0(t) &= \exp(-S_0t) \quad (k = j = 0), \\ f_k(t) &= \prod_{i=0}^{k-1}S_i\sum_{j=0}^{k}\frac{\exp(-S_jt)}{\prod\limits_{i=0,\,i\neq j}^{k}(S_i-S_j)} \\ &\quad (k = 1, 2, \ldots, Z-1, j \geq 1). \end{aligned} \tag{A2.9}$$

In the theory of random processes, a distribution of form (A2.9) (see, e.g., [72]) is called the general Erlang law (distribution) of the kth order. For $k = Z$, by integrating of the last equation of set (A2.1) and using formula (A2.9), we find

$$f_Z(t) = \prod_{i=0}^{Z-1}S_i\sum_{j=0}^{Z-1}\frac{1-\exp(-S_jt)}{S_j\prod\limits_{i=0,\,i\neq j}^{Z-1}(S_i-S_j)}. \tag{A2.10}$$

A similar formula for the case of extreme impurity recombination from the corresponding initial state $f_Z(0) = 1$ and $f_{k\neq 0}(0) = 0$ takes the form

$$\begin{aligned} f_Z(t) &= \exp(-R_Zt) \quad (k = j = Z), \\ f_k(t) &= \prod_{i=k+1}^{Z}R_i\sum_{j=k}^{Z}\frac{\exp(-R_jt)}{\prod\limits_{i=k,\,i\neq j}^{Z}(R_i-R_j)} \\ &\quad (k = 1, 2, \ldots, Z-1, j \leq Z-1). \end{aligned} \tag{A2.11}$$

Let us now consider the cases in which the initial distribution has an arbitrary form. Using the initial values of $f_k(0)$, we obtain new constants in general solution (A2.6) for the triangle matrix,

$$\hat{C}_j = C_j\left[f_0(0) + \sum_{i=1}^{j}f_i(0)\prod_{n=0}^{i-1}\frac{S_n-S_j}{S_n}\right]. \tag{A2.12}$$

Finally, we have

$$\begin{aligned} f_0(t) &= f_0(0)\exp(-S_0t) \quad (k = j = 0), \\ f_k(t) &= \prod_{i=0}^{k-1}S_i\sum_{j=0}^{k}\left[f_0(0) + \sum_{i=1}^{j}f_i(0)\prod_{n=0}^{i-1}\frac{S_n-S_j}{S_n}\right] \\ &\quad \times\frac{\exp(-S_jt)}{\prod\limits_{i=0,\,i\neq j}^{k}(S_i-S_j)} \\ &\quad (k = 1, 2, \ldots, Z-1, j \leq 1). \end{aligned} \tag{A2.13}$$

The formula for the case where recombination processes predominate has the form

$$\begin{aligned} f_Z(t) &= f_Z(0)\exp(-R_Zt) \quad (k = j = Z), \\ f_k(t) &= \prod_{i=k+1}^{Z}R_i\sum_{j=k}^{Z}\left[f_Z(0) + \sum_{i=j}^{Z-1}f_i(0)\prod_{n=i+1}^{Z}\frac{R_n-R_j}{R_n}\right] \\ &\quad \times\frac{\exp(-R_jt)}{\prod\limits_{i=k,\,i\neq j}^{Z}(R_i-R_j)} \\ &\quad (k = 1, 2, \ldots, Z-1, j \leq Z-1). \end{aligned} \tag{A2.14}$$

When charge exchange dominates over other recombination processes, we have $R_k = rk$ and the behavior of distribution function $f_k(t)$ is only determined by the

value of r and the initial distribution. It is interesting that, in this case, the values of m and D calculated by formulas (A2.14) completely coincide with those obtained from formulas (17) and (18).

REFERENCES

1. V. I. Gervids, A. G. Zhidkov, V. S. Marchenko, and S. I. Yakovlenko, in *Reviews of Plasma Physics*, Ed. by M. A. Leontovich and B. B. Kadomtsev (Énergoatomizdat, Moscow, 1982; Consultants Bureau, New York, 1986), Vol. 12.
2. V. I. Gervids, V. I. Kogan, and V. S. Lisitsa, in *Plasma Chemistry*, Ed. by B. M. Smirnov (Énergoatomizdat, Moscow, 1983), p. 3.
3. R. A. Hulse, Nucl. Technol. Fusion **3**, 259 (1983).
4. K. Behringer, *Description of the Impurity Transport Code STRAHL* (JET Joint Undertaking, Abingdon, 1987), Rep. JET-R(87)08.
5. M. Z. Tokar', Plasma Phys. Controlled Fusion **36**, 1819 (1994).
6. L. Lauro-Taroni, B. Alper, R. Giannella, *et al.*, in *Proceedings of the 21st EPS Conference on Plasma Physics and Controlled Fusion, Montpellier, 1994*, Vol. 1, p. 102.
7. C. Breton, A. Compant la Fontaine, C. D. Michelis, *et al.*, J. Phys. B **16**, 2627 (1983).
8. D. Pasini, M. Mattioli, A. W. Edwards, *et al.*, Nucl. Fusion **30**, 2049 (1990).
9. O. Demokan, F. Waelbroek, and N. Demokan, Nucl. Fusion **22**, 921 (1982).
10. A. N. Zinov'ev and V. V. Afrosimov, in *Plasma Diagnostics*, Ed. by M. I. Pergament (Énergoatomizdat, Moscow, 1990), p. 56.
11. V. A. Shurygin, Plasma Phys. Controlled Fusion **41**, 355 (1999).
12. M. Shimada, Fusion Eng. Des. **15**, 325 (1992).
13. K. Krieger, G. Fussmann, and the ASDEX Team, Nucl. Fusion **30**, 2392 (1990).
14. Equipe TFR, Nucl. Fusion **15**, 1053 (1975).
15. TFR Group, Plasma Phys. **22**, 851 (1980).
16. K. B. Fournier, D. Pacella, M. J. May, *et al.*, Nucl. Fusion **37**, 825 (1997).
17. K. Shimizu, H. Kubo, T. Takizuka, *et al.*, J. Nucl. Mater. **220–222**, 410 (1995).
18. V. A. Krupin, V. S. Marchenko, and S. I. Yakovlenko, Pis'ma Zh. Éksp. Teor. Fiz. **29**, 353 (1979) [JETP Lett. **29**, 318 (1979)].
19. R. A. Hulse, D. E. Post, and D. R. Mikkelsen, J. Phys. B **13**, 3895 (1980).
20. M. E. Puiatti, C. Breton, C. De Michelis, and M. Mattioli, Plasma Phys. **23**, 1075 (1981).
21. S. S. Sesnic, M. Bitter, K. W. Hill, *et al.*, Rev. Sci. Instrum. **57**, 2148 (1986).
22. V. S. Marchenko and S. I. Yakovlenko, Fiz. Plazmy **5**, 590 (1979) [Sov. J. Plasma Phys. **5**, 331 (1979)].
23. A. G. Zhidkov and V. S. Marchenko, Fiz. Plazmy **6**, 1352 (1980) [Sov. J. Plasma Phys. **6**, 740 (1980)].
24. V. G. Gontis and V. S. Lisitsa, Fiz. Plazmy **11**, 483 (1985) [Sov. J. Plasma Phys. **11**, 282 (1985)].
25. V. I. Gervids and D. Kh. Morozov, Fiz. Plazmy **25**, 242 (1999) [Plasma Phys. Rep. **25**, 217 (1999)].
26. V. A. Bazylev and M. I. Chibisov, Fiz. Plazmy **5**, 584 (1979) [Sov. J. Plasma Phys. **5**, 327 (1979)].
27. V. P. Shevelko and H. Tawara, Nucl. Fusion Suppl. **6**, 101 (1995).
28. V. A. Abramov, V. G. Gontis, and V. S. Lisitsa, Fiz. Plazmy **10**, 400 (1984) [Sov. J. Plasma Phys. **10**, 235 (1984)].
29. V. A. Abramov, V. S. Lisitsa, and A. Yu. Pigarov, Pis'ma Zh. Éksp. Teor. Fiz. **42**, 288 (1985) [JETP Lett. **42**, 356 (1985)].
30. F. B. Rosmej, D. Reiter, V. S. Lisitsa, *et al.*, Plasma Phys. Controlled Fusion **41**, 191 (1999).
31. V. A. Shurygin, Fiz. Plazmy **22**, 1075 (1996) [Plasma Phys. Rep. **22**, 975 (1996)].
32. V. A. Shurygin, N. N. Brevnov, and Yu. V. Gott, in *Proceedings of the 30th EPS Conference on Plasma Physics and Controlled Fusion, St. Petersburg, 2003*, Paper P-3.157.
33. A. V. Bortnikov, N. N. Brevnov, Yu. V. Gott, *et al.*, Fiz. Plazmy **21**, 672 (1995) [Plasma Phys. Rep. **21**, 634 (1995)].
34. D. S. Gray, E. M. Hollmann, D. G. Whyte, *et al.*, in *Proceedings of the 30th EPS Conference on Plasma Physics and Controlled Fusion, St. Petersburg, 2003*, Paper P-4.91.
35. A. B. Berlizov, V. I. Bugarya, V. V. Buzankin, *et al.*, in *Proceedings of the 8th International Conference on Plasma Physics and Controlled Fusion, Brussels, 1980*, Nucl. Fusion Suppl. **1**, 23 (1981).
36. V. A. Rantsev-Kartinov and V. A. Shurygin, Fiz. Plazmy **23**, 3 (1997) [Plasma Phys. Rep. **23**, 1 (1997)].
37. TFR Group, Nucl. Fusion **22**, 1173 (1982).
38. V. V. Ivanov, A. B. Kukushkin, and V. S. Lisitsa, Fiz. Plazmy **13**, 1341 (1987) [Sov. J. Plasma Phys. **13**, 774 (1987)].
39. A. B. Arutyunov, S. I. Krasheninnikov, and D. Yu. Prokhorov, Fiz. Plazmy **17**, 1150 (1991) [Sov. J. Plasma Phys. **17**, 668 (1991)].
40. V. A. Shurygin, in *Proceedings of the 26th EPS Conference on Plasma Physics and Controlled Fusion, Maastricht, 1999*, ECA **23J**, 805 (1999).
41. V. I. Gervids and D. Kh. Morozov, Fiz. Plazmy **26**, 470 (2000) [Plasma Phys. Rep. **26**, 439 (2000)].
42. V. I. Gervids, V. I. Kogan, and D. Kh. Morozov, Fiz. Plazmy **27**, 994 (2001) [Plasma Phys. Rep. **27**, 938 (2001)].
43. I. Galushkin, V. I. Gervids, and V. I. Kogan, Plasma Phys. Controlled Nucl. Fusion Res. **2**, 193 (1971).
44. Yu. N. Dnestrovskij, I. N. Inovenkov, D. P. Kostomarov, and V. F. Strizhov, Preprint No. 2665 (Kurchatov Institute of Atomic Energy, Moscow, 1976).
45. R. V. Jensen and D. E. Post, Nucl. Fusion **17**, 1187 (1977).
46. G. Fussmann, Contrib. Plasma Phys. **37**, 363 (1997).
47. E. S. Venttsel' and L. A. Ovcharov, *Theory of Random Processes and Its Engineering Applications* (Vysshaya Shkola, Moscow, 2000).

48. V. P. Chistyakov, *Course of Probability Theory* (Nauka, Moscow, 1982), p. 229.
49. L. A. Bureeva and V. S. Lisitsa, *A Perturbed Atom* (IzdAT, Moscow, 1997), p. 415.
50. F. R. Gantmakher, *Theory of Matrices* (Nauka, Moscow, 1967).
51. G. A. Korn and T. M. Korn, *Mathematical Handbook for Scientists and Engineers* (McGraw-Hill, New York, 1968; Nauka, Moscow, 1984).
52. D. E. Post and R. V. Jensen, At. Data Nucl. Data Tables **20**, 397 (1977).
53. W. Lotz, Z. Phys. **216**, 241 (1968).
54. R. A. Phaneuf, R. K. Janev, and H. T. Hunter, Nucl. Fusion, Special Suppl., 7 (1987).
55. J. E. Rice, E. S. Marmar, E. Kallne, *et al.*, Phys. Rev. A **35**, 3033 (1987).
56. P. Defrance, Nucl. Fusion Suppl. **6**, 43 (1995).
57. V. M. Povyshev, A. A. Sadavoy, V. P. Shevelko, *et al.*, *Electron-Impact Ionization Cross Sections of H, He, N, O, Ar, Xe, Au, and Pb Atoms and Their Ions in the Electron Energy Range from the Threshold up to 200 keV* (Ob'edin. Inst. Yad. Issled., Dubna, 2001).
58. F. B. Rosmej and V. S. Lisitsa, Phys. Lett. A **244**, 401 (1998).
59. G. Bertschinger, W. Biel, M. Bitter, *et al.*, in *Proceedings of the 26th EPS Conference on Plasma Physics and Controlled Fusion, Maastricht, 1999*, ECA **23J**, 661 (1999).
60. F. B. Rosmej, D. Reiter, V. S. Lisitsa, *et al.*, Plasma Phys. Controlled Fusion **41**, 191 (1999).
61. J. E. Rice, E. S. Marmar, E. Kallne, *et al.*, Phys. Rev. A **35**, 3033 (1987).
62. W. Stodiek, R. Goldston, N. Sauthoff, *et al.*, in *Proceedings of the 8th International Conference on Plasma Physics and Controlled Fusion, Brussels, 1980*, Nucl. Fusion Suppl. **1**, 9 (1981).
63. M. R. Wade, J. T. Hogan, S. L. Allen, *et al.*, Nucl. Fusion **38**, 1839 (1998).
64. M. E. Puiatti, M. Mattioli, G. Telesca, *et al.*, Plasma Phys. Controlled Fusion **44**, 1863 (2002).
65. L. Carraro, M. Mattioli, F. Sattin, *et al.*, DRFC/CAD EUR-CEA-FC-1581 (Association Euratom–CEA, Department de Recherches sur la Fusion Controlee, CEA/Cadarache, 1996).
66. M. Mattioli, K. B. Fournier, L. Carraro, *et al.*, DRFC/CAD EUR-CEA-FC-1663 (Association Euratom–CEA, Department de Recherches sur la Fusion Controlee, CEA/Cadarache, 1998).
67. S. A. Cohen, J. L. Cecchi, and E. S. Marmar, Phys. Rev. Lett. **35**, 1507 (1975).
68. R. A. Horn and C. R. Johnson, *Matrix Analysis* (Cambridge University Press, Cambridge, 1985; Mir, Moscow, 1989).
69. V. P. Il'in and Yu. I. Kuznetsov, *Tridiagonal Matrices and Their Applications* (Nauka, Moscow, 1985).
70. B. P. Demidovich and I. A. Maron, *Computational Mathematics* (Fizmatgiz, Moscow, 1963).
71. A. O. Gel'fond, *Calculation of Finite Differences* (Nauka, Moscow, 1967), p. 292.
72. E. S. Venttsel' and L. A. Ovcharov, *Probability Theory and Its Engineering Applications* (Vysshaya Shkola, Moscow, 2000).

Translated by the author

Plasma Physics Reports, Vol. 30, No. 6, 2004, pp. 473–495. From Fizika Plazmy, Vol. 30, No. 6, 2004, pp. 514–540.

PARTICLE ACCELERATION IN PLASMA

High-Energy Ion Generation by Short Laser Pulses[1]

A. Maksimchuk[1], K. Flippo[1], H. Krause[2], G. Mourou[1], K. Nemoto[3], D. Shultz[2], D. Umstadter[1], R. Vane[2], V. Yu. Bychenkov[4], G. I. Dudnikova[5], V. F. Kovalev[6], K. Mima[7], V. N. Novikov[4], Y. Sentoku[8], and S. V. Tolokonnikov[9]

[1] *Center for Ultrafast Optical Science, University of Michigan, Ann Arbor, MI 48109–2099, USA*
[2] *Oak Ridge National Laboratory, Oak Ridge, TN 37831–6372, USA*
[3] *Central Research Institute of Electric Power Industry, Tokyo 201–8511, Japan*
[4] *Lebedev Physics Institute, Russian Academy of Sciences, Leninskii pr. 53, Moscow, 119991 Russia*
[5] *Institute of Computational Technologies, Siberian Branch of Russian Academy of Sciences, Novosibirsk, 630090 Russia*
[6] *Institute for Mathematical Modeling, Russian Academy of Sciences, Miusskaya pl. 4a, Moscow, 125047 Russia*
[7] *Institute for Laser Engineering, Osaka University, 2–6 Yamada-oka, Suita, Osaka 565-0871, Japan*
[8] *General Atomics, P.O. Box 85608, San Diego, California 92186, USA*
[9] *Russian Research Centre Kurchatov Institute, pl. Kurchatova 1, Moscow, 123182 Russia*

Received June 7, 2003; in final form, September 4, 2003

Abstract—This paper reviews the many recent advances at the Center for Ultrafast Optical Science (CUOS) at the University of Michigan in multi-MeV ion beam generation from the interaction of short laser pulses focused onto thin foil targets at intensities ranging from 10^{17} to 10^{19} W/cm^2. Ion beam characteristics were studied by changing the laser intensity, laser wavelength, target material, and by depositing a well-absorbed coating. We manipulated the proton beam divergence using shaped targets and observed nuclear transformation induced by high-energy protons and deuterons. Qualitative theoretical approaches and fully relativistic two-dimensional particle-in-cell simulations modeled energetic ion generation. Comparison with experiments sheds light on ion energy spectra for multi-species plasma, the dependences of ion-energy on preplasma scale length and solid density plasma thickness, and laser-triggered isotope yield. Theoretical predictions are also made with the aim of studying ion generation for high-power lasers with the energies expected in the near future, and for the relativistic intensity table-top laser, a prototype of which is already in operation at CUOS in the limits of several-cycle pulse duration and a single-wavelength spot size. © *2004 MAIK "Nauka/Interperiodica".*

1. INTRODUCTION

Developments in laser technology have enabled high power lasers to produce multi-terrawatt femtosecond pulses that allow the examination of the fundamental physics of ion acceleration at multi-MeV energies. At focal intensities of $I > 10^{18}$ W/cm^2, high-intensity laser-triggered ion acceleration results in the formation of a multi-MeV beam propagating in the forward direction [1–4]. Experiments have already proven the possibility of transforming laser energy into collimated ultra-fast ion bunches with high efficiency (of up to several percent) when focusing ultra-short laser pulses of intensity 10^{19}–10^{20} W/cm^2 onto solid targets [3, 4]. The mechanisms and characteristics of ions triggered by the interaction of a short laser pulse with plasma are of current interest because of their possible applications to novel neutron source development and isotope production. The proof-of-principle experiments with high energy lasers which should appear the near future intend to use ultra-intense laser pulses for ion beam generation with energies useful in proton therapy, fast ignition inertial confinement fusion, radiography, neutron sources, and the study of nuclear physics phenomena with extremely short time scales. The energy content, spectra, and angular patterns of laser-triggered ions are now being studied experimentally, theoretically, and in multi-dimensional simulations.

It has long been understood [5] that fast ion generation in a laser-produced plasma is connected with hot electrons. The commonly recognized effect responsible for ion acceleration is charge separation in a plasma due to high-energy electrons driven by a laser inside the target [1–4, 6, 7], and/or an inductive electric field resulting in a self-generated magnetic field [8]. In addition, direct laser-ion interaction has been discussed for extremely high laser intensities of ~10^{22} W/cm^2 [9]. High-energy electron production up to multi-MeV energies can be accomplished using several processes, such as stimulated forward Raman scattering, resonant absorption, stochastic heating, laser wakefields, ponderomotive acceleration by standing and propagating laser pulses, "vacuum heating" due to the $\mathbf{v} \times \mathbf{B}$ component of the Lorentz force or the Brunel effect; the wave-breaking of self-modulated laser wakefields, and betatron resonance provided by laser-pulse channeling. Because of the numerous mechanisms of electron gen-

[1] This article was submitted by the authors in English.

eration, many different regimes of ion acceleration are possible that hamper their corresponding investigation. At present, our main interest is investigating the mechanisms of ion acceleration in the interaction of a laser pulse with a solid target, and their dependence on the laser-pulse and plasma parameters. Clearly, a better understanding of these mechanisms and the quantification of the dependences of the ion yield in terms of the laser pulse and plasma parameters is essential for success in the new applications for laser-triggered ion beams.

Recent publications show that there is some controversy about the origin of the high-energy ions. The results obtained from some experiments [6, 10–12] provide evidence that the observed MeV-ions were generated and accelerated in plasma at the *front of the target*, conflicting with experiments [3, 4, 13–15], which indicated that proton acceleration took place at the *back of the target*. The electrostatic model of ion acceleration suggests that the origin of the ions was the same for both of these experiments and that the only difference was in the plasma thickness, i.e., whether or not the plasma extended to the rear surface. We believe both situations are possible, depending on laser pulse characteristics and foil material conductivity. Not only is there controversy about the origin of the high-energy ions but also dramatic disagreement on hot electron penetration in solid targets [16, 17]. The latter experiments were performed using green light of approximately the same pulse-duration with laser intensities of up to 4×10^{18} and 10^{19} W/cm^2, respectively. However, the penetration depth of hot electrons in [17] was more than two orders of magnitude greater than in [16]. Two possible disparate scenarios may explain these controversies in high-energy electron and ion generation:

Scenario 1. When a solid target is highly resistive, the return current within it is strongly suppressed. In this case, hot electrons generated in the laser-plasma interaction in front of the foil penetrate only to the distance of their Debye length, λ_{Dh}. These electrons are pulled back within the target (if the foil thickness exceeds the Debye length of the hot electrons) by the electrostatic fields they set up, and return in the shape of a fountain. The Debye sheath accelerates the ions, which appear to originate from the *front of the target*.

Scenario 2. Hot electrons penetrate deep inside the foil and reach the rear of the target. Such electrons can only propagate due to the return current [18–20], which requires a high conductivity within the target. This can occur in the case of a metal target or of effective target ionization by the electrons or the electrostatic field (dielectric breakdown). Such a scenario corresponds to ion acceleration at the *back of the target*.

Clearly, there could be an intermediate situation between these two disparate scenarios in which the plasma has a non-monotonic density distribution within the target's thickness, even though the cold insulator might become a sort of conductor due to the laser prepulse, its ionization by fast electrons, the return current of slow electrons, and/or an electrical breakdown. The physical picture of this transformation arising in the bulk of the target is still incomplete. Note that paper [21] sheds some light on the latter question, demonstrating a fourfold difference in the penetration depth of fast electrons in metals and insulators.

This paper is aimed at reviewing the recent advances in multi-MeV ion beam generation from the interaction of short laser pulses, focused onto thin foil targets at intensities ranging from 10^{17} to 10^{19} W/cm^2, at the University of Michigan's Center for Ultrafast Optical Science (CUOS). We present our experimental results on high-energy proton generation with a 10 TW Nd:glass/Ti:sapphire laser at the fundamental and second harmonic frequencies, as well as our results on nuclear activation with protons and deuterons. The main emphasis of the presented study is the measurement of light ions, protons, and deuterons, although some results from the generation of heavy ions are also discussed. We report on the manipulation of a proton beam using shaped targets and different target material. We also present the results of our theoretical models and fully relativistic two-dimensional (2D) particle-in-cell (PIC) simulation of multi-MeV ion generation in the interaction of a short laser pulse with a dense plasma.

2. ION GENERATION IN THE HIGH CONTRAST CASE

In this set of experiments [2], the intensity contrast at the wavelength of 1.053 μm was ~10^4 : 1, as measured by the third-order correlation technique. Energy in the nanosecond prepulse due to amplified spontaneous emission at the fundamental frequency was as high as 1 J. The contrast was improved to an estimated 10^7 : 1 by frequency doubling of the laser light in a 4-mm KDP crystal. The energy in green light $2\omega_0$ was limited to 1 J because of the nonlinear distortion of the laser wavefront in the doubling crystal. The laser beam was focused on the surface of thin films of aluminum with a thickness of 1.8 μm at an incidence angle of 0° or 45° using an $f/3$ ($f = 16.5$ cm) off-axis parabolic mirror. The maximum focused intensity was 3×10^{18} W/cm^2.

The high-energy ion emission was recorded by CR–39 plastic nuclear track detector. To determine the maximum energy and spectrum of the ions, the detectors were covered with steps of Mylar filters having thicknesses from 2 to 50 μm. It was found that protons are the predominant component of a high-energy ion emission. These protons originate from a thin layer on a target surface contaminated with hydrocarbons and/or water vapor. Such target contamination was observed in the late 1960s in laser-matter interaction experiments with nanosecond laser pulses, as discussed in [5]. In our experiments, we observed a high-energy proton beam emerging through the rear surface as a beam with an

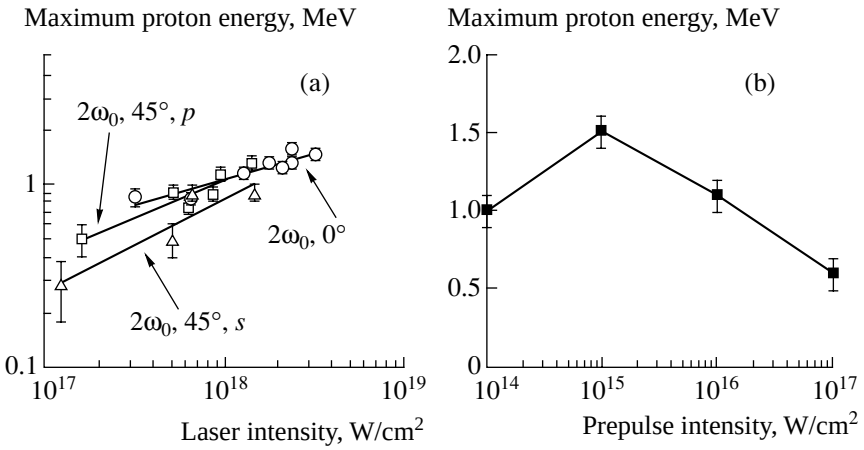

Fig. 1. Maximum proton energy in the forward direction as a function of (a) laser intensity at $2\omega_0$ for different conditions of illumination of 1.8-μm Al foil: (circles) 0°; (squares) 45°, *p*-polarization; and (triangles) 45°, *s*-polarization (the solid lines are the best power function fits to the experimental data) and (b) $2\omega_0$ prepulse intensity at 10^{18} W/cm^2 main pulse intensity (the solid line is plotted through the experimental points for better viewing).

angular divergence of about 40° ± 10°. The direction of the high energy proton beam did not depend on the angle of incidence of laser radiation and was always normal to the target surface. From this, one may conclude that the electric field of charge separation accelerating protons inside the target is directed along the target surface normal.

We studied the dependence of maximum proton energy versus laser intensity for different conditions of thin foil illumination. The highest proton energy of 1.5 MeV was observed for normal incidence at the maximum laser intensity of 3×10^{18} W/cm^2 (Fig. 1a). At a 45° angle of incidence, the maximum intensity of the beam on the target was reduced by a factor of 2 due to the increased spot size in the horizontal direction. The maximum observed proton energy, $\epsilon_i^{\max}$, was comparable for both cases at the same intensity and can be fitted as the function $\epsilon_i^{\max} \propto I^{\alpha}$, where α is between 0.3 and 0.4. Illumination with *s*-polarization at 45° produced protons with energies 200–300 keV less than those for *p*-polarization. We also observed high energy protons moving in the backward direction (in the direction of plasma expansion) for 45° laser illumination, but their energy was half that of those moving in the forward direction.

We changed the plasma gradient scale length by introducing a prepulse at $2\omega_0$, with a time delay of 50 ps in front of the main $2\omega_0$ pulse. The prepulse was varied with intensities ranging from 0.01% to 10% of the main pulse intensity of 10^{18} W/cm^2. It was found that there was an optimum prepulse intensity of about 10^{15} W/cm^2 (Fig. 1b) for maximum proton energy production. We estimate that at this intensity, the scale length of preformed plasma is several laser wavelengths. From this, we conclude that a preformed plasma that is not too extended enhances high-energy ion production.

The proton energy spectrum was measured by the foil attenuation method. Using steps of Mylar filters with thicknesses that differed by 2 μm provided a proton energy resolution of about 100 keV. The proton spectrum in Fig. 2 shows an exponential decay from energies of 400 keV to 1 MeV with a characteristic temperature of 230 keV (solid line), indicating Maxwellian-like distribution of the bulk protons. An interesting feature of the spectrum at higher energies is a plateau that ends in a sharp energy cutoff at 1.5 MeV;

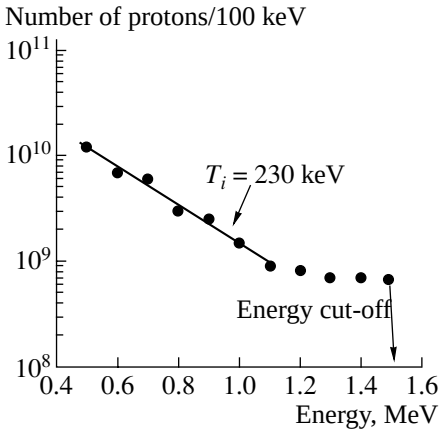

Fig. 2. Energy distribution of fast protons in the forward direction (circles), measured by attenuation of the beam in Mylar filters of different thicknesses for $2\omega_0$ illumination of 1.8-μm Al film with intensity of 2×10^{18} W/cm^2 at normal incidence. The arrow shows the sharp cutoff in proton energy at a spectral distribution below the detection threshold.

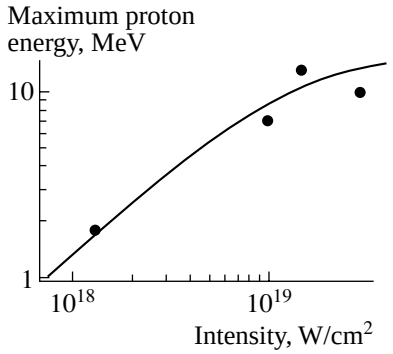

Fig. 3. Maximum proton energy dependence (dots), measured by attenuation of the beam in Mylar filters of different thicknesses for the illumination of a 10-μm Al film with laser pulse of 1.053 μm wavelength at a 45° angle of incidence.

this is typical of an electrostatic mechanism of ion acceleration.

3. ION GENERATION IN THE LOW CONTRAST CASE

These experiments were performed at the fundamental wavelength of 1.053 μm with an intensity contrast of $5 \times 10^5 : 1$. The *p*-polarized laser beam was focused on the surface of Mylar or aluminum foils of different thickness at a 45° angle of incidence. Maximum laser intensity on the target was $\approx 2 \times 10^{19}$ W/cm^2. Aluminum targets typically produced proton beams with energies almost twice as high as Mylar targets. The highest energies for aluminum and Mylar targets were 13 and 7 MeV, respectively. The maximum proton energy for aluminum foil was about three times higher than in the high contrast case (Section 2) for the same laser intensities. This confirms that preplasma enhances high-energy ion production: at an intensity contrast of $5 \times 10^5 : 1$, preplasma very likely appears before the maximum laser energy reaches the target.

We studied for the first time the dependence of maximum proton energy as a function of laser intensity for an aluminum target and found that this dependence was quite strong at $1.5 \times 10^{18} < I < 10^{19}$ W/cm^2, quite close to $\propto I$, with a tendency to saturate at higher intensities. This behavior of the maximum proton energy is illustrated in Fig. 3. The maximum proton energy for a Mylar target at $I > 4 \times 10^{18}$ W/cm^2 was also close to a $\sqrt{I}$-dependence. Qualitatively, the shape of the proton energy spectrum is similar to that observed with the high contrast laser, i.e. it is characterized by a plateau at the high end of the energy spectrum which typically has a sharp cutoff. Figure 4 presents the high-energy portion of a proton spectrum from an aluminum target. From this spectrum we can estimate that the number of protons with energy higher than 10 MeV is about 10^8. The inset of Fig. 4 shows an image of the proton beam with energy above 4 MeV. The bright elliptical region within the beam corresponds to protons that passed through 1 mm of CR–39 and thus left tracks on the rear surface of the detector. This imprint corresponds to protons with energies above 12 MeV.

Some measurements demonstrated that proton spectra from Al target may have a band structure, as shown in Fig. 5. Note that the efficiency of high-energy proton production is very sensitive to the contrast of the laser pulse. Proper laser plasma matching at the front of a target helps to achieve extreme parameters, while the production of a long preplasma significantly decreases the maximum proton energy. Figure 5, for instance, corre-

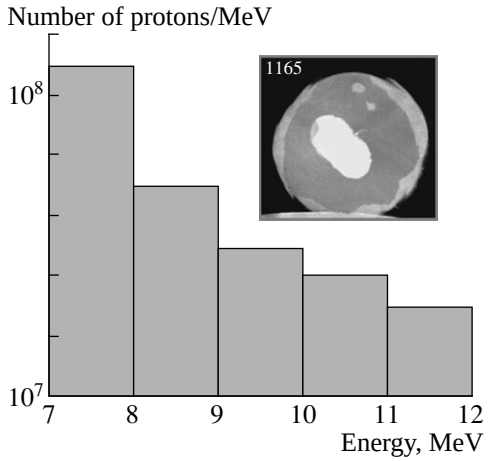

Fig. 4. Spectrum of proton beam from a 12.5-μm aluminum target at a laser intensity of ~10^{19} W/cm^2, received by track counting in the CR-39 detector. The inset shows a forward accelerated proton beam with energy above 4 MeV.

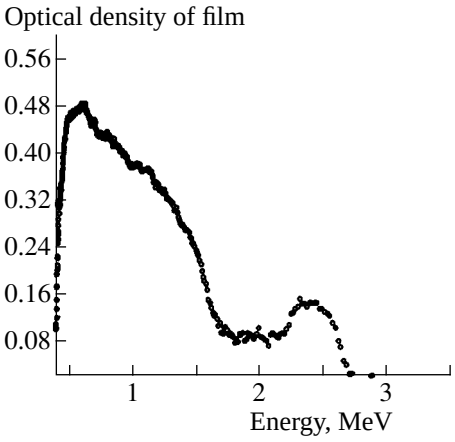

Fig. 5. Proton spectrum showing the band structure from the interaction of an 12.5-μm Al film with a laser pulse of 1.053-μm wavelength and intensity 5×10^{18} W/cm^2 at a 45° angle of incidence. The spectrum was photographed using a dipole magnetic spectrometer and X-ray film.

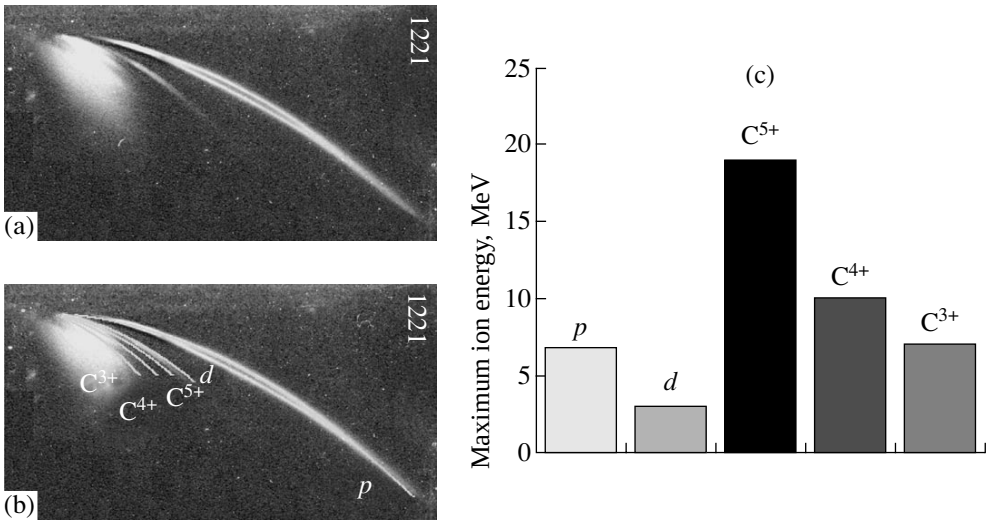

Fig. 6. (a) Ion traces obtained with a Thomson parabola spectrometer from a front deuterated Mylar target irradiated with a laser intensity of ~10^{19} W/cm^2. (b) The same as in plot (a) with ion identification (parabolas are added to better follow the traces). (c) Distribution of maximum ion energy for different ion species.

sponds to less than optimal laser contrast conditions (~10^4 : 1), so that the maximum proton energy is less than 3 MeV for a laser intensity of ~5×10^{18} W/cm^2.

Using a Thomson parabola spectrometer with parallel electric and magnetic fields (B = 0.26 T, E = 7.7 kV/cm) in an experiment with a front deuterated Mylar target, we registered proton and heavier ion emission in the forward direction in a single laser shot. Figure 6a presents an image of a CR–39 plate that was used for ion detection. We identified traces of protons, deuterons, and carbon ions: C^{5+}, C^{4+}, and C^{3+} (Fig. 6b). The maximum ion energies were measured from these traces. Figure 6c shows the maximum energies for different ion species. We found that the maximum energies for different ion species were as follow: ≈7 MeV for protons, ≈2.7 MeV for deuterons, ≈19 MeV for C^{5+}, ≈10 MeV for C^{4+}, and ≈7 MeV for C^{3+}. This corresponds to energies per nucleon of ≈7 MeV for protons, ≈1.35 MeV for deuterons, ≈1.6 MeV for C^{5+}, ≈0.8 MeV for C^{4+}, and ≈0.6 MeV for C^{3+}. This experiment provides evidence of the possibility of accelerating light ions more efficiently than heavier ions. We prove below that the protons in our experiment were accelerated predominantly from the front of the target, as in [1], while it was asserted in [3, 4] that proton acceleration came from the back of the target.

Heavier ions are more likely to be accelerated at the back of the target [22] because of high losses within the foil. We found that the C^{5+} trace was very weak, compared to the C^{4+} and C^{3+} traces. This means that a very small number of C^{5+} ions were created at the back of the target. The ionization at the back of the target was caused by the electrostatic field created by high-energy electrons penetratingthrough it. This field not only ionizes atoms but accelerates ions to high energies. In a similar experiment on a 6-μm Mylar target without a deuterated layer, no trace of C^{6+} ions was observed. From the fact that C^{4+} ions are produced in abundance and C^{5+} generation is very weak, one may find the strength of the electrostatic field at the back of the target using the Ammosov–Delone–Krainov model [23]

$$E \geq (2/3)(U_4/U_{\rm H})^{3/2} E_a, \qquad (1)$$

where $E_a = 0.51 \times 10^{10}$ V/cm is the atomic electric field, and U_N (N = 1, 2, …) and $U_{\rm H}$ are the ionization potentials of the ionized species and hydrogen, respectively. From Eq. (1) we find $E \approx (3–4) \times 10^{10}$ V/cm.

4. NUCLEAR ACTIVATION WITH DEUTERONS AND PROTONS

In our experiments at the fundamental frequency [10] with a maximum intensity of ≈6×10^{18} W/cm^2 and an intensity contrast of 5×10^5 : 1, we carried out the activation of a sample of boron isotope ^{10}B. The high-intensity laser beam was focused on a Mylar target covered by a deuterated polystyrene layer. The resultant ion beam (protons and deuterons) was used to irradiate an enriched sample of ^{10}B (enrichment 90%). A cylindrically-shaped sample 10 mm in diameter and 5 mm in thickness was positioned on the CR–39 detector with a few steps of Mylar filters to monitor the energy of the ion beam and its alignment. The deuterated polystyrene layer, ≥1 μm thick, was deposited on the front side of the 6-μm Mylar film. The experimental setup is shown in Fig. 7a.

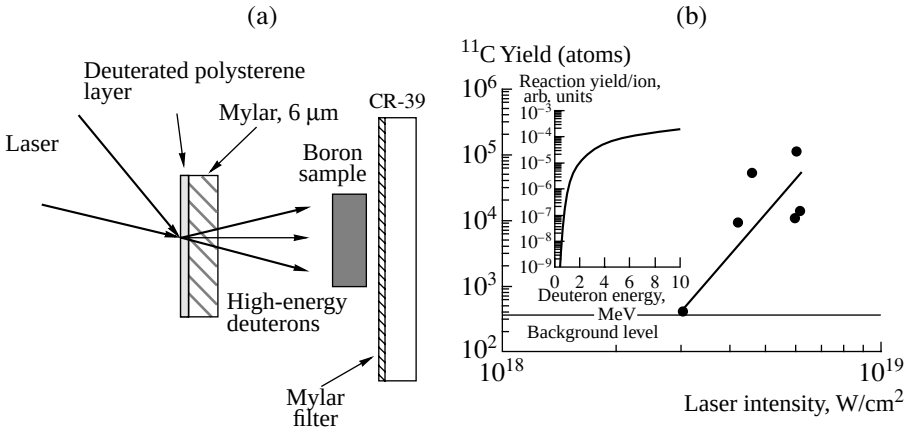

Fig. 7. Schematic diagram of boron sample activation with high-energy deuterons (a). Experimental yield of ^{11}C versus the laser intensity for the ^{10}B(d, n)^{11}C reaction (b). The inset shows calculated yield of ^{11}C per one deuteron as a function of the energy cutoff for a uniform energy distribution of deuterons.

The concentration of boron isotope ^{10}B in natural boron is about 20%. Therefore, in the enriched boron sample used, the yield of isotope ^{11}C in the reaction ^{10}B(d, n)^{11}C must be enhanced approximately by a factor of 4.5, as compared with the (p, n) reaction. The yield of the β^+-active ^{11}C was measured by counting the number of positrons emitted. The coincidence measurements require a low background count rate in order to obtain a decent signal to noise ratio. Two 3-inch NaI detectors placed opposite one another were used to detect the coincidence signal resulting from the annihilation of electrons and positrons and the production of two gamma photons with an energy of 0.511 MeV. The detection efficiency was measured as being in the range of 0.05–0.10 using a ^{22}Na radioactive source with a precisely known activity of positron emission. The background noise was found to be 1–5 count/min, while the radioactivity detection threshold was ~10 pCi.

We identified the source of this coincidence signal as the positron decay of the carbon isotope ^{11}C, which has a half-life of 20.4 min. We measured a maximum of ≈300 counts/min at 330 s after the laser shot. The maximum total yield of ^{11}C is estimated to be ~10^5; this corresponds to ≈2 nCi of radioactivity immediately after the shot. The laser was able to deliver shots with a time interval of approximately 7 min. Therefore, the accumulated effect of several shots will increase radioactivity only by a factor of 3. If a similar laser could operate with a 10-Hz repetition rate, a positron source with an activity of ≈20 μCi could be built up if the irradiation time were equal to the half-life of ^{11}C.

We observed a very sharp power dependence of the ^{11}C yield as a function of laser intensity (Fig. 7b), indicating that deuteron energies are near the threshold for the ^{10}B(d, n)^{11}C reaction, ≃2 MeV. In the same set of experiments, we measured the maximum proton energy at about 5 MeV at the highest laser intensity. The much lower deuteron energies confirm the electrostatic mechanism of ion acceleration. Deuterons are accelerated less because they are two times heavier than protons and have less mobility and higher energy losses. Since they follow behind the proton bunch, they experience a significantly smaller accelerating electric field. Consequently, they would be expected to have a lower energy than protons.

To verify that deuteron acceleration is more efficient from the front side of the target, we irradiated a 6-μm-thick Mylar target with a layer of a deuterated plastic on its back side, and performed the same ^{10}B activation experiment described above. In this case, the activation signal was not above the background level. These results indicate unequivocally that, for a dielectric target at the laser intensity and intensity contrast ratio used, deuterons are either accelerated mainly from the front side of the foil, or they acquire higher energy there, compared with that from the rear side. We relate both cases to front side ion generation.

High-energy protons may participate in the ^{11}B(p, n)^{11}C reaction, with the cross section of this reaction [24] having a higher threshold (above 3 MeV). Taking into account that the amount of ^{11}B in boron sample was only 10%, we may expect the ^{11}C yield for this reaction to be much less than that for deuterons. To verify that the (p, n) reaction does not contribute substantially to the ^{11}C yield, we focused the laser at its highest intensity on a bare Mylar film, behind which was a boron sample. In this case, no activation signal was observed.

Our experiments with aluminum targets showed that the maximum proton energy (Fig. 3) can exceed severalfold the threshold for some (p, n) reactions. Guided by this, we performed an experiment on the nuclear activation of ^{11}B and ^{63}Cu samples. The thresholds for these reactions were 3 and 4 MeV, while the maxima of the reaction cross-sections were relatively

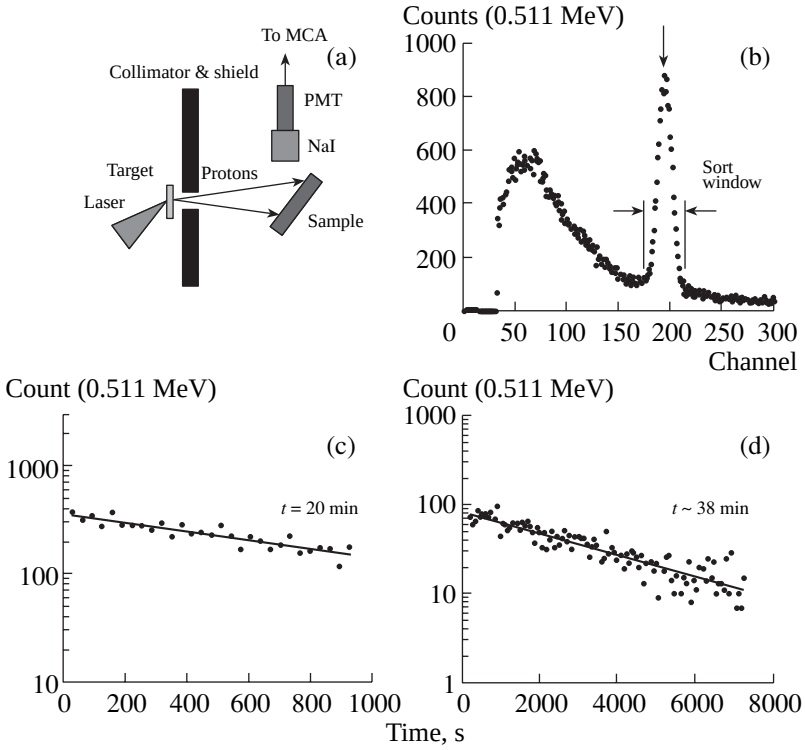

Fig. 8. Setup for activation with protons. Collimator and shield were introduced to prevent saturation of the detection system due to high-energy electrons and gamma photons during the laser shot (a). Spectrum of proton irradiated ^{11}B sample (b). Radioactive decay signals (c and d) of proton irradiated ^{11}B and ^{63}Cu samples (dots). Solid lines correspond to the decay of ^{11}C and ^{63}Zn with half-life of 20 and 38 min, respectively.

high: ≃400 and 500 mb, respectively. The products of these reactions were ^{11}C and ^{63}Zn, which are positron emitters with half-lives of 20 and 38 min, respectively. A schematic of the experimental setup is shown in Fig. 8a. Measurements of the induced radioactivity were performed in situ in the interaction chamber. A laser-triggered, high-energy proton beam irradiated a sample placed a few centimeters behind the target. The emission spectrum of the sample was monitored by a NaI detector coupled to a photomultiplier tube (PMT), with readout performed by a multi-channel analyzer (MCA). Figure 8b shows the most significant part of the ^{11}C spectrum, plotted on a vertical linear scale. A peak is clearly seen between spectral channels 180 to 220; this corresponds to the annihilation of positrons and electrons and the production of gamma photons with an energy of 0.511 MeV. The points at the lowest channel numbers are zero because the NaI signal was below the discriminator value set on the analog-to-digital converter. The broad peak well below 0.511 MeV is due to Compton scattered electrons. The gated region in Fig. 8b defines the counts that were included in the resorted signal as a function of time, thus yielding the half-life for ^{11}C. Figures 8c and 8d present experimental radioactive decay signals for proton irradiated ^{11}B and ^{63}Cu samples; the signals show the production of ~10^5 atoms of ^{11}C and ^{63}Zn.

5. PROTON BEAM CHARACTERISTICS AND MANIPULATION

The manipulation of the ion beam characteristics is an important part of the problem under discussion. From the theoretical point of view, some ideas for the manipulation of ion beams have already been proposed, e.g., in [8, 25–28]. However, these methods require great precision in the manufacturing and control of targets (features on the order of a micron, positioned with submicron accuracy at the laser focus), which is far from trivial. We carried out experiments on beam profile manipulation by modest modification of the target geometry, thereby extending the concept first proposed in [8] of tailoring a target foil and demonstrating the promise of this method.

At multi-MeV energies, the protons originating in laser-irradiated thin foils are formed into a well-collimated beam. Even at an energy of ~1 MeV, they can be confined in a quite narrow cone. Figure 9 shows a typical image of the proton beam in the forward direction (behind the target) observed in our experiment with $2\omega_0$ irradiation of a thin aluminum foil. A collimated beam of fast protons is observed, with energies as high as 1.5 MeV and total number of $\geq 10^9$, confined in a cone angle of $40° \pm 10°$.

Fig. 9. Typical image of a proton beam observed traveling in the forward direction from the interaction of a high-intensity laser with a 1.8-μm-thick aluminum foil. The proton beam passed through a 25-μm Mylar filter, corresponding to an energy above 1.2 MeV. The laser intensity on the target is 2×10^{18} W/cm^2 at $2\omega_0$ illumination normal to the target.

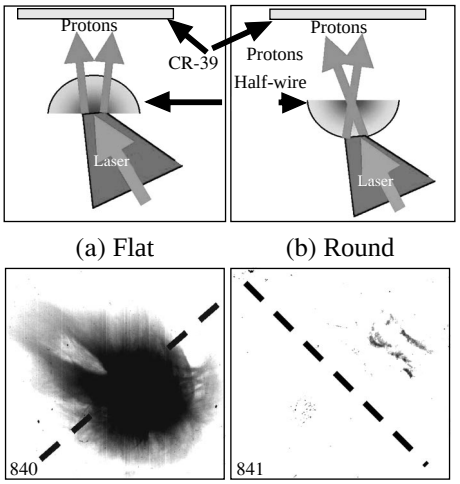

Fig. 10. Scheme of the irradiation of a 100- to 120-μm-diameter aluminum half-wire target. The protons from the flat (a) and round (b) sides of the irradiated target are recorded using the CR-39 detector. The wires were oriented approximately 45° to the vertical, as shown by dashed lines.

Using an aluminum half-wire target profile between 100–120 μm, we observed an effect analogous to that of an electrostatic cylindrical lens. The laser was focused onto either the flat or rounded surface of the half-wire, and the beam image was recorded. A CR-39 detector was used to record the protons. It was placed approximately 2 cm from the target (Fig. 10). The irradiation of the flat surface of a target having a cylindrical rear surface and vice versa is shown in Fig. 10a and Fig. 10b, respectively. A target with a flat front side surface of the half-wire produces a proton beam similar to that of an ordinary film target. When a round surface is irradiated, an uncollimated spray of protons from the flat side of the half-wire appears, such as one might expect from a cylindrical lens. The results of these experiments may support studies showing front side proton acceleration.

An important question which must addressed for the future application of laser-triggered protons is the possibility of focusing the proton beam. To investigate this, we performed experiments with shaped (concave) 25-μm aluminum foil targets. The CR-39 detector was placed 3 cm behind the target. We observed an oversaturated region in the center of the proton beam. This region appeared brighter due to a large number of overlapping tracks scattering more light. Physical inspection of this region under a microscope revealed the higher track density, differentiating it from regions of similar opacity but with lower track density. One might think that the ballistic focusing of a proton beam can be achieved only at the plane passing through the center of the target curvature. Indeed, this would be true if the proton beam emerging from a flat target were collimated. In reality, a laser-triggered proton beam has quite a large divergence; moreover, protons of different energies have different divergences. Typically, the higher energy proton component has a narrower cone. This may explain our observation of the focused part of the beam seen in Fig. 11 at distances much greater than the radius of curvature of the shaped target. According to our estimates, this focused region may correspond to the high-energy proton beam component, which would have a divergence of about 5° if a flat target were used.

Along with the difference in proton energies (Section 3), we observed a significant difference in the proton beam quality for metal (Al) and dielectric (Mylar) targets. In Figs. 12 and 13, the proton beam quality is illustrated for different proton energies. Generally, aluminum targets produce higher quality beams with more uniform proton beam profiles. In contrast, the proton beams from Mylar show significant inhomogeneity. We also found that, for both types of targets, the lower energy component of the proton beam is more structured then the higher energy component. One may imagine that the electric field that accelerates ions is more homogeneous in a conductive media, because of the presence of free electrons that provide a return current inside the target, which produces a more uniform proton beam.

Coating the front surface of a target with materials that provide a high absorption of laser light can significantly enhance the generation of hot electrons.In turn, this should lead to an increase in the efficiency of high-energy ion generation. We performed such an experiment with a so-called “laser black” target (a foil coated by soot-like substance) by coating 10 μm-thick Cu target with 5–10 μm-thick laser black, structured with a characteristic scale of 1–2 μm. The absorption in such a target is practically ideal (>96%). When laser light was focused into a spot 6-μm in diameter, we observed

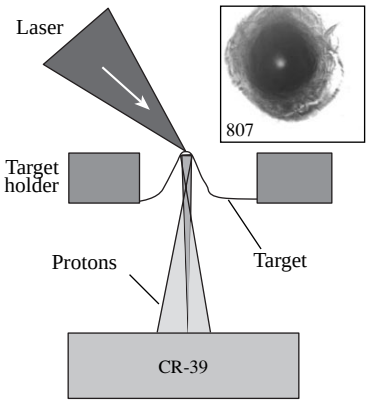

Fig. 11. Scheme of the irradiation of a curved target. Inset presents the proton beam image on the CR-39 for an energy greater than 2 MeV.

a doubling of the maximum ion energy (8.2 MeV), compared to a target without coating (4 MeV). The increase in ion energy was not followed by a reduction in proton beam quality (Fig. 14).

Borghesi *et al.* showed that point projection proton imaging [29] appears to be a powerful technique for electric field detection in laser-irradiated targets and plasmas [30, 31]. This technique was further developed by Mackinnon and coworkers [32, 33] to produce Moire fringes in a proton beam. We performed a preliminary experiment on imaging with high-energy proton beams. A free-standing copper mesh with a wire diameter of 10 μm and a period of 30 μm was illuminated by a proton beam produced in the interaction of the high-intensity laser with a thin film target. The mesh was parallel to the thin film target (Fig. 15a). The distance between the proton source and the mesh was 5 mm, while the radiochromic film was positioned at 50 mm from the source, thus providing a tenfold magnification. A shadow of the mesh was observed on the radiochromic film, as shown in Fig. 15b. The optical density modulation on the film was of the order of 0.2. It must be noted that the stopping range of 10-MeV protons in Cu is about 400 μm. Such energetic protons will lose only 0.1% of their energy in 10 μm of Cu. Such variation in energy loss across the wire was too small to produce any visible effect using our diagnostics. The current explanation of the observed phenomena is based on the assumption of a point-like proton source with very low transverse emittance, which leads to the possibility of detecting the small angle scattering experienced by protons inside a thin wire. Proton imaging can be very useful for the diagnostics of dense plasmas, and may be used to study the distribution of electric and magnetic fields in plasmas of laser-irradiated targets with high temporal and spatial resolution [29]. Unique advantages of a laser-triggered proton source are ultrashort pulse duration and absolute synchronization for use in pump-probe experiments; in addition, the point-like source provides a spatial resolution of several microns for imaging applications. Other advantages are the directionality and high brightness of proton beams, while the long stopping range of 10- to 15-MeV protons allows them to penetrate ~1-mm-thick objects.

6. ION ACCELERATION BY HOT ELECTRONS

A brief picture of ion acceleration in short-laser-pulse interaction with foils was proposed in [3, 4, 10, 34]. Electrons, accelerated in an underdense plasma (with density less than critical, n_{cr}), penetrate deep inside the target or even through it, setting up a strong electrostatic field (a Debye sheath) which accelerates ions forward and decelerates the electrons. Thus, during plasma expansion, the kinetic energy of the fast electrons is transformed into the energy of the electrostatic field, which accelerates the ions; their energy is expected to be on the level of the hot-electron energy. Similar physics were been explored in ICF studies of plasma expansion [35–42] with cold background electrons and laser heated electrons, which accelerate ions [5]. Though the key idea of using a two-electron-temperature model is the same, the typical hot-to-cold-temperature ratio is very different for the values of ICF and short laser-pulse produced plasmas. In an ICF plasma,

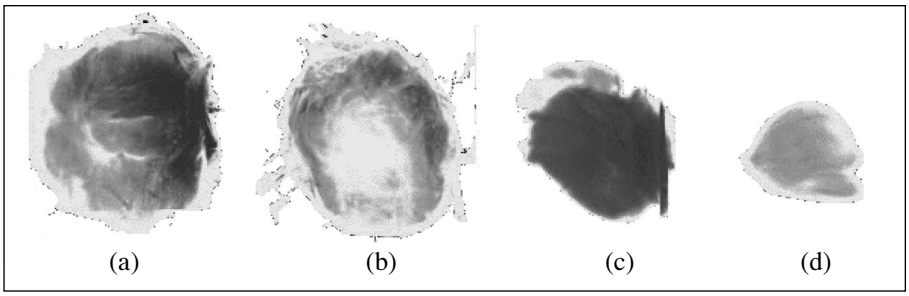

Fig. 12. Beam images on the CR-39 from a 12.5-μm-thick aluminum target showing the beam energy increase along the axis. Each image was taken from separate shots of similar energies with filters aimed to block protons below (a) 2.5, (b) 3, (c) 4.8, and (d) 7.9 MeV.

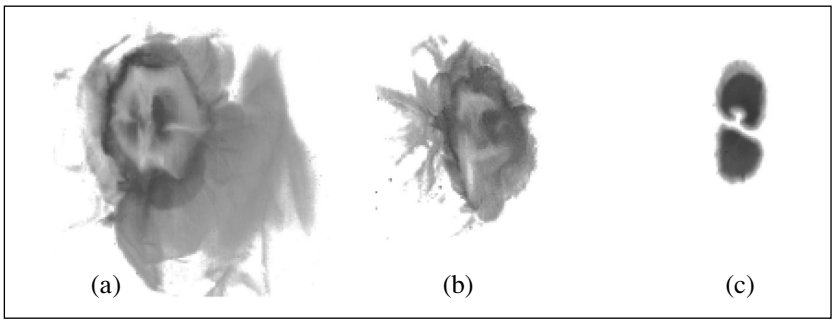

Fig. 13. Beam images on the CR-39 from a 13-μm-thick Mylar target corresponding to proton energies above (a) 1.4, (b) 2, and (c) 2.7 MeV.

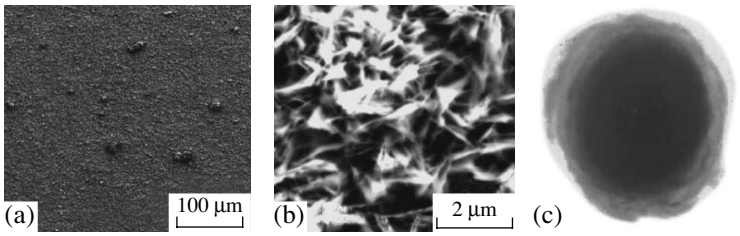

Fig. 14. (a) Low and (b) high magnification image of the surface of a "laser-black" copper target; (c) proton beam image on the CR-39 from "laser black" copper target.

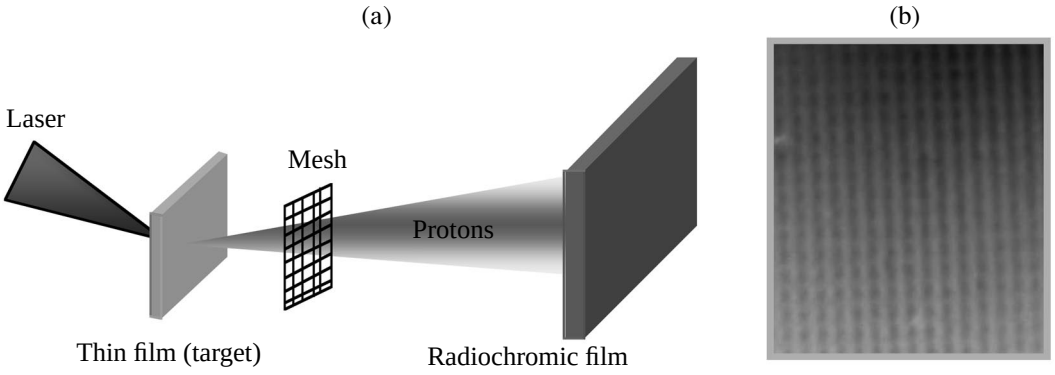

Fig. 15. (a) Setup for proton imaging of a mesh; (b) image of a mesh with 30-μm period (10-μm Cu wires) obtained with high-energy protons.

this ratio is usually less than 10^2, while it is $\geq 10^3$ for current experiments on short laser-pulse interaction with a plasma. Given that most theoretical works on ion generation include numerical calculations, such a dramatic gap between hot and cold electron temperatures requires more accurate modeling to quantify this effect.

Using certain simplified theoretical models, plasma expansion into a vacuum has long been extensively studied, ever since the work by Gurevich *et al.* [43]. Until the last decade, however, this problem was treated using hydrodynamic models only [44]. By the 1990s, the kinetic aspects of plasma expansion had already prevailed. The latest developments in the kinetic theory of plasma expansion have brought analytical results from ionacceleration [45–47]. Certainly, PIC simulations are free from such simplification and constitute a powerful tool for studying ion acceleration in short laser-pulse interactions with plasmas starting from the basic principles. Nevertheless, PIC models are quite demanding, and some physical aspects are often hidden among the numerous interfering effects included in such cumbersome simulations. This is why it is also

useful to explore simpler models which are still able to qualitatively describe the main features of ion acceleration and its characteristics in terms of plasma and laser parameters. This may provide an easy-to-use tool for the analysis of experimental data.

Considerable progress in the analytical description of ion acceleration by hot electrons has been achieved using the model of quasineutral plasma expansion. One may find this model to be oversimplified for interpreting the experiments on ion acceleration in expanding plasmas heated by ultra short laser pulses. However, it is definitely useful at long time scales (which are inaccessible to full-scale PIC simulations), when the laser pulse terminates and the plasma trends toward quasineutrality but acceleration continues. We start here from this model [46, 47].

Using the renormalization group symmetry (RGS) method in [48], it is now possible to apply the quasineutral plasma expansion model to ion acceleration. As an example, we consider a symmetrical plasma slab consisting of two ion (C and H) and two electron (cold and hot) species with density profiles following the quasineutrality condition, and use the RGS method to solve the Cauchy problem for the Vlasov equations:

$$\partial_t f^\alpha + v\partial_x f^\alpha - (e_\alpha/m_\alpha)(\partial_x\Phi)\partial_v f^\alpha = 0, \quad f^\alpha\big|_{t=0} = f_0^\alpha(x, v). \tag{2}$$

Particle distribution functions $f^\alpha(t, x, v)$ for the electrons (α = c and h for cold and hot electrons, respectively) and ions (α = 1 and 2 for heavy and light ions, respectively) are assumed to satisfy the quasineutrality condition:

$$\int dv \sum_\alpha e_\alpha f^\alpha = 0, \quad \int dv\, v \sum_\alpha e_\alpha f^\alpha = 0. \tag{3}$$

The electric potential is expressed in terms of the moments of the distribution functions:

$$\partial_x\Phi = -\int dv \sum_\alpha e_\alpha v^2 \partial_x f^\alpha \left\{\int dv \sum_\alpha \frac{e_\alpha^2}{m_\alpha} f^\alpha\right\}^{-1}. \tag{4}$$

The key is to find the RGS that provides an invariance for the solution to the initial value problem for $t \longrightarrow 0$: $f^\alpha = \mathcal{F}^\alpha(t, x, v) \equiv f_0^\alpha(x, v) + O(t)$ and to formulate the finite transformations that extend this solution to the solution for $t > 0$. Correspondingly, the RGS can be found as a subgroup of the group of point Lie transformations described by Eqs. (2) and (3). For the spatially symmetric initial distribution functions, the RGS generator appears as a linear combination of generators of projective transformations and translations along t. The finite RGS transformation defines a transformation of the phase space (x', v') at $t = 0$ to the phase space (x, v) at $t > 0$ as follows

$$x' = \frac{x}{\sqrt{1+\Omega^2 t^2}}, \quad v'^2 + \Omega^2 x'^2 = v^2 + \Omega^2 (x - vt)^2, \tag{5}$$

where the characteristic time scale $\Omega^{-1} = L_0/c_s$ can be treated physically as the ratio of the plasma slab half-thickness L_0 to the characteristic ion acoustic velocity, defined by the main ion component, $c_s = \sqrt{(T_1 + ZT_c)/(m_1 + Z_1 m_e)}$.

The distribution functions are invariants of the group transformations (5),

$$f^\alpha = f_0^\alpha(I^{(\alpha)}), \quad I^{(\alpha)} = \frac{1}{2}(v'^2 + \Omega^2 x'^2) + \frac{e_\alpha}{m_\alpha}\Phi_0(x'), \tag{6}$$

so that the distribution functions at the given time, $t \neq 0$, can be expressed in terms of their initial values. Here, the dependence of Φ_0 on self-similar variable $x' = x/\sqrt{1+\Omega^2 t^2}$ is defined by the quasineutrality condition (3), and the electric potential is given by

$$\Phi(t, x) = \Phi_0(x')(1+\Omega^2 t^2)^{-1}. \tag{7}$$

We assume that initially ($t = 0$), the ion species have Maxwellian distribution functions with densities n_{10}, n_{20} and temperatures T_1, T_2, and the electrons obey a two-temperature Maxwellian distribution function with densities and temperatures of the cold and hot components n_{c0} and n_{h0} ($n_{c0} + n_{h0} = Z_1 n_{10} + Z_2 n_{20}$) and T_c and T_h, respectively. The corresponding solution of the initial value problem reads

$$\begin{aligned} f^e &= \frac{n_{c0}}{\sqrt{2\pi}v_{Tc}}\exp(-I^{(c)}/v_{Tc}^2) + \frac{n_{h0}}{\sqrt{2\pi}v_{Th}}\exp(-I^{(h)}/v_{Th}^2), \\ f^1 &= \frac{n_{10}}{\sqrt{2\pi}v_{T1}}\exp(-I^{(1)}/v_{T1}^2), \\ f^2 &= \frac{n_{20}}{\sqrt{2\pi}v_{T2}}\exp(-I^{(2)}/v_{T2}^2), \end{aligned} \tag{8}$$

where $v_{T\alpha}^2 = T_\alpha/m_\alpha$ and the invariants $I^{(\alpha)}$ are defined as follows:

$$\frac{I^{(c)}}{v_{Tc}^2} = \mathcal{E} + \frac{(1+\Omega^2 t^2)}{2v_{Tc}^2}(v-u)^2,$$

$$\frac{I^{(h)}}{v_{Th}^2} = \mathcal{E}\frac{T_c}{T_h} + \frac{(1+\Omega^2 t^2)}{2v_{Th}^2}(v-u)^2,$$

$$\frac{I^{(1)}}{v_{T1}^2} = -\mathscr{E}\left(\frac{Z_1 T_{c0}}{T_{10}}\right) + \frac{U^2}{2v_{T1}^2}\left(1 + \frac{Z_1 m_e}{m_1}\right) + \frac{(1+\Omega^2 t^2)}{2v_{T1}^2}(v-u)^2,$$

$$\frac{I^{(2)}}{v_{T2}^2} = -\mathscr{E}\left(\frac{Z_2 T_c}{T_2}\right) + \frac{U^2}{2v_{T2}^2}\left(1 + \frac{Z_2 m_e}{m_2}\right) + \frac{(1+\Omega^2 t^2)}{2v_{T2}^2}(v-u)^2. \quad (9)$$

Here, $u = xt\Omega^2/(1+\Omega^2 t^2)$ is the local plasma velocity; $U = x\Omega/\sqrt{1+\Omega^2 t^2}$. The potential Φ is defined in the implicit form via the function $\mathscr{E}$,

$$\mathscr{E} = \frac{e\Phi}{T_c}(1+\Omega^2 t^2) + \frac{U^2}{2v_{Tc}^2}, \quad (10)$$

which obeys the transcendental equation,

$$1 + \sigma - \rho_h = \exp\left[\left(1 + \frac{Z_1 T_c}{T_1}\right)\mathscr{E} - \frac{U^2}{2v_{T1}^2}\left(1 + \frac{Z_1 m_e}{m_1}\right)\right] - \rho_h \exp\left[\left(1 - \frac{T_c}{T_h}\right)\mathscr{E}\right] + \sigma\exp\left[\left(1 + \frac{Z_2 T_c}{T_2}\right)\mathscr{E} - \frac{U^2}{2v_{T2}^2}\left(1 + \frac{Z_2 m_e}{m_2}\right)\right], \quad (11)$$

$$\rho_h = \frac{n_{h0}}{Z_1 n_{10}}, \quad \sigma = \frac{Z_2 n_{20}}{Z_1 n_{10}}.$$

The solution to this equation allows one to define the dependences of the particle distribution functions on velocity, coordinate and time.

Equations (8)–(11) give exhaustive information on the kinetics of plasma foil expansion. However, rough integral characteristics might be more useful for practical applications. Two integral characteristics (such as partial ion density, $n_q(t, x)$, and ion energy spectra, $dN_q/d\epsilon$) can be calculated from the ion distribution functions:

$$n_q = \int_{-\infty}^{\infty} dv\, f^q,$$

$$\frac{dN_q}{d\epsilon} = \frac{1}{m_q v}\int_{-\infty}^{\infty} dx\,(f^q(t, x, v) + f^q(t, x, -v)). \quad (12)$$

When integrated over the energy, $\epsilon = m_q v^2/2$, the value $dN_q/d\epsilon$ defines the total number of ions of the given species in a plasma slab per unit square.

The ion density is defined by the universal function $\mathcal{N}_q$ as follows:

$$n_q = \frac{n_{q0}}{\sqrt{1+\Omega^2 t^2}}\mathcal{N}_q(U),$$

$$\mathcal{N}_q(U) = \exp\left(\frac{Z_q T_c}{T_q}\mathscr{E} - \frac{U^2(1 + Z_q m_e/m_q)}{2v_{Tq}^2}\right). \quad (13)$$

The general form of $dN_q/d\epsilon$ given by Eqs. (8) and (12) is rather complicated, but its asymptotic behavior at $\Omega t \longrightarrow \infty$ is described by the simple expression

$$\frac{dN_q}{d\epsilon} \approx \sqrt{\frac{2}{m_q\epsilon}}\frac{n_{q0}}{\Omega}\mathcal{N}_q\left(\epsilon = \frac{m_q U^2}{2}\right). \quad (14)$$

Here, the functions $\mathcal{N}_q(U)$ are also given by Eq. (13), provided the ion energy ϵ is not very small, viz, $2\epsilon/T_q \gg (\Omega t)^{-2}$. The asymptotical spectrum of accelerated ions is similar to a Maxwellian spectrum, $\propto\exp(-v^2)$, rather than to the spectrum $\propto\exp(-v)$ corresponding to the theory of isothermal plasma expansion [43], which does take account of particle cooling during plasma expansion. The latter is an important effect, since the physics of plasma foil expansion differ from the physics of semi-infinite plasma expansion, where the isothermal regime is permitted because of the infinite source of plasma energy.

To illustrate the aforesaid, we present in Fig. 16 the dimensionless carbon and proton densities n_1/n_{c0} (C) and n_2/n_{c0} (H) as functions of the dimensionless coordinate x^2/L_0^2 for different times. This example corresponds to CH plasma expansion with H^{+1} and C^{+4} ions. We assume all ions have the same initial temperature $T_{1,2}/T_c = 0.1$ and that the hot to cold electron temperature ratio is $T_h/T_c = 1000$. The concentration of hot electrons is $\rho_h = 5\times10^{-4}$. The left-hand panel shows the ion densities for $t = 0.5(L_0/c_s)$; the right-hand panel, for $t = 2(L_0/c_s)$. The dashed lines present the benchmarks related to the densities of cold electrons, n_c/n_{c0} (short dashes), and hot electrons, n_h/n_{c0} (long dashes), respectively.

Figure 17 shows the evolution of the dimensionless ion energy spectra, $(m_1 Z_1 T_c/2)^{1/2}(\Omega/n_{10})(dN_q/d\epsilon)$, for the same parameters as in Fig. 16. According to Fig. 17, the distribution $(dN_q/d\epsilon)\sqrt{\epsilon}$ definitely takes the form $\mathcal{N}_q(\epsilon)$ for $\Omega t \gg 1$. The left-hand panel corresponds to $\Omega t = 0.5$ and the right-hand panel to $\Omega t = 2$, respectively. Both energy spectra for light and heavy ions experience a cutoff on the high-energy side of the spectra. Note that the heavy ion component affects the energy spectrum of the light ions by means of a self-consistent electric field, so that the proton spectrum has a maximum at the energy cutoff in the spectrum of car-

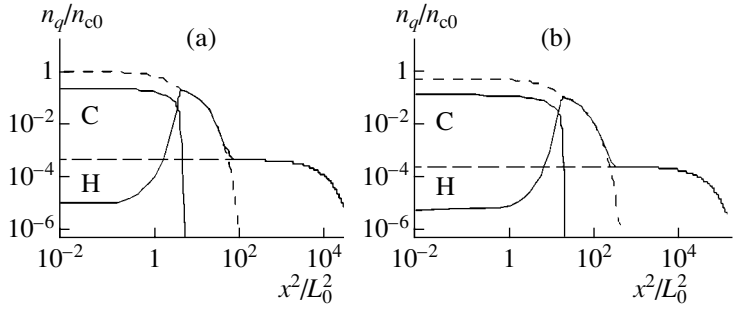

Fig. 16. Dimensionless densities of carbon ions (C) and protons (H) calculated by formulas (13) for (a) $t = 0.5(L_0/c_s)$ and (b) $t = 2(L_0/c_s)$.

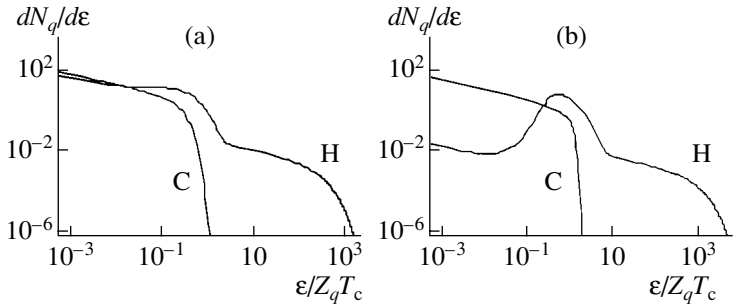

Fig. 17. Energy spectra $dN_q/d\epsilon$ of carbon ions (C) and protons (H) calculated by formulas (8) and (12) for (a) $t = 0.5(L_0/c_s)$ and (b) $t = 2(L_0/c_s)$.

bon ions. The proton energy cutoff settles at the level of the hot electron temperature, $\epsilon_{max} \sim T_h$.

Going beyond the model of quasineutral plasma expansion (which often cannot be used to interpret experiments on ion acceleration in expanding plasmas heated by ultra short laser pulses), we turn to the numeric Vlasov–Poisson model [49]. It uses the kinetic description of ions in a self-consistent electric field; this satisfies the Poisson equation, unlike the hydrodynamic model of [50]. Our Vlasov–Poisson model is well suited for modeling plasmas with many ion species.

As above, we include in this model two electron species: cold and hot. Arguing in favor of electron equilibration with the electrostatic potential on a time scale that is short compared to the plasma expansion time, most theoretical models assume that each electron species follows the Boltzmann distribution [36–38, 40–42]. We also follow this assumption, although (as was shown before) the deviations from the equilibrium electron distributions may have some quantitative effect on the parameters of the accelerated ions.

As mentioned above, we now consider both electron components (cold and hot) to be in a quasi-equilibrium state following Boltzmann distribution with temperatures T_c and T_h. Given the experimental data, one may refer to $T_c \sim 1$–2 keV and $T_h \sim 1$–10 MeV as the typical values. For short laser pulses of relativistic intensity, the hot electron temperature scales with a laser intensity quite close to the $\sqrt{I}$ dependence [51–53], so that the parameter T_h in our approach can serve as a connecting link to the laser, together with the number of hot electrons, n_h, which depends on the laser pulse energy rather than its intensity. Considering T_h and n_h as the controlling laser parameters, we aim to characterize the ion acceleration that depends on them and on the parameters of a plasma such as its thickness, temperature, and ion composition.

We consider a symmetrical plasma slab ($-L < x < L$) with an initially stepped ion density profile (at $x = \pm L$) that expands in the x-direction into the vacuum. Plasma expansion in a self-consistent electric field, $-\partial_x\Phi$, is described by the Vlasov equations for ions (2); the electrons follow Boltzmann distributions

$$n_{h,c} = n_{h0,c0}\exp(e\Phi/T_{h,c}), \tag{15}$$

where $n_{c0,h0}$ are the electron densities in the unperturbed plasma, and, instead of Eq. (3), the electric potential Φ satisfies the Poisson equation

$$\partial_{xx}\Phi = 4\pi e\left[n_{h0}\exp(e\Phi/T_h) + n_{c0}\exp(e\Phi/T_c) - \sum_\alpha Z_\alpha n_\alpha\right]. \tag{16}$$

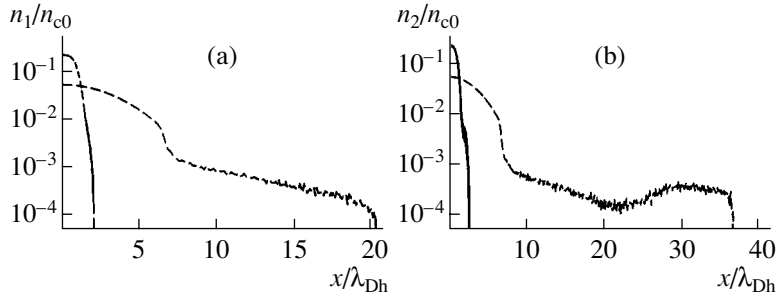

Fig. 18. Dimensionless densities of (a) carbon ions and (b) protons calculated by the Vlasov–Poisson model at $\omega_{p2}t = 1$ (solid lines) and $\omega_{p2}t = 10$ (dashed lines).

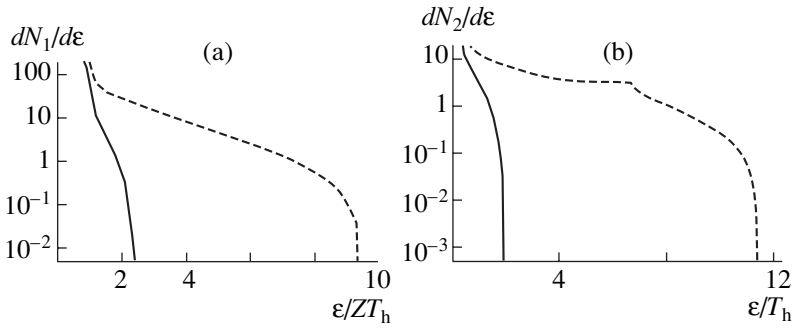

Fig. 19. Energy spectra $dN_q/d\epsilon$ of (a) carbon ions and (b) protons calculated by the Vlasov–Poisson model at $\omega_{p2}t = 1$ (solid lines) and $\omega_{p2}t = 10$ (dashed lines).

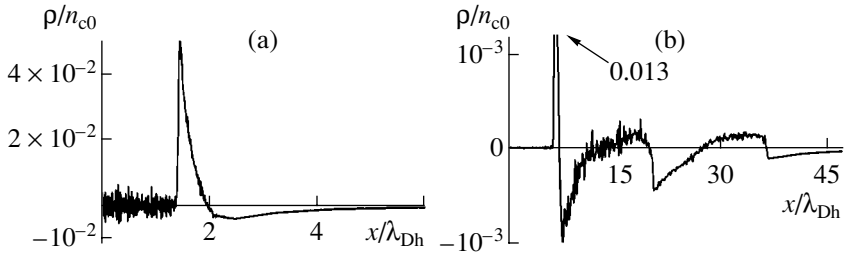

Fig. 20. The normalized space charge $\rho/n_{c0} = (Z_1 n_{10} + Z_2 n_{20} - n_{c0} - n_{h0})/n_{c0}$ calculated by the Vlasov–Poisson model at (a) $\omega_{p2}t = 1$ and (b) $\omega_{p2}t = 10$, where 0.013 indicates the maximum of ρ/n_{c0}.

The results of the numerical solutions of Eqs. (2), (15), and (16) are shown in Figs. 18, 19, and 20 for a thin CH plasma slab of a half-thickness equal to the Debye length of the hot electrons ($L = \lambda_{Dh}$). All initial plasma parameters were the same as in above example of RGS theory, except for the hot electron density, which was $\rho_h = 2 \times 10^{-3}$. Figures 18 and 19 show, respectively, the densities and energy spectra of heavy (C^{4+}) and light (H^+) ions. As should be, the protons that are accelerated by hot electrons form a halo in front of expanding plasma. At times $\omega_{p2}t \gg 1$, where ω_{p2} is the light ion plasma frequency, a band structure appears in the proton energy spectrum (Fig. 19) as in the analytical theory of quasineutral plasma (Fig. 17). At these times, the plasma is already close to a quasineutral state, although it is violated at the ion fronts of the fast protons, fast carbon ions, and bulk ions (Fig. 20). It is important to note that the maximum that precedes the cutoff in the proton energy spectrum (Fig. 19) is formed by protons that acquire additional acceleration at the heavy ion front, where the electric field has a maximum. This is entirely an effect of multi-species ion composition that can not appear in single-species plasma [50].

Unlike the theory of quasineutral plasma expansion, the high-energy part of the proton spectrum is more extended, exhibiting a proton tail with $\epsilon \gg T_h$. We

believe there are two reasons for this. First, the charge separation field, which is not included in the RGS model, increases the efficiency of ion acceleration. The charge-separation electric field peaks at the heavy ion front and effectively accelerates the light ions. Second, in contrast, the electron cooling that is allowed for in the analytic theory is not included in the numeric Vlasov–Poisson model and may result in the overestimation of the maximum proton energy. Such cooling is expected to be important if the laser pulse-duration is shorter than the typical acceleration time, which is several ω_{p2}^{-1}.

As a final note in this section, we mention that hot electrons control the ion acceleration if $n_{h0}T_h > n_{c0}T_c$. In this case the accelerating electrostatic field can be estimated from Eq. (16) as follows:

$$E \simeq \sqrt{8\pi n_{h0}T_h}. \quad (17)$$

For hot electron temperature ~1 MeV, this corresponds to Eq. (1) if the hot electron density is about the 10^{20} cm^{-3} that is typical for our experiments. As times goes by, the accelerating electric field (17) forms peaks at the ion fronts where the field amplitudes decrease over time as t^{-1}, similar to the results in [50].

7. PARTICLE ACCELERATION IN PIC SIMULATIONS

The models presented above suggest that the generation of high-energy electrons is crucial to ion acceleration. To self-consistently describe electron generation, 2D PIC simulations were performed by using the code in [54]. In this section, we present the results of such simulations for a 140-fs (FWHM) linearly polarized laser pulse with a wavelength $\lambda = 1$ μm, normally incident onto an underdense plasma slab having an exponential density profile with a spatial scale length $L =$ 5 μm [52]. Behind this was a thin dense plasma slab with a density forty times higher than critical and thickness $d = 0.25$ μm. This thickness was ten times greater than the skin depth, so the plasma slab was not transparent to the laser pulse. We used such a preplasma to model the blow-off plasma created by the laser prepulse, which interacts with the foil before the main pulse reaches the target. A laser pulse with vacuum electric field amplitude E_{y0} propagates in the x direction of an (x, y) simulation plane and has a 3-μm focal size. The normalized amplitude of the laser vector potential, $a = eE_{y0}/mc\omega_0$, was in the range $0.5 \le a \le 13.8$, corresponding to laser intensities $I\lambda^2$ of 3.3×10^{17} to 2.5×10^{20} W/cm^2 μm^2. The total simulation box was 50×10 μm, and the dense plasma target was at $x = 10$ μm. A long vacuum region was situated behind the target to reduce boundary effects. We performed simulations at different preplasma scale lengths ($0 < L/\lambda < 10$) and plasma target thicknesses ($0.1 < d/\lambda < 8$) for a laser intensity of $a = 2$. A hydrogen-deuterium plasma was chosen with 20% H and 80% D.

Our choice of a relatively thin dense plasma slab was motivated mainly by the TW scale experiments with dielectric targets [10] to model front side ion generation. According to [16], the temperature of the bulk electrons in the solid dense plasma is around 1 keV for such an experiment. Initially, only a thin skin layer less than 0.1 μm in width is heated to this temperature. During heating, the size of the hot dense plasma increases due to the energy transport of the bulk electrons inside the target. However, the heat transport velocity, $\sim f v_{Te}$, where v_{Te} is the electron thermal velocity and f is the heat flux inhibition factor, is rather low; with a subpicosecond laser pulse, a hot dense plasma cannot expand to greater than a micron in size. For example, at a pulse duration of 400 fs [10] and the commonly used value of $f \sim 0.1$, one may estimate $d \simeq 1$ μm. For the laser intensities considered here, the main laser energy is converted to hot electrons, which may penetrate at least to their Debye length. For instance, for a hot electron density of about n_{cr} and a temperature ~1 MeV, the Debye length is ~0.3λ. We follow Scenario 1 for the hot electron penetration of a highly resistive material, where the right plasma boundary is representative of the hot plasma–cold solid interface. This is likely to be relevant to the experiments in [10] with insulators. Measurements of the hot electron penetration depth [16] for the same parameters typical of the experiments in [10] have shown a rather short penetration depth of <3 μm. In order to model deeper energy deposition (due, for example, to a prepulse), we changed d in our simulations by as much as 8λ.

Thus, ion acceleration is governed entirely by the high-energy electrons generated in the preplasma. At the same time, electron motion is very complicated because of the combined effect of the pump, the reflected and self-generated fields, and the plasma inhomogeneity. In Fig. 21, we show a 2D-distribution of the electromagnetic energy and quasistatic fields (the fields averaged over the laser period): the magnetic field (B_z) and the longitudinal electrostatic field (E_x) for a subrelativistic laser intensity, $a = 1$. The reflection of laser light produces a standing wave, which is seen in Fig. 21 to be a modulation of the laser intensity on the scale of λ/2. While the laser beam forms a well-pronounced channel in the corona, the self-focusing was insignificant for the given parameters. Surface currents and the electrons expelled backwards cause a magnetic field generated by the so-called "fountain effect," with a maximum of up to 40% of the laser field (Fig. 21b).

The good correlation between the laser intensity and the modulations of the longitudinal electric field in the preplasma can be seen clearly in Fig. 21c. We have concluded that the latter is due to the ponderomotive effect at each maximum of the laser intensity. However, in an arbitrary y-slice, the electrostatic field exhibits chaotic behavior (Fig. 21d) that cannot be seen in Fig. 21c

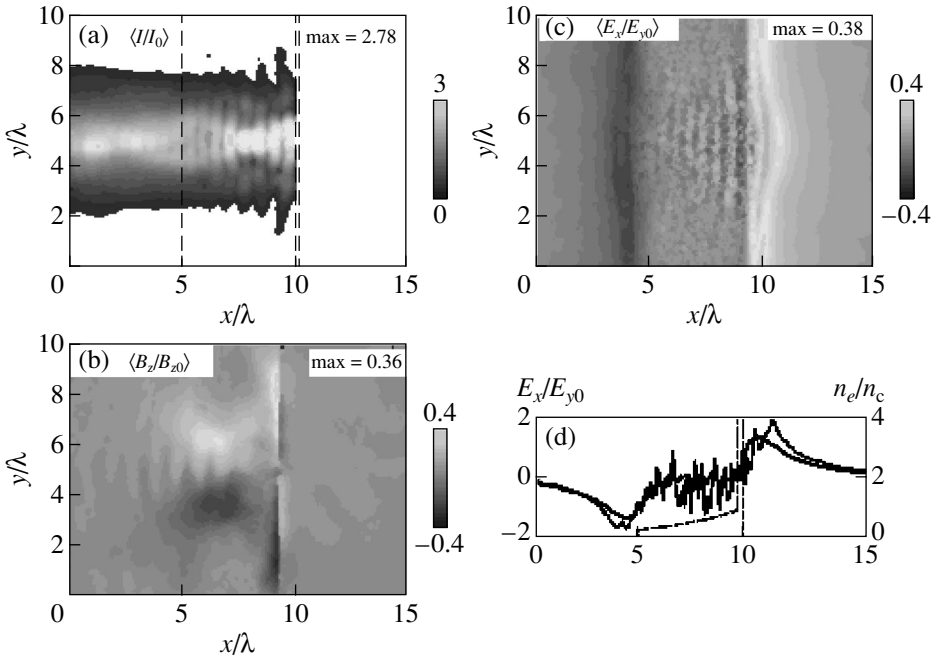

Fig. 21. The electromagnetic energy at t = 106 fs (a), the quasistatic magnetic field at t = 185 fs (b), the longitudinal electrostatic field at t = 185 fs (c), and the corresponding slice plot at y = 5 μm (d) for dimensionless laser field a = 1. Dashed lines indicate the initial plasma boundaries. All plots are time averaged over the laser period.

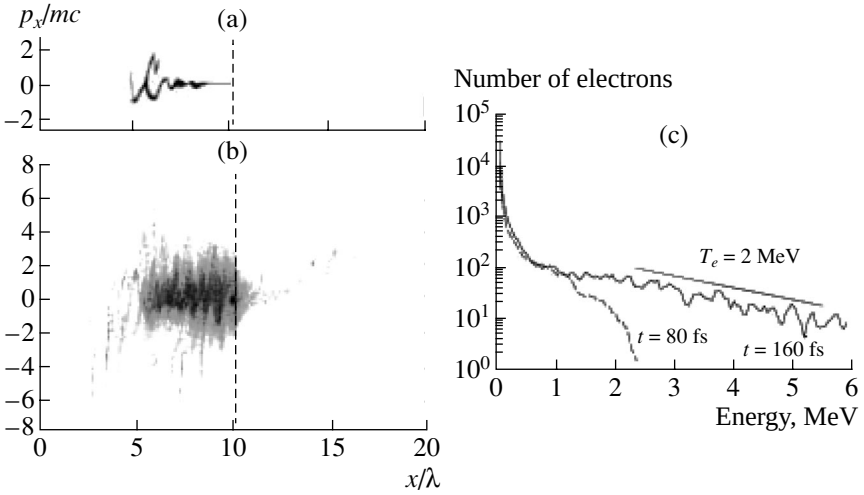

Fig. 22. The electron phase space plots (x, p_x) during the laser pulse, at (a) t = 40 fs and (b) t = 80 fs. The energy distribution of forward accelerated electrons (c) during the laser pulse, at t = 80 fs, and after it, t = 160 fs. Laser intensity corresponds to a = 1.

because of the rather small scale of the electrostatic fluctuations across the laser beam. On the other hand, averaged over the laser focal size (in order to filter out noise), this electrostatic field shows a well defined periodic structure in the x direction with a spatial scale of λ/2. The electron density has similarly strong modulations. Hence, the acceleration of electrons occurs in preplasma with a very complicated electromagnetic field structure and density. Propagating through the target, these electrons produce a strong charge separation field which reaches 40% of the laser field behind the target and smoothly decreases with distance, as shown in Fig. 21d.

The PIC model gives details of the electron energy distribution, as is shown in Fig. 22 for a = 1. The phase space plots (Figs. 22a, 22b) show space modulations on the scale of λ/2 due to the formation of a standing electromagnetic wave; this plays an important role in elec-

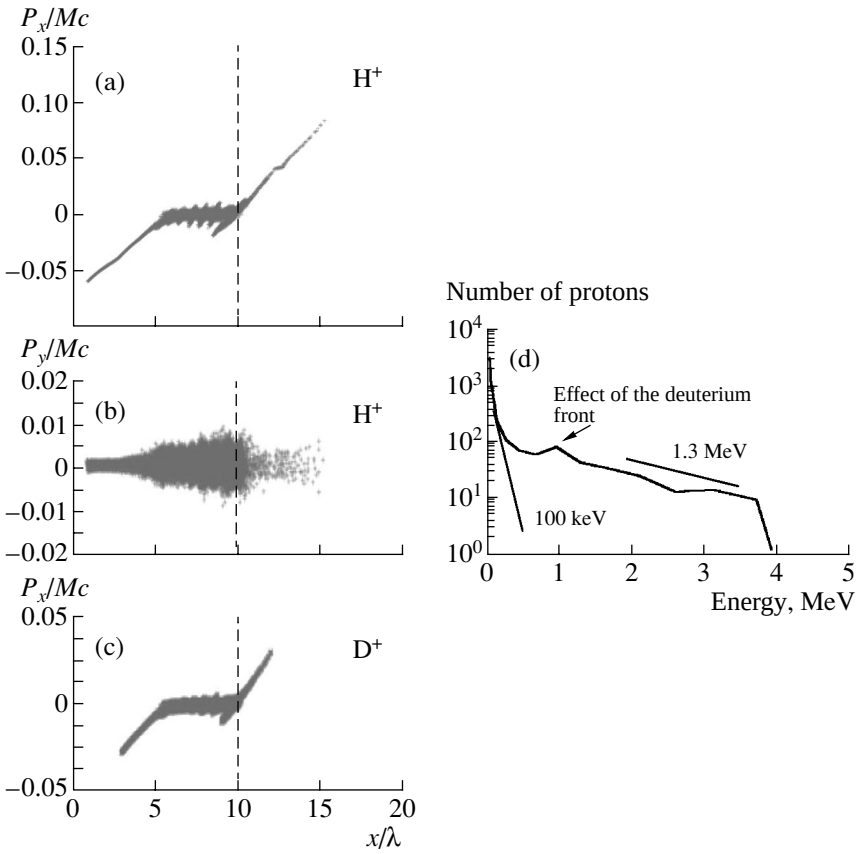

Fig. 23. The simulation results for $a = 1$: the ion phase space plots (x, p_x) (a) and (c) for H^+ and D^+ ions, respectively, and (x, p_y) (b) for H^+ ions at $t = 330$ fs. The energy distribution of forward accelerated protons is shown in the panel (d) at $t = 330$ fs. Dashed vertical line shows the position of thin overdense plasma slab; M is the ion mass for protons and deuterons, respectively.

tron heating. On this run, 60% of the laser energy was reflected; i.e., the reflectivity coefficient related to the field amplitude was $r \sim 0.8$. For $a \sim 1$, the amplitude of the longitudinal momentum oscillations due to the formation of the standing electromagnetic wave can be estimated at $p_x/mc \sim (1 + r)^2 a^2 \sim 3$, (cf. Fig. 22b). Over several laser cycles, the electron motion becomes stochastic. Thus, we conclude that for our simulations with a rather extended preplasma, stochastic electron heating is the dominant process for electron energy gain. Stochastic heating originates from the standing wave formation due to the reflection of laser light. This was proved by the simple numeric model presented in [52], where it was shown that stochastic electron heating occurs when $r > 0.2$.

The PIC simulations suggest that the preplasma, which can be attributed to the finite intensity contrast ratio of the laser pulse, makes the laser capable of producing ions in the MeV range at $I > 5 \times 10^{17}$ W/cm^2. In Figs. 23a and 23b, the longitudinal and transverse proton momenta are shown versus distance x. Comparison between 23a and 23b demonstrates that the high-energy protons are expelled as two beams, one in the forward direction and one in the backward direction, and the energy of the forward accelerated ions is higher. The energy of the deuterons is four to five times lower than that of the protons (Fig. 23c). Deuterons are two times heavier than protons and have less mobility; following behind the protons, they experience a significantly lower accelerating electric field and therefore gain less energy.

Figure 23d shows the ion energy spectrum for $a = 1$. It exhibits a low energy (100–200 keV) ion bulk and a hot ion tail (1.0–1.5 MeV) that transitions smoothly to a flat distribution with a sharp energy cutoff (4 MeV). Such a flat distribution with an energy cutoff is typical for an electrostatic mechanism of ion acceleration [2–4, 6, 55–57]. It corresponds to the maximum electric potential produced by the hot electrons. One more piece of evidence for the electrostatic nature of ion acceleration is provided by the peak in the proton distribution at an energy of ~1 MeV; this corresponds to the deuteron front and defines in turn the self-consistent accelerating field.

From our study of ion trajectories, we conclude that the maximum energy gain is obtained when the protons are accelerated from the back of an overdense plasma, in accordance with the spatial distribution of the elec-

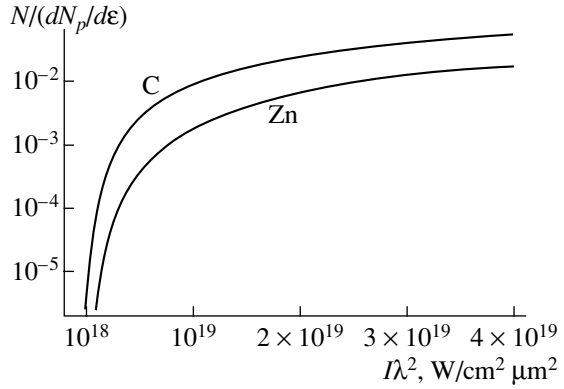

Fig. 24. The yields $N/(dN_p/d\epsilon)$ of $^{11}B(p, n)^{11}C$ and $^{63}Cu(p, n)^{63}Zn$ reactions versus laser intensity.

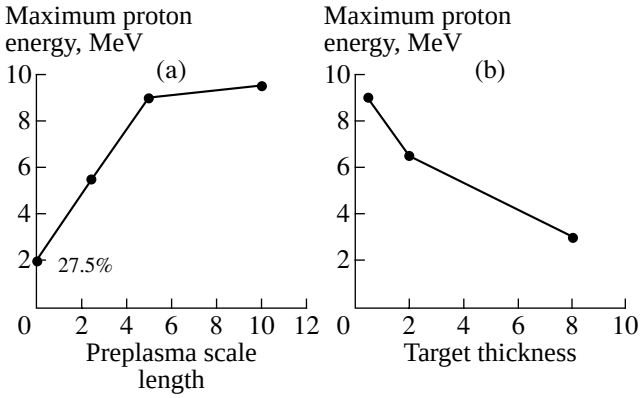

Fig. 25. Maximum proton energy versus (a) the preplasma scale length and (b) the overdense plasma thickness (in units of λ) for $a = 2$.

trostatic field (Fig. 21d). Indeed, the electric field is maximum behind the dense plasma slab so that the rear side protons respond first and the others that follow behind them are accelerated by a screened potential. However, this result needs to be reconciled with the contradictory experimental observations of ion acceleration from either the front [2, 6] or the rear surfaces [3, 4]. In experiments with a high intensity contrast ratio [2, 10], the rear surface of a solid dense plasma is in fact the front surface of a foil, because the thickness of the highly ionized region is negligible compared to the foil thickness. This is likely not the case for the experiments in which a rear-surface origin was found [3, 4], where a very intense prepulse preceded the main laser pulse.

8. COMPARISON WITH EXPERIMENTS

The PIC simulations agree with the features of high-energy ion emission observed in our experiments. By studying the dependence of the maximum ion energy ϵ_{max} on the laser intensity I ($3.3 \times 10^{17} \le I \le 2.5 \times 10^{20}$ W/cm^2), we found $\epsilon_{max} \propto I$ and $\epsilon_{max} \propto \sqrt{I}$ dependences [52] for two regimes with $a \le 1$ and $a > 1$, respectively. The physical picture behind these I and $\sqrt{I}$ dependences is quite simple and is based on the generation of hot electrons in the preformed plasma. The electrons interacting with an electromagnetic wave of $\omega_0 > ck_0$ acquire an energy $mc^2(\gamma - 1)$, where γ is the relativistic factor. This gives the scalings mc^2a^2 and mc^2a for subrelativistic and ultrarelativistic laser intensities, respectively. During stochastic heating (Section 7), a quasi-thermal electron energy distribution forms with an effective temperature T_h, which scales as $mc^2(\gamma - 1) \propto \min\{a^2, a\}mc^2$. Hence, the electrostatic potential of the charge-separation field and the ion energy both have the same dependences on the laser intensity. The latter agrees qualitatively with Fig. 3, with the dependence quite close to the $\sqrt{I}$ dependence for high intensities suggested in [57]. Given our simulation and experimental results and the experimental results for higher intensities in [3, 57], one finds that the maximum proton energy for the relativistic laser intensity is well approximated as [58]

$$\epsilon_{max}\ [\text{MeV}] \approx 3.6\lambda\sqrt{I/10^{18}}, \qquad (18)$$

where the laser intensity is in 10^{18} W/cm^2 units and the laser wavelength is in μm.

The plateau-like energy distribution of fast ions (Figs. 2, 5) agrees with both theory and our simulations (Sections 6, 7). Along with this, Fig. 2 demonstrates a Maxwellian-like distribution of the bulk protons, similar to Eq. (14), indicating an adiabatic regime of plasma expansion [46, 47, 59] rather than an isothermal one [43]. Note that proton spectra with band structures, as shown in Fig. 34, are also tolerated by theoretical models (Fig. 17, 19). Similar band structures of the proton energy spectra were also observed in the experiments in [61, 62]. That the production of protons is more efficient than that of heavy ions (Figs. 17, 19, 23c) is confirmed by the (d, n) activation experiment. Our simulations quantify the inhibition of deuteron energy when they are accelerated along with protons [10], as described in Section 4. The experimental data on the activation of a boron sample with deuterons at $I = 6 \times 10^{18}$ W/cm^2 suggest that their energy was $\simeq$2 MeV, while the proton energy was as high as 8 MeV. This is close to the simulation result that yields a deuteron energy four times lower than the proton energy.

Because of the plateau-like energy distribution of fast protons, the reaction yield can be easily estimated by using the so-called overlap integral [62]

$$N \approx \frac{1}{M}\frac{dN_p}{d\epsilon}\int_0^{\epsilon_{max}} d\epsilon(\epsilon_{max} - \epsilon)\frac{\sigma(\epsilon)}{S(\epsilon)}, \qquad (19)$$

where one may use Eq. (18) for the proton energy cutoff. This expression quantifies the number of reactions

versus the laser field intensity in a nuclear target with atoms of mass M, where laser accelerated protons react with target nuclei in a layer of thickness equal to their stopping length S [MeV cm^2/g] with the efficiency defined by their cross section σ. In Eq. (19) the value $dN_p/d\epsilon$ is the number of high-energy (multi-MeV) protons per 1 MeV range. Figure 24 shows the nuclear yield (19), normalized to the number of fast protons in the 1 MeV range as a function of laser intensity. The thresholds at 10^{18} and 2×10^{18} W/cm^2 for ^{11}B(p, n)^{11}C and ^{63}Cu(p, n)^{63}Zn reactions are clearly seen in this figure. Because the measured number of protons with energy >(3–4) MeV was ~10^7–10^8 per 1 MeV range, the production of ~10^5 atoms of ^{11}C and ^{63}Zn follows from Eq. (19); this accords with the results of our activation experiments (Section 4).

In Section 2, the existence of an optimum in the laser prepulse intensity was demonstrated for the maximum ion energy gain. The maximum proton energy shown by the experimental points in Fig. 1b increases with the prepulse intensity for a contrast ratio >10^3 and then decreases. This is in qualitative agreement with the simulation results demonstrated in Fig. 25. It is likely that at the rather low intensity $I \sim 10^{18}$ W/cm^2, the scale length of the preformed underdense plasma grows with the intensity of the prepulse without a significant increase in the volume of the overdense plasma if the prepulse intensity remains sufficiently low. Accordingly, the maximum ion energy should increase and then saturate (Fig. 25a). However, at higher prepulse intensities, one might expect enhanced solid-density plasma production before the main laser pulse reaches the target. As a result, the efficiency of the ion acceleration decreases (Fig. 25b) due to the reduction in the average density of the hot electrons that participate in ion acceleration. We predict the saturation of ion energy when the solid plasma thickness exceeds the laser pulse length (if hot electron losses in the target are small).

The interplay between these two effects should result in a dependence similar to the experimental one shown in Fig. 1b, with the maximum at some moderate contrast ratio. An ion energy decrease and saturation with the target thickness was recently observed in an experiment [13] with a high energy laser.

9. NEAR FUTURE REGIMES OF PARTICLE ACCELERATION

As powerful short-pulse laser installations tend toward the multi-PW level and tabletop lasers continue to reach record levels of peak intensity, we look forward to the next physical regimes of ion acceleration. The first regime, which is expected for quite high-power lasers of ultra-relativistic intensities, might be called the nuclear regime of laser-plasma interactions [63], because of the generation of such elementary particles as mesons and baryons that should occur as nuclei collide in such energetic plasmas. The second regime

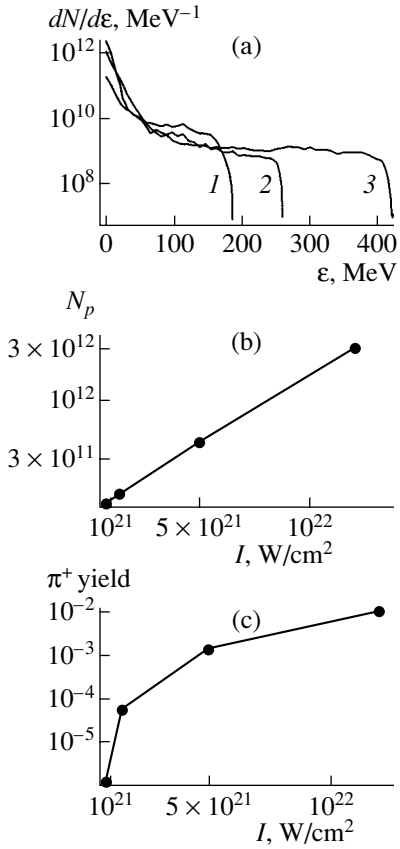

Fig. 26. (a) Energy distribution of the forward accelerated protons for laser intensities (*1*) 8×10^{20}, (*2*) 1.4×10^{21}, and (*3*) 5×10^{21} W/cm^2; (b) the number of forward accelerated protons with energy exceeding 140 MeV versus laser intensity; and (c) pion yield per a proton from the proton collisions with the C nuclei as a function of laser intensity.

deals with compact and ultrashort pulse-duration (several optical cycles) lasers, which are focused in a single-wavelength spot size to operate at relativistic intensities. The great advantage of these lasers is that they work at high repetition rates. One prototype of such a device is the CPA laser at CUOS [53]. This indirectly diode-pumped Ti:sapphire laser works at a 1-kHz repetition rate and has the advantage of being stable (1% variation), compact (it fits on a single 8' × 10' table), highly-intense (with an energy several times greater than 10^{18} W/cm^2) at a rather low level of energy (≤3 mJ) and a relatively low cost. Further improvement of this apparatus will provide a strongly relativistic intensity, $I = 10^{19}$ W/cm^2.

We have demonstrated for the first time the nuclear regime of laser-plasma interactions by pion production from accelerated protons [62]. Using 2D PIC simulations, we modeled the interaction of a short 300-fs linearly polarized pulse with a solid 5-μm-thick foil representing a uniform plasma layer with a density forty times higher than its critical value. Laser radiation with a wavelength of 1 μm was incident normally on the foil

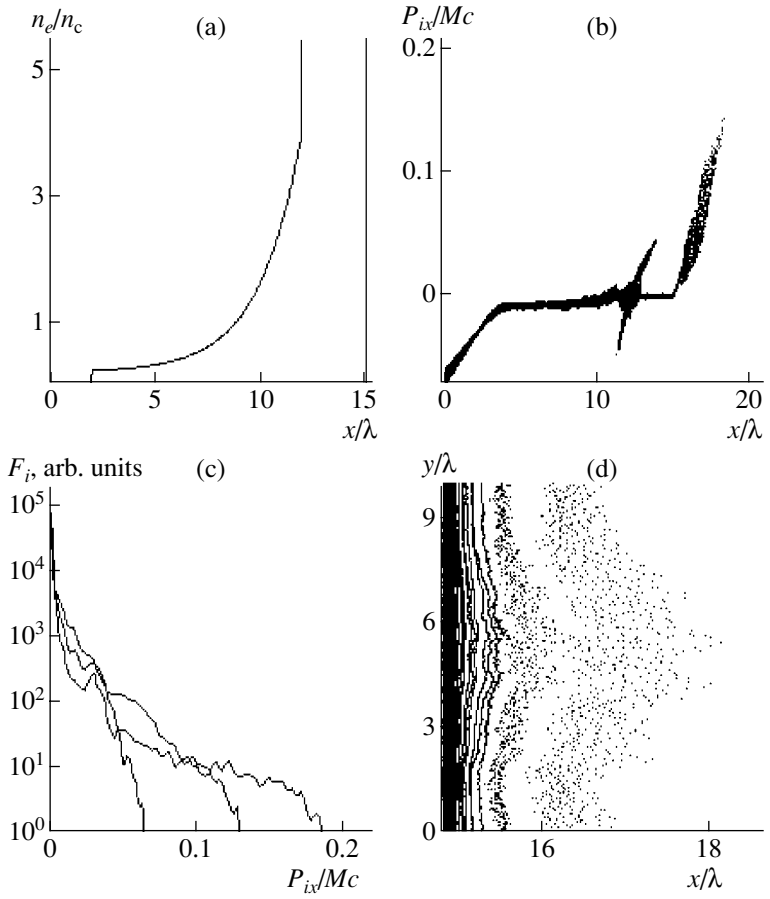

Fig. 27. (a) Initial electron density profile; (b) the ion phase space plot (x, p_{ix}) at $\omega_0 t/2\pi = 90$; (c) the ion momentum distribution functions at $\omega_0 t/2\pi = 40$, 70, and 90; and (d) spatial distribution of accelerated ions behind the foil at $\omega_0 t/2\pi = 70$.

surface. The focused spot size was 3 μm, while laser intensity varied in the range of 2×10^{20} to 5×10^{21} W/cm^2. To model a preplasma from a prepulse, a 30-μm-thick layer of rarefied plasma was placed in front of the foil. These simulations revealed plateau-like proton distributions with energy cutoffs similar to those presented in Section 7, but at much higher energies. Evidently, once the cutoff in the proton spectrum exceeds 140 MeV, protons can produce π^+ in the material behind the foil.

In Fig. 26, the energy spectra of the forward accelerated protons, the number of accelerated protons N_p with energy higher than 140 MeV, and the pion yield from a carbon target placed behind the foil are shown.

The number of high-energy protons that may produce π^+ increases in almost direct proportion to the laser intensity. Our calculations can be used to predict the laser intensity threshold for pion production. This threshold is clearly seen in Fig. 26 at $I_{th} \sim 10^{21}$ W/cm^2. At $I = 5 \times 10^{21}$ W/cm^2, the pion production yield is 10^{-3}. For 4×10^{11} accelerated protons, this provides a value of 4×10^8 particles per shot for the total π^+ yield, which is five orders of magnitude higher than the photopion yield obtained under similar conditions in [64]. Pions can be identified most simply from the $\pi\mu$ decay using the standard method, because the lifetime of a π^+ is short, $\tau_\pi = 26$ ns. At a pulse repetition rate of 1 kHz, laser muon production will offer advantages over conventional accelerator methods and provide a muon flux of 10^{14}–10^{15} s^{-1}.

In current laser techniques, the pion production threshold intensity of 10^{21} W/cm^2 can certainly be reached using low-energy lasers, provided that the pulse duration equals several femtoseconds. However, there is a fundamental limitation that requires a considerably long pulse duration: during the proton acceleration time $\tau_i \sim \sqrt{m_p/e^2 n_h}$, the laser must provide a permanent source of hot electrons. Otherwise, they cool down and are not able to accelerate ions efficiently (Section 6). Estimating the density of the hot electrons as the critical density, one obtains $\tau_i \sim 100$ fs for 1-μm laser. On the other hand, the smallest attainable focal spot size for high-power lasers is equal to several microns. Hence, it follows that, to produce pions, the laser output should be as high as several tens of joules.

In the above example of pion production in proton collisions with nuclei, the pion distribution is nearly isotropic. At the same time, for hydrogen-containing nuclear targets where pions may be produced in p–p collisions, one can expect the generation of pion and neutrino beams, provided that the proton energy far exceeds 1 GeV, i.e., at $I > 10^{23}$ W/cm^2. The lifetime of pions with energies of up to several GeV is considerably longer than $\tau_\pi = 26$ ns. This opens the way to their subsequent acceleration by the laser plasma method of particle acceleration in an underdense plasma [65] in order to produce ultrahigh-energy pions, which are as yet present only in cosmic rays. However, in contrast to the latter, the laser generation of ultrahigh energy pions is predictable. Note that one may consider laser-triggered muon production as a potential source for the so-called Muon Spin Rotation/Relaxation/Resonance (μSR) technique [66]. The μSR technique is now used to tackle on an atomic scale fundamental problems in condensed matter physics and chemistry that cannot be investigated by other means.

Finally, we turn to ion acceleration by ultra-short laser pulses, only one order of magnitude longer than the laser period, focused into very small spots with sizes comparable to the laser wavelength. A prototype of such a table top laser is now in operation at CUOS within the limits of a pulse duration of only a few cycles and a single-wavelength spot size. Our 2D PIC simulations using the UMKA code developed by the Institute of Computational Technologies [67, 68] were performed for a linearly polarized laser pulse propagating normally to a plasma target (hydrogen) in the x direction of an (x, y) simulation plane. This target models a solid dense plasma slab of thickness 3λ, with a rare plasma in front of it to simulate the blow-off plasma created by the laser prepulse that interacts with the foil before the main pulse reaches the target. The dense plasma slab has an electron density forty times higher than critical. The total simulation box is $40\lambda \times 10\lambda$. The preplasma is at $x > 2\lambda$ with an electron density that grows from $0.25n_{cr}$ to $4n_{cr}$. The laser pulse propagates in the x direction from left to right with a vacuum electric field dimensional amplitude $a = 7$. It has the small focal size 2λ and length 12λ. The position of the laser beam axis corresponds to $y = 5\lambda$. There is a 2λ vacuum layer before the plasma target and a significantly longer vacuum region behind it to reduce boundary effects. Our PIC model used 50 particles per cell.

The short laser pulse effectively generates electrons in the preplasma. The plasma density profile, which is shown in Fig. 27a, is not extraordinary and has a characteristic size of 10λ. However, it calls for about 50% of the laser energy to be transformed into electrons with an energy ≥3 MeV; these penetrate through the target and accelerate ions up to 18 MeV. This is demonstrated in Figs. 27b and 27c, in which the ion phase space plot and distribution function are shown. The ions escape from the rear side of the foil as a well collimated jet (Fig. 27d). The total numbers of fast electrons and protons with an energy ≥3 MeV are ~10^{11} and ~10^{10}, respectively. Although lasers with a pulse duration ≤100 fs are not optimal for high-energy ion generation [63], this provides hope that a laser with an energy of 100–200 mJ can be used to initiate most conventional nuclear reactions through the practical use of fast protons. For instance, the simulation performed allows us to predict that a radioactive ^{11}C source can gain around 1 Ci by using Ti:sapphire laser with an energy of ~100 mJ and a 100-Hz repetition rate.

10. SUMMARY

We have presented here the results from our experimental advances in the generation of high-energy ions in the interaction of a high-intensity short pulse laser with thin film targets. The characteristics of high-energy ions were measured and their correlation with laser intensity, wavelength, intensity contrast ratio, and the material and shape of the target were found. High-energy deuterons and protons were used to perform experiments on nuclear transformations ^{10}B(d, n)^{11}C, ^{11}B(p, n)^{11}C, and ^{63}Cu(p, n)^{63}Zn. Using shaped targets, we observed proton beam focusing and found that the target conductivity has a considerable impact on the quality of the generated proton beams. The experiments performed shed light on the means intended for the optimization of laser-based ion sources.

Either because of imperfect laser compression or amplified spontaneous emission, background light accompanies a short intense pulse and arrives at the focus first. For the current laser intensities 10^{19}–10^{21} W/cm^2 and typical contrast ratios 10^5–10^6 the corresponding prepulse intensity is as high as 10^{14}–10^{16} W/cm^2, which is more than enough for plasma creation. Typically, such a prepulse lasts from several hundreds of picoseconds to a few nanoseconds. Hence, the peak of a high intensity laser pulse arrives after the onset of plasma creation and expansion, and deposits its energy in an underdense long-density-scalelength plasma, rather than directly at the solid density. Numerous mechanisms of hot electron generation take place in such an underdense plasma; these are crucial for high-energy ion generation. We believe that preplasma formation should be taken into account in experimental and theoretical studies of ion acceleration. The manipulation of the preplasma in terms of its size and density profile, as well as arranging for optimum laser–plasma matching (including self-focusing in a preplasma), are important factors in creating a high-energy ion source with desirable properties.

The physical models of ion acceleration by fast electrons presented here provide an easy-to-use tool for estimating ion characteristics by means of their electron parameters. The corresponding correlation measurements might be an interesting subject for experiments on laser triggered ions. The 2D PIC simulations

performed qualitatively agree with the experiments. Using PIC simulations, we obtained scalings for ion energy with laser intensities I and $\sqrt{I}$ for the sub- and relativistic regimes, and described the dependences of ion generation on both the preformed and overdense plasma sizes. The observed increase of the maximum ion energy with greater preplasma thickness and its saturation demonstrates that an ideal laser pulse with a very high contrast ratio is not optimal for effective high-energy ion generation. The latter appears to be a result of the suppression of hot electron generation in a short-density scalelength underdense plasma. Finally, our PIC simulations predict the threshold of pion production for a Petawatt-class laser and the threshold of MeV ion generation for a table-top laser with a pulse duration of several cycles and a single-wavelength spot size.

One may expect that the development of laser-driven ion acceleration will result in several important applications. If protons were laser accelerated to 100–150 MeV energies, they could be useful for proton therapy, which is now limited to cyclotrons and the associated large magnets required to transport the proton beams to the patient. Protons are superior to other forms of ionizing radiation for cancer treatment due to their lower straggling and their ability to precisely deposit their energy in tissue. Protons and deuterons with energies of several MeV could be useful for isotope production. The production of short-lived isotopes in micro-samples using a high repetition rate laser might be promising for medicine, biology, and educational purposes. Laser-accelerated proton beams could be used as a tool for radiography and imaging in material science and for fundamental nuclear research on the picosecond time scale. A laser-based meson factory is also seen as one future application of laser- accelerated proton beams with energy above 150 MeV.

ACKNOWLEDGMENTS

The authors would like to thank T. Lin and M. Rever for their help with the CR-39 processing. This work was partly supported by the U.S. National Science Foundation (a FOCUS Grant), the Russian Foundation for Basic Research (project nos. 03-02-16428 and 02-01-00185), and INTAS (grant nos. 01-0233 and 01-0572).

REFERENCES

1. E. L. Clark, K. Krushelnick, J. R. Davies, *et al.*, Phys. Rev. Lett. **84**, 670 (2000).
2. A. Maksimchuk, S. Gu, K. Flippo, *et al.*, Phys. Rev. Lett. **84**, 4108 (2000).
3. S. P. Hatchett, C. G. Brown, T. E. Cowan, *et al.*, Phys. Plasmas **7**, 2076 (2000).
4. R. A. Snavely, M. H. Key, S. P. Hatchett, *et al.*, Phys. Rev. Lett. **85**, 2945 (2000).
5. S. J. Gitomer, R. D. Jones, F. Begay, *et al.*, Phys. Fluids **29**, 2679 (1986).
6. K. Krushelnick, E. L. Clark, M. Zepf, *et al.*, Phys. Plasmas **7**, 2055 (2000).
7. Yu Wei, V. Bychenkov, Y. Sentoku, *et al.*, Phys. Rev. Lett. **85**, 570 (2000).
8. Y. Sentoku, T. V. Liseikina, T. Zh. Esirkepov, *et al.*, Phys. Rev. E **62**, 7271 (2000).
9. S. V. Bulanov, N. M. Naumova, T. Zh. Esirkepov, *et al.*, Pis'ma Zh. Éksp. Teor. Fiz. **71**, 593 (2000) [JETP Lett. **71**, 407 (2000)].
10. K. Nemoto, A. Maksimchuk, S. Banerjee, *et al.*, Appl. Phys. Lett. **78**, 595 (2001).
11. N. Izumi, Y. Sentoku, H. Habara, *et al.*, Phys. Rev. E **65**, 036413 (2002).
12. M. Zepf, E. L. Clark, F. N. Beg, *et al.*, Phys. Rev. Lett. **90**, 064801 (2003).
13. A. J. Mackinnon, M. Borghesi, S. Hatchett, *et al.*, Phys. Rev. Lett. **86**, 1769 (2001).
14. J. Badziak, E. Woryna, P. Parys, *et al.*, Phys. Rev. Lett. **87**, 215001 (2001).
15. A. J. Mackinnon, Y. Sentoku, P. K. Patel, *et al.*, Phys. Rev. Lett. **88**, 215006 (2002).
16. Z. Jiang, J. C. Kieffer, J. P. Matte, *et al.*, Phys. Plasmas **2**, 1702 (1995).
17. L. Gremillet, F. Amiranoff, S. D. Baton, *et al.*, Phys. Rev. Lett. **83**, 5015 (1999).
18. A. R. Bell, J. R. Davies, S. Guerin, and H. Ruhl, Plasma Phys. Controlled Fusion **39**, 653 (1997).
19. J. R. Davies, A. R. Bell, M. G. Haines, and S. M. Guerin, Phys. Rev. E **56**, 7193 (1997).
20. J. R. Davies, A. R. Bell, and M. Tatarakis, Phys. Rev. E **59**, 6032 (1999).
21. F. Pisani, A. Bernardinello, D. Batani, *et al.*, Phys. Rev. E **62**, 5927 (2000).
22. M. Hegelich, S. Karsch, G. Pretzler, *et al.*, Phys. Rev. Lett. **89**, 085002 (2002).
23. M. V. Ammosov, N. B. Delone, and V. P. Kraĭnov, Zh. Éksp. Teor. Fiz. **91**, 2008 (1986) [Sov. Phys. JETP **64**, 1191 (1986)].
24. Experimental Nuclear Reaction Data File http://www.nndc.bnl.gov/nndc/exfor.
25. G. S. Sarkisov, V. Yu. Bychenkov, and V. T. Tikhonchuk, Pis'ma Zh. Éksp. Teor. Fiz. **69**, 20 (1999) [JETP Lett. **69**, 20 (1999)].
26. Kh. Rul', S. V. Bulanov, T. E. Cowan, *et al.*, Fiz. Plazmy **27**, 387 (2001) [Plasma Phys. Rep. **27**, 363 (2001)].
27. S. V. Bulanov and V. S. Khoroshkov, Fiz. Plazmy **28**, 493 (2002) [Plasma Phys. Rep. **28**, 453 (2002)].
28. S. C. Wilks, A. B. Langdon, T. E. Cowan, *et al.*, Phys. Plasmas **8**, 542 (2001).
29. M. Borghesi, A. Schiavi, D. H. Campbell, *et al.*, Plasma Phys. Controlled Fusion **43**, A267 (2001).
30. M. Borghesi, D. H. Campbell, A. Schiavi, *et al.*, Phys. Plasmas **9**, 2214 (2002).
31. M. Borghesi, S. Bulanov, D. H. Campbell, *et al.*, Phys. Rev. Lett. **88**, 135002 (2002).
32. A. J. Mackinnon, P. K. Patel, D. W. Price, *et al.*, Rev. Sci. Instrum. **74**, 1917 (2003).

33. A. J. Mackinnon, P. K. Patel, D. W. Price, *et al.*, Appl. Phys. Lett. **82**, 3188 (2003).
34. S. C. Wilks, W. L. Kruer, M. Tabak, and A. B. Langdon, Phys. Rev. Lett. **69**, 1383 (1992).
35. E. J. Valeo and I. B. Bernstein, Phys. Fluids **19**, 1348 (1976).
36. B. Bezzerides, D. W. Forslund, and E. L. Lindman, Phys. Fluids **21**, 2179 (1978).
37. L. M. Wickens, J. E. Allen, and P. T. Rumsby, Phys. Rev. Lett. **41**, 243 (1978).
38. L. M. Wicken and J. E. Allen, J. Plasma Phys. **22**, 167 (1979).
39. J. Denavit, Phys. Fluids **22**, 1384 (1979).
40. A. Gurevich, D. Anderson, and H. Wilhelmsson, Phys. Rev. Lett. **42**, 769 (1979).
41. M. A. True, J. R. Albritton, and E. A. Williams, Phys. Fluids **24**, 1885 (1981).
42. L. M. Wickens and J. E. Allen, Phys. Fluids **24**, 1894 (1981).
43. A. V. Gurevich, L. V. Pariĭskaya, and L. P. Pitaevskiĭ, Zh. Éksp. Teor. Fiz. **49**, 647 (1965) [Sov. Phys. JETP **22**, 449 (1965)].
44. C. Sack and H. Schamel, Phys. Rep. **156**, 311 (1987).
45. D. S. Dorozhkina and V. E. Semenov, Phys. Rev. Lett. **81**, 2691 (1998).
46. V. F. Kovalev, V. Yu. Bychenkov, and V. T. Tikhonchuk, Pis'ma Zh. Éksp. Teor. Fiz. **74**, 12 (2001) [JETP Lett. **74**, 10 (2001)].
47. V. F. Kovalev, V. Yu. Bychenkov, and V. T. Tikhonchuk, Zh. Éksp. Teor. Fiz. **122**, 264 (2002) [JETP **95**, 226 (2002)].
48. V. F. Kovalev, V. V. Pustovalov, and D V. Shirkov, J. Math. Phys. **39**, 1170 (1998).
49. V. Yu. Bychenkov, D. Batani, G. I. Dudnikova, *et al.*, in *Book of Abstracts of the 11th International Conference on Laser Optics, St. Petersburg, 2003*, p. 29.
50. P. Mora, Phys. Rev. Lett. **90**, 185002 (2003).
51. A. G. Zhidkov, A. Sasaki, I. Fukumoto, *et al.*, Phys. Plasmas **8**, 3718 (2001).
52. Y. Sentoku, V. Yu. Bychenkov, K. Flippo, *et al.*, Appl. Phys. B **74**, 207 (2002).
53. G. I. Dudnikova, V. Yu. Bychenkov, A. Maksimchuk, *et al.*, Phys. Rev. E **67**, 026416 (2003).
54. Y. Sentoku, H. Ruhl, K. Mima, *et al.*, Phys. Plasmas **6**, 2855 (1999).
55. G. S. Sarkisov, V. Yu. Bychenkov, V. N. Novikov, *et al.*, Phys. Rev. E **59**, 7042 (1999).
56. A. Pukhov, Z. M. Sheng, and J. Meyer-ter-Vehn, Phys. Plasmas **6**, 2847 (1999).
57. E. L. Clark, K. Krushelnick, M. Zepf, *et al.*, Phys. Rev. Lett. **85**, 1654 (2000).
58. V. Yu. Bychenkov, V. Rozmus, A. Maksimchuk, *et al.*, Fiz. Plazmy **27**, 1076 (2001) [Plasma Phys. Rep. **27**, 1017 (2001)].
59. V. F. Kovalev and V. Yu. Bychenkov, Phys. Rev. Lett. **90**, 185004 (2003).
60. R. Decoste and B. H. Ripin, Phys. Rev. Lett. **40**, 34 (1978).
61. M. Allen, Y. Sentoku, P. Audebert, *et al.*, Phys. Plasmas **10**, 3283 (2003).
62. V. Yu. Bychenkov, Y. Sentoku, S. V. Bulanov, *et al.*, Pis'ma Zh. Éksp. Teor. Fiz. **74**, 664 (2001) [JETP Lett. **74**, 586 (2001)].
63. D. Umstadter, Phys. Plasmas **8**, 1774 (2001).
64. S. Karsch, D. Habs, T. Schatz, *et al.*, Laser Part. Beams **17**, 565 (1999).
65. T. Tajima and J. M. Dawson, Phys. Rev. Lett. **43**, 267 (1979).
66. http://musr.triumf.ca.
67. S. V. Bulanov, V. A. Vshivkov, G. I. Dudnikova, *et al.*, Fiz. Plazmy **23**, 284 (1997) [Plasma Phys. Rep. **23**, 259 (1997)].
68. S. V. Bulanov, V. A. Vshivkov, G. I. Dudnikova, *et al.*, Fiz. Plazmy **25**, 764 (1999) [Plasma Phys. Rep. **25**, 701 (1999)].

Plasma Physics Reports, Vol. 30, No. 6, 2004, pp. 496–518. Translated from Fizika Plazmy, Vol. 30, No. 6, 2004, pp. 541–562.

PLASMA ELECTRONICS

Hybrid Microwave Oscillators with a Virtual Cathode

A. E. Dubinov*, I. A. Efimova*, K. E. Mikheev*, V. D. Selemir*, and V. P. Tarakanov**

**All-Russia Research Institute of Experimental Physics, Russian Federal Nuclear Center, Sarov, Nizhni Novgorod oblast, 607188 Russia*

***Institute for High Energy Densities, Associated Institute for High Temperatures, Russian Academy of Sciences, Izhorskaya ul. 13/19, Moscow, 125412 Russia*

Received June 18, 2003; in final form, September 1, 2003

Abstract—A review is given of the developments and theoretical investigations of a fundamentally new class of microwave devices, namely, hybrid microwave oscillators with a virtual cathode, which combine the useful properties of virtual cathodes with the advantages of those traditional microwave oscillators that operate with subcritical-current beams and have a high efficiency in generating ultrarelativistic electron beams. Among such devices are the following: a hybrid diffractional microwave oscillator with a virtual cathode, a hybrid gyrodevice with a virtual cathode, a hybrid beam–plasma vircator, a hybrid gyrocon with a virtual cathode, a hybrid Cherenkov oscillator with a virtual cathode, a hybrid microwave oscillator of the "vircator + traveling-wave tube" type, an original two-beam tube with a virtual cathode, and a klystron-like vircator. © *2004 MAIK "Nauka/Interperiodica".*

1. INTRODUCTION

Microwave oscillators with a virtual cathode (VC), such as vircators, reflex triodes, and reditrons [1–3], constitute a special class of devices whose operation requires that the electron beam current be higher than the vacuum limiting current. Unlike this class of devices, the oscillators of other classes are capable of operating only with electron beam currents below the vacuum limit. That is why only microwave oscillators with a VC can be regarded as truly high-current devices: it is in these oscillators that a power level of several tens of gigawatts (22 GW [4]) has been achieved.

However, in a recent paper [5], Selemir *et al.* analyzed their own experimental results and a great deal of data from the literature. On the basis of this analysis, they found that, at ultrarelativistic electron energies (the relativistic factor being $\gamma \gg 1$), the operation efficiency of a microwave oscillator with a VC becomes low (less than 1%).

In this connection, it seems worthwhile to combine the useful properties of VCs with the advantages of those traditional microwave oscillators that operate with subcritical-current beams and have a high efficiency in generating microwaves with ultrarelativistic electron beams. About three years ago, this idea led us to recognize that it is necessary to design and develop a fundamentally new class of microwave devices—hybrid microwave oscillators with a VC. In recent years, more than ten types of hybrid oscillators have been developed in which a vircator is combined with such traditional devices as a traveling-wave tube (TWT), a klystron, a beam–plasma oscillator, a diffractional oscillator, a two-beam tube, and others. Here, we review the ideas and results of theoretical studies of most of the viable oscillator schemes, some of which have already been successfully tested in experiments.

Before proceeding to a description of particular schemes, let us consider the general principles of developing hybrid microwave oscillators with a VC in the context of the useful properties of VCs:

(i) The electron density in a VC is, as a rule, higher than that in other beam cross sections by one order of magnitude or more.

(ii) The position of the VC oscillates in time with a frequency of about $\sim 2\omega_p$.

(iii) The potential of the VC also oscillates in time with a frequency of about $\sim 2\omega_p$, which leads to a deep modulation of the transmitted electron beam.

(iv) The VC reflects some of the beam electrons, thereby giving rise to an additional two-beam interaction.[1]

Note that, in a klystron buncher, the beam is first modulated in velocity and then (after passing through the drift tube) in density. In contrast, the VC immediately results in the density modulation of both the transmitted and reflected electron beams [7, 8]. It is preferable to modulate an ultrarelativistic beam by a VC because modulation by a klystron can only be provided with very long drift tubes or else laborious efforts are required to shorten them [9].

[1] It should be noted that, at present, considerable research is being carried out in the new field of microwave electronics—vacuum–solid-state microwave electronics, which is predominantly based on the ideas and methods of traditional vacuum microwave electronics [6]. An important point is that the principles of operation of this new generation of devices are supposed to have much in common with those of hybrid microwave oscillators with a VC.

1063-780X/04/3006-0496$26.00 © 2004 MAIK "Nauka/Interperiodica"

Properties (i) and (ii) can be used to excite open and closed cavities. Hybrid devices in which the cavity is excited by a VC oscillating about a fixed position are the subject of Section 2. Along with a conventional vircator and a conventional reflex triode, this class of devices, in our opinion, includes a hybrid diffractional microwave oscillator with a VC (Section 2.1), hybrid gyro-devices with a VC (Section 2.2), and a hybrid beam–plasma vircator (Section 2.3).

If a VC were set into translational motion, it would be capable of exciting electrodynamic structures and cavities. Devices in which a VC executes translational motion are dealt with in Section 3. This principle of operation may underlie the performance of a hybrid gyrocon with a VC (Section 3.1), which makes use only of property (i). If a VC were set into superluminal motion, it, being an extremely dense electron formation, could be used to achieve Cherenkov generation. This principle may underlie the operation of a hybrid Cherenkov oscillator with a VC (Section 3.2).

In traditional schemes, use is often made of the two-section structure of a microwave oscillator, in which the first section plays the role of a modulator or a buncher of the beam, while the second section plays the role of a shaper of radiation (Section 4). In hybrid microwave oscillators with a VC, the function of the vircator may be twofold. In a hybrid microwave oscillator of the "vircator + TWT" type (Section 4.1) and in an original two-beam tube (Section 4.2), property (iii) of the VC allows it to function as a modulator of the beam. In a klystron vircator (Section 4.3), property (iv) enables the VC to act as a shaper of radiation.

Almost all of the hybrid microwave oscillators considered in the present review were developed and designed at the Russian Federal Nuclear Center All-Russia Research Institute of Experimental Physics (RFNC-ARRIEP). The oscillators reviewed here were analyzed theoretically using the KARAT code (a fully self-consistent, relativistic electromagnetic computer code) [10].

Since hybrid microwave oscillators with a VC have only recently been recognized as providing a new direction in microwave electronics, they have received little experimental study. The first such hybrid device—a virtod, or a hybrid of a vircator and a backward-wave tube (BWT)—went into operation at the Kharkov Institute for Physics and Technology (KIPT) [11], and was followed by a hybrid device (klystron + vircator) at the Moscow Engineering Physics Institute (MEPI) [12] and a virtod (vircator + TWT) at the RFNC-ARRIEP [13].

2. HYBRID MICROWAVE OSCILLATORS BASED ON THE EXCITATION OF THE CAVITY BY AN OSCILLATING VIRTUAL CATHODE

2.1. Hybrid Diffractional Microwave Oscillator with a Virtual Cathode

At present, diffractional microwave oscillators (DMOs) serve as the main tool for generating centimeter and millimeter radiation [14]. The principle of operation of such oscillators is based on the passage of an electron beam along a diffraction grating placed in a multimode cavity and on the interaction of the beam with a diffracted field, with the result that the beam is modulated and the radiation is amplified. A particularly important point here is that the radiative instability can only be achieved by modulating an electron beam and by passing its denser parts through the decelerating phases of the electromagnetic field. It should be noted that, in quite a number of operating regimes, a DMO cannot be tuned to achieve the radiative instability.

In some cases, this drawback can be overcome by using self-modulating beams, in which case the direct transfer of energy from the beam to the field can be realized by proper phasing. Under certain conditions, the role of such beams may be played by drifting electron beams with a VC.

Now we return briefly to the mechanism for self-modulation of an electron beam: because of the periodic variations in the height of the potential barrier near a VC, the VC alternately transmits and reflects the beam electrons; as a result, the transmitted beam is fully modulated at the frequency of VC oscillations, and the reflected beam is modulated in the same manner but is in antiphase with the transmitted beam.

Oscillators whose operation is based on the extraction of energy from a modulated transmitted beam (e.g., during the excitation of klystron cavities) are well known in microwave technology. Electron beams with a VC also seem to be a promising means of exciting DMO cavities.

There are several versions of the design and manufacture of DMOs based on beams with a VC:

(i) the VC is formed in an individual equipotential cavity and a modulated transmitted beam is injected into the DMO cavity through a grid;

(ii) the VC is formed after the beam has left the DMO cavity, in which case the cavity is excited by the modulated beam reflected from the VC; and

(iii) the VC is formed immediately inside the DMO cavity.

Let us briefly discuss these versions. The first one is of interest because the VC can be formed in a small high-quality cavity, thereby providing a monochromatic modulation of the transmitted beam current. This circumstance is important for the fine tuning of the DMO. However, the limiting current for the formation of a VC in the DMO cavity can turn out to be much lower than that required to form a VC in a small cavity.

As a result, in the DMO cavity, an additional "parasitic" VC may form that executes asynchronous oscillations and thereby destroys the monochromatic regime of microwave generation.

The second possible version of the implementation of DMOs is similar in design to the reflex DMOs known in the literature [14]. A particularly important point in this version is that the VC should be formed after the injected beam has passed through the cavity; this, in turn, requires that the limiting current for the cavity be higher than the current of the injected beam. The limiting current in the DMO cavity is usually low because of its large size; this is why it is fairly difficult to form a VC behind the DMO cavity. This difficulty can be overcome by installing an electrostatic reflector behind the DMO cavity, just as is done in reflex DMOs. However, the VC formed in such a decelerating electrostatic field [3] does not oscillate and the reflected electron beam is unmodulated. In addition, if the current of the injected beam in the DMO cavity is close to the limiting current, then the reflected beam gives rise to a VC immediately inside the cavity.

Hence, a serious shortcoming of the first two versions is that, at high beam currents, parasitic VCs have a high probability of being formed in an uncontrolled manner within the DMO cavity. As a result, we arrive at the third version, i.e., at the idea of the intentional formation of a VC inside the DMO cavity.

We carried out computer simulations of the operation of the first and third versions of a DMO excited by a beam with a VC (there was no need to simulate the second version because the results of thorough numerical investigations of reflex DMOs have already been presented in the literature).

The geometric representations of the first and third versions of a DMO with a VC are shown, respectively, in Fig. 1a and Fig. 2a, in which all dimensions used in our computations are indicated. Both versions were simulated in the (x, z) coordinates under the assumptions that the system is uniform in the y direction and that the cavities are affected by a strong magnetic field of 50 kG directed along the z axis.

DMO cavities were modeled in the form of a closed cavity bounded by conducting walls. One of the walls is a diffraction grating in the form of a periodic structure of ripples with square shape that are capable of reradiating a substantial amount of microwave energy in the vertical direction. The parameters of the structure are as follows: the height of the ripples is 0.5 cm, the width of the ripples is 1 cm, and the ripple period is 2 cm. The opposite wall is a focusing mirror. The side walls of the cavity are plane grids that are transparent to electrons and act as a mirror-reflecting surface for an electromagnetic wave. In the first version of a DMO with a VC, a small cavity in which an additional VC forms is adjacent to the left wall of the main cavity (Fig. 1a). The calculations were carried out on a 51×101 mesh, with 10 mesh points on the period of the diffraction grating.

An electron beam begins to be injected into the small cavity of a DMO (in the first version) or into the DMO cavity (in the second version) at the time $t = 0$. The linear beam current density (along the y axis) has a magnitude of 2.5 kA/cm and is constant in time, the beam energy is 100 eV, and the beam width is 1 cm.

The accuracy of the computations described below was monitored by checking the energy balance: the error did not exceed 2%.

An instantaneous phase diagram of an electron beam in the system with an additional small cavity is presented in Fig. 1b, which shows that, as we feared, two VCs do indeed form in the beam (one in the small cavity of the DMO and the other in the main cavity).

Figure 2b displays the phase diagram of an unmodulated electron beam some time after it has been injected into the DMO cavity. The structure of the phase diagram allows us to conclude that the VC in the DMO cavity has been formed in the desired fashion.

In our simulations, we investigated the modulation of the transmitted electron beam in the cross section shown by the light dashed line in Fig. 2a. The calculated time evolution of the beam current is given in Fig. 3.

The dynamics of accumulation of the electromagnetic energy (or, more precisely, of the electric and magnetic energies) in the DMO cavity is shown in Fig. 4, from which we can see that, over a long time, the total energy density (uniform in the y direction) increases substantially, reaching a value of more than 10 J/cm.

The curious spatiotemporal dynamics of the electromagnetic energy in the cavity is illustrated in Fig. 5, which displays the instantaneous distributions of the electromagnetic energy density, calculated for times separated by an interval of 0.1 ns. The unsteady pattern of the distributions provides evidence of the stochastic (turbulent) nature of the interaction of the electron beam with a VC and with the field in the cavity. Against the background of the turbulence, however, solitary waves of the electromagnetic energy density are observed that run along the cavity toward the circular mirror and back from it; these waves can be utilized by correctly choosing the position of the energy extraction unit.

In simulations, we varied the parameters of the electron beam and of the diffraction grating, with the result that the total electromagnetic energy in the cavity was proportional to the beam energy.

Hence, our model simulations of a DMO with a VC have demonstrated that the third version of the oscillator is workable and holds promise for operating with moderately relativistic electron beams.

The concept of a DMO with a VC above the diffraction grating was first proposed by Dubinov and

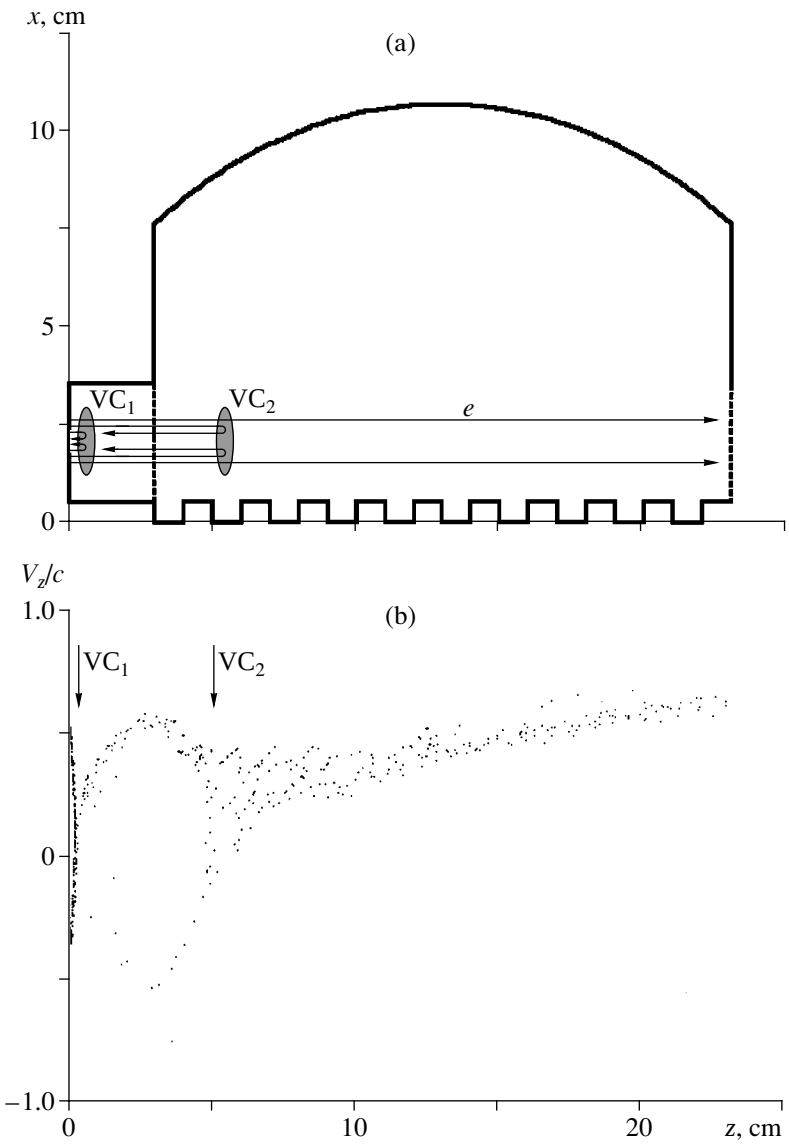

Fig. 1. Simulation of the first version of a DMO: (a) geometry of the device (the symbols $VC_{1,2}$ refer to the virtual cathodes, and the arrows indicate the electron trajectories), and (b) phase portrait of the beam.

Mikheev [15], who also presented the results of the irrelevant simulations.

2.2. Hybrid Gyro-Devices with a Virtual Cathode

Here, we discuss the following idea: if the electrons in the output cavity of a microwave oscillator were set in rotational motion, then it might be expected that the efficiency of energy transfer from the beam to the radiation would increase substantially, provided that the rotation rate of the electrons coincides with their bounce frequency in the potential well between the emitting cathode and the VC.

In the context of the implementation of this idea, we considered two schemes based on the formation of a nonuniform axisymmetric magnetic field within the region where the beam interacts with the electrodynamic structure.

The first scheme—a hybrid cusptron with a VC—assumes the formation of a magnetic cusp in the region behind the VC, in which case the cusp changes the longitudinal motion of the transmitted beam into rotational motion [16].

We studied the hybrid cusptron by simulating its operation and searching for the optimum distance between the VC and the magnetic cusp at which the radiation power is maximum.

The geometric representation of the first scheme of a cusptron is shown in Fig. 6, in which all the dimensions used in our computations are indicated.

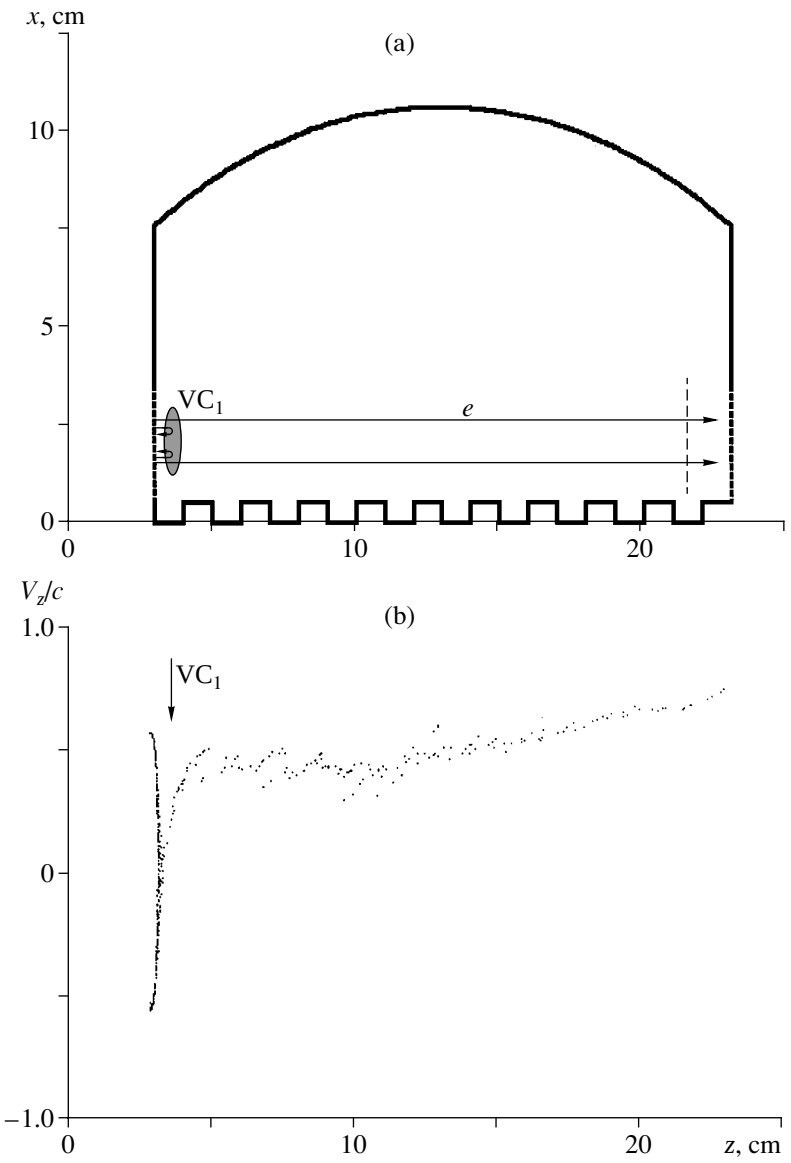

Fig. 2. Simulation of the third version of a DMO: (a) geometry of the device (the symbol VC_1 refers to the virtual cathodes, the arrows indicate the electron trajectories, and the light dashed line shows the cross section for which the time evolution of the current was calculated), and (b) phase portrait of the beam.

The simulations were carried out under the following assumptions. The system is influenced by an axial magnetic field with a strength of 5 kG, which decreases linearly within the cusp to a strength of –5 kG on a spatial scale of 1 cm. Near the output window (34 cm < z < 40 cm), the magnetic field also varies linearly: it increases from –5 kG to zero, thereby ensuring that the transmitted electrons are lost at the wall of the drift tube of the device in order to close the reverse-current conductor and to prevent the electrostatic charging of the exit window and its damage. In the first step of the calculations, the code evaluated the magnetic field distribution over the entire length of the system from a given on-axis magnetic field configuration by numerically solving the equation $\nabla \mathbf{H} = 0$. The geometry of the magnetic field lines is also presented in Fig. 6.

It is assumed that a rectangular high-voltage pulse of amplitude 1.5 MV is applied to the cathode and causes it to emit an electron current of 10 kA, which is high enough for the formation of a VC.

The evolution of the power of the generated microwave radiation was followed within a time interval of 10 ns by calculating the flux of the Poynting vector field in a cross section lying between the window for extracting radiation and the place where the transmitted electrons are lost at the wall of the drift tube (in Fig. 6, this cross section is indicated by the dashed vertical line at

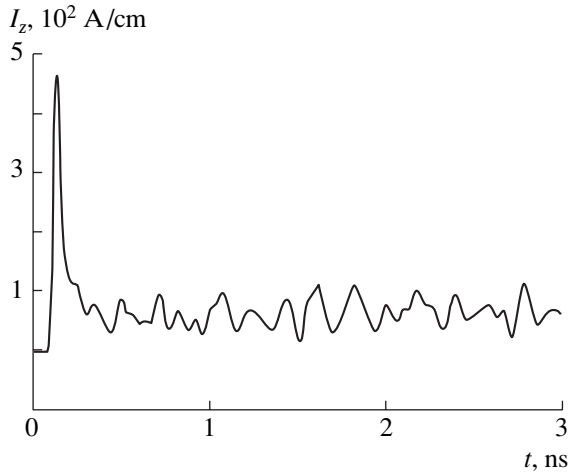

Fig. 3. Time evolution of the current in a DMO.

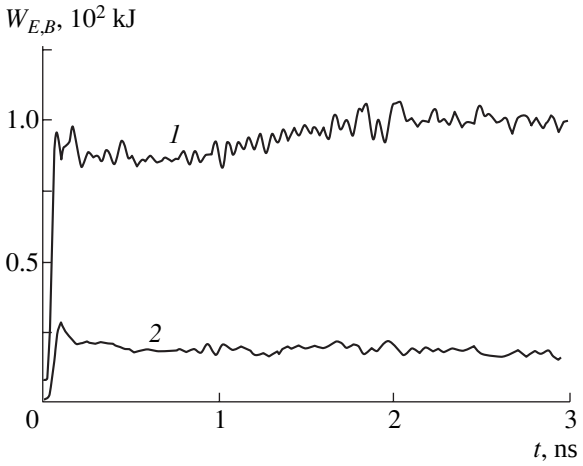

Fig. 4. Dynamics of the electromagnetic energy accumulation in a DMO cavity: (*1*) the energy of the electric component of the electromagnetic field W_E and (*2*) the energy of the magnetic component W_B.

z = 39 cm). A typical calculated time evolution of the radiation power is demonstrated in Fig. 7.

The generated microwave power was calculated for different distances between the VC and the cusp (the longitudinal coordinate of the cusp was varied from 10.5 cm to 30.5 cm with a spatial step of 0.5 cm). Figure 8 shows the averaged (over a time of 10 ns) output power calculated as a function of the coordinate of the cusp center. For comparison, the dashed line shows the power generated in a conventional vircator without a cusp. From Fig. 8, we can see that a hybrid cusptron is less efficient than a vircator. Simulations carried out for other values of the parameters of the problem (the varied parameters being the accelerating voltage, the beam

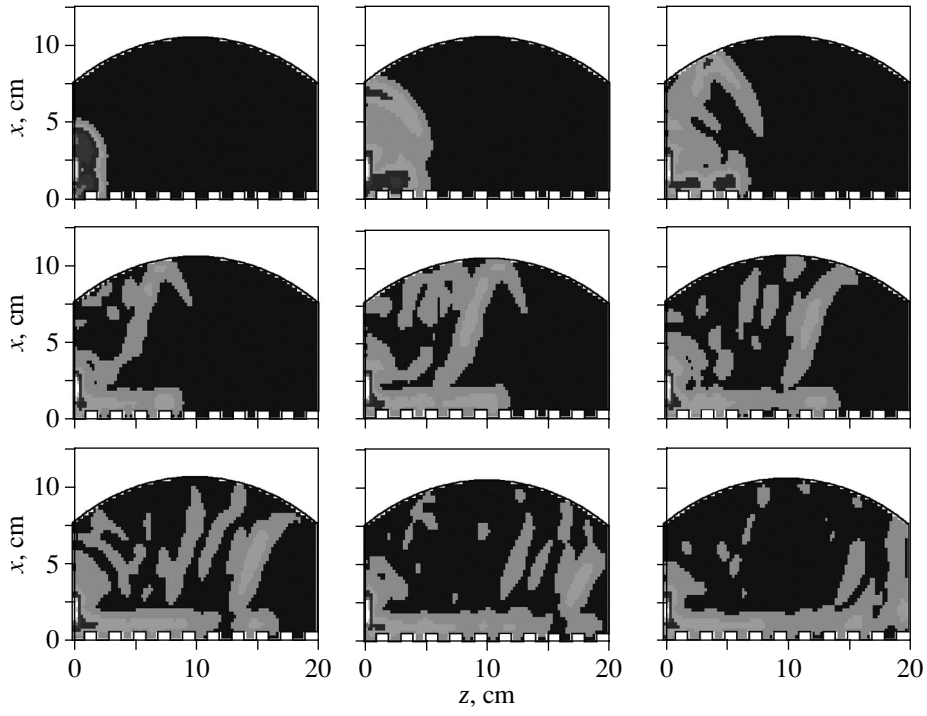

Fig. 5. Instantaneous distributions of the electromagnetic energy density in a DMO cavity, calculated for times separated by an interval of 0.1 ns. The energy density is higher in the lighter regions. The time increases from left to right and from top to bottom.

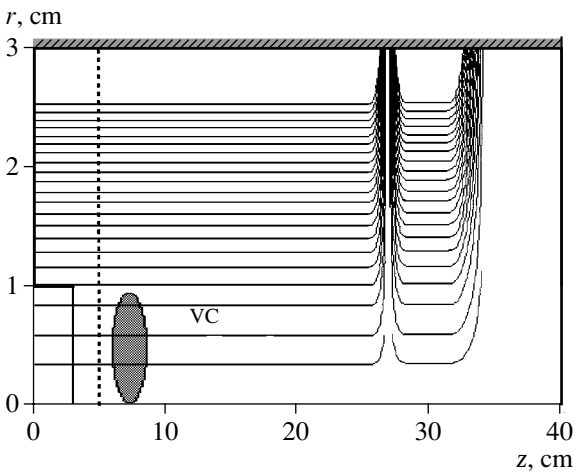

Fig. 6. Calculated configuration of a hybrid cusptron with a VC.

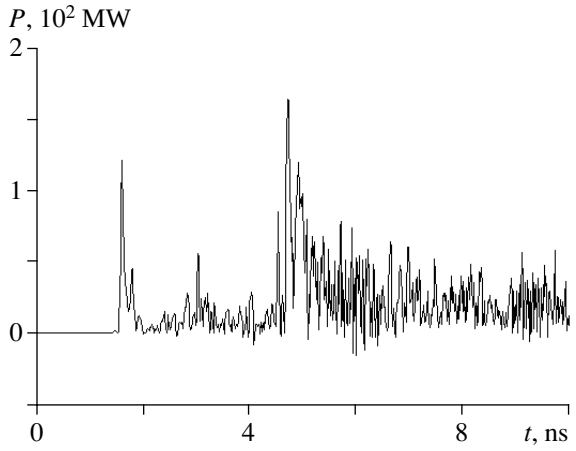

Fig. 7. Typical example of the time evolution of the microwave power generated by a hybrid cusptron with a VC, calculated for the cross section shown by the light vertical dashed line in Fig. 6. The average output power is equal to $\langle P \rangle = 18.717$ MW.

current, and the magnetic field gradient in the cusp) produced a similar result.

The second scheme assumes the formation of a nonuniform magnetic field in the potential well between the emitting cathode and the VC, in which case the magnetic cusp acts to change the longitudinal motion of both the injected and reflected beams into rotational motion. This scheme, which was proposed ten years ago by Selemir *et al.* [17], was also mentioned in [18, 19] and was investigated in [20]. Recall that the original idea of this scheme was based on other assumptions.

Kwan and Snell [21] proposed a novel concept for a vircator—a reditron (a term derived from the words "reflex electron discrimination tube," which is based essentially on the discrimination of the electrons reflected from the VC so that the diode is left unperturbed. Kwan and Snell thought that this discrimination should increase the generation efficiency. However, in [22, 23], it was shown that this way does not provide feedback in the microwave oscillator and leads to the disruption of the radiative instability. That is why, in developing the reditron concept, Selemir *et al.* [17] proposed a reditron in which not all of the reflected electrons are discriminated but only the ones of lower energy, which have already transferred their energy to radiation and lost their synchronous nature. The required sorting of electrons in the "emitting cathode–anode grid–VC" region can be provided by a potential well created in this region by an externally applied longitudinal magnetic field with a minimum at the anode grid.

However, the objective of our simulations was to investigate a broader problem, namely, how the generation characteristics of the vircator depend on the presence of a magnetic field minimum and of a magnetic field maximum in the interaction region. It was found that the change of the translational motion of the beam electrons into rotational motion has a greater effect than does the discrimination of the lower energy electrons.

The geometric representation of a vircator with a nonuniform magnetic field is shown in Fig. 9, in which all dimensions used in our computations are indicated.

The simulations were carried out under the following assumptions. The system is in an axial magnetic field with a strength of 5 kG, which decreases linearly to zero near the exit window ($25 < z < 27$ cm) to ensure that the transmitted electrons are lost at the wall of the drift tube. By using an additional solenoid (or by other means), it is possible to create a magnetic field nonuniformity in the interaction region between the emitting cathode and the VC. The configuration of the nonuniform magnetic field in this region was chosen as follows: the field increases linearly along the system axis

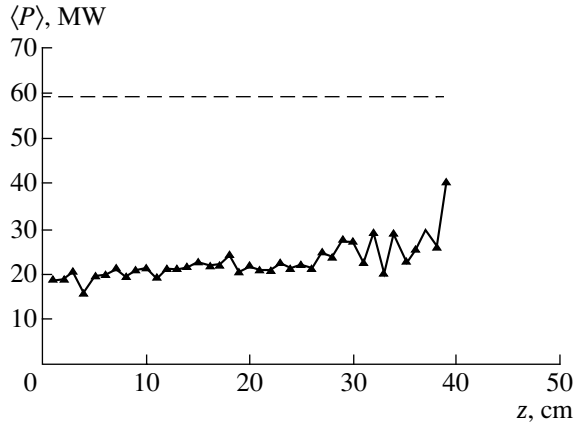

Fig. 8. Average microwave power generated by a hybrid cusptron with a VC as a function of the coordinate of the cusp center (the dashed line shows the averaged power in a conventional vircator without a cusp).

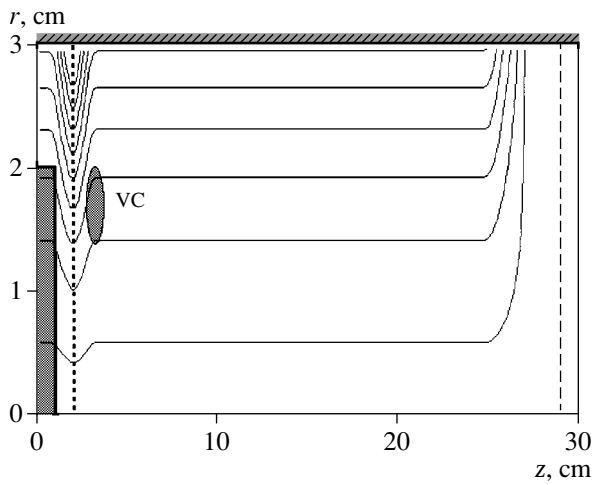

Fig. 9. Configuration of a vircator with a nonuniform magnetic field in the potential well between the cathode and the VC.

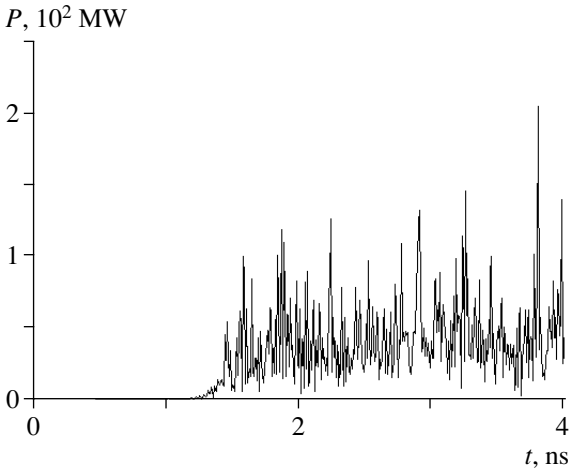

Fig. 10. Typical example of the time evolution of the microwave power generated by a vircator with a nonuniform magnetic field. The average output power is equal to $\langle P \rangle$ = 10.942 MW.

from the emitting cathode to the anode grid and then it decreases linearly from the anode grid to the VC, at which it takes on the same value as at the emitting cathode. The geometry of the lines of a nonuniform magnetic field with a maximum at the anode grid is also presented in Fig. 9.

It is assumed that the cathode emits an electron current of 15 kA under the action of a 200-kV rectangular high-voltage pulse.

The evolution of the power of the generated microwave radiation was followed within a time interval of 5 ns by calculating the flux of the Poynting vector field in a cross section lying between the window for extracting radiation and the place where the transmitted electrons are lost at the wall of the drift tube (in Fig. 9, this cross section is indicated by the light dashed vertical line at z = 29 cm). A typical calculated time evolution of the radiation power is demonstrated in Fig. 10.

The generated microwave power was calculated for different magnetic fields at the anode grid (the field strength was varied over the range 2–11 kG). Figure 11 shows the averaged (over a time of 5 ns) output power computed as a function of the magnetic field strength at the anode grid.

It follows from this figure that, when the magnetic field has a minimum in the range of 2–4 kG, the generated microwave power is almost five times higher than that in a conventional vircator with a uniform magnetic field. In this case, we are actually dealing with the loss of lower energy electrons at the anode tube (i.e., with the regime of a reditron with the discrimination of the lower energy electrons). Moreover, it was found that fast electrons in this nonuniform magnetic field acquire a significant rotational motion in the transverse direction, which favors the generation of the TE mode by the electron cyclotron motion, as in the case considered in [24]. For a weaker magnetic field at the anode (from 0 to 2 kG), all electrons escape from the interaction region before reaching the anode grid and, consequently, do not generate microwaves.

When the magnetic field has a maximum in the range of 6–8 kG, the generated microwave power is nearly three times higher than the power generated in a conventional vircator with a uniform magnetic field. In this case, as expected, the only effect is that associated with the electron cyclotron motion, while the escape of the lower energy electrons has no effect. For maximum magnetic field strengths above 8 kG, the VC does not form and the oscillator operates as a gyro-device at a power level about two times higher than that in a vircator with a uniform magnetic field.

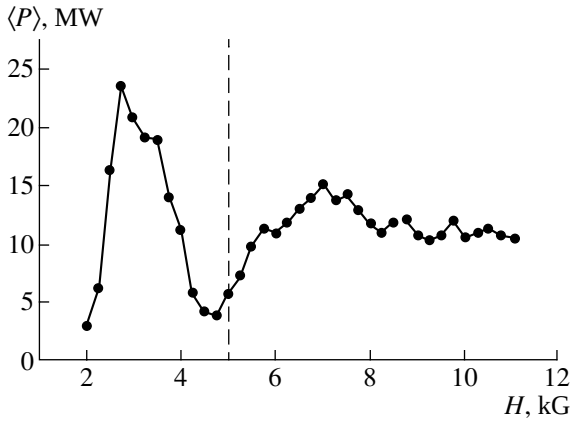

Fig. 11. Average microwave power generated by a vircator with a nonuniform magnetic field as a function of the magnetic field strength at the anode grid (the dashed line refers to the case of a uniform magnetic field).

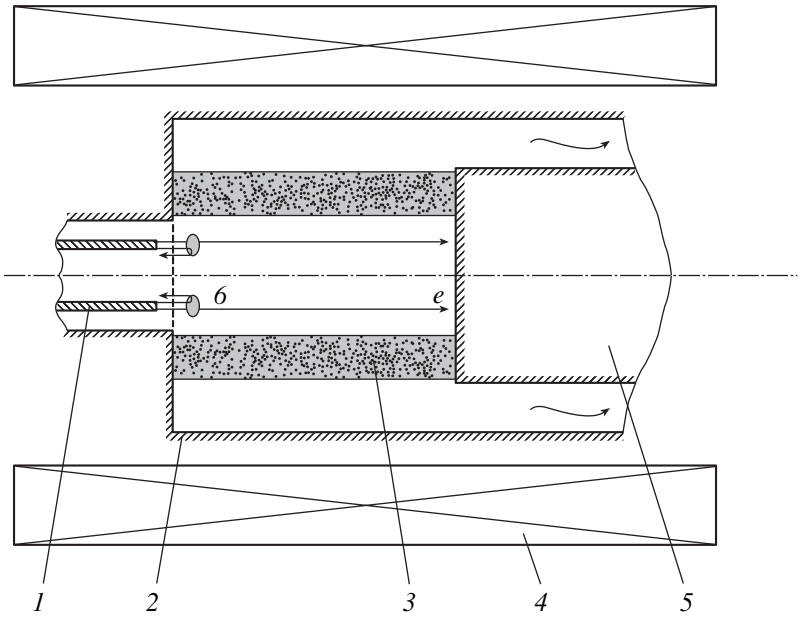

Fig. 12. Schematic of a beam–plasma vircator: (*1*) cathode, (*2*) anode, (*3*) plasma, (*4*) magnetic-field solenoid, (*5*) collector, and (*6*) virtual cathode. The right arrows indicate the electron trajectories, and the wavy arrows show the direction in which the generated radiation is extracted.

Hence, we have shown that, by applying a nonuniform magnetic field to the interaction region, it is possible to increase both the generated microwave power and the generation efficiency, regardless of whether the nonuniform magnetic field has a minimum or a maximum.

2.3. Beam–Plasma Vircator

Beam–plasma oscillators occupy an important place in relativistic microwave electronics [25]. The main advantage of this type of oscillator is that it provides continuous electronic control of the generated power spectrum by changing the electron plasma density and/or the plasma geometry, in contrast to the mechanical control in vacuum oscillators. Up to now, however, a study has been made only of low-current beam–plasma oscillators operating with electron beam currents far below the vacuum limiting current.

At the same time, as was mentioned in the Introduction, vacuum vircators capable of generating microwave power at a very high level have found widespread application in high-power microwave electronics.

Based on an analysis of the above advantages of the beam–plasma oscillators and vircators, we arrived at the idea of combining an overcritical-current electron beam and an electrodynamic plasma structure in one device—a beam–plasma vircator [26]—in order to provide electronic control of the generated power spectrum over a wide parameter range while simultaneously achieving the highest possible generation efficiency.

We carried out computer simulations of the operating regimes of a beam–plasma vircator. A geometric representation of the vircator, similar to that of a low-current beam–plasma oscillator [27], is shown in Fig. 12. The vircator was modeled as a "cathode–anode–collector" coaxial system under the following assumptions. The cathode emits an annular electron beam with a diameter of 2 cm, the wall thickness being 0.5 cm. The anode is composed of two adjacent tubular sections: the diameter of the diode section is 3 cm, and the diameter of the beam drift section is 14 cm. The anode grid installed at the contact between the anode sections is transparent to electrons. The distance between the cathode edge and the anode grid is 0.5 cm. At the exit side of the vircator, there is a collector 10 cm in diameter, which, together with the anode, form an output feeder with a wave impedance of 20 Ω. The length of the drift region is 10 cm. The entire system is in a strong external longitudinal (directed along the *z* axis) magnetic field of 50 kG.

In the drift region, a magnetized electron beam propagates within a preformed collisionless electron–ion plasma. The outer diameter of the annular plasma cylinder is 10 cm, the thickness of the cylinder wall being 2 cm. The beam and the plasma were both modeled by a particle-in-cell method.

A rectangular high-voltage pulse with an amplitude of –100 kV and a duration of 10 ns is applied to the cathode. The anode and the collector are both held at a zero potential. Under these conditions, the cathode emits an electron beam with a current of 10 kA.

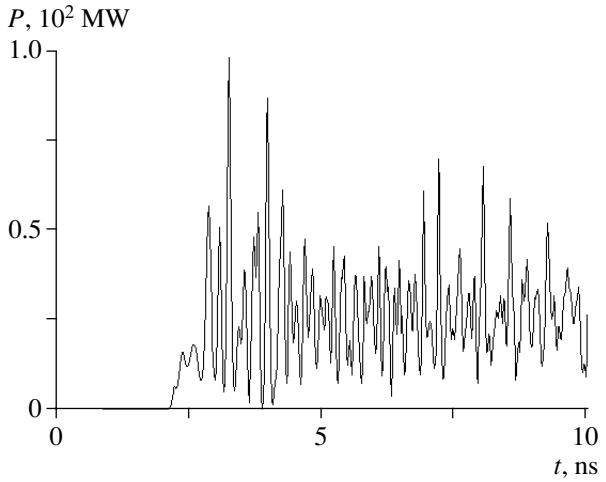

Fig. 13. Typical example of the calculated time evolution of the output power of a beam–plasma vircator. The average output power is equal to $\langle P \rangle = 15.93$ MW.

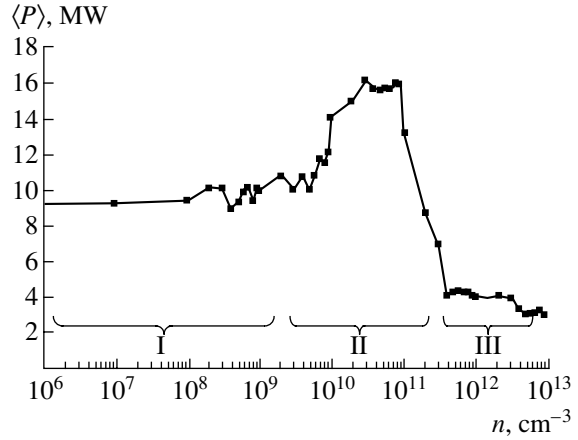

Fig. 14. Averaged (over a time of 10 ns) output power as a function of the plasma density (I) in the regime of a vacuum vircator, (II) in the regime of a beam–plasma vircator, and (III) in the cutoff regime.

The output power of the vircator was evaluated from the flux of the Poynting vector field in the output feeder, where there are no beam electrons and plasma particles. A typical calculated time evolution of the radiation power in the feeder is given in Fig. 13.

In order to compare a beam–plasma vircator with a conventional vacuum vircator, we calculated the averaged (over a time of 10 ns) output power as a function of the plasma density in the range from 0 to 10^{13} cm^{-3}. The results of these calculations are illustrated in Fig. 14.

An analysis of the dependence displayed in this figure shows that there are three characteristic regions: region I (from about 0 to 10^9 cm^{-3}), which corresponds to the operation of a vacuum vircator at a moderate mean power of 9 MW; region II (from 10^9 to 10^{11} cm^{-3}), which corresponds to the operation of a beam–plasma vircator at an elevated power level of 17 MW; and region III (above 10^{11} cm^{-3}), in which the leading-out feeder is screened from the VC by the plasma and which thus corresponds to the cutoff regime.

Hence, we can conclude that the use of an annular plasma waveguide in the beam drift region in a vircator promotes a substantial increase (up to a factor of 2) in the output microwave power. We emphasize that, in a beam–plasma vircator, a very important role is played by the annular plasma geometry. In this connection, we can mention a plasma vircator that was proposed in [28] and in which the drift region is entirely filled with a homogeneous plasma. Although in such a vircator, as in the vircator under analysis here, the plasma favors an increase in the limiting beam current, filling the entire drift region with an inhomogeneous plasma can lead to the difficulties that are commonly encountered in extracting microwave radiation.

3. HYBRID MICROWAVE OSCILLATORS WITH A VIRTUAL CATHODE IN TRANSLATIONAL MOTION

3.1. Gyrocon with a Virtual Cathode

Gyrocons have found wide applications as power supplies for linear accelerators of charged particles. Gyrocons are microwave oscillators consisting of the following units connected in series: a unit for forming an electron beam (an electron gun), a unit for accelerating the electron beam (an accelerating tube with a power supply), a circular beam deflection cavity with a master microwave oscillator as a power supply, a drift tube, a ring cavity connected to the drift tube through a ring slit, and an electron collector [29]. Gyrocons can also contain electrostatic deflection systems placed within the drift tube and magnets installed near the ring cavity.

The basic principle of operation of a gyrocon can be described as follows. An accelerated electron beam is passed through a circular deflection cavity with an external master power-supply microwave oscillator. The cavity deflects the beam electrons in such a way that they remain on a conical surface and move along its straight generatrices while forming a helix that is wound around the cone and whose end describes a circle coincident with the ring slit of the cavity. As a result, the point at which the beam enters the ring cavity runs along the entire ring slit over and over again, so that the entering beam electrons excite a running wave within the cavity. The electric field of the running wave decelerates the electrons and acts to convert their kinetic energy into the wave energy. The remaining energy of the electrons is dissipated in the collector.

The gyrocons described in [29] are disadvantageous in that they have a low generation efficiency. The technical problem is thus to increase the efficiency of con-

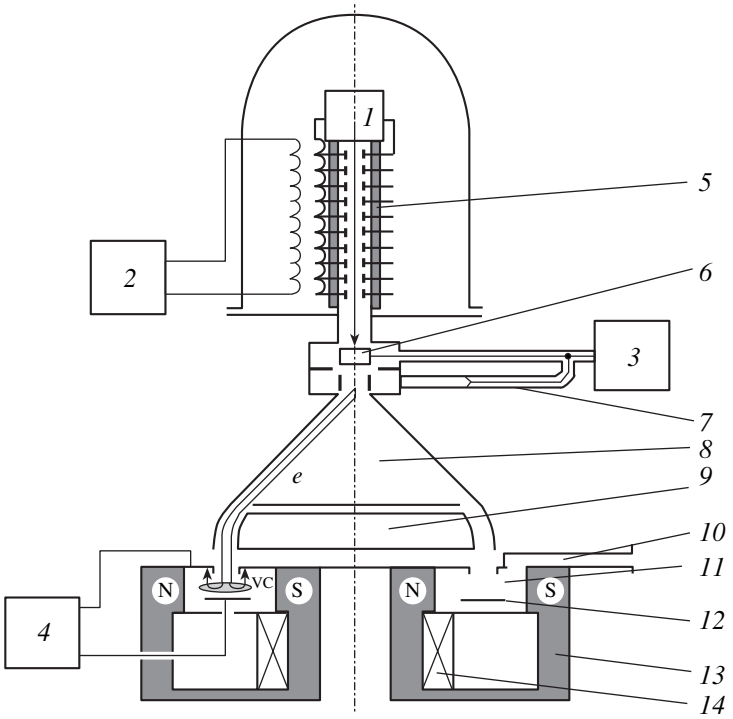

Fig. 15. Schematic of a gyrocon with a VC in which the beam is injected through the end wall of the cavity: (*1*) electron gun, (*2*) power source for the accelerating tube, (*3*) master microwave oscillator for supplying the circular beam deflection cavity, (*4*) additional voltage source, (*5*) accelerating tube, (*6*) deflector plates of the circular beam deflection cavity, (*7*) feeders, (*8*) drift tube, (*9*) electrostatic deflecting system, (*10*) output waveguide, (*11*) ring cavity, (*12*) additional electrode, (*13*) magnet core, and (*14*) magnet solenoid.

version of the kinetic energy of the electrons into the wave energy in a gyrocon.

In order to solve this problem, Dubinov *et al.* [30] proposed a new gyrocon with an additional electrode installed inside the ring cavity and connected electrically to an additional voltage source. The electric potential φ produced by this source at this electrode, relative to the wall of the ring cavity, satisfies the condition $\varphi < -W/e$, where W is the energy of the electrons at the exit from the accelerating tube and $-|e|$ is the charge of an electron.

The principle of operation of such a gyrocon is based on the fact that, in the ring cavity, the additional electrode produces a decelerating electrostatic field strong enough to stop the electrons that have entered the cavity and to reflect them back toward the entrance. This indicates the formation of a VC. As a result, within the ring cavity of the gyrocon, the formed VC runs along a circular path and excites a microwave. The generation efficiency of the gyrocon in question is higher than that of the gyrocons described in [29] because the electron density in the VC is several orders of magnitude higher than that in a conventional gyrocon.

Two design schemes of a gyrocon are shown in Figs. 15 and 16, in which we see all of the component elements of familiar gyrocons, namely: (*1*) an electron gun, (*2*) a power source for an accelerating tube, (*3*) a master microwave oscillator feeding the circular beam deflection cavity, (*5*) an accelerating tube, (*6*) deflector plates of the circular beam deflection cavity, (*7*) feeders, (*8*) a drift tube, (*9*) an electrostatic deflecting system, (*10*) an output waveguide, (*13*) the magnet core, and (*14*) the magnet solenoid. All these elements of the new gyrocon can be of the same dimensions as in conventional gyrocons, can have the same technical structure and the same physical parameters, and can be made of the same materials.

However, in the ring cavity (*11*) of the new gyrocon, there is a hermetically sealed insulated entry for applying a negative potential to an additional electrode (*12*), which can have, e.g., the form of a thin ring-shaped metal disk (Fig. 17). The role of the additional voltage source (*4*) can be played by a Marx pulsed-voltage generator. The potential applied by the voltage source (*4*) to the additional electrode (*12*) should satisfy the condition $\varphi < -W/e$, which can easily be achieved by proper control of the voltage source operation.

Since the trajectories of the electrons reflected from the VC differ from those of the electrons approaching the VC, the role of the electron collector can be played by the wall of the ring cavity (*11*), which has a ring slit. In order for this wall to be capable of functioning as a collector, it should be sufficiently massive.

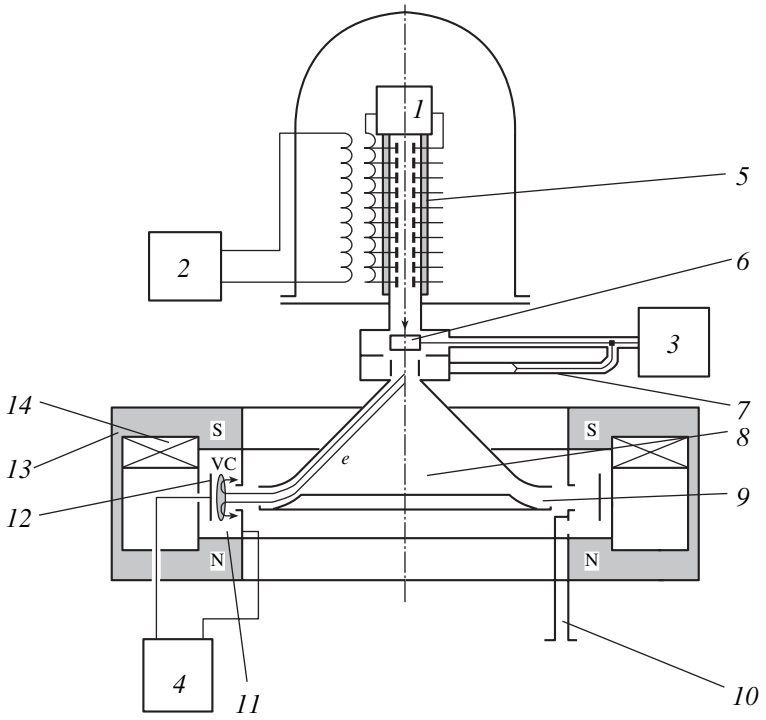

Fig. 16. Schematic of a gyrocon with a VC in which the beam is injected through the inner side wall of the cavity. The notation is the same as in Fig. 15.

The principles of operation of the new gyrocon have much in common with those of conventional ones, so that, in all gyrocons, the beam behaves in the same manner before it enters the ring cavity (*11*). However, in the new gyrocon, the beam electrons that have entered the ring cavity (*11*) experience a decelerating force in the field of the additional electrode (*12*); as a result, they come to a stop and start to move backward, forming a VC. They then reach the wall of the ring cavity (*11*) and are absorbed there.

Hence, a VC runs along the ring cavity (*11*) and excites a microwave, which is extracted from the cavity through the output waveguide (*10*). The high electron density in the VC makes it possible to solve the above technical problem.

In order to check whether or not the new idea is correct, we carried out numerical simulations of the excitation of a ring cavity in a conventional and a new gyrocon. This was done using the KARAT code under the following assumptions.

In both cases, the outer and inner radii of the ring cavity are equal to 6 and 3.5 cm, respectively. An electron beam produced by the internal electrode is injected radially, as is shown in Fig. 16. The beam parameters are as follows: the line current density is 5 A/cm, the electron energy is 511 keV, and the linear velocity of the injection spot along the surface of the internal electrode of the cavity is 2×10^{10} cm/s. In the cavity, the external magnetic field is absent.

Figures 18a and 18b show instantaneous phase diagrams of a beam in a conventional and a new gyrocon, respectively.

Instantaneous distributions of the squared azimuthal microwave electric field (which is proportional to the generation efficiency) in a conventional and a new gyrocon are shown in Figs. 19a and 19b, respectively. The microwave field strength and generation efficiency in the new gyrocon are clearly seen to be appreciably

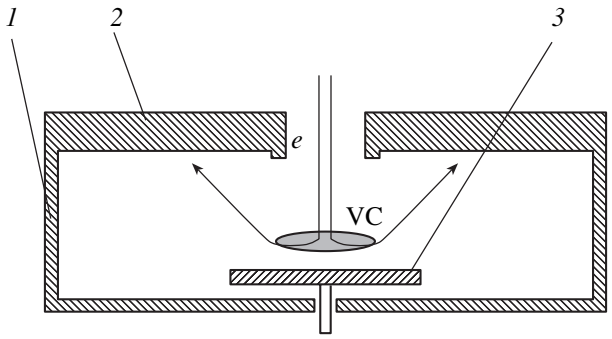

Fig. 17. Schematic of the inner part of the gyrocon cavity into which the beam is injected through the end wall: (*1*) the side wall of the ring cavity, (*2*) the cavity wall having a slit and operating as a collector, and (*3*) an additional electrode. The electron trajectories are shown by arrows.

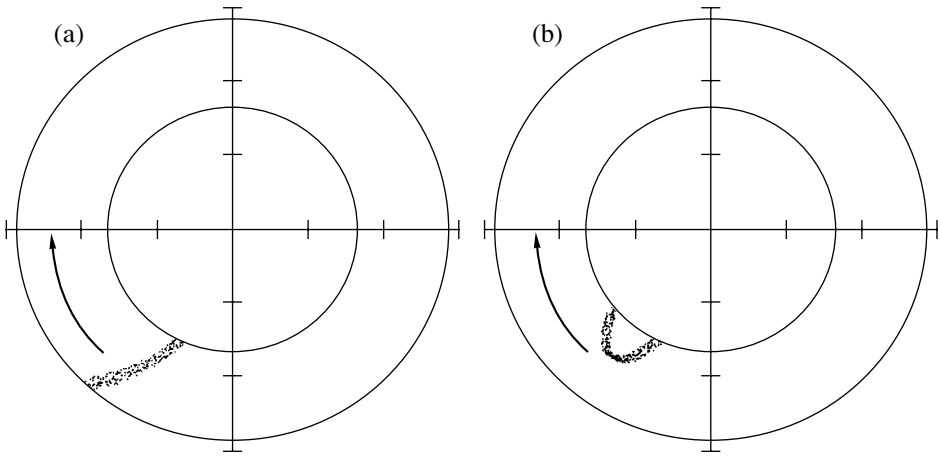

Fig. 18. Instantaneous phase portraits of an electron beam in the ring cavity into which the beam is injected through the inner side wall in (a) a conventional gyrocon and in (b) a gyrocon proposed here. The arrows indicate the direction of rotation of the beam electrons.

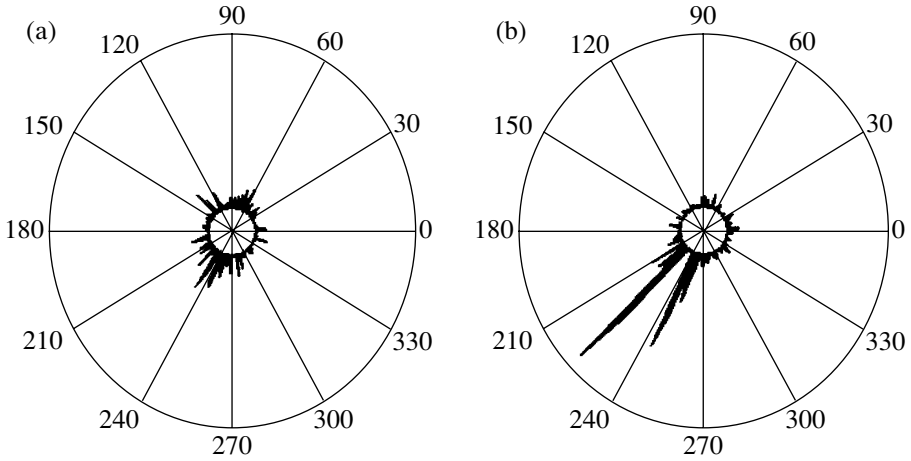

Fig. 19. Instantaneous distributions of the squared azimuthal microwave electric field (which is proportional to the generation efficiency) at the same instant as in Fig. 18 in (a) a conventional gyrocon and in (b) a gyrocon proposed here.

higher than those in the conventional gyrocon. This result confirms the correctness of the idea proposed in [30].

3.2. Simulations of a Cherenkov Oscillator with a Superluminous Virtual Cathode

Carron and Longmire (United States) [31] and Lazarev and Petrov (RFNC-ARRIEP) [32] proposed a new type of microwave oscillator supplied by a high-power flux of X radiation or γ radiation. Let us briefly explain the essence of their proposal.

When a plane wave of γ photons is incident on a plane surface such that the wave vector **k** of the incident wave makes an angle φ_0 with the normal to the surface, the "speckle" moves along the surface at a speed $v = c/\sin\varphi_0$ greater than the speed of light in free space (see Fig. 20).

The electrons that are knocked out of the surface of the plane screen by γ photons propagate predominantly in the direction of the vector **k**. The moving superluminous photoemission front can serve as a source of Cherenkov radiation.

However, for a photoemission current of high density, it is incorrect to ignore the space-charge effects because, within the flow of photoelectrons, a VC can develop, the front of which, under certain conditions, propagates along the photoemitter surface at a speed greater than *c*.

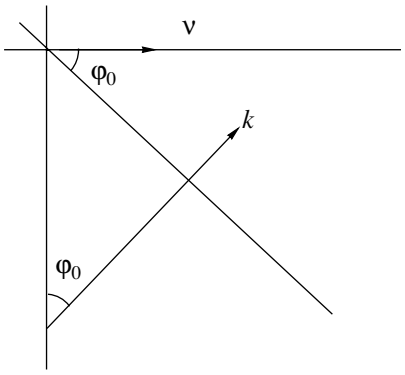

Fig. 20. Plane pulse of γ photons incident on a plane photoemitter.

The kinematics of a superluminous VC was analyzed in [33], in which a microwave oscillator with such a VC was for the first time simulated self-consistently with allowance for the space charge of an electron flux.

In this section, we present the results of numerical calculations of the electron dynamics in a situation in which the plane front of a flux of γ photons is incident onto a plane photoemitter, serving as the plane wall of a semi-infinite plane vacuum waveguide. The computations were carried out using the KARAT code.

Figures 21–23 demonstrate the numerical results calculated for the following parameter values: the transverse dimension of the waveguide is 5 cm, the angle of incidence of γ photons to the photoemitter is $\varphi_0 = 30°$ (which corresponds to an electron emission front moving with the velocity $v = 2c$), and the longitudinal dimension of the emission spot is 7 cm (which corresponds to a pulse of γ photons with a duration of slightly more than 1 ns). For these parameter values, the energy of the emitted electrons is 1 MeV. The direction of emission coincides with the direction of the wave vector **k** of the front of the flux of γ photons (in the coordinate system used in calculations, the *x* axis points along the emitter and the *z* axis is perpendicular to it). The emission current density per unit length in the *y* direction is equal to 10^3 A/cm.

Different stages of the formation of the electron configuration in the (*x*, *z*) plane are illustrated in Fig. 21, in which we can see a superluminous hollow electron semi-cylinder (with its axis pointing in a direction perpendicular to the plane of the figure), which moves along the *x* axis and is surrounded by a halo of the transmitted electrons. As for the electrons reflected from the VC, their dynamics is observed to be as follows. In the laboratory frame of reference, they all have $v_x > 0$ and follow nearly cycloidal paths while moving along the surface of the semi-cylinder from its front toward its trailing edge. This dynamics of the reflected electrons is confirmed by Fig. 22, which shows their calculated phase diagrams at a time of 0.6 ns.

Figure 23 displays the calculated instantaneous spatial distributions of the potential $\Phi(x, z)$ and of the field component $E_z(x, z)$ at a time of 0.8 ns. It can be seen that the electromagnetic field detaches from the semi-cylinder and form a cone similar to the Cherenkov cone, so that the system as a whole radiates analogously to a source of Cherenkov light.

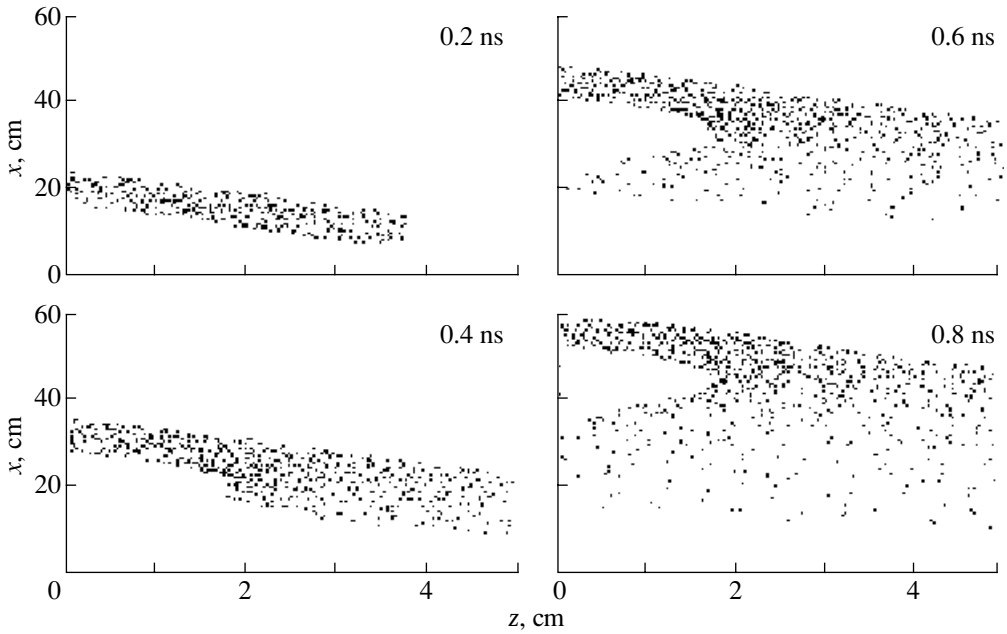

Fig. 21. Electron distributions in the (*x*, *z*) plane at different times.

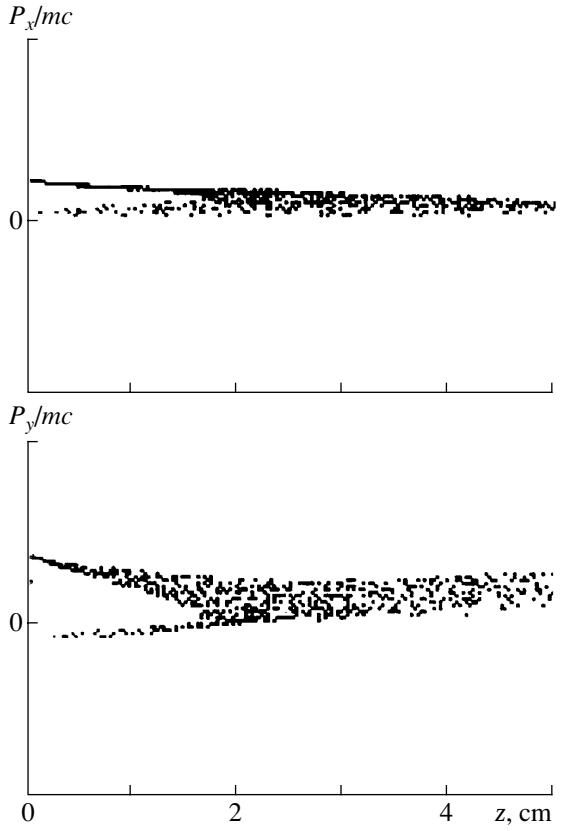

Fig. 22. Instantaneous phase portraits of the beam electrons at the time $t = 0.6$ ns: (a) $-P_x/mc$ vs. z and (b) $-P_z/mc$ vs. z.

One interesting result deserves mention here. It is well known that, in conventional vircators, the electric potential near the VC oscillates about a mean value approximately equal to the cathode potential. This indicates that, in the rest frame of the VC, the potential near the VC during the injection of 1-MeV electrons should be about 1 MV. In the laboratory frame, in which the VC is superluminous, this potential is about 150 kV. In order to construct a mathematical description of the transition from the VC rest frame to the laboratory frame, it is necessary to generalize Lorentz transformations to superluminous relative velocities [34]. For the 4-potential (A_x, A_y, A_z, Φ), these transformations were derived in [33]:

$$A_x' = \begin{cases} \gamma\left(A_x - \Phi\dfrac{v}{c}\right) \\ \varepsilon\gamma\left(\Phi - A_x\dfrac{c}{v}\right) \end{cases}, \quad \Phi' = \begin{cases} \gamma\left(\Phi - A_x\dfrac{v}{c}\right) & \text{for } v < c \\ \varepsilon\gamma\left(A_x - \Phi\dfrac{c}{v}\right) & \text{for } v > c \end{cases} \tag{1}$$

$$A_y' = A_y,\ A_z' = A_z.$$

Here, we have introduced the notation $\varepsilon = \operatorname{sgn} v$ and the Lorentz factor for relative superluminal motions has the form

$$\gamma = \begin{cases} (1 - v^2/c^2)^{-1/2} & \text{for } v < c \\ (1 - c^2/v^2)^{-1/2} & \text{for } v > c \end{cases}. \tag{2}$$

In order to calculate the potential correctly, transformations (1) should be used with the vector potential component A_x associated with the longitudinal (along the photoemitter) electron current component. Estimates from formulas (1) show that the value of the potential Φ near the VC corresponds approximately to the value obtained in numerical simulations.

Physically, the fact that the VC potential in the laboratory frame is lower than that in the VC frame indicates that, at the reflection point (at which $v_z = 0$), the longitudinal velocity component v_x is nonzero; i.e., the total kinetic energy of the electron is positive, so that its motion can be reversed by a lower potential barrier.

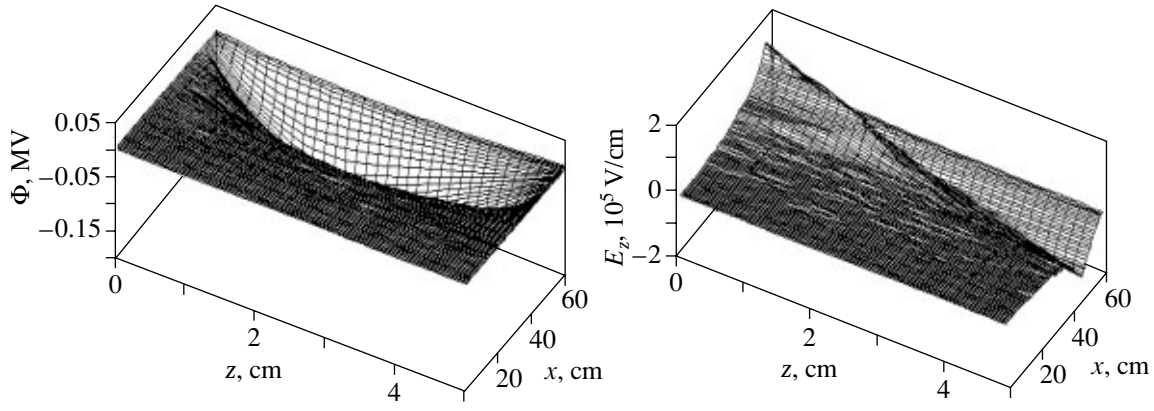

Fig. 23. Instantaneous distributions of the potential $\Phi(x, z)$ and of the field component $E_z(x, z)$ at the time $t = 0.8$ ns.

In addition, note that Bessarab *et al.* [35] proposed an oscillator with a superluminous VC moving along a parabolic surface.

4. TWO-SECTION HYBRID MICROWAVE OSCILLATORS WITH A VC

4.1. "Vircator + TW" Hybrid Oscillator (Virtod)

It is well known that an oscillating VC modulates the electron beam current passing through it [7, 8]. This circumstance allows the use of electron beams with a VC for both microwave generation and collective ion acceleration.

One of the interesting ideas in the development of microwave oscillators with a VC is that of a hybrid oscillator in which the transmitted electron current modulated by the VC is passed through a slowing-down structure designed to operate as a BWT [11]. A microwave excited in the BWT returns to the VC, thereby providing feedback in the oscillator, and the microwave radiation is extracted from a region near the VC. Thus, such a hybrid oscillator, which has been called a virtod, is a combination of a vircator and a BWT.

A virtod—a hybrid microwave oscillator of the "vircator + TWT" type—was implemented practically at the RFNC-ARRIEP. As compared to a conventional TWT, the principle of operation of this virtod scheme is based on the passage of a modulated electron beam through the slowing-down structure, which is thus excited by both the beam and the microwave radiation from the vircator containing a high-quality cavity.

The electrodynamic structure of a TWT was modeled as an open cavity in the form of a part of a rippled waveguide of circular cross section in an external uniform magnetic field.

Figure 24 shows a virtod configuration that differs from a relativistic TWT in having an anode grid and from a conventional vircator in having a slowing-down structure within the drift tube.

Theoretical analysis of the operation of the virtod clearly shows that placing the anode grid in an arbitrary position within the virtod does not always increase its generation efficiency above that of the underlying TWT. In order to increase the generation efficiency, it is necessary to choose the position of the grid in such a way that, on the one hand, a VC could form in the drift tube and, on the other hand, the frequency of oscillations of the VC would be a multiple of the eigenfrequency in the TWT (i.e., the frequency at which the TWT generates microwaves).

Numerical simulations of the virtod that were carried out with this objective showed that, for an underlying TWT based on an I-3000 linear induction accelerator with a 2.4-MeV electron beam, the optimum distance between the cathode and the anode is equal to 6 cm.

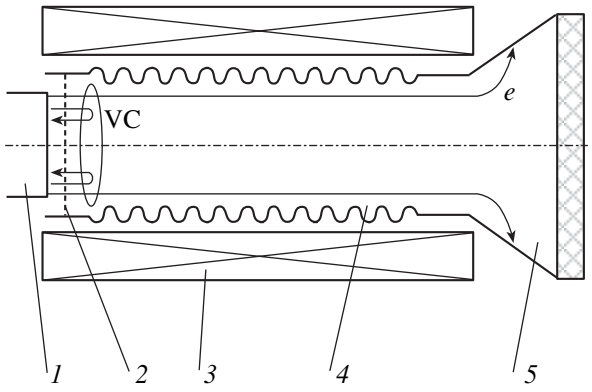

Fig. 24. Schematic of a virtod: (*1*) cathode, (*2*) anode grid, (*3*) magnetic-field solenoid, (*4*) electrodynamic structure, and (*5*) horn antenna.

The underlying TWT was capable of generating microwave radiation pulses with a peak power of 3 GW [36]. In the virtod experiments of [13], the microwave generation efficiency was increased by a factor of 1.6.

Hence, our simulations made it possible to increase the generation efficiency of a virtod and the microwave power generated in it as compared to those of a TWT. Note that, in [37], another scheme of a hybrid oscillator—a combination of a TWT and a vircator—was proposed and substantiated (it should be stressed that, in this scheme, the role of the modulator is played by the TWT).

4.2. Two-Beam Tube with a Virtual Cathode

In [38, 39], a new principle for constructing microwave tubes with long-term interaction was proposed. The idea is to create a space-charge wave with a phase velocity higher than the speed of light in vacuum or in a waveguide without using any slowing-down structures. This is achieved by simultaneously forming two monoenergetic density-modulated electron beams with different velocities and by passing them through the same channel in the same direction. The modulation frequencies of the beams, ω_1 and ω_2, should satisfy the condition $\left|\frac{v_1 v_2(\omega_1 - \omega_2)}{\omega_1 v_2 - \omega_2 v_1}\right| > v_{ph}$, where v_1 and v_2 are the electron velocities in the beams and v_{ph} is the phase velocity of the microwave generated in the channel at the frequency $\omega = |\omega_1 - \omega_2|/2$. Under this condition, the phase velocity of the space-charge beat wave is higher than v_{ph}, and, moreover, the system can operate in the TWT regime and in the BWT regime.

Let us explain why the above condition provides the possibility of microwave generation.

We consider two collisionlessly interpenetrating, partially overlapping, density-modulated, monoenergetic beams moving with different velocities v_1 and v_2

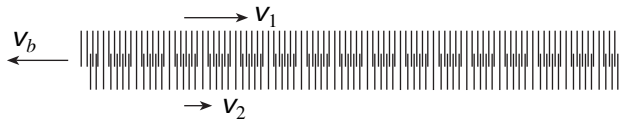

Fig. 25. Schematic diagram of the formation of a beat wave (for the sake of definiteness, the case of the BWT regime is presented).

in the same direction. This is illustrated in Fig. 25, which schematically shows the instantaneous positions of the density maxima in the form of two sets of lines with the same width but with different spatial periods. We see that the sets partially overlap one another, forming a low-frequency space-charge beat wave.

In the case at hand, the beat wave is one of the several space-charge waves that can be excited in the beams. To avoid misunderstanding, we assume that the phase velocity of this beat wave is equal to $v_b = v_{sc}$. Let us estimate the frequency ω_b and phase velocity v_b of the beat wave.

We represent the current density of each beam in the form

$$j_{1,2} = j_0\left[1 + \cos\left(\omega_{1,2}t - \frac{\omega_{1,2}}{v_{1,2}}z\right)\right], \quad (3)$$

where z is the coordinate in the propagation direction of the beams.

The total current density can then be expressed as

$$j = j_0\left[1 + \cos\left(\omega_1 t - \frac{\omega_1}{v_1}z\right)\right]$$

$$+ j_0\left[1 + \cos\left(\omega_2 t - \frac{\omega_2}{v_2}z\right)\right] = 2j_0\left\{1 + \cos\left[\frac{\omega_1 + \omega_2}{2}t \right.\right. \quad (4)$$

$$\left.\left. - \left(\frac{\omega_1}{v_1} + \frac{\omega_2}{v_2}\right)\frac{z}{2}\right]\right\}\left\{1 + \cos\left[\frac{\omega_1 - \omega_2}{2}t - \left(\frac{\omega_1}{v_1} - \frac{\omega_2}{v_2}\right)\frac{z}{2}\right]\right\}.$$

The last factor on the right-hand side of this expression describes the beat wave. The frequency ω_b and phase velocity v_b of this wave can be found by simple mathematical manipulations:

$$\omega_b = \frac{|\omega_1 - \omega_2|}{2}, \quad (5)$$

$$v_b = \frac{v_1 v_2(\omega_1 - \omega_2)}{\omega_1 v_2 - \omega_2 v_1}. \quad (6)$$

Analyzing these expressions, we readily see that, by adjusting the velocities v_1 and v_2 and the frequencies ω_1 and ω_2, the absolute value of the beat wave phase velocity v_b can be made greater than any velocity value specified in advance, e.g., the speed of light c in free space or even the phase velocity v_{ph} of the longitudinal wave in a smooth waveguide or in an isotropic plasma (recall that, in the last two cases, we have $v_{ph} > c$).

In the channel, the beat wave with such phase velocity generates a longitudinal microwave with the frequency $\omega = \omega_b$ by the Cherenkov mechanism for the generation of longitudinal waves.

It is, of course, always possible to choose the required values of the parameters v_1, v_2, ω_1, and ω_2. Two examples of such a choice are as follows (the corresponding electron kinetic energies T_1 and T_2 are given in parentheses):

(i) For $v_1 = 2.5 \times 10^8$ m/s ($T_1 = 413.4$ keV), $v_2 = 2.7 \times 10^8$ m/s ($T_2 = 661.2$ keV), $\omega_1/2\pi = 10$ GHz, and $\omega_2/2\pi = 12$ GHz, the beat wave parameters are $v_b = 4.5 \times 10^8$ m/s and $\omega_b/2\pi = 1$ GHz.

(ii) For $v_1 = 2 \times 10^8$ m/s ($T_1 = 174.8$ keV), $v_2 = 2.9 \times 10^8$ m/s ($T_2 = 1484.9$ keV), $\omega_1/2\pi = 9.5$ GHz, and $\omega_2/2\pi = 12$ GHz, the beat wave parameters are $v_b = -4.085 \times 10^8$ m/s and $\omega_b/2\pi = 1.25$ GHz.

The positive value of the phase velocity of the beat wave indicates that the beat wave propagates in the same direction as the beams; in this case, the microwave is generated in the TWT regime.

The minus sign in front of the phase velocity of the beat wave in the second example indicates that the beat wave propagates in the direction opposite to the propagation direction of the beams; in this case, the microwave is generated in the BWT regime.

The parameter ranges in which microwaves are generated in free space ($|v_b| > c$) in the TWT regime and in the BWT regime are demonstrated in Fig. 26 in the coordinate plane (μ, ξ) (where $\mu = v_1/v_2$ and $\xi = \omega_1/\omega_2$). Figure 26 also applies to cases in which the role of the channel is played by a smooth waveguide or by an isotropic plasma, the only difference is that the corner angles α of the hatched sectors corresponding to the TWT and BWT regimes are smaller. These angles are equal to (see Fig. 26)

$$\alpha_{TWT} = \frac{\pi}{4} - \arctan\frac{(v_{ph}/v_1) - 1}{v_{ph}/v_1}; \quad (7)$$

$$\alpha_{BWT} = -\frac{\pi}{4} + \arctan\frac{(v_{ph}/v_1) + 1}{v_{ph}/v_1}. \quad (8)$$

Hence, in cases in which the role of the channel is played by a smooth waveguide or by an isotropic plasma, microwave Cherenkov radiation in free space can be generated in both the TWT and BWT regimes, in contrast to the conclusions traditionally presented in manuals on physics [40].

As for the two-beam electron microwave tube that was proposed in [38, 39] and is capable of operating in the TWT regime and in the BWT regime, it generates an electromagnetic wave with the phase velocity characteristic of the channel. It is this feature that ensures

the emission of the generated wave into free space without losses and reflections, thereby providing a higher generation efficiency of the tube.

The above generation condition can be satisfied by choosing the type of electromagnetic wave and its frequency and by calculating its phase velocity. Thus, if, in example (i), we choose a TM_{11} wave and consider a channel in the form of a rectangular waveguide with a cross-sectional area of $a \times b$, then we obtain the following expression for the wave phase velocity:

$$v_{ph} = \frac{c}{\sqrt{1 - (\omega_{cr}/\omega)^2}}, \quad (9)$$

where the critical frequency of the waveguide is equal to

$$\omega_{cr} = \pi c \sqrt{\frac{1}{a^2} + \frac{1}{b^2}}. \quad (10)$$

In fact, the problem of satisfying the generation condition reduces to that of correctly choosing the transverse dimensions of the waveguide.

Note also that the microwave tube in question can operate with both partially and completely overlapping modulated beams and even with beams separated by a small distance.

It is easy to understand that the modulating section of the klystron cavity type or in the form of a part of helix is unsuitable for the practical implementation of the proposed scheme. The reason is that such a section modulates the electron beams not only in density but also in velocity, so that the beams cease to produce a beat wave.

This problem can be overcome by applying other types of beam modulators whose operation is based on the gating principle, e.g., by using the following two modulators, in which the beam is modulated only in density:

(i) A photocathode controlled by a repetitive pulsed laser, in which case the beam modulation frequency is specified by the repetition rate of the laser pulses and the beam electron velocity is determined by the voltage across the cathode–anode gap (a modulator of the lasertron type [41]).

(ii) An oscillating VC that is produced within the beam by its space charge and periodically transmits and reflects the beam electrons, in which case the beam modulation frequency is set by the beam density (or by the beam current) and the electron velocity is determined by the voltage across the cathode–anode gap (a modulator of the vircator type [7]).

Of course, other types of modulators can also be used.

Schematic representations of a tube with a modulator of the vircator type operating in the TWT regime and in the BWT regime are given in Figs. 27 and 28, respectively.

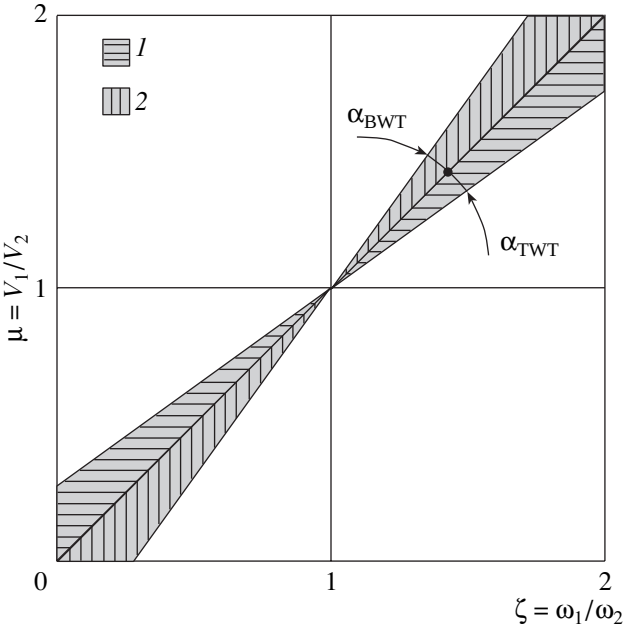

Fig. 26. Plot in the (μ, ξ) plane, showing the parameter ranges in which microwaves can be generated in different regimes: (*1*) TWT regime and (*2*) BWT regime.

In the tubes shown in Figs. 27 and 28, the beams are formed as a result of explosive emission at the cathodes, are accelerated, and pass through the anode diaphragm openings. Further, the space charge of the beams produces oscillating VCs within them. The oscillations of the VCs, which transmit the beam electrons, modulate the beams in density without modulating them in velocity. Then, the process proceeds in a manner analogous to that described above. The required oscillation frequency of the VCs and, accordingly, the modulation frequency of the beam can be set by varying the distance between the cathode and the anode diaphragm.

In all cases, the required beam velocities are set by choosing the accelerating voltage across the cathode–anode diaphragm gap.

The operation of the tube was simulated numerically by the particle method using the KARAT code. It was shown that, in example (i), the direction of the Poynting vector coincides with the propagation direction of the beams and, in example (ii), the direction of the Poynting vector is opposite to the propagation direction of the beams.

4.3. The Magnetically Insulated Klystron-like Vircator

As was mentioned above, among vircators, there is a separate group of magnetically insulated vircators (MIVs) in which the VC can form at a large distance from the emitting cathode. The distinctive feature of such vircators is the presence of an externally applied

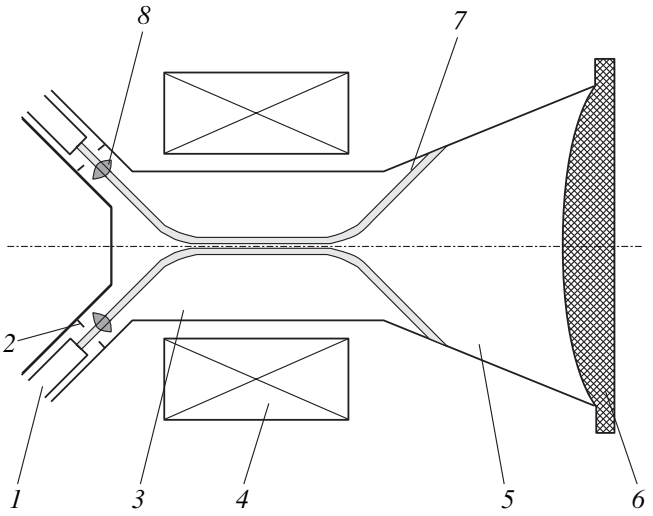

Fig. 27. Schematic of a two-beam tube with a VC operating in the TWT regime: (*1*) cathode, (*2*) anode diaphragm openings, (*3*) channel, (*4*) magnetic-field solenoid, (*5*) horn antenna, (*6*) window for extracting radiation, (*7*) electron beam, and (*8*) virtual cathode.

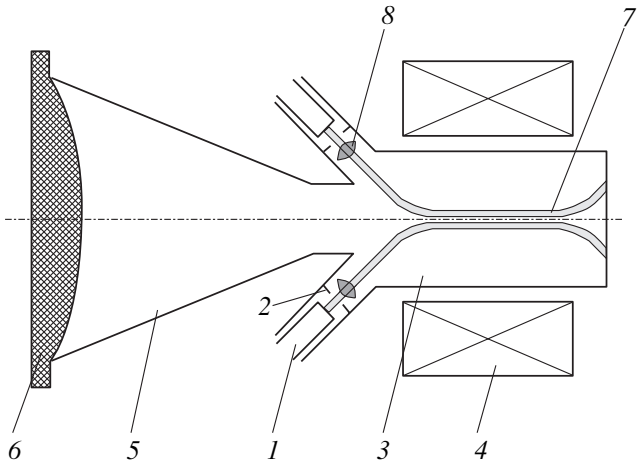

Fig. 28. Schematic of a two-beam tube with a VC operating in the BWT regime: (*1*) cathode, (*2*) anode diaphragm openings, (*3*) channel, (*4*) magnetic-field solenoid, (*5*) horn antenna, (*6*) window for extracting radiation, (*7*) electron beam, and (*8*) virtual cathode.

strong longitudinal magnetic field, which, on the one hand, allows operation without anode grids and, on the other, provides the possibility of increasing the time during which the cathode plasma bridges the diode gap. As a result, it becomes possible to generate microwave pulses of microsecond duration.

However, it was shown in [42] that the beams in such vircators may be subject to specific instabilities

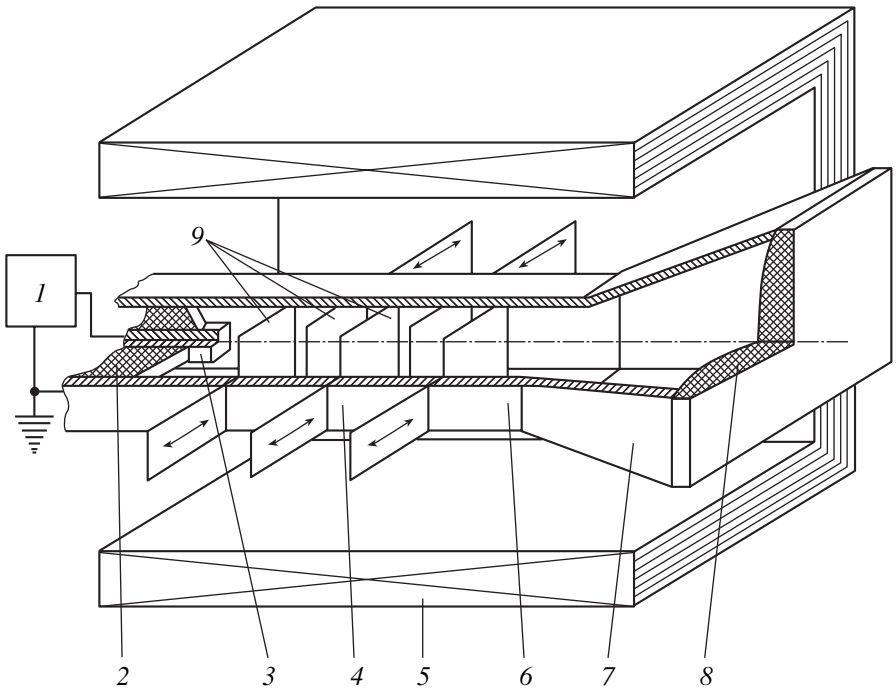

Fig. 29. Schematic of a magnetically insulated klystron vircator: (*1*) power source, (*2*) insulator, (*3*) cathode, (*4*) anode, (*5*) solenoid, (*6*) drift tube, (*7*) horn antenna, (*8*) window for extracting microwave radiation, and (*9*) grids (the arrows indicate the directions in which the grids can be moved to control the widths of the gaps).

that force them to evolve to a strongly turbulent state. It was also shown that the absence of an anode grid reduces the efficiency of the beam bunching [43].

At this point, we mention a new field of research that has recently appeared in the development of MIV technology: in order to increase the beam bunching efficiency, the diode region is equipped with various resonant electrodynamic structures. Thus, in an MIV proposed and designed at the MEPI [12, 44], the resonant structure consists of two cavities of the klystron type, and, in the MIV proposed in [37], the resonant structure has the form of a periodic rippled waveguide.

In our opinion, however, the most efficient MIV is the klystron-like MIV proposed in [45], in which a sequence of anode grids (or foils) forms a chain of side-coupled cavities (Fig. 29). Let us list the advantages of this vircator:

(i) the chain of coupled cavities makes it possible to modulate an electron beam in the same way as does a drift-tube klystron;

(ii) the sequence of gaps between the anode grids and the waveguide wall provides a distributed feedback between the VC and the emitting cathode, in which case the phase of the feedback wave can be controlled by varying the width of the gaps; and

(iii) the sequence of grids held at the anode potential prevents a dangerous effect—the relaxation of the beam to a compressed state.

We carried out self-consistent full-scale computer simulations of the proposed vircator in order to confirm the ideas underlying its operation. The calculations were performed using the KARAT code.

The geometric representation of the computation region is shown in Fig. 30a, in which all the dimensions used in our computations are indicated. The system was assumed to be uniform in the *y* direction.

The geometric dimensions of the component elements of the vircator were chosen to be as follows: the width of the waveguide (held at the anode potential) was 7 cm, the cathode width was 5 cm, and the beam width was 3 cm.

The anode grids were assumed to be equidistant, and the width δ of the gaps between the ends of the grids and the waveguide wall (Fig. 30a) was varied from δ = 0 cm to δ = 7 cm with the spatial step Δδ = 0.2 cm. The two limiting cases, δ = 0 cm and δ = 7 cm, correspond, respectively, to a regime without a VC and to a purely klystron regime of the electron beam modulation.

The external longitudinal magnetic field was assumed to have a strength of 50 kG in the modulating section and to decrease to zero outside it. Also, the magnetic field was assumed to begin to decrease at a certain distance from the VC in order for the electric circuit containing the reverse-current conductor to be closed.

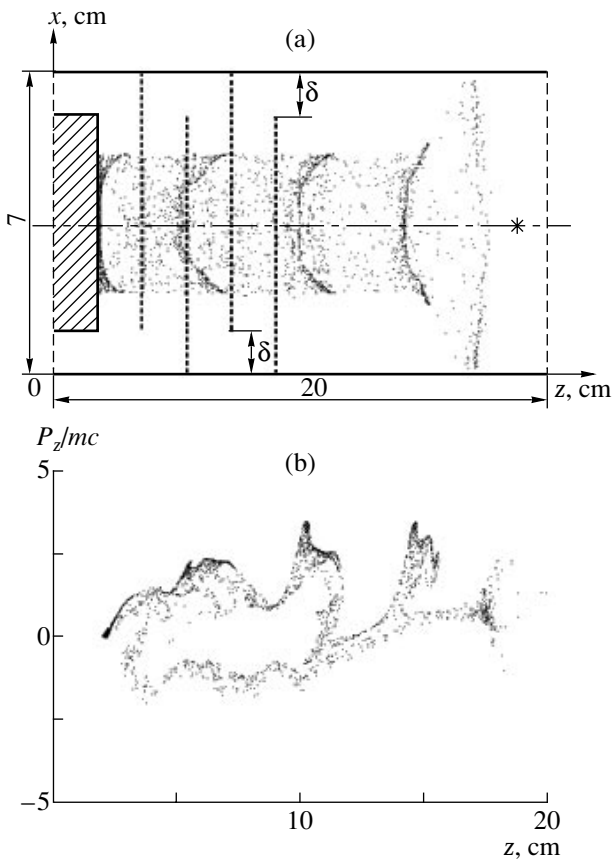

Fig. 30. (a) Geometry of the computation region with an instantaneous configuration of the electron beam and (b) instantaneous phase portrait of the beam.

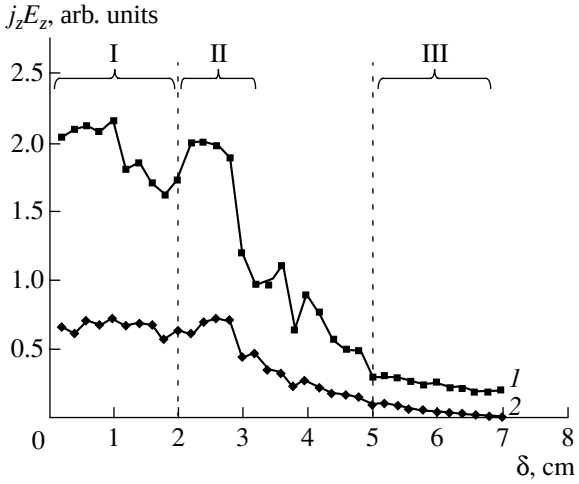

Fig. 31. (*1*) The peak value of the product j_zE_z and (*2*) its value averaged over a time of 10 ns, calculated as functions of the gap width δ. The braces indicate different regimes of operation: (I) klystron modulation regime, (II) klystron-like vircator regime, and (III) TWT generation regime.

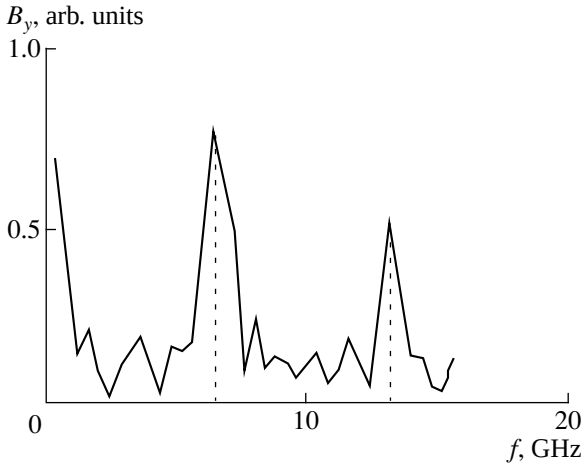

Fig. 32. Typical spectrum of microwave radiation generated in the klystron-like vircator regime.

The cathode potential relative to the anode was set at –500 kV. The calculations were carried out on a 43 × 121 mesh.

Figure 30a also shows the instantaneous distribution of the electrons in the beam in the klystron-like vircator regime. Figure 30b presents a typical calculated phase diagram of the beam electrons in this regime. It can be seen that the beam does not evolve to a compressed state and that pronounced electron bunches form, consisting of the electrons that are more energetic than those in the injected beam.

We calculated the energy characteristics of the generated microwave radiation—the maximum and averaged values of the product j_zE_z (where j_z is the current density in the z direction and E_z is the z component of the electric field) at the location of the probe (shown by an asterisk in Fig. 30a). In Fig. 31, we plot the dependence of j_zE_z as a function of the gap width δ.

An analysis of this dependence shows that, in the range of δ values from 0 to 2 cm, the generation regime corresponds to the klystron modulation regime (see region I in Fig. 31). In this range, the product j_zE_z reaches its maximum value.

In the range of δ values from 2 to 5 cm, the generation is most efficient in the regime of the proposed klystron-like vircator (see region II). The spectrum of the microwaves generated in this regime was computed using fast Fourier transforms (Fig. 32). It can be seen that the microwaves are generated at the fundamental frequency $f = 7$ GHz. We also readily observe the generation at the second harmonic of the fundamental frequency.

In the range of δ values from 5 to 7 cm, it was found that the VC does not form (region III in Fig. 31). In this range, the microwaves are generated in the TWT regime.

The main results of these investigations, which were published in [46], can be summarized as follows:

(i) The above ideas about the behavior of an electron beam in the proposed klystron-like MIV have been confirmed.

(ii) The dependence of the maximum and averaged values of the energy characteristic j_zE_z on the gap width δ has been calculated. This dependence shows that there are three different possible regimes of operation: the klystron modulation regime, the klystron-like vircator regime proposed here, and the generation regime in which the VC does not form.

(iii) The spectrum of the generated microwaves has been obtained, the fundamental generation frequency being $f = 7$ GHz.

5. CONCLUSIONS

We have considered for the first time a new direction in the technology of microwave oscillators with a VC—the development of hybrid microwave oscillators with a VC. We have classified them and presented the results from simulating their operation. In the Introduction, the main features and principles of operation of such devices have been formulated.

It has been proposed to excite the cavity of a diffractional microwave oscillator by an electron beam with a VC. We have considered the advantages and disadvantages of three versions of such an oscillator: in the first version, the VC is formed in the beam before the beam enters the cavity; in the second version, the VC is formed in the beam after the beam has left the cavity; and, in the third version, the VC is formed immediately inside the cavity. We have carried out computer simulations of the first and third versions.

We have analyzed characteristic features of the microwave generation in vircators with a nonuniform magnetic field and have shown that the generation can be substantially enhanced by the electron cyclotron effects.

We have substantiated the idea of a beam–plasma vircator and have carried computer simulations of its operation. We have determined that, under the same supply conditions, such a vircator is capable of generating a microwave power two times higher than that generated in a conventional vacuum vircator.

We have described a new gyrocon with a VC and have computationally substantiated its high generation efficiency in comparison to conventional gyrocons.

We have presented the results from simulating a microwave oscillator based on a superluminous VC. Such oscillators are supplied by fluxes of X radiation or γ radiation. Simulations show that microwave radiation is generated by the Cherenkov mechanism. We have revealed and explained a substantial decrease in the VC potential.

We have presented the results of investigating a virtod—a hybrid microwave oscillator of the "vircator + TWT" type. Virtod experiments and simulations of its operation show that the virtod provides a generation efficiency higher than the total efficiency of its component elements—a vircator and a TWT.

We have substantiated the principle of the generation of electromagnetic waves in a two-beam electron microwave tube. This principle implies that two electron beams with different velocities (energies) are formed simultaneously, are modulated in density without being modulated in velocity, and then are passed through the same channel in the same direction. The modulation frequencies of the beams, ω_1 and ω_2, must satisfy a certain condition under which the phase velocity of the space-charge beat wave is higher than v_{ph}; in this case, the system can operate in the TWT regime and in the BWT regime. Such modulation of the beams can be provided by a VC.

The results of simulating a magnetically insulated klystron-like vircator with a distributed feedback show that it can generate microwaves very efficiently.

The investigations reviewed in the present paper show that it is possible to speak of a new direction in relativistic microwave electronics—the technology of microwave oscillators with a VC, which may in a number of cases prove to be more efficient than traditional vircators and reflex triodes.

REFERENCES

1. A. A. Rukhadze, S. D. Stolbetsov, and V. P. Tarakanov, Radiotekh. Élektron. (Moscow) **37**, 385 (1992).
2. A. E. Dubinov and V. D. Selemir, Zarubezhn. Radioélektron., No. 4, 54 (1995).
3. A. E. Dubinov and V. D. Selemir, Radiotekh. Électron. (Moscow) **47**, 645 (2002).
4. A. Bromborsky, F. Agee, M. Bollen, *et al.*, Proc. SPIE **873**, 51 (1988).
5. V. D. Selemir, A. E. Dubinov, and N. V. Stepanov, in *Book of Scientific Works of Russian Federal Nuclear Center–All-Russia Institute of Experimental Physics* (RFNCTs-VNIIÉF, Sarov, 2003), Vol. 4, p. 184.
6. D. I. Trubetskov, A. G. Rozhnev, and D. V. Sokolov, *Lectures on Vacuum Microwave Microelectronics* (Kolledzh, Saratov, 1996).
7. V. I. Kurilko and Ya. B. Fainberg, Pis'ma Zh. Tekh. Fiz. **2**, 397 (1976) [Sov. Tech. Phys. Lett. **2**, 154 (1976)].
8. A. M. Ignatov and A. A. Rukhadze, Kratk. Soobshch. Fiz., No. 11, 13 (1977).
9. D. M. Benevolenskiĭ, G. P. Gogolev, and S. M. Movnin, Peterb. Zh. Élektron., No. 5, 28 (1995).
10. V. P. Tarakanov, *User's Manual for Code KARAT* (Berkley, Springfield, 1992).
11. N. P. Gadetskiĭ, I. I. Magda, S. I. Naĭsteter, *et al.*, Fiz. Plazmy **19**, 530 (1993) [Plasma Phys. Rep. **19**, 273 (1993)].
12. O. V. Garkusha, Yu. S. Ivanova, A. N. Novozhilov, *et al.*, in *Proceedings of the Scientific Session of Moscow Institute of Engineering Physics* (MIFI, Moscow, 2002), Vol. 8, p. 23.
13. V. D. Selemir, A E. Dubinov, E. E. Dubinov, *et al.*, Pis'ma Zh. Tekh. Fiz. **27** (14), 25 (2001) [Tech. Phys. Lett. **27**, 583 (2001)].
14. V. P. Shestopalov, *Diffraction Electronics* (Vysshaya Shkola, Kharkov, 1976).
15. A. E. Dubinov and K. E. Mikheev, Izv. Vyssh. Uchebn. Zaved. Radioélektron., No. 6, 55 (2002).
16. M. J. Rhee and W. W. Destler, Phys. Fluids **17**, 1574 (1974).
17. V. D. Selemir, A. E. Dubinov, and N. V. Stepanov, RF Patent No. 2044361, Byull. Izobret., No. 26 (1995).
18. V. D. Selemir, B. V. Alekhin, V. E. Vatrunin, *et al.*, Fiz. Plazmy **20**, 689 (1994) [Plasma Phys. Rep. **20**, 621 (1994)].
19. B. V. Alyokhin, A. E. Dubinov, V. D. Selemir, *et al.*, IEEE Trans. Plasma Sci. **22**, 945 (1994).
20. A. E. Dubinov and V. D. Selemir, Pis'ma Zh. Tekh. Fiz. **27** (13), 64 (2001) [Tech. Phys. Lett. **27**, 557 (2001)].
21. T. J. T. Kwan and C. M. Snell, US Patent No. 4730170 (1987).
22. V. E. Vatrunin, A. E. Dubinov, V. D. Selemir, *et al.*, *Fractals in Applied Physics*, Ed. by A. E. Dubinov (VNIIÉF, Arzamas-16, 1995), p. 47.
23. A. E. Dubinov and V. D. Selemir, Pis'ma Zh. Tekh. Fiz. **24** (4), 41 (1998) [Tech. Phys. Lett. **24**, 142 (1998)].
24. K. G. Kostov, I. G. Yovchev, and N. A. Nikolov, Electron. Lett. **35**, 1647 (1999).
25. M. V. Kuzelev, O. T. Loza, A. A. Rukhadze, *et al.*, Fiz. Plazmy **27**, 710 (2001) [Plasma Phys. Rep. **27**, 669 (2001)].
26. A. E. Dubinov, K. E. Mikheev, and V. D. Selemir, Prikl. Fiz., No. 2, 13 (2002).
27. M. V. Kuzelev, A. D. Poezd, A. A. Rukhadze, *et al.*, Mat. Model. **1** (11), 34 (1989).
28. A. N. Didenko, M. A. Zav'yalov, V. I. Perevodchikov, *et al.*, RF Patent No. 2127925, Byull. Izobret., No. 8 (1999).
29. G. I. Budker, M. M. Karliner, I. G. Makarov, *et al.*, At. Énerg. **44**, 397 (1978).
30. A. E. Dubinov, I. A. Efimova, and V. P. Tarakanov, in *Proceedings of the Scientific Session of Moscow Institute of Engineering Physics* (MIFI, Moscow, 2003), p. 141.
31. N. J. Carron and C. L. Longmire, IEEE Trans. Nucl. Sci. **23**, 1897 (1976).
32. Yu. N. Lazarev and P. V. Petrov, Pis'ma Zh. Éksp. Teor. Fiz. **60**, 625 (1994) [JETP Lett. **60**, 634 (1994)].
33. A. E. Dubinov, V. D. Selemir, N. V. Stepanov, *et al.*, in *Plasma Physics Investigations*, Ed. by V. D. Selemir and A. E. Dubinov (RFYaTs-VNIIEF, Sarov, 1998), p. 299.
34. V. S. Barashenkov and M. Z. Yur'ev, Kratk. Soobshch. Ob'edin. Inst. Yad. Issled., No. 5, 5 (1994).
35. A. V. Bessarab, A. E. Dubinov, Yu. N. Lazarev, *et al.*, RF Patent No. 2175154 (1999).

36. A. I. Pavlovskiĭ, V. S. Bosamykin, V. D. Selemir, *et al.*, in *Relativistic Microwave Electronics* (Inst. Prikl. Fiz. Ross. Akad. Nauk, Nizhni Novgorod, 1992), No. 7, p. 81.
37. V. D. Selemir, A. E. Dubinov, and N. N. Makarova, RF Patent No. 2157017 (1998).
38. A. E. Dubinov, RF Patent No. 2189661 (2001).
39. A. E. Dubinov, Ob'edin. Nauchn. Zh., No. 14, 58 (2002).
40. V. P. Zrelov, *Cherenkov Radiation* (Atomizdat, Moscow, 1968).
41. A. N. Lebedev and É. A. Perel'shteĭn, in *Relativistic Microwave Electronics* (Inst. Prikl. Fiz. Akad. Nauk SSSR, Gorki, 1990), No. 6, p. 217.
42. A. M. Ignatov and V. P. Tarakanov, Phys. Plasmas **1**, 741 (1994).
43. V. D. Grigor'ev and A. E. Dubinov, Pis'ma Zh. Tekh. Fiz. **22** (7), 70 (1996) [Tech. Phys. Lett. **22**, 299 (1996)].
44. O. V. Garkusha, Candidate's Dissertation (MIFI, Moscow, 2000).
45. A. E. Dubinov, N. N. Makarova, and V. D. Selemir, RF Patent No. 2158041 (1999).
46. A. E. Dubinov and I. A. Efimova, Peterb. Zh. Élektron., No. 1, 60 (2001).

Translated by G.V. Shepekina

Plasma Physics Reports, Vol. 30, No. 6, 2004, pp. 519–526. Translated from Fizika Plazmy, Vol. 30, No. 6, 2004, pp. 563–570.

PLASMA ELECTRONICS

Generation of Transition Radiation in the Form of Electromagnetic Surface Waves by Electron Bunches

Yu. O. Averkov and V. M. Yakovenko

Usikov Institute of Radiophysics and Electronics, National Academy of Sciences of Ukraine, ul. Akademika Proskury 12, Kharkov, 61085 Ukraine

Received April 16, 2003; in final form, September 19, 2003

Abstract—The generation of transition radiation in the form of electromagnetic surface waves by a nonrelativistic electron bunch as it crosses the vacuum–semiconductor interface or a thin semiconductor plate in vacuum is investigated. A study is made of a bunch that has the shape of an ellipsoid of revolution, with a uniform charge density distribution over its volume, and moves along the normal to the interface. When the energy dissipation in the semiconductor is taken into account, the spectrum of the transition radiation emitted in the form of surface waves comprises a peak whose width is comparable to its mean frequency. It is shown that, in each of the two cases under consideration, the generation efficiency, defined as the ratio of the radiated energy to the kinetic energy of the bunch electrons, is maximum for a bunch of certain dimensions. The dependence of the radiated energy and of the generation efficiency on the thickness of a thin semiconductor plate is investigated for given bunch dimensions. It is found that the corresponding dependences have a maximum, which can be explained as being due the competition between the two effects: as the plate thickness increases, on the one hand, the region where the radiation is generated becomes larger, so that the radiation power increases, and, on the other hand, the dissipative energy losses become higher. *© 2004 MAIK "Nauka/Interperiodica".*

1. INTRODUCTION

It is well known that, as a linearly and uniformly moving charged particle crosses the boundary between two media of different refractive indices, it emits electromagnetic waves. The properties of these waves have been studied quite well [1, 2]. The radiation emitted by a charged particle bunch can differ substantially from that emitted by an individual charged particle. In particular, the charged bunch can emit transition radiation in the form of broadband electromagnetic pulses. In recent years, the problem of the generation of such pulses has received much attention [3–5], because it is important from both a scientific and a practical point of view (e.g., for creating new models of pulsed radars). Thus, Balakirev and Sidel'nikov [3] showed that a transition radiation pulse generated by an electron bunch as it crosses a conducting screen coincides exactly in shape with the bunch current pulse. In this case, the efficiency of conversion of the bunch kinetic energy into the electromagnetic pulse energy can be fairly high (up to several tens of percent). A detailed spectral analysis of transition radiation pulses generated during the injection of charged particle bunches through the end metal wall into a semi-infinite cylindrical waveguide was performed by Balakirev and Onishchenko [4]. They showed that the signal spectrum is fairly broad. It is produced by oscillations at all natural frequencies and all natural wavenumbers of a given waveguide. The spectrum is peaked at approximately the critical frequencies of the waveguide. They also showed that, as the bunch length increases, the number of the spectral harmonics becomes smaller and the generation efficiency decreases sharply. The features of the spectral and angular characteristics of the transition radiation generated by a spherical charged particle bunch as it crosses the boundary between two media were studied by Bolotovskiĭ and Serov [5], who showed that additional peaks appear in the angular spectrum of the radiation when the bunch radius is greater than the wavelength of the emitted wave, i.e., when the condition for the emission of coherent radiation fails to hold.

In the papers cited above, a study was made of the transition radiation in the form of electromagnetic waves emitted in arbitrary directions. Here, we show that transition radiation in the form of electromagnetic surface waves can be generated by an electron bunch as it crosses the vacuum–semiconductor interface or passes through a thin semiconductor plate in vacuum. We also investigate how the radiated energy and generation efficiency depend on the bunch dimensions and on the plate thickness.

2. GENERATION OF PULSES OF SURFACE WAVES PROPAGATING ALONG THE BOUNDARY BETWEEN TWO MEDIA

We consider a semiconductor that occupies the upper half-space $z > 0$ and has the plane $z = 0$ as a boundary. An electron bunch moves along the z axis with the velocity $v \ll c$ (where c is the speed of light in a vacuum) and crosses the semiconductor surface from

1063-780X/04/3006-0519$26.00 © 2004 MAIK "Nauka/Interperiodica"

the vacuum side. We consider a bunch having the shape of an ellipsoid of revolution about the z axis and denote the semiaxes of the ellipsoid by b (along the axis of revolution) and by a (in the perpendicular direction). The bunch current density is determined by the formula

$$j_b = env\int\limits_{(V_b)} \delta(\mathbf{r}-\mathbf{r}_0-\mathbf{v}t)d\mathbf{r}_0, \quad (1)$$

where $\delta(x)$ is the Dirac delta function, n is the bunch density, $\mathbf{r}_0$ is the position vector of an individual bunch electron, and $V_b = \frac{4}{3}\pi a^2 b$ is the bunch volume. The electromagnetic fields are represented in terms of Fourier integrals as follows:

$$\mathbf{E}(\mathbf{r}, t) = \frac{1}{v}\int \mathbf{E}(\boldsymbol{\kappa}, \omega) \times \exp\{i[\boldsymbol{\kappa}\cdot\boldsymbol{\rho} + k_z z - \omega t]\}d\boldsymbol{\kappa}d\omega, \quad (2)$$

where $\boldsymbol{\kappa}$ and $\boldsymbol{\rho}$ are the components of the wave vector and position vector in the xy plane, $k_z = \omega/v$ for the field of a bunch electron, $k_z = \lambda_l$ for the radiation field, and $\lambda_l^2 = (\omega/c)^2\varepsilon_l - \kappa^2$ ($l = 1, 2$). The subscripts 1 and 2 refer to the vacuum and semiconductor, respectively. In order for the radiation fields to decrease within each of the media away from the interface between them, it is necessary that the conditions $\mathrm{Im}\{\lambda_1\} = \lambda_1'' < 0$ and $\mathrm{Im}\{\lambda_2\} = \lambda_2'' > 0$ be satisfied. The wave equation for the Fourier component $\mathbf{E}(\omega, \mathbf{r})$ has the form

$$\Delta\mathbf{E}_l(\omega, \mathbf{r}) + \frac{\omega^2}{c^2}\varepsilon_l(\omega)\mathbf{E}_l(\omega, \mathbf{r}) = 4\pi\left\{\frac{\nabla\rho(\omega, \mathbf{r})}{\varepsilon_l(\omega)} - i\frac{\omega v}{c^2}\rho(\rho, \mathbf{r})\right\}, \quad (3)$$

where $\rho(\omega, \mathbf{r}) = en/(2\pi)^3\int \exp[i\,\mathbf{k}\cdot(\mathbf{r}-\mathbf{r}_0)]d\boldsymbol{\kappa}d\mathbf{r}_0$ is the Fourier component of the bunch density and $\varepsilon_1 = 1$. The dielectric permittivity of the semiconductor, $\varepsilon_2(\omega)$, is given by the expression

$$\varepsilon_2(\omega) = \varepsilon_2'(\omega) + i\varepsilon_2''(\omega) = \varepsilon_0\left[1 - \frac{\Omega_0^2}{\omega(\omega + i\nu)}\right], \quad (4)$$

where $\Omega_0 = \sqrt{4\pi e^2 N/\varepsilon_0 m}$, N is the electron density in a semiconductor, ε_0 is the dielectric constant of the crystal lattice of the semiconductor, m is the effective mass of an electron in a semiconductor, and ν is the relaxation rate of the momentum of the semiconductor-plasma electrons. The Fourier components of the bunch fields have the form

$$\mathbf{E}_{1,2}^b(\mathbf{k}) = \frac{ei}{2\pi^2}\frac{1}{\varepsilon_{1,2}}\frac{(\omega/c^2)\varepsilon_{1,2}\mathbf{v} - \mathbf{k}}{k^2 - (\omega/c)^2\varepsilon_{1,2}}F(\mathbf{k}),$$
$$\mathbf{H}_{1,2}^b(\mathbf{k}) = \frac{\varepsilon_{1,2}}{c}\mathbf{v}\times\mathbf{E}_{1,2}(\mathbf{k}), \quad (5)$$

where the spatiotemporal Fourier component of the bunch density, $F(\mathbf{k}) = F(\omega, \boldsymbol{\kappa})$, results from the integration of expression (1) for the beam current density over $\mathbf{r}_0$:

$$F(\omega, \boldsymbol{\kappa}) = nV_b f(\omega, \boldsymbol{\kappa}), \quad (6)$$

$$f(\omega, \boldsymbol{\kappa}) = \frac{3}{(\omega b/v)^2 + \kappa^2 a^2} \times\left[\frac{\sin(\sqrt{(\omega b/v)^2 + (a\kappa)^2})}{\sqrt{(\omega b/v)^2 + (a\kappa)^2}} - \cos(\sqrt{(\omega b/v)^2 + (a\kappa)^2})\right]. \quad (7)$$

Under the condition $|f(\omega, \boldsymbol{\kappa})| \approx 1$, the transition radiation from all of the bunch electrons can be considered coherent. In this case, the effective bunch charge $q_{\mathrm{eff}} = enV_b|f(\omega, \boldsymbol{\kappa})|$ is equal to $q_{\mathrm{eff}} \approx enV_b$ [1]. For $a = b$, $nV_b = 1$, and $\left|\sqrt{(\omega b/v)^2 + (a\kappa)^2}\right| \ll 1$, we obtain $F(\omega, \boldsymbol{\kappa}) = f(\omega, \boldsymbol{\kappa}) = 1$, so that expressions (5) go over to the corresponding expressions derived in [6] for the fields of one electron. The components $\mathbf{E}_l^r(\omega, \boldsymbol{\kappa})$ and $\mathbf{H}_l^r(\omega, \boldsymbol{\kappa})$ of the radiation fields can be found from the continuity conditions for the tangential field components $\mathbf{E}_l(\omega, \boldsymbol{\kappa}) = \mathbf{E}_l^b(\omega, \boldsymbol{\kappa}) + \mathbf{E}_l^r(\omega, \boldsymbol{\kappa})$ and for the normal component of the electric induction vector, $\mathbf{D}_l(\omega, \boldsymbol{\kappa}) = \varepsilon_l\mathbf{E}_l(\omega, \boldsymbol{\kappa})$ at the boundary between the two media:

$$\mathbf{E}_{1\perp}^r(\omega, \boldsymbol{\kappa}) = \frac{ei}{2\pi^2}\frac{\boldsymbol{\kappa}\lambda_1}{\zeta}\eta F(\omega, \boldsymbol{\kappa}),$$
$$E_{1z}^r(\omega, \boldsymbol{\kappa}) = -\frac{ei}{2\pi^2}\frac{\kappa^2}{\zeta}\eta F(\omega, \boldsymbol{\kappa}), \quad (8)$$

$$\mathbf{H}_1^r(\omega, \boldsymbol{\kappa}) = -\frac{ei}{2\pi^2 c}\frac{k_z\varepsilon_1\boldsymbol{\kappa}\times\mathbf{v}}{\zeta}\eta F(\omega, \boldsymbol{\kappa}), \quad (9)$$

where

$$\eta = \left(\frac{\varepsilon_2}{\varepsilon_1} - \frac{v}{\omega}\lambda_2\right)\Big/\left(k^2 - \frac{\omega^2}{c^2}\varepsilon_1\right) + \left(-1 + \frac{v}{\omega}\lambda_2\right)\Big/\left(k^2 - \frac{\omega^2}{c^2}\varepsilon_2\right),$$
$$\zeta = \varepsilon_2\lambda_1 - \varepsilon_1\lambda_2. \quad (10)$$

The radiation fields in the second medium are given by the same formulas (8)–(10) but with subscript 1

replaced by subscript 2. When account is taken of the radiation energy dissipation, the wave vector κ acquires an imaginary part; i.e., we have $\kappa = \kappa' + i\kappa''$.

The dispersion relation for surface waves is determined from the condition $\varsigma = 0$ and has the form

$$\kappa' = \kappa_0' = \frac{\omega}{c}\mathrm{Re}\left\{\sqrt{\frac{\varepsilon}{1+\varepsilon}}\right\}, \qquad (11)$$

where $\varepsilon = \varepsilon_2$. When the radiation energy dissipation in a semiconductor is taken into account, the dispersion curve has a turning point, at which it turns back and then enters the region where $\varepsilon' > -1$ [7–9].

In what follows, we will consider the surface waves satisfying the conditions $\varepsilon' < -1$ and $|\varepsilon'| \gg \varepsilon''$ ($|\lambda_1''| > \lambda_1'$, $|\lambda_2''| > \lambda_2'$). Such surface waves are called Fano modes [9, 10]. The amplitudes of the fields of the Fano modes remain nonoscillating (owing to the conditions in parentheses) and decrease exponentially away from the interface between two media. By virtue of the condition $|\varepsilon'| \gg \varepsilon''$, the flux of the energy carried by the modes is mostly confined to the interface. That is why, in calculating the energy characteristics, we assume that the normal component of the energy flux is much less than its tangential component and thus can be ignored.

In order to determine the energy expended by the bunch to generate a surface wave, it is necessary to determine the energy flux carried by the wave through the side surface of a circular cylinder with its axis pointing along the direction of the bunch trajectory. Taking into account the pole $\varsigma(\omega, \mathbf{\kappa}) = 0$ and going through the standard manipulations [6], we obtain the following expression for the energy of the surface wave emitted by the bunch along its trajectory in vacuum:

$$S_1(\rho \longrightarrow \infty) = -\frac{c\rho}{2}\int_{-\infty}^{\infty} dt \int_0^{\infty} \mathrm{Re}\{E_z^r(\mathbf{r}, t)H_\varphi^{r*}(\mathbf{r}, t)\}dz$$

$$= -\frac{e^2}{v^2}\int_{\varepsilon'(\omega)<-1} \frac{\omega\kappa_0'|\kappa_0|^3|\eta|^2|F(\omega, \kappa_0)|^2}{\lambda_{10}''\left|(\partial\zeta/\partial\kappa)_{\kappa_0}\right|^2} \qquad (12)$$

$$\times \exp(-2\kappa_0''\rho)d\omega,$$

where $\rho = \sqrt{x^2 + y^2}$, $\kappa_0'' = \frac{\omega}{c}\mathrm{Im}\left\{\sqrt{\frac{\varepsilon}{1+\varepsilon}}\right\}$, $\lambda_1 = \frac{\omega}{c}\frac{1}{\sqrt{1+\varepsilon}}$, $\lambda_2 = \frac{\omega}{c}\frac{1}{\sqrt{1+\varepsilon}}$, $\lambda_{10}'' = \lambda_1''(\kappa_0') = -\frac{\omega}{c}[(1+\varepsilon')^2 + \varepsilon''^2]^{-1/4}\cos(\psi_\lambda/2) < 0$, and $\psi_\lambda = \arctan[-\varepsilon''/(1+\varepsilon')]$.

Figure 1 shows the spectral energy density of the transition radiation $W_1(\omega) = dS_1(\omega)/d\omega$ (curve *1*) and the quantity $|f(\omega)|$ (curve *2*) calculated as functions of frequency in the case of a semi-infinite gallium arsenide (GaAs) semiconductor for the following parameter values: $\varepsilon_0 = 12.53$, $m = 0.067m_0$ (where m_0 is the mass of a free electron), $N = 10^{16}$ cm^{-3}, $\nu = 10^{11}$ s^{-1}, $v = 0.1c$, $n = 10^{12}$ cm^{-3}, $a = 10^{-2}$ cm, $b = 5 \times 10^{-3}$ cm, and $|\mathbf{\rho}| = 1$ cm. The dotted line *3* refers to the frequency $\Omega_{sp} = \sqrt{\varepsilon_0\Omega_0^2/(\varepsilon_0 + 1) - \nu^2}$, at which $\varepsilon' = -1$. For these parameter values, the number of electrons in the bunch is $nV_b \approx 2 \times 10^6$ and the maximum bunch current $I_{b\max} = enV_b v$ is equal to $I_{b\max} \approx 3 \times 10^9$ esu ≈ 1 mA. In what follows, the above values of the semiconductor and bunch parameters will be assumed to be fixed, except for the bunch radius and the length $|\mathbf{\rho}|$ of the position vector. Figure 1 implies that the spectral energy density $W_1(\omega)$ has a pronounced first peak at a frequency of $\omega_{\max} \approx 0.15\Omega_0$ and that, at higher frequencies, it exhibits small-amplitude oscillations. The full width at half-maximum of the first peak is approximately equal to $\Delta\omega_{\max} \approx 0.27\Omega_0 \approx 2\omega_{\max}$. The frequency at which the first peak occurs satisfies the condition $\kappa'(\omega_{\max})|\mathbf{\rho}| = \kappa_{\max}'|\mathbf{\rho}| \sim 10 \gg 1$, under which expression (12) was derived. Note that the leftmost point of the dependence $W_1(\omega)$ corresponds to the frequency $\omega = \omega^*$ (shown by the dotted line *4*), at which the equality $|\varepsilon'| = \varepsilon''$ is valid. This equality indicates that, at frequencies $\omega \le \omega^*$, the normal component of the radiation energy flux can no longer be assumed to be less than its tangential component, so that, in this frequency range, expression (12) fails to hold. For the dependence $W_1(\omega)$ given in Fig. 1, the imaginary part of the dielectric permittivity at $\omega = \omega_{\max}$ can be considered small because $|\varepsilon'(\omega_{\max})/\varepsilon''(\omega_{\max})| \approx 9$.

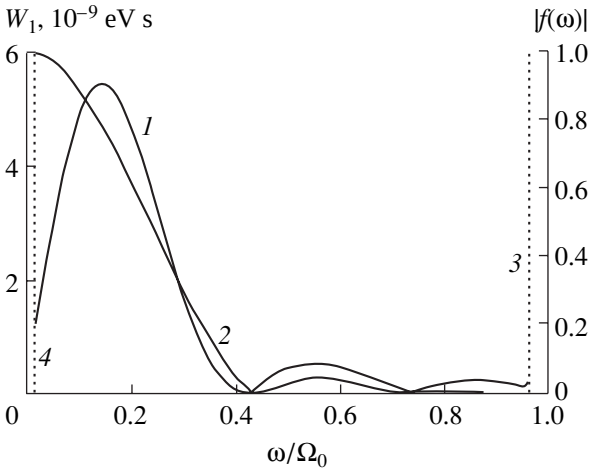

Fig. 1. Plots of $W_1(\omega)$ and $|f(\omega)|$ for $a = 10^{-2}$ cm, $b = 5 \times 10^{-3}$ cm, and $|\mathbf{\rho}| = 1$ cm in the case of a semi-infinite semiconductor.

From Fig. 1, we can see that, at $\omega = 0$, the function $|f(\omega)|$ has a maximum value of unity, $|f(\omega)| = 1$, and, at $\omega = \omega_{\max}$, it is close to unity, $|f(\omega_{\max})| \approx 0.8$. The latter circumstance indicates that the emitted radiation is almost perfectly coherent: all bunch electrons emit radi-

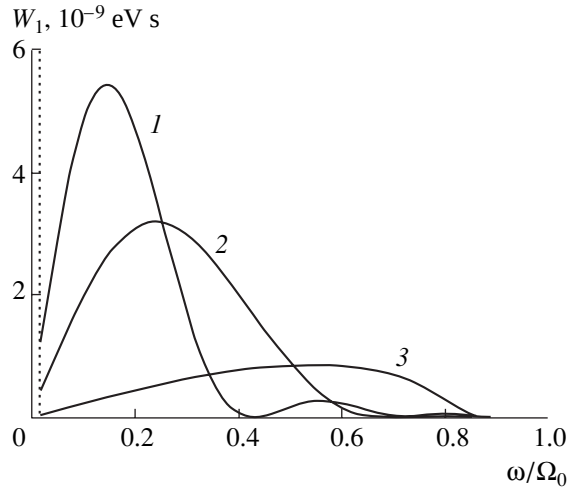

Fig. 2. Plots of $W_1(\omega)$ for $a = 10^{-2}$ cm; $|\boldsymbol{\rho}| = 1$ cm; and $b =$ (*1*) 5×10^{-3}, (*2*) 2×10^{-3}, and (*3*) 10^{-3} cm in the case of a semi-infinite semiconductor.

ation coherently, so that the total radiation coming from the bunch is far more intense than the sum of the waves emitted by individual electrons. In fact, in the case at hand, we have $q_{\text{eff}} = enV_b|f(\omega_{\max})| \approx 1.5 \times 10^{-3}$ esu ~ $enV_b \approx 2 \times 10^{-3}$ esu, so that the bunch radiates as a coherent entity, and we can write $W_1 \propto (nV_b)^2$.

For $a/b \sim 1$ and $v \ll c$, the inequality $(\omega b/v)^2 \gg |a\kappa|^2$ is satisfied and the expression $\left|\sqrt{(\omega b/v)^2 + (a\kappa)^2}\right|$ can be replaced by its approximation $\omega b/v = 2\pi b/\lambda_{VK}$, where $\lambda_{VK} = 2\pi v/\omega$ is the Van Kampen wavelength [11]. The first (main) maximum in the function $|f(\omega)|$ occurs at $\omega = 0$, i.e., at $\omega b/v \ll 1$ ($b \ll \lambda_{VK}/2$), in which case the bunch length $2b$ is shorter than the wavelength of the Van Kampen wave. For $\omega b/v \gg 1$, the function $|f(\omega)|$ has maxima at $\omega b/v \approx \pi k$ ($b \approx k\lambda_{VK}/2$), where k is an integer much larger than unity. This indicates that such maxima occur when the bunch length $2b$ is much longer than the Van Kampen wavelength. Numerical estimates show that the first peak in the dependence $W_1(\omega)$ occurs under the condition $\omega b/v \approx \pi/2$ (or, equivalently, $2b \approx \lambda_{VK}/2$), in which case the bunch is as long as one-half of the Van Kampen wave. The positions of the second and subsequent peaks in the dependence $W_1(\omega)$ almost exactly coincide with those of the corresponding maxima in the function $|f(\omega)|$. At the frequency corresponding to the first peak in the spectral energy density, the function $|f(\omega)|$ is close to unity, $|f(\omega_{\max})| \approx 0.8$, so that the transition radiation at this frequency can be considered almost coherent. The above analysis allows us to draw the following conclusions: First, the transition radiation emitted in the form of surface waves by an electron bunch comprises a pulse whose spectral energy density comprises a sequence of oscillations with sharply decreasing amplitudes. Second, for nonrelativistic ellipsoidal bunches with nearly the same semiaxes a and b (i.e., for $a/b \sim 1$), the peaks in the radiation spectral energy density occur when the bunch length and the Van Kampen wavelength satisfy certain resonance conditions. Note that, in the general case (e.g., in the case of bunches such that $a \gg b$), and even for $v \ll c$, these resonance conditions contain the bunch semiaxes, the Van Kampen wavelength, and the wavelength $2\pi/\kappa'$ of the emitted radiation. Thus, for $\omega b/v \sim a\kappa'$ and $\kappa' \gg \kappa''$, the first peak in the spectral energy density occurs under the condition $\left|\sqrt{(\omega b/v)^2 + (a\kappa)^2}\right| \approx \left|\sqrt{(\omega b/v)^2 + (a\kappa')^2}\right| \approx \pi/2$, and, for $\omega b/v \gg 1$, the peaks in $W_1(\omega)$ occur under the conditions $\left|\sqrt{(\omega b/v)^2 + (a\kappa')^2}\right| \approx \pi k$, where k is an integer much larger than unity.

Figure 2 shows the plots of $W_1(\omega)$ for $|\boldsymbol{\rho}| = 1$ cm and for bunches with $a = 10^{-2}$ cm and with $b =$ (*1*) 5×10^{-3}, (*2*) 3×10^{-3}, and (*3*) 10^{-3} cm. From this figure, we see that, as the longitudinal bunch dimension decreases, the first peak in the spectral energy density is displaced toward higher frequencies and its amplitude becomes smaller. The change in the transverse bunch dimension leads merely to a change in the heights of the peaks (because $W_1 \propto a^4$) but does not significantly affect their positions. This latter circumstance stems from the inequality $\omega_{\max} b/v \gg a\kappa'_{\max}$, which is satisfied for nonrelativistic bunches such that $a/b \sim 1$. For $a \gg b$, we have $\omega_{\max} b/v \sim a\kappa'_{\max}$ (which holds for $v \ll c$), so that the increase in the transverse bunch dimension a leads not only to an increase in the height of the first peak in the spectral energy density but also to its displacement toward lower frequencies. In this connection, we note that the displacement reduces the ratio $|\varepsilon'(\omega_{\max})/\varepsilon''(\omega_{\max})|$. Numerical estimates show that, for $\nu = 10^{11}$ s^{-1} and for bunches with $a \approx 10^{-2}$ cm and $b \leq 5 \times 10^{-3}$ cm, this ratio is $|\varepsilon'(\omega_{\max})/\varepsilon''(\omega_{\max})| \sim 10$. Consequently, the slower the electron momentum relaxation rate in the semiconductor, the larger the dimensions of the bunches that can be used to generate high-intensity pulses of transition radiation in the form of surface waves.

Numerical analysis of expression (12) for the transition radiation energy shows that, with increasing bunch length, the radiation energy S_1 increases monotonically in the range of b values satisfying the condition $\kappa'_{\max}|\boldsymbol{\rho}| \gg 1$. In this range of b values, the generation efficiency θ, defined as the ratio of the transition radiation energy to the kinetic energy of the bunch electrons, has a maximum. Figure 3 shows the plots of $S_1(b)$ and $\theta(b)$ for $a = 10^{-2}$ cm and $|\boldsymbol{\rho}| = 1$ cm. The presence of a maximum in the dependence $\theta(b)$ can be explained as being due to the fact that, as the bunch length increases above a certain value, the transition radiation becomes

less coherent and the kinetic energy of the bunch electrons increases faster than does the radiation energy.

3. GENERATION OF PULSES OF SURFACE WAVES PROPAGATING ALONG A SEMICONDUCTOR PLATE

Here, we consider a semiconductor plate in vacuum. The plate is bounded by the planes $z = -d$ and $z = 0$. An electron bunch moves along the normal to the plate. We assume that the energy lost by the bunch is small in comparison to its kinetic energy, so that its velocity can be considered constant. For the semiconductor plate, we adopt the same parameter values as those for the semi-infinite semiconductor. As in the previous section, the radiation fields can be found from the continuity conditions for the tangential field components $\mathbf{E}(\omega, \boldsymbol{\kappa}) = \mathbf{E}^b(\omega, \boldsymbol{\kappa}) + \mathbf{E}^r(\omega, \boldsymbol{\kappa})$ and for the normal component of the electric induction vector, $\mathbf{D}(\omega, \boldsymbol{\kappa}) = \varepsilon(\omega)\mathbf{E}(\omega, \boldsymbol{\kappa})$, at the boundaries $z = -d$ and $z = 0$ [12]:

$$E_z^r(\mathbf{r}, t) = \frac{ie}{\pi}\int\frac{\kappa^3}{\omega}\chi(\omega, \kappa)J_0(\kappa\rho)F(\omega, \kappa) \times \exp[-(\xi_1 z + i\omega t)]d\kappa d\omega, \quad (13)$$

$$H_\varphi^r(\mathbf{r}, t) = \frac{e}{\pi c}\int\frac{\kappa^2}{\omega}\chi(\omega, \kappa)J_1(\kappa\rho)F(\omega, \kappa) \times \exp[-(\xi_1 z + i\omega t)]d\kappa d\omega, \quad (14)$$

where $J_0(x)$ and $J_1(x)$ are zero- and first-order Bessel functions, respectively, and

$$\chi(\omega, \kappa) = \chi_1(\omega, \kappa)/\chi_2(\omega, \kappa), \qquad \xi_l = \sqrt{\kappa^2 - \omega^2\varepsilon_l/c^2}, \quad (15)$$

$$\chi_1(\omega, \kappa) = (\xi_2 - \varepsilon\xi_1)(\varepsilon\gamma_3 + \xi_2\gamma_4) \times \exp(-d\xi_2) + (\xi_2 + \varepsilon\xi_1)(\varepsilon\gamma_3 - \xi_2\gamma_4)\exp(d\xi_2) + 2\varepsilon\xi_2(\gamma_1 + \xi_1\gamma_2), \quad (16)$$

$$\chi_2(\omega, \kappa) = -\Delta_0(\omega, \kappa)\Delta_1(\omega, \kappa)\Delta_2(\omega, \kappa), \quad (17)$$

$$\Delta_0(\omega, \kappa) = (\xi_2 + \varepsilon\xi_1)^2\exp(d\xi_2) - (\xi_2 - \varepsilon\xi_1)^2\exp(-d\xi_2), \quad (18)$$

$$\Delta_1(\omega, \kappa) = \left[\kappa^2 + \frac{\omega^2}{v^2}(1 - \beta^2)\right], \qquad \Delta_2(\omega, \kappa) = \left[\kappa^2 + \frac{\omega^2}{v^2}(1 - \beta^2\varepsilon)\right], \quad (19)$$

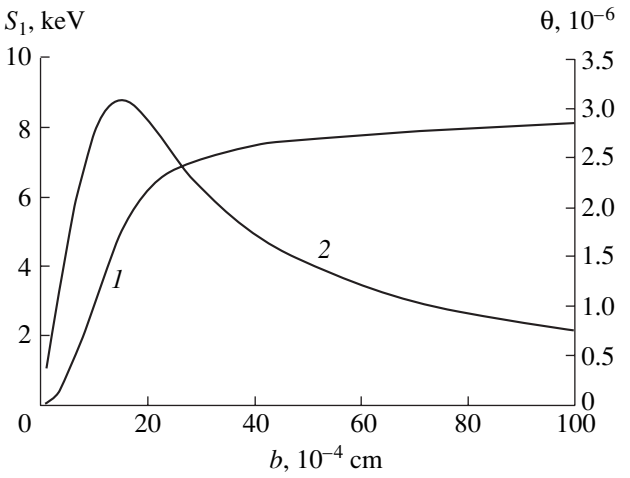

Fig. 3. Plots of (*1*) $S_1(b)$ and (*2*) $\theta(b)$ for $a = 10^{-2}$ cm and $|\boldsymbol{\rho}| = 1$ cm in the case of a semi-infinite semiconductor.

$$\gamma_1 = -i\frac{\omega}{v}\frac{1-\varepsilon}{\varepsilon}\left[\kappa^2 + \frac{\omega^2}{v^2}(1 - \beta^2\varepsilon - \beta^2)\right]\exp\left(-i\frac{\omega}{v}d\right), \qquad \gamma_2 = -\frac{\omega^2}{c^2}(1-\varepsilon)\exp\left(-i\frac{\omega}{v}d\right), \quad (20)$$

$$\gamma_3 = i\frac{\omega}{v}\frac{1-\varepsilon}{\varepsilon}\left[\kappa^2 + \frac{\omega^2}{v^2}(1 - \beta^2\varepsilon - \beta^2)\right], \qquad \gamma_4 = -\frac{\omega^2}{c^2}(1-\varepsilon). \quad (21)$$

The dispersion relation for surface waves is determined from the condition $\Delta_0 = 0$:

$$\Delta_0(\omega, \kappa) = (\xi_2 + \varepsilon\xi_1)^2\exp(d\xi_2) - (\xi_2 - \varepsilon\xi_1)^2\exp(-d\xi_2) = 0. \quad (22)$$

As in the case of a semi-infinite semiconductor, we consider the Fano modes, for which $\varepsilon'(\omega) < -1$ and, by virtue of the condition $|\varepsilon'(\omega)| \gg \varepsilon''(\omega)$, the Poynting vector lies almost entirely in the plane of the boundary. The solutions to dispersion relation (22) have the form

$$\varepsilon(\omega) = -\frac{\xi_2}{\xi_1}\coth\left(\xi_2\frac{d}{2}\right), \quad \varepsilon(\omega) = -\frac{\xi_2}{\xi_1}\tanh\left(\xi_2\frac{d}{2}\right). \quad (23)$$

These solutions were investigated in detail in [13, 14].

Let us determine the energy expended by a charged bunch to emit a surface wave along the plate surface in the region $z > 0$ in vacuum. Taking into account the poles in the integrands in expressions (13) and (14) that correspond to the roots of the equation $\Delta_0 = 0$, we obtain the following expression for the electromagnetic energy flux through the side surface of a circular cyl-

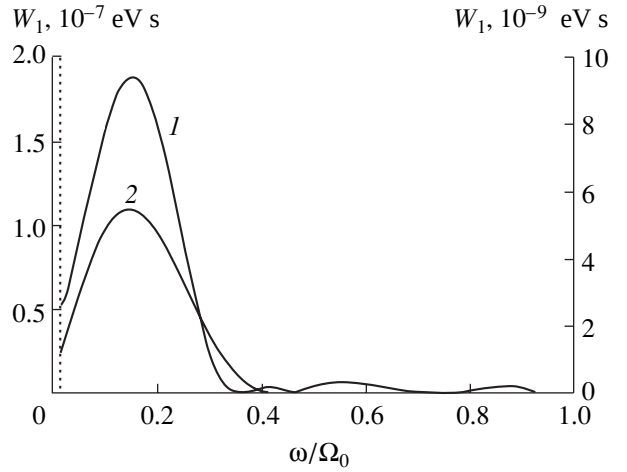

Fig. 4. Plots of $W_1(\omega)$ for $a = 10^{-2}$ cm, $b = 5 \times 10^{-3}$ cm, and $|\boldsymbol{\rho}| = 0.1$ cm in the case of (*1*) a semiconductor plate and of (*2*) a semi-infinite semiconductor.

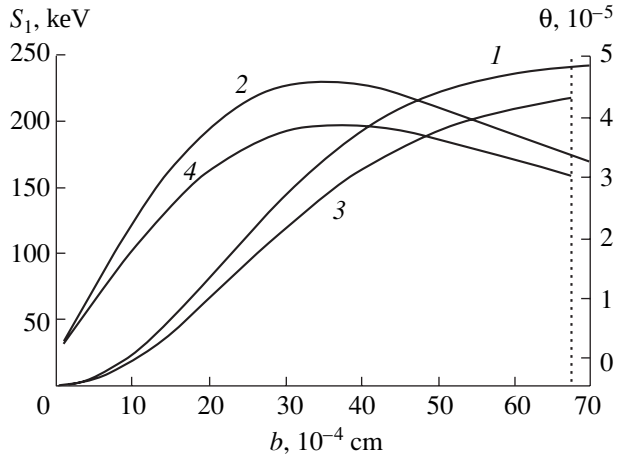

Fig. 5. Plots of (*1*, *3*) $S_1(b)$ and (*2*, *4*) $\theta(b)$ for $a = 10^{-2}$ cm and $|\boldsymbol{\rho}| =$ (*1*, *2*) 0.1 and (*3*, *4*) 0.12 cm in the case of a semiconductor plate.

inder with its axis pointing in the direction of the velocity **v**:

$$S_1(|\boldsymbol{\rho}| \longrightarrow \infty) = e^2 \sum_l \int_{\varepsilon'(\omega) < -1} \frac{\kappa_l' |\kappa_l|^3 |\chi_1(\omega, \kappa_l)|^2 |F(\omega, \kappa_l)|^2}{\omega \xi_{1l}' |(\partial \Delta_0/\partial \kappa)_l|^2 |\Delta_1(\omega, \kappa) \Delta_2(\omega, \kappa)|^2} \times \exp[-2\kappa_l'' \rho] d\omega, \quad (24)$$

where l is the index of the root of dispersion relation (22), $\xi_{1l}' = \mathrm{Re}\{\xi_{1l}\} > 0$, and $\kappa_l'' = \mathrm{Im}\{\kappa_l\} > 0$. Numerical analysis of expression (24) shows that, in the frequency range in which $\varepsilon(\omega) < -1$, the largest contribution to the radiation energy comes from the low-frequency branch of the spectrum [13, 14]. In the frequency range in which $-1 < \varepsilon(\omega) < 0$, the wave damping is so strong that the radiation energy is negligibly low in comparison with that in the frequency range in which $\varepsilon(\omega) < -1$.

In Fig. 4, curve *1* shows the plot of $W_1(\omega)$ calculated for $d = 10^{-4}$ cm, $|\boldsymbol{\rho}| = 0.1$ cm, $a = 10^{-2}$ cm, and $b = 5 \times 10^{-3}$ cm in the case of a semiconductor plate (left coordinate axis) and curve *2* shows an analogous plot calculated for the same values of a, b, and $|\boldsymbol{\rho}|$ in the case of a semi-infinite semiconductor (right coordinate axis). We see that, in the case of a plate, the first peak in the spectral energy density is more than one order of magnitude higher than that in the case of a semi-infinite semiconductor and, moreover, is more highly localized in frequency than the latter. In the case of a plate, the peaks in the spectral energy density become lower and are displaced toward higher frequencies as the bunch length increases, just as in the case of a semi-infinite semiconductor. Note that the leftmost points in the plots of $W_1(\omega)$ correspond to the frequency $\omega = \omega_{\min}$, below which the inequality $|\varepsilon'(\omega)| \gg \varepsilon''(\omega)$ fails to hold and radiative modes are generated. The analysis dealing with the presence of peaks in the dependence $W_1(\omega)$ in the case of a semi-infinite semiconductor is also valid for a semiconductor plate. In addition, the behavior of the spectral energy density as a function of the transverse bunch dimension does not differ qualitatively between the two cases. It should be noted, however, that the displacement of the peak in the spectral energy density toward lower frequencies with increasing a (for bunches such that $a \gg b$) can result in a situation when, in the range $\omega > \omega_{\min}$, there will be only the descending part of the first peak in the dependence $W_1(\omega)$ and its oscillating tail. For the above parameters of the semiconductor, and for bunches with $b \le 10^{-2}$ cm (at $\rho \sim 0.1$ cm), this situation arises when the transverse bunch dimension lies in the range $a \ge 10^{-2}$. An increase in $|\boldsymbol{\rho}|$ also causes the first peak in the dependence $W_1(\omega)$ to be displaced toward the radiative range. Thus, for a, $b \le 10^{-2}$ cm and $d = 10^{-4}$ cm, the first peak in the dependence $W_1(\omega)$ falls in this range at $|\boldsymbol{\rho}| \sim 1$ cm.

Figure 5 shows the plots of the radiation energy $S_1(b)$ (curves *1*, *3*) and the generation efficiency $\theta(b)$ (curves *2*, *4*) for $d = 10^{-4}$ cm and $a = 10^{-2}$ cm and for $|\boldsymbol{\rho}| = 0.1$ cm (curves *1*, *2*) and $|\boldsymbol{\rho}| = 0.12$ cm (curves *3*, *4*). The plots are calculated for the range of b values such that $\kappa_{\max}' |\boldsymbol{\rho}| \gg 1$ (for $|\boldsymbol{\rho}| = 0.12$ cm, this range is to the left of the vertical dashed line). From Fig. 5, we can see that the radiation energy increases monotonically as the longitudinal bunch dimension b increases and there are peaks in the dependence $\theta(b)$. In the case at hand, we have $b_{\max} \gg d$. The value of $b_{\max}$ increases with increasing $|\boldsymbol{\rho}|$ (i.e., with increasing distance from the point at

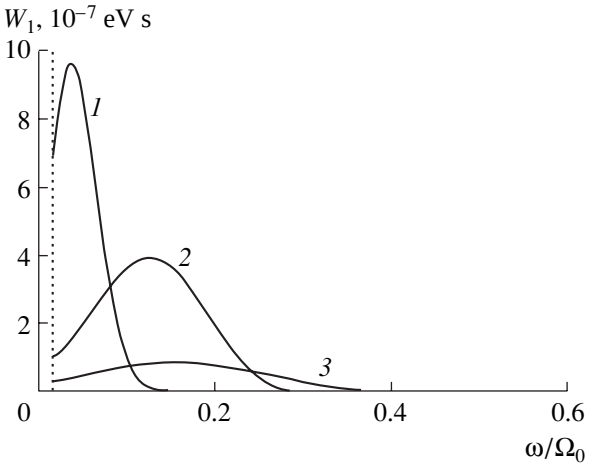

Fig. 6. Plots of $W_1(\omega)$ in the case of a semiconductor plate for $a = 10^{-2}$ cm; $b = 5 \times 10^{-3}$ cm; $|\boldsymbol{\rho}| = 0.1$ cm; and $d =$ (*1*) 10^{-5}, (*2*) 5×10^{-5}, and (*3*) 2×10^{-4} cm.

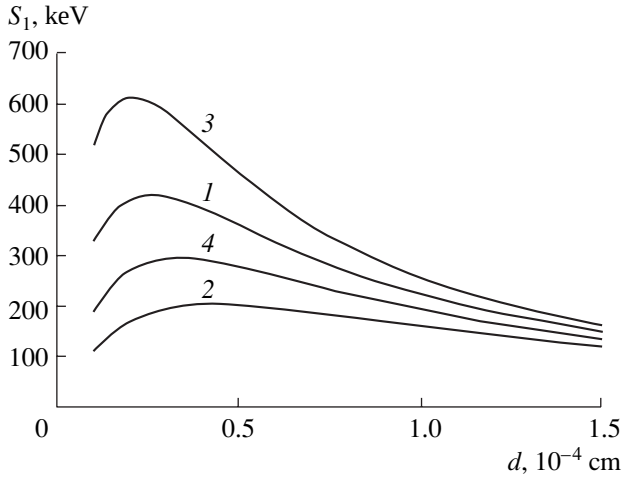

Fig. 7. Plots of $S_1(d)$ for $a = 10^{-2}$ cm, $b = 5 \times 10^{-3}$ cm, and different values of $|\boldsymbol{\rho}|$ and ν: (*1*) $\nu = 10^{11}$ s^{-1} and $|\boldsymbol{\rho}| = 0.1$ cm, (*2*) $\nu = 10^{11}$ s^{-1} and $|\boldsymbol{\rho}| = 0.15$ cm, (*3*) 8×10^{10} s^{-1} and $|\boldsymbol{\rho}| = 0.1$ cm, and (*4*) $\nu = 8 \times 10^{10}$ s^{-1} and $|\boldsymbol{\rho}| = 0.15$ cm.

which the bunch flies into the plate to the point of observation of the pulse).

We now examine how the dependence $W_1(\omega)$ and the radiation energy change with plate thickness. Figure 6 shows the plots of $W_1(\omega)$ calculated for $|\boldsymbol{\rho}| = 0.1$ cm, $a = 10^{-2}$ cm, and $b = 5 \times 10^{-3}$ cm and for $d =$ (*1*) 10^{-5}, (*2*) 5×10^{-5}, and (*3*) 2×10^{-4} cm. We can see that, as the plate thickness decreases, the peak increases in height, becomes narrower, and is displaced toward lower frequencies. In turn, as the plate thickness decreases within the range indicated above, the radiation energy first increases, reaches its maximum value, and then decreases. Figure 7 shows the plots of $S_1(d)$ calculated for $a = 10^{-2}$ cm and $b = 5 \times 10^{-3}$ cm and also for $\nu = 10^{11}$ s^{-1} and $|\boldsymbol{\rho}| =$ (*1*) 0.1 and (*2*) 0.15 cm and for $\nu = 8 \times 10^{10}$ s^{-1} and $|\boldsymbol{\rho}| =$ (*3*) 0.1 and (*4*) 0.15 cm. We can see that there are peaks in the radiation energy. The appearance of these peaks can probably be explained by the fact that, as d increases, the region where the transition radiation is generated becomes larger and, consequently, the radiation energy S_1 becomes higher. On the other hand, an increase in d is accompanied by an increase in the energy losses within the plate, so that the radiation energy S_1 decreases. The thickness $d_{max} = d(S_{1max})$ can be regarded as the plate thickness for which the contributions from these two effects are equal. From Fig. 7, we can also see that, as $|\boldsymbol{\rho}|$ increases (ν being constant) and as ν increases ($|\boldsymbol{\rho}|$ being constant), the peaks in the radiation energy decrease in height and are displaced toward larger values of d. A decrease in the heights of the peaks in the radiation energy with increasing $|\boldsymbol{\rho}|$ at a fixed value of ν (curves *1*, *2* and curves *3*, *4*) and with increasing ν at a fixed value of $|\boldsymbol{\rho}|$ (curves *3*, *1* and curves *4*, *2*) is directly associated with an increase in the dissipative energy losses within the plate. In both cases, the displacement of the peaks toward larger values of d can be explained as being due to the increase in the size of the region where the transition radiation is generated. For $\nu = 10^{11}$ cm, the plots of the generation efficiency $\theta(d)$ are qualitatively similar in shape to the plots of the radiation energy $S_1(d)$, in which case the generation efficiency is on the order of $\theta \sim 10^{-5}$–10^{-4}. The peaks in the dependence $\theta(d)$ increase in height with decreasing $|\boldsymbol{\rho}|$ and ν, as is the case with the dependence $S_1(d)$.

Numerical calculations show that, at fixed values of $|\boldsymbol{\rho}|$ and ν, the heights and positions of the peaks in $S_1(d)$ and $\theta(d)$ also change with changing a and b. Thus, an increase in the bunch dimensions leads to an increase in the heights of the peaks in S_1 and θ and to a displacement of the peaks toward smaller values of d. In this case, the heights of the peaks are more sensitive to the transverse bunch dimension, while the positions of the peaks are more sensitive to the longitudinal bunch dimension. The latter circumstance stems from the nonrelativistic nature of the bunch motion. The displacement of the peaks in $S_1(d)$ and $\theta(d)$ toward smaller values of d can be explained by the fact that, for a sufficiently large bunch, the thinner the plate, the more coherent the transition radiation. On the other hand, as $d \longrightarrow 0$, the peaks in the spectral energy density of the transition radiation are displaced toward the radiative spectral range ($\omega_{max} < \omega_{mim}$), while, in the nonradiative range ($\omega > \omega_{min}$), there remains only the oscillating tail of the dependence $W_1(\omega)$. Consequently, although the transition radiation becomes more coherent as $d \longrightarrow 0$, the radiation energy begins to decrease for d values smaller than a certain critical value below which $\omega_{max} < \omega_{min}$.

4. CONCLUSIONS

Hence, we have theoretically investigated the transition radiation generated in the form of electromagnetic surface waves by a nonrelativistic electron bunch as it crosses the vacuum–semiconductor interface or passes through a thin semiconductor plate in vacuum.

The bunch is assumed to have the shape of an ellipsoid of revolution, with a uniform charge density distribution over its volume, and to move along the normal to the interface between the two media. The energy characteristics of the transition radiation were calculated with allowance for dissipative energy losses within the semiconductor. It has been shown that the spectrum of the transition radiation generated in the form of surface waves comprises a sequence of oscillations with sharply decreasing amplitudes and a pronounced first peak, whose width is comparable to its mean frequency. It has been established that, in order for the peaks to appear in the radiation spectrum, the bunch dimensions, the radiation wavelength, and the wavelength of the Van Kampen wave should satisfy certain resonance conditions. It has been found that, in each of the two cases under consideration, the generation efficiency, which is equal to the ratio of the radiation energy to the kinetic energy of the bunch electrons, is maximum for a bunch of certain dimensions. That this maximum does indeed exist is attributed to the fact that, as the bunch length increases above a certain value, the transition radiation becomes less coherent and the total kinetic energy of the bunch electrons increases faster than does the radiation energy. For a semiconductor plate, we have also investigated how the radiation energy and generation efficiency depend on the plate thickness at prescribed bunch dimensions. It has been demonstrated that each dependence has a maximum, which can be explained as being due the competition between the two effects: as the plate thickness increases, on the one hand, the region where the radiation is generated becomes larger, so that the radiated energy increases, and, on the other hand, the dissipative energy losses within the plate become higher.

It has also been concluded that, when the dissipation of radiation energy in the semiconductor is taken into account, the requirement for the Poynting vector (which describes the energy flux of the transition radiation pulses) to lie almost entirely in the plane of the interface between the two media imposes restrictions on the maximum bunch dimensions.

ACKNOWLEDGMENTS

We are grateful to V.I. Karas' for a discussion of the results obtained and his useful remarks.

REFERENCES

1. V. L. Ginzburg and V. N. Tsytovich, *Transition Radiation and Transition Scattering* (Nauka, Moscow, 1984; Hilger, New York, 1990).
2. M. L. Ter-Mikaelyan, Usp. Fiz. Nauk **171**, 597 (2001) [Phys. Usp. **44**, 571 (2001)].
3. V. A. Balakirev and G. L. Sidel'nikov, Zh. Tekh. Fiz. **69** (10), 90 (1999) [Tech. Phys. **44**, 1209 (1999)].
4. V. A. Balakirev, I. N. Onishchenko, D. Yu. Sidorenko, and G. V. Sotnikov, Zh. Tekh. Fiz. **72** (2), 88 (2002) [Tech. Phys. **47**, 227 (2002)].
5. B. M. Bolotovskiĭ and A. V. Serov, Zh. Tekh. Fiz. **72** (1), 3 (2002) [Tech. Phys. **47**, 1 (2002)].
6. V. Ya. Éĭdman, Izv. Vyssh. Uchebn. Zaved. Radiofiz. **8**, 188 (1965).
7. B. G. Martin and R. F. Wallis, Phys. Rev. B **13**, 3339 (1976).
8. B. G. Martin, A. A. Maradudin, and R. F. Wallis, Surf. Sci. **77**, 416 (1978).
9. N. L. Dmitruk, V. G. Litovchenko, and V. L. Strizhevskiĭ, *Surface Polaritons in Semiconductors and Dielectrics* (Naukova Dumka, Kiev, 1989).
10. R. S. Brazis, Litov. Fiz. Sb. **21** (4), 73 (1981).
11. A. S. Kingsep, *Introduction to Nonlinear Plasma Physics* (Mosk. Fiz.-Tekh. Inst., Moscow, 1996).
12. V. E. Pafomov, Tr. Fiz. Inst. Akad. Nauk SSSR **16**, 94 (1961).
13. N. N. Beletskiĭ, E. A. Gasan, and V. M. Yakovenko, Izv. Vyssh. Uchebn. Zaved. Radiofiz. **30**, 1391 (1987).
14. N. N. Beletskiĭ, V. M. Svetlichnyi, D. D. Khalameĭda, and V. M. Yakovenko, *Microwave Phenomena in Inhomogeneous Semiconductor Structures* (Naukova Dumka, Kiev, 1991).

Translated by I.A. Kalabalyk

Plasma Physics Reports, Vol. 30, No. 6, 2004, pp. 527–530. Translated from Fizika Plazmy, Vol. 30, No. 6, 2004, pp. 571–574.

PLASMA DIAGNOSTICS

Density Measurements in a Tenuous Plasma by a High-Frequency Resonator with a Periodic Structure

B. I. Ivanov and V. P. Prishchepov

National Science Center, Kharkov Institute of Physics and Technology, Kharkov, 61108 Ukraine

Received July 23, 2003; in final form, October 1, 2003

Abstract—It is proposed to measure plasma densities in the range of 10^5–10^9 cm^{-3} by a high-frequency resonator with a periodic structure consisting of annual high-frequency electrodes mounted on oppositely directed racks. The method proposed substantially increases the proportionality factor between the electron density and the shift of the resonator eigenfrequency. This factor is determined by the calibration method using an electron beam with given parameters. The calibration ensures an accuracy of about 10% for density measurements in a plasma produced by a 5-MeV proton beam propagating in air at pressures of 10^{-2}–10^{-5} torr. © *2004 MAIK "Nauka/Interperiodica".*

The resonator method for measuring the plasma density is widely used in plasma diagnostics in the density range of $n \sim 10^8$–10^{14} cm^{-3} [1, 2]. Unfortunately, the high-frequency hollow cylindrical resonators that are usually used for this purpose cannot be employed at $n \ll 10^8$ cm^{-3}. However, nonintrusive electron density measurements in tenuous plasmas are of primary importance, e.g., in space research, beam physics, electronics, etc. Thus, in [3], it was shown that probe measurements in space plasma (which are traditionally used to determine the plasma density in this case) often give erroneous results. For this reason, it is desirable to verify probe measurements in space plasma by the nonintrusive resonator method. This, however, requires that the sensitivity of the method be substantially increased.

In the absence of an external magnetic field or when this field is present but the longitudinal (magnetic field–aligned) component of the high-frequency electric field is much larger than its transverse component ($E_z^2 \gg E_r^2$), the plasma permittivity is described by the well-known expression $\varepsilon = 1 - \omega_0^2/\omega^2$. In this case, the electron density measured by the resonator method is determined as

$$n \cong \frac{2f^2}{10^8 F}\frac{\Delta f}{f}, \qquad (1)$$

where

$$F = \int_{V_P} \mathbf{E}^2 dV / \int_{V_R} \mathbf{E}^2 dV$$

is the form factor, f is the resonator eigenfrequency, Δf is the shift of the eigenfrequency in the presence of plasma, E is the high-frequency electric field, V_P is the plasma volume, and V_R is the resonator volume.

It follows from Eq. (1) that the minimum electron density that can be measured by this method is equal to

$$n_{\min} \cong \frac{2f\Delta f_{\min}}{10^8 F} \cong \frac{2f^2}{10^9 FQ}, \qquad (2)$$

where, as usual, it is assumed that $\Delta f_{\min} \cong f/(10Q)$ and Q is the resonator Q factor.

The plasma is usually located at the resonator axis, the plasma radius being much smaller than the resonator radius. In this case, we have $E_z^2 \gg E_r^2$ inside the plasma. For typical diagnostic parameters ($f \approx 3$ GHz, $Q \approx 3000$, and $F \approx 0.03$), the minimum measurable plasma density is $n_{\min} \sim 10^8$ cm^{-3}. To decrease the minimum measurable plasma density, it is necessary to decrease the resonator eigenfrequency and increase the resonator Q factor and form factor.

Our experiments have shown that a high-frequency resonator with a specific periodic structure meets these conditions. When the fundamental mode of the resonator is excited, the high-frequency currents flowing along the inner surface of the cylindrical wall correspond to the H_{111} oscillation mode and the internal resonator structure produces a longitudinal spatially periodic high-frequency electric field on the resonator axis. This periodic structure consists of annual high-frequency electrodes mounted on oppositely directed comb- or pin-type racks (see Fig. 1). These slow-wave structures, which were first proposed at the Kharkov Institute of Physics and Technology, are now being used in linear ion accelerators [4]. Due to such geometry, the fundamental frequency of a resonator with the same dimensions is substantially reduced because of the additional capacitance and inductance of the periodic structure, whereas the form factor substantially increases because the longitudinal high-frequency field is concentrated near the resonator axis. For this type of

1063-780X/04/3006-0527$26.00

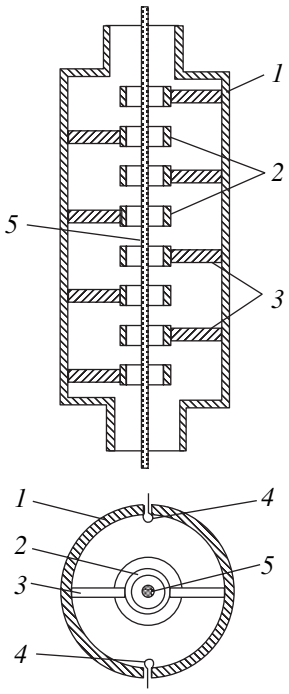

Fig. 1. Schematic of the resonator: (*1*) resonator housing, (*2*) annual high-frequency electrodes, (*3*) oppositely directed electrode racks, (*4*) high-frequency coupling loops, and (*5*) plasma column or electron beam.

resonators, the problems of a decrease in the fundamental frequency and an increase in the high-frequency longitudinal field inside the annual high-frequency electrodes are discussed in [4].

A drawback of the method is that the form factor is rather difficult to calculate. To overcome this drawback, we used a specific calibration method. The method is based on the fact that, in a certain (rather wide) parameter range, an electron beam has the same high-frequency characteristics as the plasma (in particular, when the beam velocity is much smaller than the wave phase velocity, the Doppler shift of the probing frequency can be ignored). To find the form factor, a pulsed electron beam with known parameters (and, therefore, with a known electron density) was passed along the resonator axis at a residual gas pressure of 5×10^{-7} torr. The shift of the resonator eigenfrequency was measured for different modes at different electron beam densities, while the form factor F was calculated by formula (1). It should be noted that the increase in the gas pressure from 5×10^{-7} to 3×10^{-6} torr had no effect on the measurement results; hence, the density of the plasma produced through the ionization of the residual gas by the electron beam was negligibly small. Estimates performed with account taken of the ionization cross sections and the escape of secondary electrons from the plasma show that the plasma density is one to two orders of magnitude lower than the electron beam density. The calibration with an electron beam was performed for the fundamental mode of the resonator with a periodic structure and for several modes of the hollow resonator. The parameters of the resonator with a periodic structure were as follows: the length was 30 cm; the diameter was 10 cm; the diameter and length of the annual high-frequency electrodes were 3 cm and 1.8 cm, respectively; the distance between the electrodes was 1.7 cm; and the structure period was 7 cm. In our experiments, oppositely directed comb-type electrode racks were used. The frequency of the fundamental resonator mode was 628 MHz, the Q factor was Q = 4500, and the wave phase velocity was 4.4×10^9 cm/s. The parameters of the calibration beam were as follows: the energy was 100 eV, the current was 1–10 mA, the duration of the flat top of the current pulse was up to 25 μs, the diameter was 1 cm; and the electron density was $n \sim 10^7$–10^8 cm^{-3}. Similar measurements were performed for a hollow resonator in the absence of a periodic structure. In this case, the resonator eigenfrequency was in the range 1700–3800 MHz, the Q factor was 3000–6000, the electron beam energy was 10 keV, the current was 0.1–1 A, the duration of the flat top of the current pulse was up to 20 μs, the beam diameter was 1 cm; and the electron beam density was $n \sim 10^8$–10^9 cm^{-3}. In both cases, the electron beam propagated in a uniform magnetic field of $H_z \approx 500$ Oe. The condition $E_r^2 \ll E_z^2$ was satisfied for the longitudinal modes of the hollow resonator (E modes) and for the fundamental mode of the resonator with a periodic structure. It should be noted that, at low electron densities and temperatures ($n < 3 \times 10^7$ cm^{-3}, $T_e \sim 0.1$ eV), the calibration can be performed at rather low magnetic fields such that $f_0^2 \ll f_c^2 \ll f^2$, where $f_0 = \omega_0/2\pi$ is the plasma frequency and f_c = 2.8 H [Oe] MHz is the electron cyclotron frequency ($H \approx 70$ Oe). Plasma density measurements can be performed in the absence of a magnetic field, because the plasma permittivity for the transverse component of the high-frequency electric field is almost the same as for the longitudinal component (in this case, one can assume that $E_r^2 \sim E_z^2$ and the plasma radius can be relatively large). For a hollow resonator, the calibration was also performed for the transverse high-frequency modes (H modes). If, in this case, $f^2 \sim f_c^2$, then the plasma density measurements must be performed at the same magnetic field as that used for calibration. As a result, we obtained a series of linear dependences of the shift of the resonator eigenfrequency on the electron density. These dependences were used to determine the form factors (see table). It can be seen from the table that the measured eigenfrequencies of a hollow resonator are lower than the calculated ones by 5–10% because there were holes (equipped by cutoff waveguides) at the resonator ends that served for pumping-out and the injection of the electron beam and plasma (see Fig. 1). In particular, when the diameter and length of the hollow resonator

Table

Oscillation mode / Hollow resonator	Frequency, MHz	Form factor (theory)	Form factor (experiment)	Range of density measurements, cm^{-3}
E_{010}	2076	0.036	0.036	10^8–10^{10}
E_{012}	2314	0.030	0.033	10^8–10^{10}
E_{013}	2568	0.025	0.027	10^8–10^{10}
E_{014}	2887	0.020	0.023	10^8–10^{10}
E_{015}	3253	0.015	0.017	10^8–10^{10}
E_{016}	3634	0.0090	0.0012	10^8–10^{10}
H_{011}	3424	0.0011	0.0015	10^9–10^{10}
H_{211}	2863	–	0.0003	10^9–10^{10}
H_{111}	1750	–	0.03	10^8–10^{10}
H_{113}	2195	–	0.035	10^8–10^{10}
H_{115}	2898	–	0.025	10^8–10^{10}
Resonator with a periodic structure	628	–	0.15	10^6–10^8

are respectively 10 and 30 cm, the calculated resonance frequencies for the oscillation modes E_{010}, E_{012}, E_{015}, H_{011}, and H_{111} are 2.30, 2.51, 3.40, 3.69, and 1.83 GHz, respectively.

The measurement results allow us to draw the following conclusions:

(i) For the hollow resonator, the measured form factors agree with the calculated ones, which confirms the validity of the calibration procedure.

(ii) The eigenfrequency of the resonator with a periodic structure is three to four times lower than that of the hollow resonator with the same size.

(iii) The form factor for the resonator with a periodic structure is three to four times higher than that for the hollow resonator.

(iv) At $Q = 4500$, according to the criterion $\Delta f_{\min} \cong f/10Q$, the resonator with a periodic structure can be used to measure plasma densities down to $n_{\min} \cong 10^6$ cm^{-3}.

(v) The accuracy of electron density measurements is about 10%.

It should be noted that, with some special methods for measuring small frequency shifts, such that $\Delta f_{\min} \cong f/(100Q)$ (see, e.g., [5]), the minimum measurable density at the given parameters can be reduced to $n_{\min} \cong 10^5$ cm^{-3}.

Let us discuss plasma density measurements in near space. It is well known [3] that, at altitudes of 100–800 km, the plasma density is 10^5–10^6 cm^{-3}, the Debye length is $\lambda_D \approx 0.3$–1.0 cm, and the temperature onboard a satellite is in the range 10–100 K. For comparison, in the calibration electron beam, the temperature of which is determined by the cathode and is about 1500 K and the density is 10^5–10^6 cm^{-3}, the Debye length λ_D is 0.5–0.9 cm (which satisfactorily agrees with the space-plasma Debye length). This fact can be taken into consideration in calibrating the device for measurements in a plasma column of radius $\sim\lambda_D$. (We note that, when investigating the propagation of electromagnetic waves in thin electron and plasma columns, a situation can occur in which the column length is much larger than λ_D, while the plasma radius is $\sim\lambda_D$ [6].)

To make density measurements in the range of $n \sim 10^5$ cm^{-3} more reliable and also to progress to the range of $n \sim 10^4$ cm^{-3}, it is necessary to increase the resonator sensitivity. This can be done by (i) doubling the size of the resonator and the measured object (a beam or plasma), in which case the form factor will remain the same, the frequency of the fundamental mode will decrease twice, and the minimum measurable electron density will decrease fourfold; (ii) doubling the ratio of the plasma (beam) radius to the radius of the annual electrode (see Fig. 1; items *2*, *5*), in which case the form factor will increase nearly fourfold; or (iii) decreasing the resistivity of the resonator material, which takes place in space or laboratory experiments at temperatures of nearly 100 K, when, e.g., the resistivity of copper decreases by a factor of 6 to 7 and the Q factor of the high-frequency resonator (and consequently its sensitivity) substantially increases in comparison with those at normal conditions.

Based on the results of our experiments, we can conclude that the resonator proposed can be used for nonintrusive measurements of the plasma density in near space (in addition to conventional probe measurements) and for calibrating plasma probes in laboratory benches simulating space plasmas.

In conclusion, we note that a resonator with a periodic structure was used to measure the density of a plasma produced by a pulsed proton beam with an energy of 5 MeV and a current of 30 mA. The beam

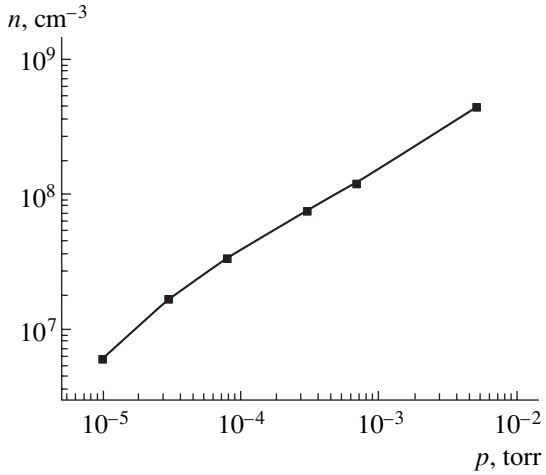

Fig. 2. Density of the plasma produced by a pulsed proton beam with an energy of 5 MeV and a current of 30 mA as a function of the air pressure.

propagated along the resonator axis at an air pressure of 10^{-5}–10^{-2} torr. Figure 2 shows the plasma density measured during the beam propagation as a function of the air pressure. In this case, the plasma density in the range of 10^6–10^9 cm^{-3} was measured.

ACKNOWLEDGMENTS

We thank V.N. Belan, V.A. Kiselev, and A.F. Linnik for their help in performing experiments with a proton beam and also V.I. Karas' for the discussion of the results obtained.

REFERENCES

1. V. E. Golant, *Microwave Methods in Plasma Research* (Nauka, Moscow, 1968).
2. I. N. Moskalev and A. M. Stefanovskiĭ, *Plasma Diagnostics by Means of Open Cylindrical Resonators* (Énergoatomizdat, Moscow, 1985).
3. *Plasma Diagnostics*, Ed. by W. Locht-Holtgreven (North-Holland, Amsterdam, 1968; Mir, Moscow, 1971), Chap. 11.
4. P. M. Zeĭdlits and V. A. Yamnitskiĭ, At. Energ. **10**, 469 (1961).
5. C. G. Montgomery, *Technique of Microwave Measurements* (McGraw-Hill, New York, 1948; Sov. Radio, Moscow, 1949), Vol. 1.
6. J. D. Lawson, *The Physics of Charged-Particle Beams* (Clarendon, Oxford, 1977; Mir, Moscow, 1980).

Translated by E.L. Satunina

Plasma Physics Reports, Vol. 30, No. 6, 2004, pp. 531–541. Translated from Fizika Plazmy, Vol. 30, No. 6, 2004, pp. 575–585.

LOW-TEMPERATURE PLASMA

Repetitive Torch in a Coaxial Waveguide: Temperature of the Neutral Component

É. M. Barkhudarov*, S. I. Gritsinin*, G. V. Dreĭden, V. Yu. Knyazev*, V. A. Kop'ev*, I. A. Kossyĭ*, M. A. Misakyan*, G. V. Ostrovskaya**, and V. P. Silakov*****

**Prokhorov Institute of General Physics, Russian Academy of Sciences, ul. Vavilova 38, Moscow, 119991 Russia*

***Ioffe Physicotechnical Institute, Russian Academy of Sciences, Politekhnicheskaya ul. 26, St. Petersburg, 194021 Russia*

****Keldysh Institute of Applied Mathematics, Russian Academy of Sciences, Miusskaya pl. 4, Moscow, 125047 Russia*

Received July 2, 2003

Abstract—The temperature of the neutral component in a repetitive microwave torch excited in an argon jet injected into atmospheric air is measured using different optical methods. The microwave energy is efficiently converted into the thermal energy of the argon jet. The gas temperature is maximum at the nozzle, where it reaches 4.5–5.0 kK, and decreases to 2.5–3.0 kK along the jet. The torch plasma, which is not in thermal equilibrium, drastically influences the working gas and the surrounding air. © *2004 MAIK "Nauka/Interperiodica".*

1. INTRODUCTION

Microwave discharges excited in coaxial waveguides are widely used in physical experiments and various technological applications (see, e.g., [1–3]). Experiments carried out in recent years at the Institute of General Physics of the Russian Academy of Sciences (see [4–6]) have made a substantial contribution to the physics of coaxial microwave discharges. The design of the microwave torch under study is shown schematically in Fig. 1.

The central waveguide electrode, which is shorter than the outer electrode, also serves as a gas pipeline through which the working gas is supplied to the nozzle. The discharge is excited near the nozzle surface and then forms a plasma jet extended along the *z* axis. The microwave source is a conventional magnetron (with a wavelength of $\lambda_f = 12$ cm and an average power of $P \leq 1$ kW) used in domestic microwave ovens. The microwave radiation is generated in the pulse-periodic mode.

Microwave torches were excited in atomic and molecular gases and various gas mixtures. Most of the studies were carried with an argon jet injected into atmospheric air. The argon flow rate was 20–100 l/min.

In [6], the dynamics of the torch formation was investigated and the electron density in the torch was measured. The experiments showed a rather complicated picture (which cannot be adequately described by the surfatron discharge model [1]) of the formation and maintenance of a microwave torch in each of the subsequent microwave pulses.

It was found that a microwave pulse passes through the initial stage in which the magnetron radiation is generated in the form of a sequence of short (with a duration of ≤1 μs) high-power spikes. After a relatively short delay time (≥150 μs), the microwave pulses become to be accompanied by the plasma bursts that are localized near the nozzle of the central electrode. The sequence of bursts is followed by the generation of an ionization wave that propagates along the *z* axis and forms the bulk of the torch. The first ionization wave is followed by a train of waves that leave the nozzle and overtake the first wave.

The plasma jet formed by the end of a microwave pulse consists of a bright core adjacent to the nozzle and extended along the *z* axis by 1.0–1.5 cm and a less bright region with a substantially greater volume (the bulk of the torch).

The electron density in the core is as high as $n_e \simeq 10^{16}$ cm^{-3}, while in the bulk of the torch, it is (1–3) × 10^{14} cm^{-3}.

The determination of the gas temperature in the plasma jet is of interest from the standpoint of both developing a physical and physicochemical model of a microwave plasma torch and using such torches in various technological applications. The gas temperature T_g and the degree to which the electron temperature T_e is higher than the gas temperature (the degree to which the torch plasma is far from thermal equilibrium) determine the efficiency of the plasmochemical processes occurring inside and outside the gas-discharge region. The objective of our study was to measure the temperature of the neutral component of an argon torch injected into atmospheric air.

1063-780X/04/3006-0531$26.00 © 2004 MAIK "Nauka/Interperiodica"

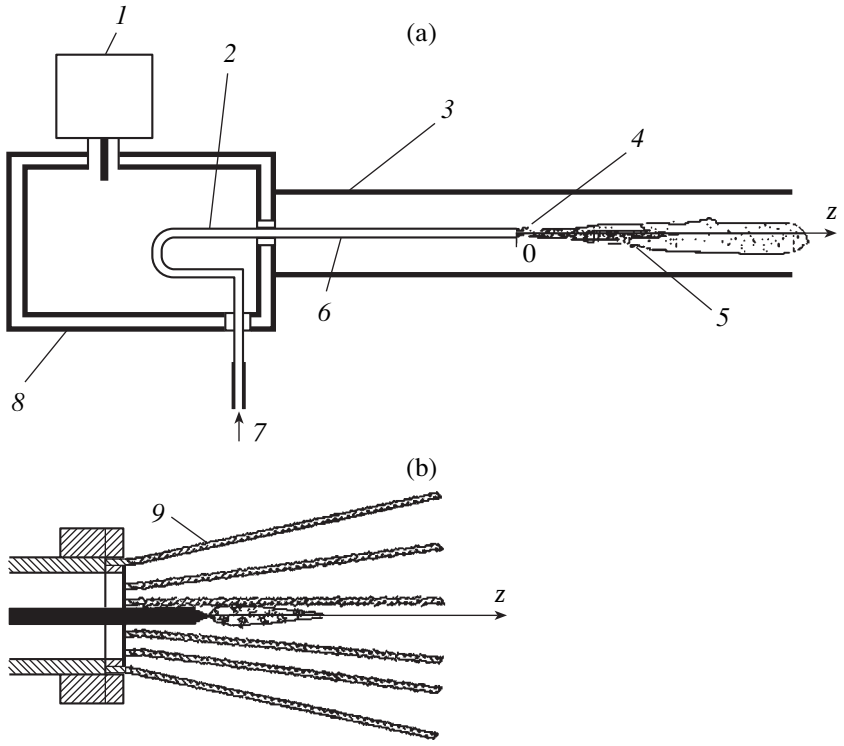

Fig. 1. (a) Schematic of a coaxial microwave plasmatron with an ordinary design of a coaxial line, and (b) an outer coaxial electrode that ends with a set of rods (basket): (*1*) magnetron, (*2*) loop for the output of microwaves from the rectangular cavity, (*3*) outer electrode, (*4*) nozzle, (*5*) plasma jet, (*6*) inner electrode, (*7*) working gas, (*8*) rectangular cavity, and (*9*) copper rods.

2. EXPERIMENTAL LAYOUT AND DIAGNOSTIC TECHNIQUES

The experimental layout is shown in Fig. 2, and the design of the microwave plasmatron generating a torch in atmospheric air is depicted in Fig. 1. Distinguishing features of the microwave plasmatron are, first, the method of transferring the microwave energy from the magnetron to a coaxial waveguide and, second, the design of the outer electrode of the coaxial line, which ends with a set of rods forming a basket surrounding the nozzle and the torch (Fig. 1b). The rods act as a solid screen for microwaves and, at the same time, allow free access to the torch for various diagnostics and for pieces to be processed.

The working gas (argon) was injected through the central electrode. The argon flow rate was ≤20 l/min, the average magnetron power was $P \simeq 800$ W, and the radiation frequency was $f \simeq 2.45$ GHz. The magnetron operated in the pulse-periodic mode (the pulse duration was $\tau_i \simeq 8$ ms, and the interval between pulses was $\tau_d \simeq 12$ ms).

The gas temperature was measured by the following diagnostics shown schematically in Fig. 2:

(i) Observations of the total spectrum with an S2000 Ocean Optics spectrometer with an operating spectral interval of $200 \le \lambda \le 850$ nm. The spectrum was averaged over several magnetron pulses. The spectrum was measured at different points along the z axis, starting from the nozzle of the microwave torch. The spatial resolution was $\Delta z \simeq 1$ mm, and the spectral resolution was $\Delta\lambda \simeq 1.2$ nm. A distinctive feature of this method is that it allows one to reliably measure the continuous spectrum of the torch within a wide wavelength range and to determine the radiation temperature of the torch.

(ii) Measurements of the torch radiation in the short-wavelength range ($300 \le \lambda \le 395$ nm) with an HR2000 Ocean Optics spectrograph, the operating spectral interval of which includes the second positive system of molecular nitrogen (the $C^3\Pi_u \longrightarrow B^3\Pi_g$ transition). The torch spectrum was measured in different regions along the z axis. The spectral resolution was $\Delta\lambda \cong 0.05$ nm. This method allowed us to determine the rotational temperature of nitrogen molecules from the relative intensity of the lines of the nitrogen vibrational–rotational spectrum.

(iii) Optical interferometry (a Mach–Zehnder interferometer), which allows measurements of the gas density perturbations in the torch and in the surrounding air. The light source was an OGM-20 ($\lambda = 0.66$ μm) laser. The exposure time was about 30 ns. For an isobaric process, variations in the gas density uniquely determine variations in the gas temperature.

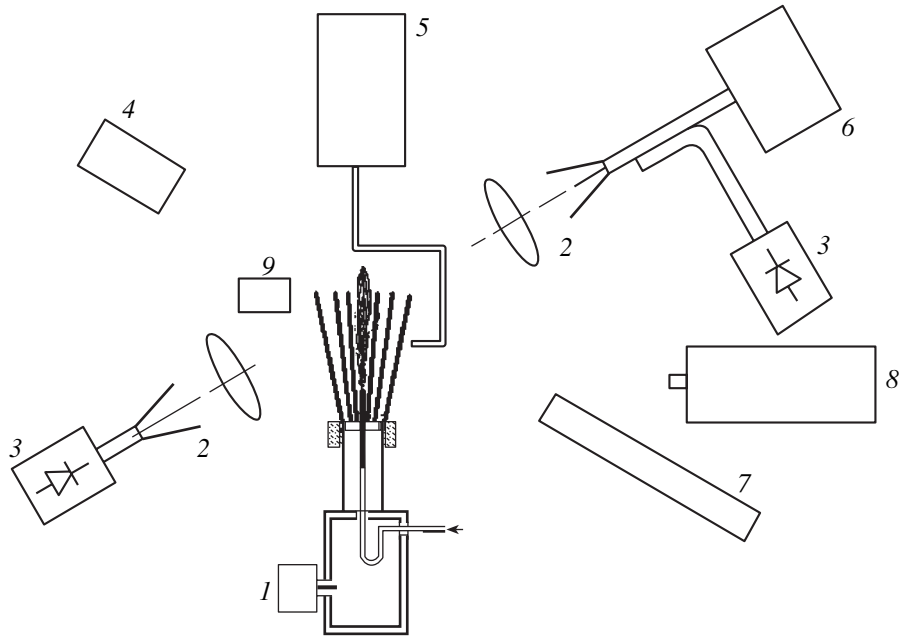

Fig. 2. Experimental layout: (*1*) microwave torch, (*2*) diagnostic microwave horn antennas and lenses, (*3*) microwave detector, (*4, 7*) components of the interferometric system (photographic camera, OFGM-20 laser, etc.), (*5*) S2000 spectrograph, (*6*) diagnostic microwave oscillator, (*8*) HR2000 spectrograph, and (*9*) collimated photodiode.

The total emission spectrum was measured when the torch was excited in pure argon and in argon with an admixture of metal (tungsten) grains with a size on the order of 30 μm and when thin ceramic rods were inserted into the argon torch.

3. MEASUREMENT RESULTS

Figure 3 shows characteristic torch spectra measured with the S2000 spectrograph at different distances from the nozzle. The spectra contain both the continuous and line components. An analysis shows that the line emission in the long-wavelength range of $700 \le \lambda \le 850$ nm is related to argon atoms (except for one line identified as an atomic oxygen line). In addition to the atomic lines, there are molecular bands that can be identified as molecular nitrogen bands (in particular, the second positive system of N_2). However, in view of the objectives of this paper, the third component of the spectrum, namely, continuum spectrum (which can be compared to the spectrum of a Planckian radiator) is of primary importance. If the continuum spectrum is nearly Planckian, then it can be used to determine the radiation temperature (and, probably, the gas temperature) of the torch.

The spectral intensity of the equilibrium (Planckian) radiator I_λ is given by the expression [7]

$$I_\lambda = (\text{const}/\lambda)^4[\exp(hc/\lambda kT) - 1]^{-1}. \quad (1)$$

In the spectral range where the inequality $\exp(hc/\lambda kT) \gg 1$ holds, expression (1) can be reduced to the form

$$1.4388 \times 10^8/\lambda = B - T\ln(I_\lambda\lambda^4), \quad (2)$$

where λ is expressed in Å, T is the radiator temperature in K, I_λ is in arbitrary units, and B is a constant that is independent of λ.

In the coordinates $x = \ln(I_\lambda\lambda^4)$ and $y = 1.4388 \times 10^8/\lambda$, the spectrum of a Planckian radiator is described by a linear function, whose slope gives the radiator temperature.

The above procedure was applied to spectra similar to those illustrated in Fig. 3. Drawing a fitting straight line through the measured curve as is shown in Fig. 4, we determine the torch radiation temperature T, which is identified with the gas temperature T_g.

The question as to whether the radiation temperature of the argon torch may be identified with the gas temperature will be discussed below. Here, we note only that an advantage of the method described above is that we need no information on the emissivity of the radiation source, so that absolute measurements of the radiation intensity are unnecessary.

The temperature T_g determined by the above method is shown in Fig. 5 as a function of the axial distance from the plasmatron nozzle.

The above nonintrusive method of determining the gas temperature from the continuum spectrum of the torch radiation with the help of the S2000 spectrograph

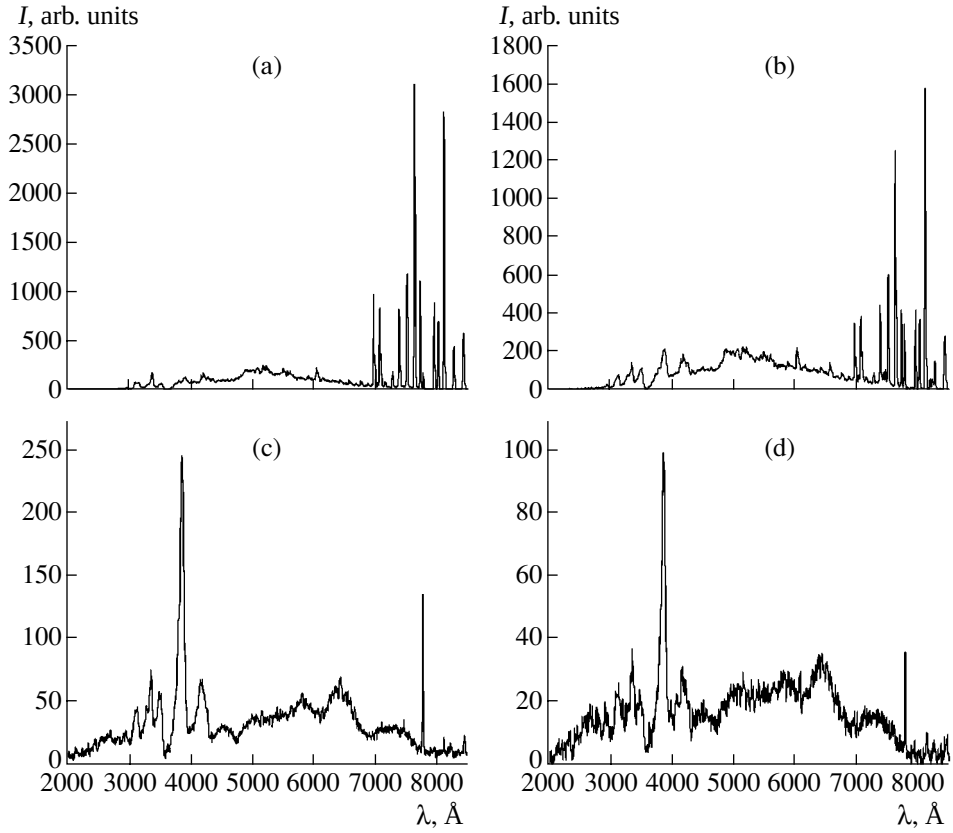

Fig. 3. Typical emission spectra of a microwave argon torch at different distances from the nozzle: z = (a) 0.1, (b) 0.5, (c) 1.0, and (d) 2.0 cm.

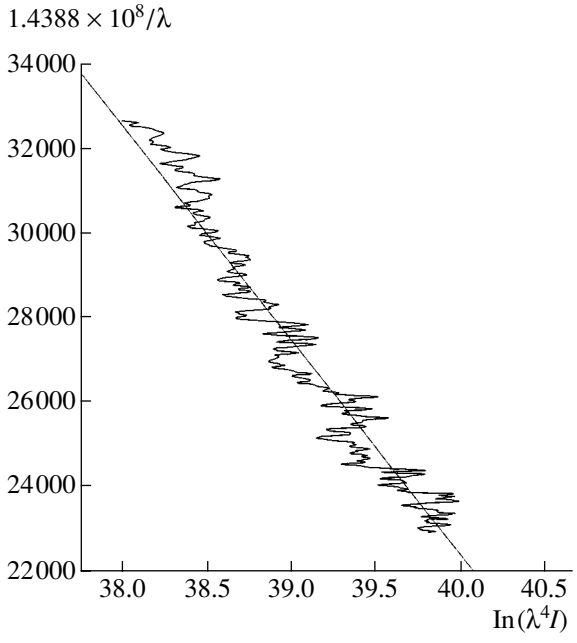

Fig. 4. Continuum emission spectrum of an argon torch and its fit by a straight line according to formula (2).

can be supplemented with diagnostics of the optical emission from solid bodies introduced into the torch and heated by the plasma and the hot gas. An obvious disadvantage of these diagnostics is that the torch is perturbed by the introduced bodies. On the other hand, their advantage is that they allow one to avoid uncertainty in identifying the radiation temperature with the temperature of the solid probe and, apparently, the gas temperature.

In one of the contact diagnostics, tungsten grains (30–40 μm in size) were injected into the working gas (argon) with the use of a specially developed dispenser. The number density of grains was no higher than 10 cm^{-3}. The injection of grains was accompanied by a sharp increase in the intensity of the torch radiation (see Fig. 6a). At the same time, the spectral distribution of the intensity I_λ in the wavelength range of $450 \le \lambda \le 650$ nm was very similar to a Planckian spectrum (Fig. 6b). Since the radiating tungsten grains were small in size, it was reasonable to assume that their temperature was equal to the gas temperature: $T \cong T_g$.

The axial profile of the temperature T measured during the injection of grains into the torch is shown in Fig. 7.

Let us also consider the results of measurements of the temperature of a 0.5-mm-diameter ceramic pipe

inserted into the torch. The measurements were performed with the S2000 spectrograph. A typical emission spectrum of the probe is shown in Fig. 8a. This spectrum is close to a Planckian spectrum, except for a well-pronounced potassium doublet superimposed on the continuum (Fig. 8b). Figure 9 shows the temperature of a pipe positioned at different distances from the nozzle. It can be seen from the figure that this temperature does not exceed 2300 K (which is somewhat higher than the melting temperature of ceramics). Optical measurements performed with the use of a solid probe allow us to conclude that the gas temperature throughout the entire torch volume is no lower than 2300 K: $T_g \geq 2300$ K.

From the torch emission spectra recorded with the help of the HR2000 spectrograph, we were able to determine the rotational temperature of molecular nitrogen. Under our experimental conditions, this temperature was close to the gas temperature. Figure 10 illustrates typical spectra observed at different distances from the nozzle. An analysis shows that, immediately near the nozzle, the emission spectrum in the range of $300 \leq \lambda \leq 395$ nm is dominated by the bands of neutral molecular nitrogen. As the distance from the nozzle increases, the bands of molecular nitrogen ions become dominating.

From the relative intensity of the vibrational–rotational spectral lines of the second positive system of nitrogen, we estimated the rotational temperature T_r of nitrogen molecules in the plasma region lying immediately near the nozzle. In this plasma region, the spectrum of the second positive system is not superimposed by the lines of molecular nitrogen ions.

The integral intensity I_ν of a rotational line in the emission spectrum is determined by the expression [8]

$$I_\nu = C\nu^4_{J',J''} n_{N_2} S_{J',J''} \exp\{-B_C J'(J'+1)/kT_r\}, \quad (3)$$

where $\nu_{J',J''}$ is the frequency of the rotational transition; J' and J'' are the rotational quantum numbers of the upper and lower levels, respectively; C is a factor independent of J' and J''; n_{N_2} is the density of nitrogen molecules; $S_{J',J''}$ is the Henly–London factor; B_C is the rotational constant of the term $C^3\Pi_u$; and k is the Boltzmann constant. Assuming that the frequency $\nu_{J',J''}$ depends only slightly on J and $B_C = 1.815$ cm^{-1}, expression (3) can be reduced to the form

$$0.88\ln(I_\nu/S_{J',J''}) = -J'(J'+1)/T_r + \text{const}. \quad (4)$$

Plotting the dependence of the logarithm of the reduced intensity on $J'(J'+1)$ and approximating it by a straight line (i.e., assuming a Boltzmann distribution over rotational levels), we can determine the rotational temperature (and, consequently, the gas temperature) from the slope of this straight line. Figure 11 shows the dependence of this kind at $z = 1$ cm. The temperature determined from the slope of the fitting line is $T_r \approx T_g \approx 2100$ K.

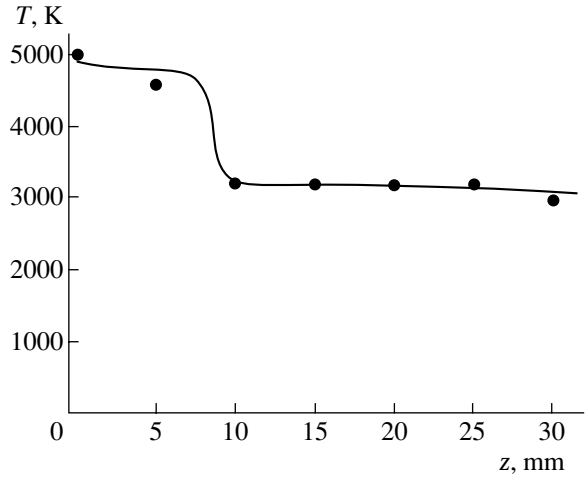

Fig. 5. Longitudinal temperature profile in a microwave argon torch.

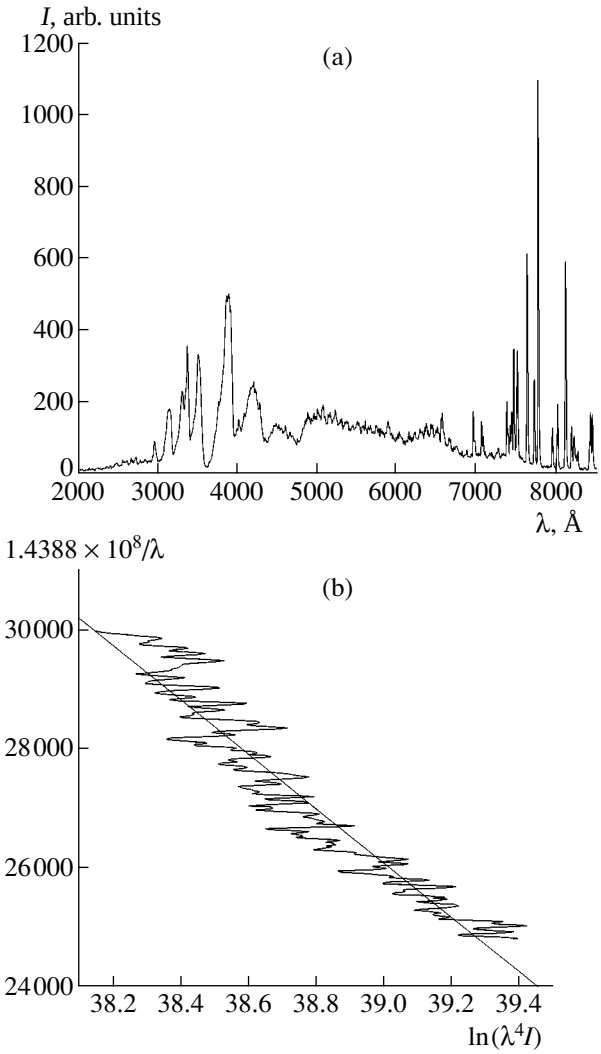

Fig. 6. Emission spectrum of a microwave torch generated in a mixture of Ar with tungsten grains: (a) the total spectrum of the microwave torch and (b) the continuum spectrum and its fit by a straight line according to formula (2).

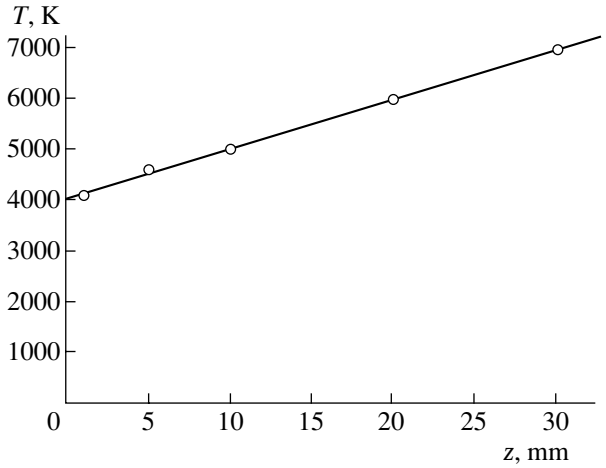

Fig. 7. Longitudinal temperature profile in a microwave torch generated in a mixture of Ar with tungsten grains.

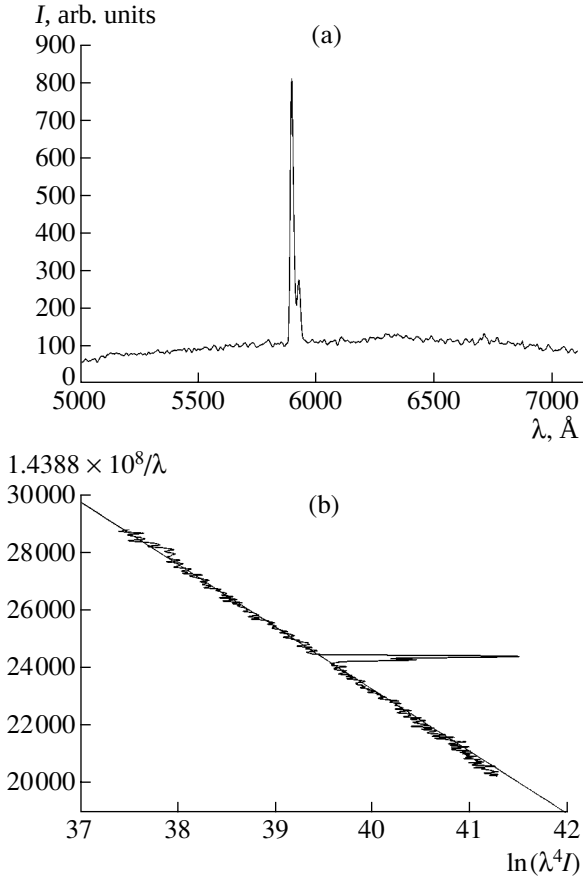

Fig. 8. Typical emission spectrum of a probe (a ceramic pipe) inserted into the torch: (a) the total emission spectrum of the probe and (b) the probe emission spectrum and its fit by a straight line according to formula (2).

Finally, we consider the results of laser interferometry. Interferograms of the microwave torch were recorded at different times t_d (counted from the leading edge of a microwave pulse), so that the density distribution of the working gas ρ_{Ar} was measured during a pulse and also between successive pulses. Figure 12 demonstrates typical interferograms of an argon torch (at a gas flow rate of ≈20 l/min). Straight lines emerging from the nozzle along the z axis are shadows of the basket rods. The nozzle itself produces a shadow at the top of the figure. The nozzle diameter (≃6 mm) can be used as a spatial scale. The laser beam passed through the torch in the direction orthogonal to the z axis.

A qualitative analysis of interferograms shows that the gas flow near the nozzle is laminar. Fringe shifts are clearly defined, so that the interferogram can be processed in a standard manner (see [9]) to recover the spatial distribution of the working gas density $\rho_{Ar}(r, z)$.

As the distance from the core along the z axis increases, the flow becomes turbulent; hence, the recovery of the spatial distribution of ρ_{Ar} is region is hardly possible. Thus, laser interferometry allows us to determine the gas temperature (assuming that the process is isobaric) only immediately near the nozzle (inside the core).

The relative change in the gas density is determined by the relation

$$\Delta\rho_{Ar}/(\rho_{Ar})_0 \approx \Delta K\lambda_l/l(N_{Ar} - 1), \quad (5)$$

where $\Delta\rho_{Ar} = (\rho_{Ar})_0 - \rho_{Ar}$ is the change in the working gas density averaged over a segment l of the laser beam, which is perpendicular to the z axis; ΔK is the fringe shift; λ_l is the diagnostic laser wavelength ($\lambda_l \simeq 7 \times 10^{-5}$ cm); N_{Ar} is the refractive index of the working gas (under our experimental conditions, neutral Ar atoms in the ground state make a major contribution to N_{Ar}).

Under our experimental conditions, formula (5) can be reduced to the form

$$\Delta\rho_{Ar}/(\rho_{Ar})_0 \approx 0.23\Delta K/l, \quad (6)$$

where l is in cm.

Substituting the size l of the gas region perturbed by the torch and the value of ΔK in the core, we find

$$\Delta\rho_{Ar}/(\rho_{Ar})_0 \geq 0.9. \quad (7)$$

This means that the gas temperature in the core is

$$T_{g1} \geq 10T_{g0} \approx 3000 \text{ K}.$$

Unfortunately, the insufficient accuracy of the method (the fringe shift can be measured with an accuracy no better than 0.1 of the fringe width) does not allow us to correctly determine the temperature in the core when this temperature is higher 3000 K.

4. DISCUSSION OF RESULTS

The determination of the gas temperature in an argon plasma jet generated by a microwave plasmatron turned out to be a rather complicated problem, because the torch is difficult to investigate using the diagnostics commonly employed in gas-discharge experiments.

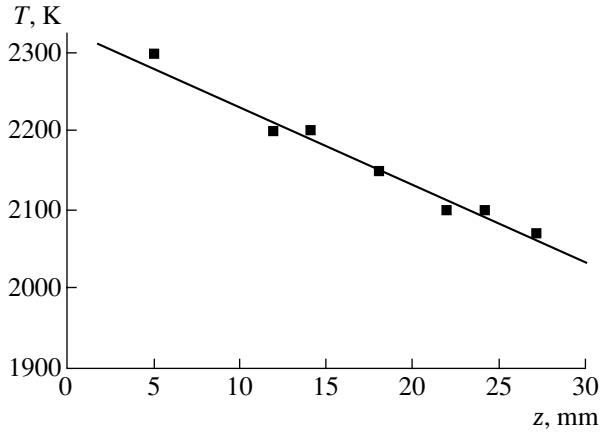

Fig. 9. Temperature of a ceramic probe at different distances of the torch nozzle.

Thus, laser interferometry failed to operate outside the core because of the strong gas-flow turbulence. Inside the core, where it is impossible to measure the fringe shifts smaller than 0.1 of the fringe width, the interferometry gives only a lower estimate of T_g: $T_g \geq 3000$ K.

The rotational temperature T_r is also very difficult to determine from the vibrational–rotational bands of nitrogen molecules. Outside the core, at large distances from the nozzle, the neutral molecular nitrogen bands are superimposed by the bands of molecular nitrogen ions. At the same time, in the core itself, nitrogen is replaced with argon ejected from the nozzle of the central electrode of the coaxial line. As to the temperature $T_r \simeq T_g \cong 2100$ K measured near the nozzle, it seems that this temperature characterizes the state of air weakly heated in the radial direction by the argon plasma.

The only workable diagnostics that allowed us to determine the gas temperature along the entire torch was the method based on the measurements of the continuum spectrum in the long-wavelength range. It appeared that this spectrum was Planckian with a radiation temperature *T*. The fact that the radiation temperature T can be identified with the gas temperature follows from a comparison of the measured radiation temperature of a pure argon torch with the results of measurements of the radiation temperature of the gas with injected tungsten grains, as well as from the data of laser interferometry of the gas heated by the torch. Laser interferometry gives a rather high gas temperature in side the core ($T_g \geq 3000$ K). This fact confirms the assumption that radiation is in equilibrium with the gas, i.e., that the equality $T_g \simeq T$ is satisfied ($T \simeq 4000$–5000 K).

The tungsten grain temperature, which was determined from the Planckian emission spectrum of the grains, rapidly reaches the temperature of the ambient gas because of the small grain size. However, the grains themselves substantially influence the torch thermodynamics. As a result, the torch temperature increases due to the intensified deexcitation of electronically excited argon atoms, as well as due to exothermal oxidation reactions of tungsten with air oxygen. The latter processes are seemingly responsible for an increase in the gas temperature with increasing distance from the plasmatron along the *z* axis (see Fig. 7). However, immediately near the nozzle, where the oxidation processes do not manifest themselves, the grain temperature is close to the gas temperature and is determined by the radiation temperature of the argon torch ($T_g \cong 4000$ K) (cf. Figs. 7 and 5).

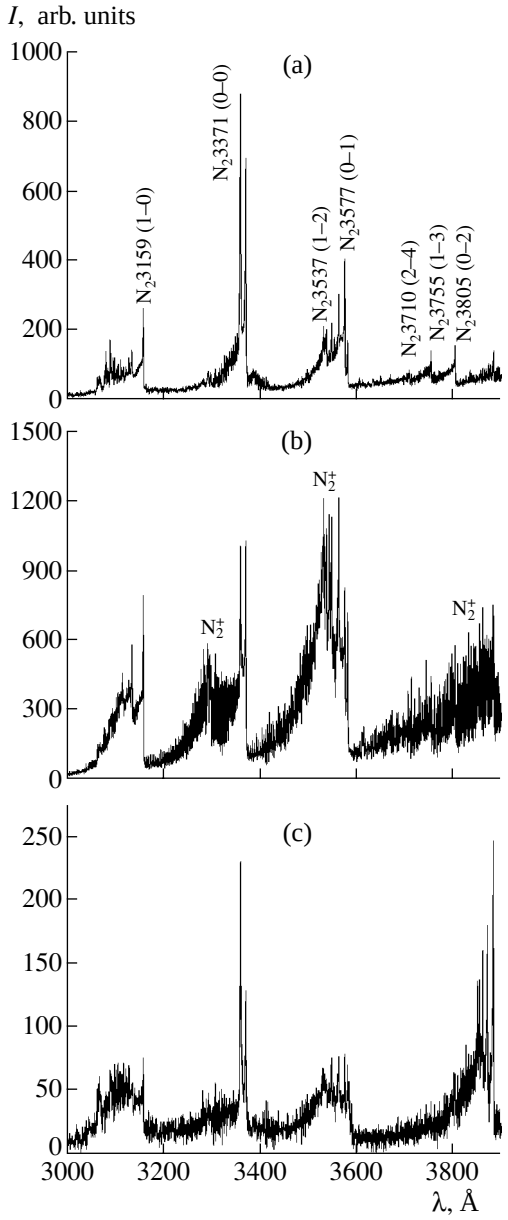

Fig. 10. Emission spectra of an argon torch observed by an HR2000 spectrograph at (a) $z \leq 01$ cm, (b) $z = 0.5$ cm, and (c) $z = 1.5$ cm.

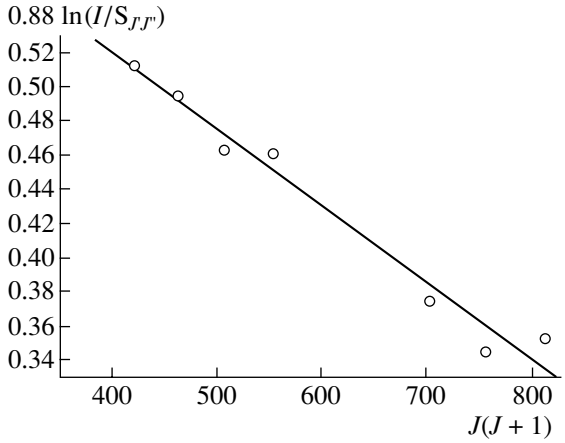

Fig. 11. Measured mission intensity of the second positive system of molecular nitrogen at a distance of $z \le 0.1$ cm from the nozzle (symbols) and its fit by a straight line according to formula (4).

The measurements of the radiation temperature of a ceramic pipe inserted into the torch may be regarded as a test method for measuring the temperature from the continuum spectrum (Fig. 9). The result obtained, i.e., the fact that the temperature throughout the entire plasma jet is close to the ceramics melting temperature, testifies that the calibration of the spectral measurements is correct and the method is workable (a ceramics temperature close to 2300 K was also independently determined by a Raynger MX4 standard pyrometer).

The above arguments in support of the equality $T_g \cong T$ are based on the data obtained by different experimental methods. Below, we will consider a kinetic scheme that shows that, under the given conditions, the optical continuum can be in equilibrium with the gas. A starting point for the formulation of the kinetic scheme is a reasonable assumption that the source of continuum radiation that is in equilibrium with the gas is an air layer adjacent to the torch, so that the temperature of this layer is close to the torch temperature. In fact, in the air layer adjacent to the argon core (where $n_e \approx 10^{16}$ cm^{-3}, $T_e > T_g$), as well as in the argon–air mixture behind the core (where $n_e \ge 10^{14}$ cm^{-3}, $T_e > T$), the excitation of the electronic term $A^3\Sigma_u^+$ of nitrogen molecules must proceed very efficiently, so that the population of this term becomes higher than the equilibrium population, e.g., due to the intense processes

$$\begin{array}{l} N_2(X, v_X) + e \longrightarrow N_2(A, v_A) + e \\ \qquad\qquad\quad \longrightarrow N_2(B, W^3, B') + e \\ \qquad\qquad\quad\quad\ \longrightarrow N_2(A) \end{array} \qquad (8)$$

or

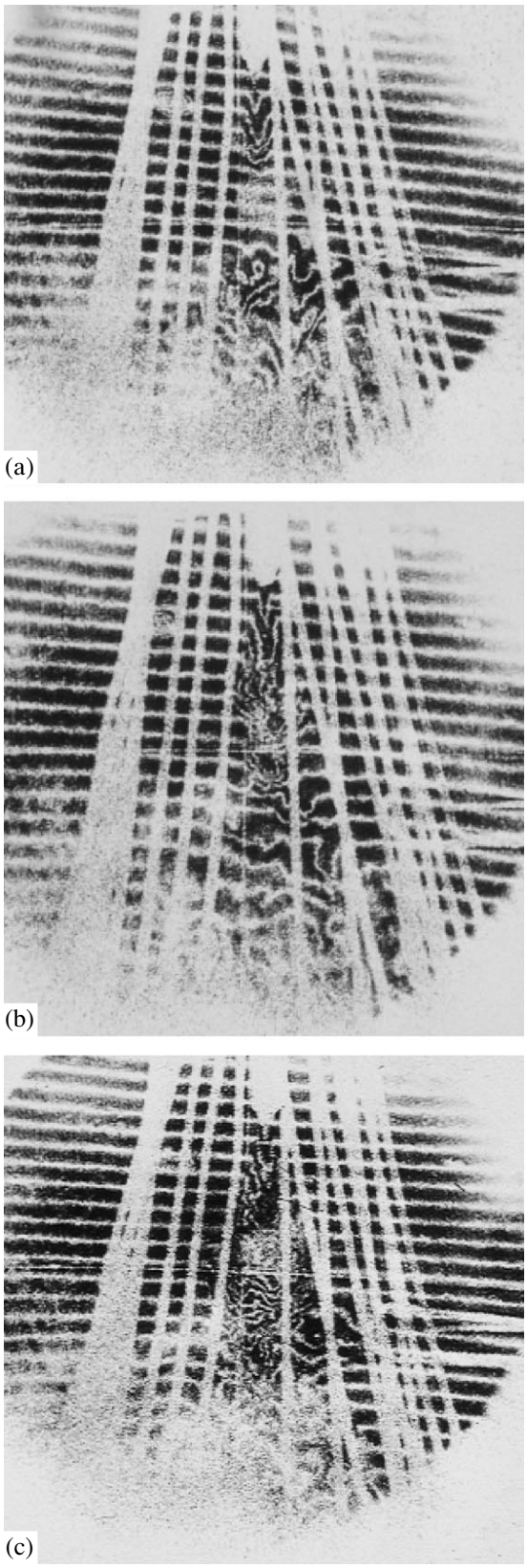

Fig. 12. Typical interferograms of an argon torch observed at different times t_d: (a) 0.34, (b) 1.38, and (c) 2.6 ms.

$$\begin{gathered} N_2(X, v_X) + \mathrm{Ar}(i) \xrightarrow{k^{(i)}_{v_X - v_C}} N_2(C, v_C) + \mathrm{Ar}(^1S_0), \quad i = 1, 2, 3, 4, \\ \qquad\qquad\qquad\qquad\qquad\qquad \hookrightarrow N_2(A) \\ (i = 1 \longrightarrow {}^3P_2;\ i = 2 \longrightarrow {}^3P_1;\ i = 3 \longrightarrow {}^3P_0;\ i = 4 \longrightarrow {}^1P_1), \end{gathered} \tag{9}$$

or due to the radiation transitions

$$N_2(C, v_C) \xrightarrow{A^{(2^+)}_{v_C - v_B}} N_2(B, v_V) + \hbar\omega \tag{10}$$

and

$$N_2(B, v_B) \xrightarrow{A^{(1^+)}_{v_B - v_A}} N_2(A, v_A) + \hbar\omega. \tag{11}$$

When the state $N_2(A)$ in a strongly heated gas is highly populated via mechanisms (8)–(11),[1] the populations of the vibrational–rotational levels of the term $A^3\Sigma_u^+$ and the levels $B^3\Pi_g$, v_B, J_{v_B}; $W^3\Delta_u$, v_W, and J_{v_W} will obey a Boltzmann law for thermodynamic equilibrium:

$$\begin{aligned} n_{\Lambda, v_\Lambda, J_{v_\Lambda}} &= n_{A^3\Sigma_u, v_A = 0, J_{v_A} = 0} \frac{g_\Lambda}{g_{A^3\Sigma_u^+}} (2J_{v_\Lambda} + 1) \\ &\times \exp(-(E_{\Lambda, v_\Lambda, J_{v_\Lambda}} - E_{A, 0, 0})/kT). \end{aligned} \tag{12}$$

Here, g_Λ is the statistical weight of the electronic state Λ of a N_2 molecule ($\Lambda \longrightarrow A^3\Sigma_u^+$; $B^3\Pi_g$, and $W^2\Delta_u$) and $E_{\Lambda, v_\Lambda, J_{v_\Lambda}}$ is the excitation energy of the level Λ, v_Λ, J_{v_Λ}. According to Boltzmann distribution (12), the distribution of the energy supplied by electrons and/or excited argon atoms to this system of terms of the N_2 molecule is governed by the fast processes of RT, VT, and ET relaxation, and also by the processes of *VV*' exchange of vibrational photons between electronically excited molecules $N_2(A, B, W)$ and molecules $N_2(X, v_x)$ and $O_2(X, v_x)$. As a result, we arrive at a realistic mechanism for the formation of continuum in the spectrum of optical radiation that is in equilibrium with the gas and is associated with the first positive system of nitrogen molecules (the transitions $B^3\Pi_g$, v_B, $J_{v_B} \longrightarrow A^3\Sigma_u^+$, v_A, J_{v_A}, at which excited N_2 molecules emit photons with wavelengths $\lambda \in$ (4500 Å, 10500 Å)) [13]. The continuum spectrum of the torch in the wavelength range under study (4500 Å $\le \lambda \le$ 6500 Å) may be explained by the overlapping of bands inside the first positive system and, what is more important, by the fact that the gas is strongly heated and the molecular lines overlap because of their substantial broadening [7]. Indeed, under our experimental conditions, when the air molecular density is in the range of $0.5 \times 10^{19} \le n_{\mathrm{air}} \le 2.5 \times 10^{19}$ cm^{-3}, the broadening of the spectral lines at a gas temperature of 5000 K is $(\Delta k)^*_{1/2} \ge (\Delta k)^{(B-B)}_{1/2} \simeq 0.1$–$0.5$ cm^{-1} (the lower estimate for the line half-width was calculated based on the theory of the Van der Waals interaction of colliding particles (see [14, 15]).[2] An analysis also shows that, under our experimental conditions, the Stark broadening of the torch emission lines can play a significant (probably, even decisive) role in the formation of the continuum spectrum.

The continuum spectrum of the torch emission can also be attributed to microscopic grains of the material of the central electrode (or metal plasmoids produced by microexplosions at the nozzle edge) that are introduced into the gas in the stage of the torch ignition and are then entrained by the gas flow along the *z* axis, being in thermal equilibrium with the gas.

Thus, based on the results of all the diagnostics applied, we can conclude that the gas temperature in the torch is maximum in the core ($T_g \cong$ 4000–5000 K) and gradually decreases (down to $T_g \cong$ 2500–3000 K) along the jet.

The electron density in the core ($n_{ec} \simeq 10^{16}$ cm^{-3}) and in the bulk of the torch ($n_{et} \simeq (1$–$3) \times 10^{14}$ cm^{-3}) substantially exceeds the density corresponding to the thermal equilibrium conditions. This means that the torch plasma is not in thermal equilibrium and the electron temperature is substantially higher than the neutral-gas temperature.

The problem of the heating of the molecular and atomic components of the plasma in the microwave torch under study is of particular interest and must be solved self-consistently, taking into consideration the electrodynamic, kinetic, and gasdynamic phenomena. Here, we restrict ourselves to simple estimates that con-

[1] Data on the integral rate constants of the processes involved and also information on the channels of the deexcitation of electronically excited nitrogen molecules in nitrogen–oxygen mixtures are presented in [10]. The rate constants of processes (9)–(11) can be taken from [11, 12]: $\sum k^{(1)}_{0-v_C} = 3.6 \times 10^{-11}$ cm^3/s, $\sum k^{(2)}_{0-v_C} = 0.9 \times 10^{-11}$ cm^3/s, $\sum k^{(3)}_{0-v_C} = 1.6 \times 10^{-11}$ cm^3/s, $\sum k^{(4)}_{0-v_C} = 4.7 \times 10^{-11}$ cm^3/s, $A^{(1^+)} \approx 1.5 \times 10^5$ s^{-1}, $\sum A^{(2^+)}_{0-v_B} = 2.72 \times 10^7$ s^{-1}, $\sum A^{(2^+)}_{1-v_B} = 2.74 \times 10^7$ s^{-1}, $\sum A^{(2^+)}_{2-v_B} = 2.71 \times 10^7$ s^{-1}, $\sum A^{(2^+)}_{3-v_B} = 2.65 \times 10^7$ s^{-1}, and $\sum A^{(2^+)}_{4-v_B} = 2.54 \times 10^7$ s^{-1}.

[2] An analysis of the λ = 4800–6500 Å emission of molecular nitrogen with allowance for the data on the Frank–Condon factors in [16] shows that the average distance between the fine-structure spectral lines at T = 5000 K is about 0.3 cm^{-1}.

firm the possibility of efficiently heating the torch generated by a microwave coaxial plasmatron.

The high density of electrons and their relatively high temperature (according to [17], it attains 2–3 eV) can result in the fast heating of the neutral component to temperatures observed experimentally in the core. Thus, the characteristic heating time of the neutral component (τ_n) by the plasma electrons can be estimated from the expression

$$\tau_n \approx \nu_{\text{eff}}^{-1} \delta^{-1} n_m / n_e, \quad (13)$$

where $\nu_{\text{eff}} \simeq 4 \times 10^9 p$ (p being the pressure expressed in torr) [18], δ is the fraction of the electron energy transferred to neutrals in one collision event, and n_m is the density of the neutral component.

The propagation time of the working gas through the core of length L_c is

$$\tau_{fl} \approx L_c / v_g, \quad (14)$$

where v_g is the longitudinal velocity of the gas flow. For argon at $n_e = 10^{16}$ cm^{-3}, $n_m \simeq (1–2) \times 10^{19}$ cm^{-3}, and $v_g \simeq 20$ m/s, we have

$$\tau_n \ll \tau_{fl} \quad (15)$$

even we assume that the energy is transferred from electrons to argon atoms in elastic collisions only.

Therefore, we can expect that the neutral component inside the core will be rapidly heated to a temperature of $T_g \simeq (4–5)$ kK $< T_e \simeq (20–30)$ kK.

Outside the core, the process of gas heating by the plasma electrons is no longer dominant because the density n_e is more than two orders of magnitude lower than the electron density in the core. However, in this case, such mechanisms as the deexcitation of electronically excited argon atoms by the gas molecules may come into play. Moreover, a substantial contribution to gas heating can be made by the mechanism suggested in [17]: the charge exchange of argon ions with air molecules incoming in the torch and the subsequent recombination of N_2^+, and O_2^+ molecular ions.

An analysis shows that the energy expended on the gas heating in the torch is nearly equal to the energy of a microwave pulse:

$$V_c \varepsilon_c + V_t \varepsilon_t \approx P_i \tau_i, \quad (16)$$

where P_i and τ_i are the peak power and duration of a microwave pulse; V_c and V_t are the volumes of the core and bulk of the torch; and ε_c and ε_t are the energy densities required to heat the gas in the core and bulk of the torch to temperatures of $(T_g)_c$ and $(T_g)_t$, respectively. This equality demonstrates the high absorption efficiency of the pumping wave, whose energy is finally converted into gas heating.

5. CONCLUSIONS

The measurements performed have shown that the microwave energy supplied to a repetitive torch generated in an argon jet injected into atmospheric air in a coaxial waveguide is efficiently converted into the thermal energy of the gas jet. The gas temperature is maximum in the core, located near the plasmatron nozzle (4.5–5.0 kK), and decreases gradually to 2.5–3.0 kK in the axial direction. The torch plasma, which is not in thermal equilibrium ($T_e \gg T_g$), can drastically influence the working gas and the surrounding air.

The area of possible applications of the device under study is rather wide. Thus, it is expedient to study the possibility of employing a coaxial microwave plasmatron to generate hydrogen (via the decomposition of natural water-containing gases and water vapor), to decompose chlorofluorocarbons and poison gases, to neutralize the harmful components of industrial exhausts, to weld metals in a chemically inactive atmosphere without using combustible gases, etc.

ACKNOWLEDGMENTS

We thank A.G. Frank for her continuing interest in this study and S.Yu. Bogdanov for his assistance in experiments and fruitful discussions. This work was supported in part by the International Science and Technology Center (project no. 908) and the Netherlands Organization for Scientific Research (NWO) (project no. 047.011.000.01).

REFERENCES

1. M. Moisan, J. Margot, and Z. Zakrzewski, *High-Density Plasma Sources* (Noyes, New Jersey, 1995).
2. M. Moisan, G. Sauve, Z. Zakrzewski, and J. Hubert, Plasma Sources Sci. Technol. **3**, 584 (1994).
3. Y. Mitsuda, T. Yoshida, and K. Akashi, Rev. Sci. Instrum. **60**, 249 (1989).
4. S. I. Gritsinin, I. A. Kossyi, A. A. Letunov, *et al.*, in *Proceedings of the 15th International Symposium on Plasma Chemistry, Orleans, 2001*, Ed. by A. Bouchoule *et al.*, Vol. 4, p. 1479.
5. S. I. Gritsinin, I. A. Kossyi, and N. I. Malykh, in *Proceedings of the 14th International Symposium on Plasma Chemistry, Prague, 1999*, Vol. 2, p. 675.
6. S. I. Gritsinin, V. Yu. Knyazev, I. A. Kossyĭ, *et al.*, Fiz. Plazmy **30**, 283 (2004) [Plasma Phys. Rep. **30**, 255 (2004)].
7. Ya. B. Zel'dovich and Yu. P. Raizer, *Physics of Shock Waves and High-Temperature Hydrodynamic Phenomena* (Nauka, Moscow, 1966; Academic, New York, 1967).
8. G. Herzberg, *Molecular Spectra and Molecular Structure* (Van Nostrand, New York, 1939; Inostrannaya Literatura, Moscow, 1949), Vols. 1–3.
9. A. N. Zaidel' and G. V. Ostrovskaya, *Laser Methods in Plasma Studies* (Nauka, Leningrad, 1977).

10. I. A. Kossyi, A. Yu. Kostinsky, A. A. Matveyev, and V. P. Silakov, Plasma Sources Sci. Technol. **1**, 207 (1992).
11. B. M. Smirnov, *Excited Atoms* (Énergoizdat, Moscow, 1982).
12. Y. Itikawa, M. Hayashi, A. Ichimura, *et al.*, J. Phys. Chem. Ref. Data **15**, 985 (1986).
13. L. A. Kuznetsova, N. E. Kuz'menko, Yu. Ya. Kuzyakov, and Yu. A. Plastinin, *Probabilities of Optical Transitions in Diatomic Molecules* (Nauka, Moscow, 1980).
14. I. I. Sobel'man, *Introduction to the Theory of Atomic Spectra* (Fizmatgiz, Moscow, 1963; Springer-Verlag, Berlin, 1979).
15. A. A. Radtsig and B. M. Smirnov, *Reference Data on Atoms, Molecules, and Ions* (Atomizdat, Moscow, 1980; Springer-Verlag, Berlin, 1985).
16. N. E. Kuz'menko, L. A. Kuznetsova, and Yu. Ya. Kuzyakov, *Frank–Condon Factors of Diatomic Molecules* (Mosk. Gos. Univ., Moscow, 1984).
17. J. Jonkers, A. Hartgers, L. J. M. Selen, *et al.*, Plasma Sources Sci. Technol. **8**, 49 (1999).
18. Yu. P. Raizer, *Physics of Gas Discharge* (Nauka, Moscow, 1987; Springer-Verlag, Berlin, 1991).

Translated by N.F. Larionova

Plasma Physics Reports, Vol. 30, No. 6, 2004, pp. 542–548. Translated from Fizika Plazmy, Vol. 30, No. 6, 2004, pp. 586–592.

LOW-TEMPERATURE PLASMA

Effect of the Nonlocal Nature of the Electron Energy Spectrum on the Dissociation of Oxygen Molecules in a Discharge

K. S. Klopovskiy, D. V. Lopaev, O. V. Proshina, A. T. Rakhimov, and T. V. Rakhimova

Skobeltsyn Institute of Nuclear Physics, Moscow State University, Vorob'evy gory, Moscow, 119899 Russia

Received July 24, 2003; in final form, September 18, 2003

Abstract—The effect of the nonlocal nature of the electron distribution function on the dissociation rate of oxygen molecules in a dc glow discharge is studied. The concentration of oxygen atoms and the probability of their loss at the discharge tube wall are measured as functions of the discharge parameters by means of the time-resolved actinometric method involving argon atoms. An analysis of the measurement data in terms of both a discharge model in which the effect of the nonlocal nature of the electron energy spectrum is taken into account and a model in which this effect is ignored makes it possible to thoroughly investigate the balance of oxygen atoms in the discharge. The production rate of $O(^3P)$ atoms and their concentration in the plasma are calculated with allowance for the nonlocal nature of the electron energy distribution function. The calculated values agree well with the experimental data and differ substantially from those obtained using a spatially homogeneous distribution function. © *2004 MAIK "Nauka/Interperiodica".*

1. INTRODUCTION

Plasma technologies are now widely employed in many sectors of industry, in particular, in micro- and nanoelectronics. As a rule, such technologies are based on low-pressure discharges, which provide the possibility of creating highly nonequilibrium and chemically active media. It is well known that such nonequilibrium conditions in the medium are associated primarily with the nonequilibrium character of the plasma particles: the electron temperature is much higher than the ion and gas temperatures. The nonequilibrium character of the electrons causes neutral active particles (atoms, radicals, and excited neutrals) to become chemically nonequilibrium; in this situation, the concentrations of such particles are determined by the electron temperature and exceed their equilibrium values by many orders of magnitude. In most cases, a decrease in pressure (or, more precisely, in the parameter *pd*, where *p* is the gas pressure and *d* is the characteristic plasma dimension) is accompanied by a marked increase in the reduced electric field in the discharge plasma; as a result, the electron energy spectrum becomes nonlocal and anisotropic [1–10]. At moderate pressures, the main mechanism by which radicals are produced is the electron-impact dissociation of molecules. The threshold energy for this process is fairly high; as a rule, it appreciably exceeds the electron temperature. Consequently, the nonlocal nature of the electron spectrum can be expected to have a fairly large effect on the molecular dissociation.

In this work, we present the results of investigations of the kinetics of oxygen atoms in the ground state $O(^3P)$ in dc glow discharges initiated in a long cylindrical tube. In such experimental geometry, the electric field in the positive discharge column is uniform along the tube axis but it is highly nonuniform in the radial direction. This discharge structure provides correct measurements of both the concentration of $O(^3P)$ atoms and the rate of their production, because, at $pd < 10$ torr cm (here, *d* is the tube diameter), heterogeneous recombination proceeds in the kinetic regime and is the main loss mechanism for oxygen atoms. In [9–12], it was shown that, in pure O_2, the nonlocal nature of the electron energy distribution over the discharge tube cross section is important only at $pd < 1$ torr cm. Hence, by investigating the dynamics of the production of $O(^3P)$ atoms in a glow discharge in oxygen over a wide range of *pd* values (from 0.1 to 10 torr cm), in which the electron energy spectrum changes from being strongly nonlocal to very weakly nonlocal, it is possible to test the correctness of the nonlocal kinetic scheme against a simpler local model applicable for high *pd* values in order to correctly compare the experimental data obtained for lower *pd* values with the results calculated with allowance for the nonlocal nature of the electron energy distribution function (EEDF).

2. EXPERIMENT

It is known that, at low pressures, the heterogeneous recombination of oxygen atoms is the main mechanism by which they are lost. Since the probability for $O(^3P)$ atoms to be lost at a quartz glass surface is fairly low ($\sim 10^{-3}$), the range of *pd* values at which oxygen atoms are lost in the kinetic regime (when the characteristic time required for the particles to diffuse to the surface is much shorter than their lifetime) extends up to about 6–8 torr cm. In this case, from the kinetic equation for the concentration of $O(^3P)$ atoms averaged over the dis-

1063-780X/04/3006-0542$26.00 © 2004 MAIK "Nauka/Interperiodica"

charge tube cross section, we see that the steady-state concentration of these atoms is determined by the balance between their production within the plasma volume and their loss at the tube wall:

$$Diss \approx \nu_q[O(^3P)]. \quad (1)$$

Here, $\nu_q = \gamma_0 \frac{v_T}{d}$ is the loss rate of $O(^3P)$ atoms at the tube surface, γ_0 is the probability of the heterogeneous recombination of the atoms, d is the tube diameter, and v_T is the thermal velocity of the atoms near the tube surface. The sum of the rate constants of the processes of production of oxygen atoms is denoted by *Diss*. In a glow discharge plasma, the main production processes are those of electron-impact dissociation of O_2 molecules:

$$e + O_2 \longrightarrow O_2(^3\Pi_g) \longrightarrow O(^3P) + O(^3P) \quad \text{(6.1-eV threshold)}, \quad (2)$$

$$e + O_2 \longrightarrow O_2(B^3\Sigma_u^-) \longrightarrow O(^3P) + O(^1D) \quad \text{(7.34-eV threshold)}, \quad (3)$$

$$e + O_2 \longrightarrow O_2(^1\Pi_g) \longrightarrow O(^3P) + O(^1S) \quad \text{(9.1-eV threshold)}. \quad (4)$$

Therefore, by measuring the quantities on the right-hand side of Eq. (1), it is possible to experimentally determine the averaged (over the discharge tube cross section) rate constants of processes (2)–(4). In turn, by comparing the experimentally obtained rate constants with the calculated ones, it is possible to investigate the effect of the nonlocal nature of the electron energy spectrum on the dissociation of oxygen molecules. It is these measurements that were carried out in our experiments by the time-resolved actinometric method.

A schematic of the experiment is illustrated in Fig. 1. The discharges were initiated in two molybdenum glass tubes with an inner diameter of 12 mm, fabricated at different times. The distance between the electrodes was 49 cm. The pressure was varied in the range 0.1–3 torr and the current density was varied in the range 1–40 mA/cm^2. The concentration of oxygen atoms was measured by the actinometric method involving argon atoms. In our previous experiments [12], the atomic oxygen concentration was measured from the $O(3p^3P \longrightarrow 3p^3S)$ and $Ar(2p_9–1s_2)$ transitions at wavelengths of 844.6 nm and 811.5 nm, respectively. In the experiments described here, we also used these transitions, keeping in mind the fact that, according to the calculations of [13], the contribution of the dissociative excitation of O_2 molecules to the emission intensity at a wavelength of 844.6 nm is minimal. However, the results of measuring the concentration of $O(^3P)$ atoms from the $O(3p^5P \longrightarrow\longrightarrow 3p^5S)$ transition at λ = 771.1 nm and $Ar(2p_1–1s_5)$ transition at λ = 750.3 nm, which are often used in the actinometry of oxygen atoms, showed that, at reduced pressures (such that pd < 1 torr cm), actinometric measurements of the concentration of $O(^3P)$ atoms from the ratio of the 844-nm and 811-nm spectral line intensities are subject to large systematic errors. That is why we also carried out test measurements of the concentration of oxygen atoms from resonant vacuum ultraviolet (VUV) absorption in the $O(2p^3P \longrightarrow 3p^3S)$ transition at λ = 130 nm. As a source of VUV radiation, we used surface-wave discharges in an Ar : O_2 or a He : O_2 mixture with a small (~1%) amount of oxygen. Surface-wave discharges with a power of 30–100 W were excited in a quartz tube with an inner diameter of 15 mm by a microwave oscillator (f = 2.45 GHz) with the help of a surfatron-type cavity. The discharge tube was connected to the VUV source and VUV monochromator through the MgF_2 windows. The oxygen line emission from the resonant transition at λ = 130 nm was recorded at the exit from the vacuum monochromator by a FÉU-142 sun-blind photomultiplier. Unfortunately, because of the low resolution of the VUV monochromator, we were unable to achieve good resolution of the profiles of the fine structure of the resonant emission lines of atomic oxygen in the VUV source; as a consequence, we failed to perform precise absolute calibration of the results of measuring the resonant absorption by $O(^3P)$ atoms from their concentration. As for the estimates of the concentration of $O(^3P)$ atoms from the absorption at the wings of the spectral lines of the fine structure at λ = 130 nm, they were found to essentially coincide with the results of actinometric measurements using the 777-nm oxygen emission line and 750-nm argon emission line and

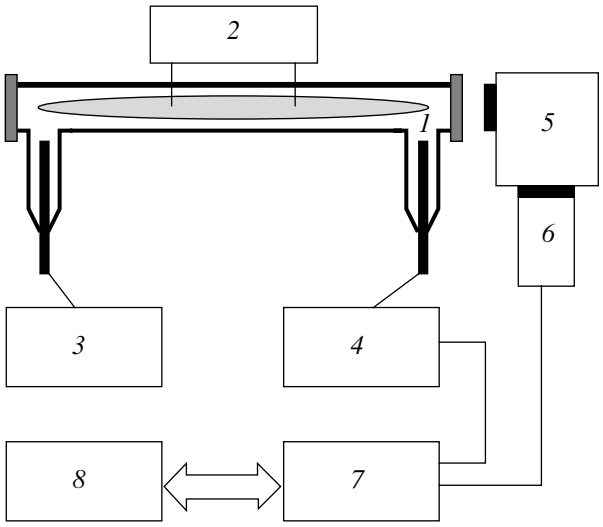

Fig. 1. Experimental layout: (*1*) discharge tube, (*2*) two-probe system for measuring the electric field dynamics, (*3*) high-voltage power supply, (*4*) discharge-current modulation circuit, (*5*) monochromator, (*6*) photomultiplier, (*7*) digital oscilloscope, and (*8*) computer.

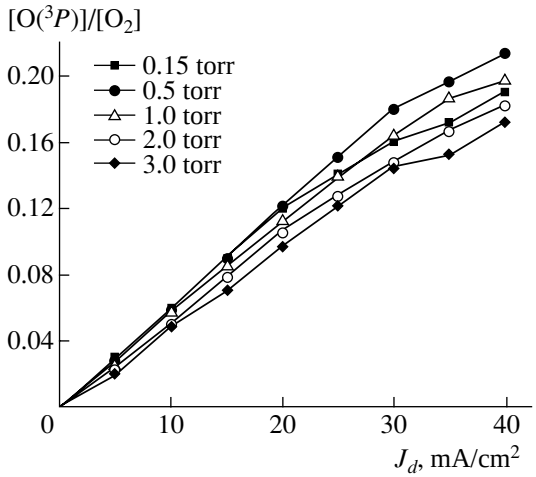

Fig. 2. Ratio $[O(^3P)]/[O_2]$ versus discharge current density at different oxygen pressures ([*N*] denotes the concentration of the particles of species *N*). The data are provided by actinometric measurements of the concentration of $O(^3P)$ atoms from the ratio of the I_{777}^{O} and I_{750}^{Ar} spectral line intensities.

also with the data known from the literature [13, 14]. A more important point is, however, that the relative measurements of the concentration of $O(^3P)$ atoms by the resonant VUV absorption method and by the actinometric method yielded the same dependence of the concentration on the discharge parameters. This indicates that, on the one hand, actinometric measurements of the concentration of $O(^3P)$ atoms from the ratio of the O 777-nm and Ar 750-nm spectral line intensities produce correct results and, on the other hand, there may be a systematic error in analogous actinometric measurements using the O 844-nm spectral line and Ar 811-nm spectral line. Our analysis shows that the systematic error observed in the latter case is apparently associated with the measurement inaccuracies near the threshold cross section for the excitation of the $2p_9$ radiating level of an argon atom. Hence, the results of actinometric measurements of the concentration of $O(^3P)$ atoms from the ratio of the O 777.1-nm and Ar 750.3-nm spectral line intensities are more reliable; it is for this reason that they were used in our work.

The results of actinometric measurements of the concentration of $O(^3P)$ atoms from the ratio of the I_{777}^{O} and I_{750}^{Ar} spectral line intensities are illustrated in Fig. 2, which shows the degree of dissociation $[O(^3P)]/[O_2]$ measured as a function of the discharge current at different gas pressures. In our opinion, such representation of the experimental data is more correct and illustrative: it is independent of the radial profile of the gas pressure because the radial profiles of the concentrations of $O(^3P)$ atoms and of O_2 atoms are determined by the gas temperature by virtue of the fact that the oxygen atoms have a low probability of being lost at the tube wall. The gas temperature T_g at the discharge axis was measured from the resolved structure of the *P* branch of the $O_2(b^1\Sigma_g^+,\ v = 0) \longrightarrow O_2(X^3\Sigma_g^-,\ v = 0)$ band of the oxygen molecule. However, we failed to completely resolve the fine structure of the *P* branch (the Q^P and P^P branches). However, as was shown in [15], this circumstance does not introduce errors in the results of measuring the gas temperature T_g, provided that the measurement accuracy is up to 5–7%. From Fig. 2, we can readily see that the degree of dissociation of oxygen molecules, $[O(^3P)]/[O_2]$, is a linear function of the discharge current and is essentially independent of the gas pressure over the entire pressure range under investigation (in our experiments, the maximum and minimum gas pressures differed by a factor of about 20, in which case the reduced electric field changed by a factor of approximately 3, from about 80 Td at 3 torr to about 250 Td at 0.15). In [12], it was shown that taking into account the nonlocal nature of the EEDF appreciably changes the values of the rate constants for the electron impact excitation of the atomic levels and, consequently, the intensities of the spectral lines. In this case, however, the ratios of the rate constants for the excitation of states with nearly the same energy thresholds, as well as the ratios of the spectral line intensities, essentially coincide with those calculated from the local approximation. Hence, we have

$$\frac{k_{\text{nonloc}}^{0}}{k_{\text{nonloc}}^{\text{Ar}}} \approx \frac{k_{\text{loc}}^{0}}{k_{\text{loc}}^{\text{Ar}}}, \tag{5}$$

where $k_{\text{loc}}^{\text{O}}$ and $k_{\text{loc}}^{\text{Ar}}$ are the averaged (over the discharge tube cross section) rate constants for the excitation of oxygen and argon atoms calculated from the local EEDF and $k_{\text{nonloc}}^{\text{O}}$ and $k_{\text{nonloc}}^{\text{Ar}}$ are the averaged (over the discharge tube cross section) excitation rate constants calculated with allowance for the nonlocal nature of the EEDF. Relationship (5) yields

$$\frac{k_{\text{nonloc}}^{0}}{k_{\text{nonloc}}^{0}} \approx \frac{k_{\text{nonloc}}^{\text{Ar}}}{k_{\text{loc}}^{\text{Ar}}}, \tag{6}$$

which indicates that the actinometric method can be used to investigate the rate of dissociation of oxygen molecules in a plasma with a nonlocal electron energy distribution.

In order to measure the probabilities of surface recombination of $O(^3P)$ atoms, we used the following approach. If an equilibrium state of a steady discharge plasma is disturbed sufficiently rapidly by one or another means, then different plasma components will relax on markedly different time scales. It is well known that these time scales are governed by the corresponding particle-loss processes. Since, at reduced

pressure, the chemical kinetic processes are slower, the concentration of $O(^3P)$ atoms will relax in the background of the plasma electrons, which have already relaxed to an equilibrium distribution and whose density has already reached its equilibrium value. Under the assumption that the main loss mechanism for oxygen atoms is heterogeneous recombination, an analysis of the curves describing the change $\delta[O(^3P)](t)$ in the density of oxygen atoms in kinetic processes in a modulated discharge makes it possible to obtain the probabilities of the surface recombination of atomic oxygen under specific discharge conditions. In our experiments, the discharge plasma equilibrium was disturbed by slightly modulating the discharge current by rectangular pulses with a modulation depth of 5–20%. Since the ratios of the rate constants for the excitation of radiating atomic states depend very slightly on the reduced electric field E/N [12, 13], the use of the actinometric method makes it possible to eliminate an experimental error resulting from the possible nonlocal nature of both the EEDF and electron density after the current changes stepwise. The fact that the electron density n_e in an oxygen-containing plasma relaxes on a long time scale is attributed to the processes of associative electron detachment from negative ions in their collisions with oxygen atoms and metastable singlet oxygen molecules [9].

Figure 3a shows representative waveforms of the discharge current (J_d) and of the intensities of the 777.1-nm spectral line of oxygen atoms (I_{777}^{O}) and the 750.3-nm spectral line of argon atoms (I_{750}^{Ar}) in a modulated discharge. In this figure, the intensities are reduced to a common scale, i.e., the intensity of the emission line of argon atoms is normalized to that for oxygen atoms, $I_{777}^{O} = C_{Ar}^{O} I_{750}^{Ar}$. The reason is that, in order to provide a correct description of the time evolution of the concentration of oxygen atoms $\delta[O(^3P)]$ in a modulated discharge, it is necessary only to know the behavior of the relative intensities of the spectral lines. Figure 3b shows the time evolution of the intensity ratio I_O/I_{Ar} and also the exponential fittings of this ratio in the stages in which it increases and decreases. We can see that the exponents describing the behavior of ratio I_O/I_{Ar} in the stages of its increase and its decrease coincide with good accuracy. This indicates that the method proposed here is applicable to the study of the heterogeneous recombination of atoms and, accordingly, the approach based on the balance equation (1) can legitimately be used to investigate dissociation of oxygen molecules in a discharge.

Figure 4 shows the probability γ_O of loss of oxygen atoms at the tube wall as a function of oxygen pressure p for different discharge currents J_d. The probabilities of loss in heterogeneous recombination are known to depend not only on the discharge conditions but also on the material of the tube and the state of its surface. That is why, in order to provide a correct comparison between the probabilities obtained experimentally and those calculated numerically, we carried out experiments with two tubes of molybdenum glass of the same grade, one fabricated ten years later than the other. In experiments with each of these tubes, we carried out a full cycle of actinometric measurements of the concentration of oxygen atoms and the rates of their loss in the positive discharge column. From Fig. 4, we can readily see that, although the probabilities $\gamma_O(p, J_d)$ obtained in experiments with each of the tubes are similar in shape, they nonetheless differ in absolute value. This difference can stem from different structures of the surfaces of the tubes. Since the probabilities $\gamma_O(p, J_d)$ are similar in shape in both series of experiments, the active surface centers at which the atoms are absorbed and lost are presumably of the same physical nature. However, the number of such centers at the surfaces of the tubes can be different (recall that the surface loss probability is directly proportional to the number of these centers) because it depends more on the method and conditions of fabrication of the tube material than on the material itself. Hence, in comparing the calculated values of γ_O with the experimentally obtained values, the absolute measurements can be regarded as having an accuracy of ±50%. As for the shape of the probability $\gamma_O(p, J_d)$, it is derived from the relative measurements and is thus reproducible with an accuracy of better than 10%. That is why the correctness of the calculations of the dissociation rates of oxygen molecules and, accordingly, of the probabilities of the heterogeneous recombination of $O(^3P)$ atoms were primarily checked against the shapes of the probability $\gamma_O(p, J_d)$ that were obtained from the relative measurements.

3. NUMERICAL MODEL

Numerical simulations were carried out with a self-consistent computer model of a dc glow discharge in pure O_2. This model was developed in our earlier papers [9, 11, 12] in studying the nonlocal nature of the EEDF, the spatial distributions of negative ions, and their kinetics. The model was described in detail in [16]. To proceed further, we should make the following brief remarks.

In [9, 11, 12], based on a comparison of the results from different approaches to solving the Boltzmann equation with the results from exact calculations of the electron distribution function by a particle-in-cell–Monte Carlo (PIC–MC) method, it was shown that, for $pd \le 0.5$ torr cm, the well-known and most widely used local approach, in which the EEDF at a given point in space is a function of the local value of the electric field, does not adequately describe both the electron kinetics and discharge structure. It was also shown that, by using different simple approaches in which the nonlocal nature of the EEDF is taken into account, it is pos-

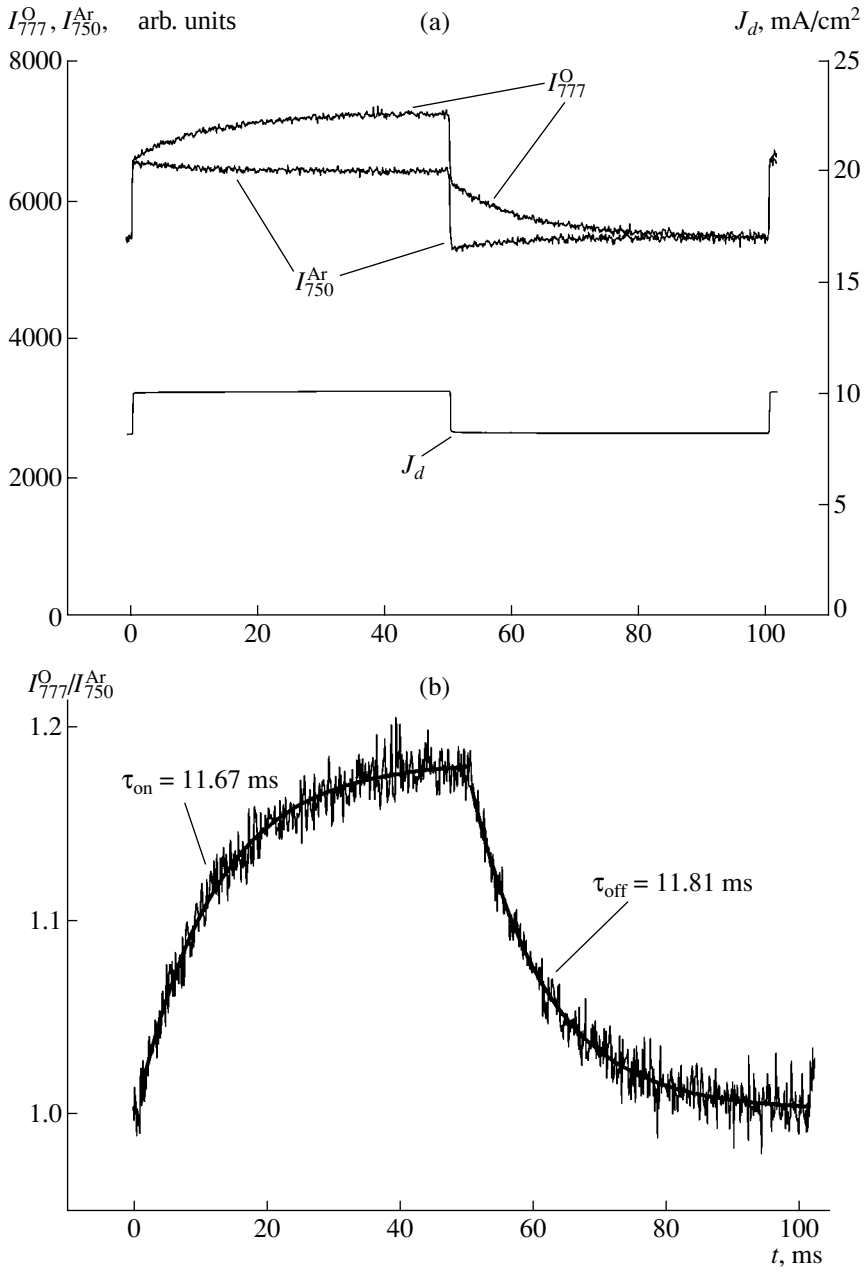

Fig. 3. (a) Representative waveforms of the discharge current (J_d) and of the intensities of the 777.1-nm spectral line of oxygen atoms (I^{O}_{777}) and the 750.3-nm spectral line of argon atoms (I^{Ar}_{750}) in a modulated discharge at an oxygen pressure of p_{O_2} = 0.4 torr. (b) Temporal dynamics of the ratio of the intensities of the spectral lines of oxygen atoms (I^{O}_{777}) and argon atoms (I^{Ar}_{750}) in a modulated discharge at an oxygen pressure of p_{O_2} = 0.4 torr (see Fig. 3a). The heavy curves are for the exponential fittings of the ratio I^{O}_{777}/I^{Ar}_{750} in the stages of its increase and its decrease. Also shown are the characteristic loss times for oxygen atoms obtained from the results of fitting to the experimental data.

sible to correctly describe the structure of the discharge in a slightly nonuniform field.

It is known [14] that, in discharges in O_2, the concentrations of metastable oxygen molecules $O_2(a^1\Delta_g)$ and of metastable oxygen atoms can be fairly high, so that collisions of electrons with such molecules and atoms may have an effect on the EEDF. Our calculations of the EEDF for $O(^3P)$ and $O_2(a^1\Delta_g)$ concentrations above those observed experimentally showed that collisions of electrons with these metastable particles

can be ignored. That is why, in our work, we did not solve a general set of equations consisting of the Boltzmann equation and chemical kinetic equations for plasma particles of all species. The rate constants of the processes involving the electrons were calculated independently of the already calculated EEDF.

The radial profiles of the concentrations of different plasma components were calculated from the solutions to the continuity equations under the assumptions that the rate constants of the reactions involving the electrons and the electron diffusion coefficient are determined only by the local value of the axial electric-field component E_z in a plasma and that the drift velocities in the r and z directions are determined, respectively, by the radial and axial components of the electric field. In [7, 9, 17, 18], it was shown that ion heating in the longitudinal electric field E_z can substantially increase the rate of ion diffusion in the radial direction, thereby changing the radial profiles of the concentrations of ions of different species. In our simulations, the effect of the ion heating by the axial electric field on both the ion diffusion coefficient and ion–molecule reactions was taken into account in essentially the same manner as was done in [9].

The set of continuity equations was closed by Poisson's equation for the radial electric-field component. It was assumed that the longitudinal component E_z is independent of r, so that it could be determined from a given value of the total current in the axial direction.

The probabilities $\gamma_O(p, J_d)$ were calculated according to Eq. (1) with the dissociation rate averaged over the discharge tube cross section. The concentration of $O(^3P)$ atoms was set equal to the experimentally measured concentration.

4. DISCUSSION OF THE RESULTS

Preliminary calculations showed that, in accordance with the results of [11, 12], the nonlocal nature of the electron kinetics is actually important in the range $pd \leq$ 0.5 torr cm: the local and nonlocal models yield markedly different values of the rate constants for exciting the high-lying states and of the dissociation and ionization rate constants. Thus, the averaged (over the discharge tube cross section) dissociation rate constants calculated in the local and nonlocal approximations for a pressure of 0.1 torr differ by a factor of almost 2. However, the ratios of the rate constants for the excitation of atomic levels calculated from the two models coincide within an accuracy of 1–2%, in complete agreement with relationship (6). This indicates that the nonlocal EEDF can also be correctly described by a local discharge model, provided that the coefficients accounting for the nonlocal effects in a well-studied process (e.g., ionization) are known or are calculated in advance. This conclusion can easily be confirmed by comparing the numerical results with the results of measuring the discharge current and electric field in a plasma. We made such a comparison for the ionization rate constant and convinced ourselves that relationship (6) is correct. Then, we used this relationship to determine the ratios of the ionization rate constants averaged over the discharge tube cross section, $k^{\text{ion}}_{\text{nonloc}}/k^{\text{ion}}_{\text{loc}}$, and the same ratios of the dissociation rate constants, $k^{\text{diss}}_{\text{nonloc}}/k^{\text{diss}}_{\text{loc}}$, in the exact numerical discharge model, whereas the electron spectrum was calculated using the combined PIC–MC method in a local discharge model in which the EEDF was determined by solving the homogeneous Boltzmann equation. Since the calculations based on the combined PIC–MC method required a larger amount of computer time, we were able to simulate only a limited number of discharge regimes. Using the results of these simulations, we determined how the ratio $k^{\text{diss}}_{\text{nonloc}}/k^{\text{diss}}_{\text{loc}}$ depends on the discharge conditions, namely, on the gas pressure and discharge current. In order to carry out simulations for a wide range of discharge parameters, the effect of the nonlocal nature of the electron spectrum on the dissociation of oxygen molecules was also investigated by using the local model and the already computed ratios $k^{\text{diss}}_{\text{nonloc}}/k^{\text{diss}}_{\text{loc}}$.

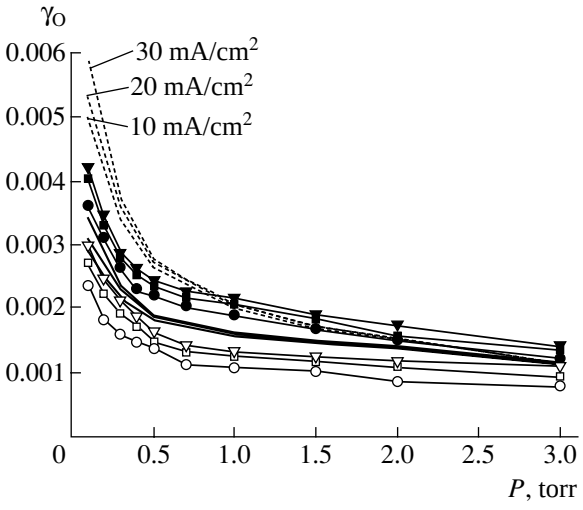

Fig. 4. Probability of loss of oxygen atoms at the wall of the molybdenum tube, γ_O, vs. oxygen pressure at different discharge current densities: 10 (circles), 20 (squares), and 30 (triangles) mA/cm^2. The open symbols show the experimental data obtained with the "older" molybdenum tube (fabricated in 1987), and the closed symbols show the data obtained with the "newer" molybdenum tube (fabricated in 1997). The dashed curves illustrate the results of calculating γ_O by the local discharge model (see text), and the heavy solid curves illustrate the results of calculating γ_O by the nonlocal discharge model (see text).

The probabilities of the heterogeneous recombination of oxygen atoms were calculated according to Eq. (1) in the local and nonlocal discharge models. The results of these calculations are illustrated in Fig. 4. We

can see that, in the range $pd > 1$ torr, in which the electron spectrum is only slightly nonlocal, the models yield the same results and, moreover, the calculated probabilities $\gamma_O(p, J_d)$ are similar to the experimentally measured ones not only in shape but also in absolute value. However, for lower gas pressures such that $pd <$ 1 torr cm, the difference between the results calculated in the local model and the experimental data becomes considerable and goes far beyond the limits of experimental error, while the nonlocal model, as before, correlates well with the experiment. This indicates that it is important to take into account the nonlocal nature of the electron spectrum in studying various plasmochemical processes in low-pressure discharges. Thus, most of the present-day plasmochemical reactors for surface treatments (such as those for plasma etching and for gas-phase deposition of films in microelectronics) operate in the range $pd < 0.2$–0.5 torr cm. Very often, however, plasmochemical processes in such reactors are modeled without allowance for the nonlocal electron kinetics. This, of course, significantly reduces the predictive capability of computer models that are being developed for the reactors and can even be a source of erroneous conclusions that may be drawn from the results of an analysis of experiments on the basis of these models.

From the experimental results illustrated in Fig. 4, it can easily be seen that the probability of the heterogeneous recombination of oxygen atoms is not constant but varies with the discharge conditions. For discharges in molybdenum glass tubes, it increases with increasing discharge current and decreasing gas pressure. This means that the probability of surface losses of $O(^3P)$ atoms does indeed depend on many factors and processes (the nature of the active surface centers, the occupation degree, the surface diffusion of the adsorbed particles, the ion bombardment of the surface, etc.) and thereby should be interpreted as a mechanism for surface recombination of the atoms. Such a dependence can provide a key to studying the mechanisms by which active plasma particles interact with the surfaces. This issue requires a separate investigation and will be addressed in the near future.

5. CONCLUSIONS

Using a dc glow discharge in pure oxygen as an example, we have investigated the effect of the nonlocal nature of the EEDF on the dissociation of oxygen molecules. To do this, we experimentally measured the concentrations of oxygen atoms and the rates of their loss as functions of the discharge parameters. An analysis of the experimental results by the nonlocal and local models (i.e., with and without allowance for the nonlocal nature of the electron energy spectrum) shows that the nonlocal nature of the EEDF has a significant effect on the concentration of oxygen atoms. Hence, in investigating plasmochemical processes in low-pressure discharges and in developing reactors that operate at low pressures, a correct interpretation of the results obtained is possible only when the nonlocal electron kinetics is taken into account.

ACKNOWLEDGMENTS

This work was supported in part by the Russian Foundation for Basic Research, project no. 02-02-17373.

REFERENCES

1. U. Kortshagen, Phys. Rev. E **49**, 4369 (1994).
2. V. I. Kolobov and V. A. Godyak, IEEE Trans. Plasma Sci. **23**, 503 (1995).
3. U. Kortshagen, I. Pukrovski, and L. D. Tsendin, Phys. Rev. E **51**, 6063 (1995).
4. U. Kortshagen, G. J. Parker, and J. E. Lawler, Phys. Rev. E **54**, 6746 (1996).
5. C. K. Birdsall, IEEE Trans. Plasma Sci. **19**, 102 (1991).
6. *Electron Kinetics and Applications of Glow Discharges*, NATO ASI Ser., Ser. B **367** (1998).
7. V. A. Feoktistov, V. V. Ivanov, A. M. Popov, *et al.*, J. Phys. D **30**, 423 (1997).
8. V. A. Feoktistov, D. V. Lopaev, K. S. Klopovsky, *et al.*, J. Nucl. Mater. **200**, 309 (1993).
9. V. V. Ivanov, K. S. Klopovskiy, D. V. Lopaev, *et al.*, IEEE Trans. Plasma Sci. **27**, 1279 (1999).
10. V. V. Ivanov, K. S. Klopovskiy, D. V. Lopaev, *et al.*, Pis'ma Zh. Éksp. Teor. Fiz. **63**, 511 (1996) [JETP Lett. **63**, 537 (1996)].
11. V. V. Ivanov, K. S. Klopovskiy, D. V. Lopaev, *et al.*, Fiz. Plazmy **26**, 1038 (2000) [Plasma Phys. Rep. **26**, 972 (2000)].
12. V. V. Ivanov, K. S. Klopovskiy, D. V. Lopaev, *et al.*, Fiz. Plazmy **26**, 1046 (2000) [Plasma Phys. Rep. **26**, 980 (2000)].
13. D. Pagnon, J. Amorim, J. Nahorny, *et al.*, J. Phys. D **28**, 1856 (1995).
14. G. Gousset, C. M. Ferreira, M. Pinheiro, *et al.*, J. Phys. D **24**, 290 (1991).
15. M. Touzeau, M. Vialle, A. Zellagui, *et al.*, J. Phys. D **24**, 41 (1991).
16. V. V. Ivanov, K. S. Klopovskiy, D. V. Lopaev, *et al.*, Preprint No. 2000-16/620 (Institute of Nuclear Physics, Moscow State University, Moscow, 2000).
17. R. N. Franklin, P. G. Daniels, and J. Snell, J. Phys. D **26**, 1638 (1993).
18. V. I. Kolobov and D. J. Economou, Appl. Phys. Lett. **72**, 656 (1998).

Translated by G.V. Shepekina